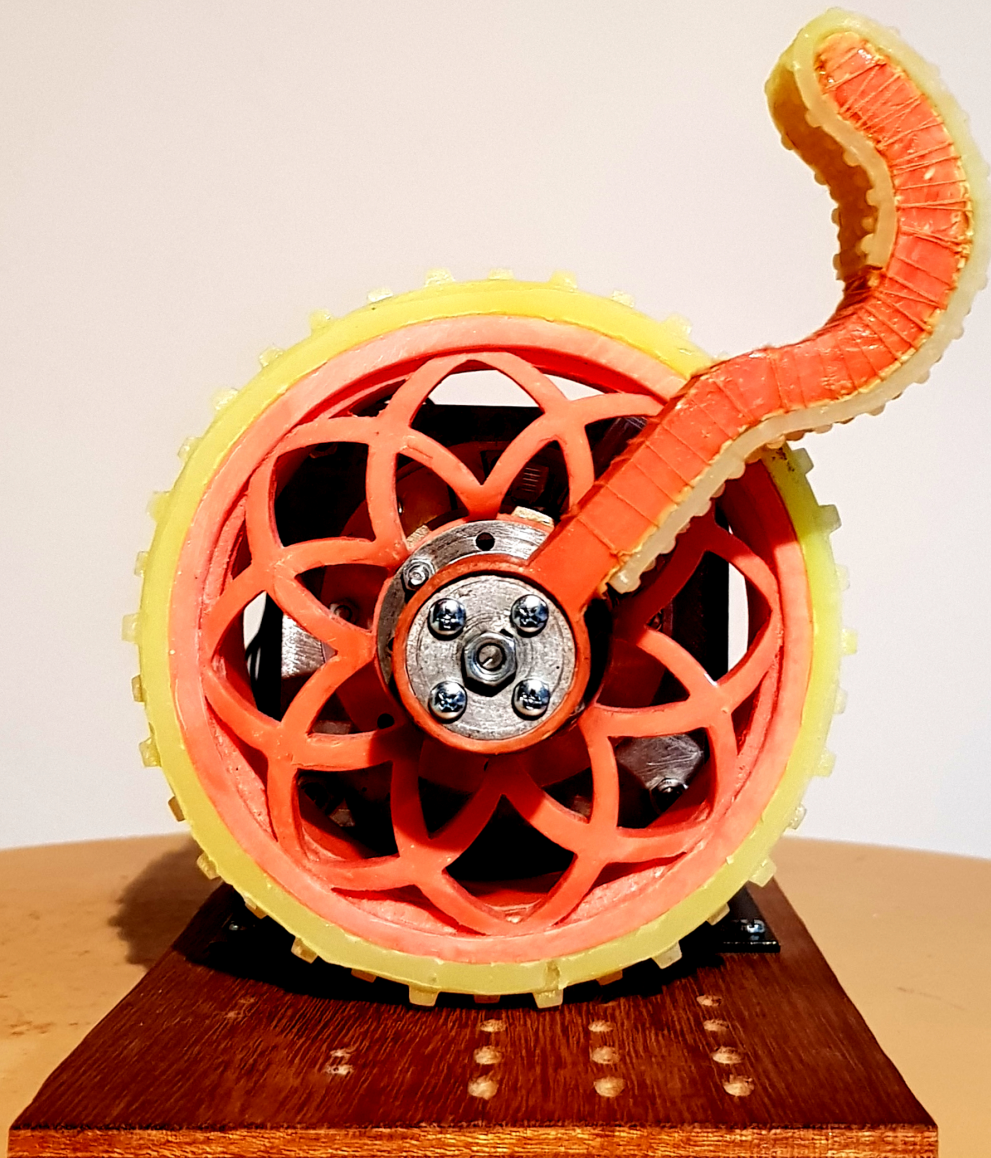# Development of a module with driving and walking capability

Study in the feasibility for application with a ZebRo robot

L.I. Bongaardt

TUDelft

Delft
University of
Technology

Intelligent Mechanical Systems

Development of a module with driving and walking capability

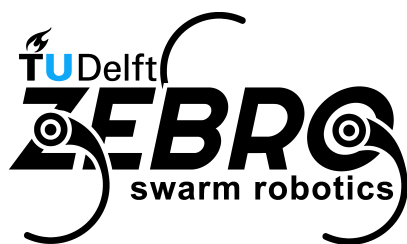**Study in the feasibility for application with a ZebRo robot**

MASTER OF SCIENCE THESIS

For the degree of Master of Science in Intelligent Mechanical Systems at Delft University of Technology

L.I. Bongaardt

April 9, 2021

Faculty of Mechanical, Maritime and Materials Engineering (3mE) · Delft University of Technology

DELFT UNIVERSITY OF TECHNOLOGY
DEPARTMENT OF
BIOMECHANICAL DESIGN (BMD)

The undersigned hereby certify that they have read and recommend to the Faculty of
Mechanical, Maritime and Materials Engineering (3mE) for acceptance a thesis
entitled

DEVELOPMENT OF A MODULE WITH DRIVING AND WALKING CAPABILITY

by

L.I. BONGAARDT

in partial fulfillment of the requirements for the degree of

MASTER OF SCIENCE INTELLIGENT MECHANICAL SYSTEMS

Dated: <u>April 9, 2021</u>

Supervisor(s):

                                             Ir.Dr. Chris Verhoeven

                                Prof.Dr. Robert Babuška, M.Sc.

Reader(s):

                                             Ir.Dr. Chris Verhoeven

                                Prof.Dr. Robert Babuška, M.Sc.

                                    Dr. Cosimo Della Santina

Abstract

At present time, there is an increasing interest in the development of mobile autonomous robots. These robots can be deployed in Search & Rescue missions or explore outer-space terrains like the Moon or Mars. One such robot is the Zesbenige Robot (ZebRo), developed at the Delft University of Technology (TU-Delft). ZebRo is a small, light-weight robot with six One-Degree-of-Freedom (DoF) C-shaped legs and walks with an insect inspired gait. It is being developed for outer-space missions and in addition offers a platform for research on robotic mobility.

Walking is a natural form of locomotion and offers great mobility on rough terrain. It is however slow and less energy efficient in comparison to driving, an artificial form of locomotion invented by humans. But whereas driving is more efficient, it is only suitable for relatively flat surfaces. Because both forms have their strengths and drawbacks, a new approach is to combine the two into a hybrid walking-driving technology.

In this research we will examine the feasibility of applying hybrid walking-driving technology to the ZebRo robot. The objective is to increase its speed and energy efficiency on flat surfaces, while maintaining its mobility and robustness on rough terrain.

The research starts by exploring a variety of options and combinations and reducing those to the five most promising concepts. The best concept was chosen by weighing the concepts on five criteria: Walking ability, Driving ability, Robustness, Efficiency and Compatibility with the ZebRo-platform. The chosen concept consists of a ZebRo-robot with six modules. Each module has a One-DoF leg and a wheel, with their respective axles in-line with a coupling and a motor. The coupling is then able to switch power from the motor between the leg and the wheel. To study the feasibility of the concept, one module was developed into a prototype, tested and evaluated.

To design the best wheel and leg for the prototype, a number of simulations were done with models of a wheel and a C-shaped leg using multi-body dynamics software. We discovered that the leg should be optimized for grip to maximize its ability to overcome obstacles. And we found that the wheel diameter should be as large as possible to maximize its driving ability. For the prototype the leg was therefore chosen to have a hook-shaped design, so as give it better grip in combination with the wheel. The wheel diameter was limited by the dimensions of the robot and was chosen to have a diameter of 12cm.

We could not find a suitable existing coupling which matches the functionality, dimensions and torque requirements for this application. Therefore it was decided to develop a custom design. This coupling consists of an electro-magnet and springs that pull and push an armature between friction-plates mounted to the Leg-axle and the Wheel-axle. When disengaged, the coupling drives the Wheel-axle while keeping the Leg-axle fixed. When engaged, the coupling drives the Leg-axle and the Wheel-axle is free.

A prototype was build and tested with different speeds of the motor. We measured electrical power consumption of the module overall and of the electro-magnet by itself. We also measured output torque and speed of both the Leg-axle and the Wheel-axle. With the test results, we evaluated the module and were able to set up some performance projections for a complete robot with six modules.

In conclusion, the new module was found to have great potential. It can reduce energy consumption by a third and offer a 50% increase in speed in driving mode at the cost of 5.6% more energy consumption in walking mode. Where driving is assumed to be possible on terrain with a maximum surface roughness of 3cm. The drawback is that the coupling is still unable to transfer sufficient torque to the axles at this point due to faults with the armature design. The module also does not yet meet the criteria for robustness, due to its complexity and vulnerability to shocks and temperature influences, which is required for the robot to go on missions.

For future research, we could identify four possible avenues. First is to continue development of the current prototype. The focus should be on the simplification and weight reduction of the coupling. Second possibility is to explore a design with store-bought components which could increase its robustness. The functionalities of the coupling might have to be divided into separate functions in order to cover all the requirements. The third option is to consider a second motor and possibly split the Leg-axle and the Wheel-axle. This could offer full control over both axles and reduce complexity at the same time. The last possibility is to consider a mono-shape with both leg and wheel integrated into one form. This is expected to achieve relatively modest gains in driving ability, but at almost no cost in added complexity.

Table of Contents

List of Figures

Preface & Acknowledgements

Robots have always been a fascinating topic for me. The ways in which they interact with people and their cognitive abilities sets them apart from any other machine and can sometimes even make them feel like living things. And they have the potential to greatly advance mankind as well. Whether it is with assistance in daily life, exploration of space or to perform rescue missions in hazardous environments, robots are applicable in many different scenarios. This document is part of my Master of Science graduation thesis in which I hope to make a contribution to the advancement of robots. Locomotion on rough terrain is still one of the most challenging aspects of robotics. Insufficient reliability and efficiency makes walking technology as of yet prohibitive, so wheels are still used in most practical applications. But driving is not very suitable for rough-terrain. This is why there have been attempts to combine the two forms of locomotion. Hybrid walker-wheeler locomotion is a relatively unexplored field where we might discover new solutions.

This work has sometimes been difficult to write and I could not have done it without the help of some great people around me. I would like to thank my parents and my brother for their continuing support and patience. I would also like to thank my supervisors, prof.dr.ir. Chris Verhoeven and Dr.ir. Robert Babuška, for their assistance and their guidance during the writing of this thesis. And finally I would to thank Hans Duivenvoorde, who called me every week with feedback and advice.

Delft, University of Technology   L.I. Bongaardt
April 9, 2021

"In the future, airplanes will be flown by a dog and a pilot. And the dog's job will be to make sure that if the pilot tries to touch any of the buttons, the dog bites him."

— Scott Adams

Chapter 1

Introduction

1-1 Context and Motivation

Throughout history there has always been a drive to improve mobility on land. The desire of men to travel made us domesticate animals, we invented wheels and motors and we developed extensive networks of roads and infrastructure. Today we are able to travel far and wide with great speed and efficiency, but there are still a few big challenges left. Travelling on unprepared surfaces, where wheels can not be easily used, is still difficult. Sometimes we are even forced to resort back to horses or sled dogs. And now that mankind has started to explore space, we encounter entire worlds with unprepared surfaces and the limitations of conventional transport are becoming ever more apparent.

Negotiating rough terrain is an issue for robots as well. In Search & Rescue missions, when robots are sent to disaster zones, they often have to negotiate debris, stairs or obstacles. This is what prompted engineers to build walking robots, such as Zesbenige Robot (ZebRo)[1], depicted in figure 1-1. It is a small-size walking robot inspired by the way insects move. With its six legs it has the ability to climb obstacles and negotiate rough terrain. ZebRo has a simple architecture that minimizes complexity and increases efficiency. It has only six motors and simple C-shaped legs with One-Degree-of-Freedom (DoF) that can be easily replaced or substituted. ZebRo was created by a research group at the Delft University of Technology (TU-Delft). The ultimate goal is to be deployed in outer-space missions, such as to the moon, where it will explore and collect samples. The ZebRo has become a platform for a wide range of research areas, including walking technology, swarm technology, modular architecture or energy consumption.

ZebRo is also the basis for this research, in which we try to contribute to the robot's abilities. One of the major drawbacks to walking robots is that they still can not
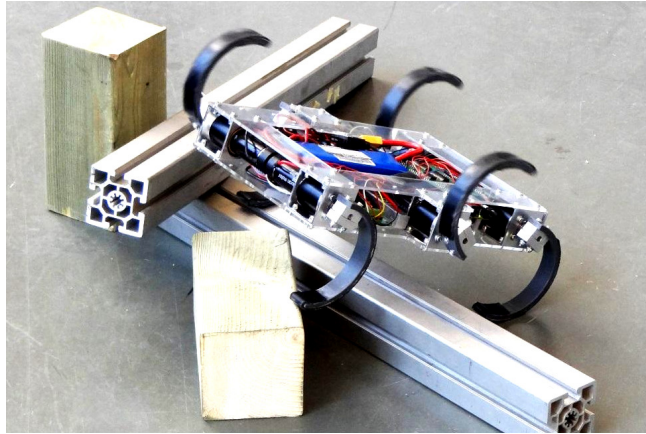
Figure 1-1: ZebRo

match the speed or efficiency of wheeled robots. They are also more complex, having more DoF and more parts, which create more possibilities of failure. It is because of these limitations, that walking machines are still not commonly used in real-world applications. In this thesis, we will explore the possibilities of hybrid walker-wheeler technology for the ZebRo.

1-2   Hybrid Walker-Wheeler Robots

Hybrid walker-wheeler technology is a relatively new approach to robot mobility. Hybrid walker-wheeler robots combine a form of wheeled locomotion with walker technology, attempting to harness the advantages of both. They use wheels on smooth terrain, saving energy and utilising better speed, while switching to legs in order to negotiate obstacles. Hybrid robots have been developed in many different configurations. One example is Quattroped[2], figure 1-2. This thesis follows on a previously conducted Literature Survey[3], in which this subject was studied in great length. For the scope of this research, we will only summarise the conclusions and recommendations.
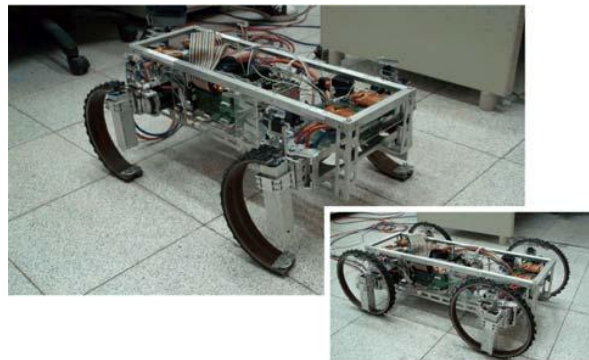
Figure 1-2: Quattroped

The Literature Survey identified a trade-off between walking ability and efficiency. Hybrid robots can be placed on a spectrum, the Spectrum of Hybrid Robots, depending on their driving and walking capability. A robot with greater walking ability has greater obstacle negotiation, but loses points on speed, efficiency and robustness. Whereas a robot with greater driving ability has great speed and efficiency, but is less capable in obstacle negotiation. It was therefore recommended to consider the intended application of a robot and identify the amount of obstacle negotiation and the amount of driving ability that is required.

Furthermore, the survey identified the importance of robustness. Mobile robots are often intended for autonomous missions in hazardous or remote environments, where humans are unable to assist. They must be able to endure dust, mud, shocks and be able to navigate around stairs, debris and other obstacles. When they are intended for outer-world exploration missions, in addition they must operate for a long time, possibly years, without any maintenance or backup. This makes robustness a crucial feature for these robots.

The current state-of-the-art, meaning robots that are the most popular in real-world applications, are simple robots with mostly driving ability and small adaptations to increase rough terrain mobility. Figure 1-3 shows 510 PackBot[4], which is widely used in Search & Rescue missions. Low complexity, resulting in high robustness, and great speed are important factors for its success. Another popular robot is Curiosity[5], shown in figure 1-4. This robot was successfully deployed on Mars. Its low complexity is an important reason for its success as well, in combination with great energy efficiency.

Figure 1-3: 510 PackBot   **Figure 1-4:** Curiosity

For future research, it was suggested to either 'move left' or to 'move right'. 'Move Left' means to start with a mostly driving robot and add walker features, thereby moving left on the Spectrum of Hybrid Robots. The intention is to preserve speed and efficiency, but increase rough terrain mobility. Alternatively, we could 'move right' on the Spectrum and start with a mostly walking robot, then apply wheeling features. The intention is to preserve its walking capabilities, while increasing speed and efficiency.

1-3   Research questions

In this thesis we will attempt to contribute to the current state-of-the-art of hybrid walker-wheeler robots and to apply this technology to the ZebRo platform. Since the ZebRo is a walker robot, we will 'move right' on the Spectrum of Hybrid Robots and add driving features aiming to increase its speed and efficiency, while trying to preserve its walking capability and robustness. These goals can be captured in the following research question:

> *Is it possible to develop a hybrid walker-wheeler robot, applied with the ZebRo platform, that increases its speed and energy efficiency on flat surfaces, while maintaining its robustness and walking capability on rough terrain?*

We will break this question down into ten sub-questions, which will be discussed in the upcoming chapters.

(I) What are the requirements for a ZebRo robot equipped with hybrid walker-wheeler technology?
This item refers to the requirements in relation to compatibility with the ZebRo platform as well as requirements that derive from its mission. These requirements will be used as the criteria to evaluate concepts and serve as the basis for evaluating the performance of the final prototype.

(II) What are the possible options and concepts for a hybrid walker-wheeler robot?
The goal here is to get an overview of the different options for driving and walking ability and their combinations. These combinations will then be judged on their feasibility and the most prospective combinations are developed into concepts. The concepts will be scored with respect to the criteria derived from the requirements and finally we will arrive at the best concept for further development.

(III) What are the characteristics of a C-leg and a wheel and how can we apply these in the design of a hybrid module?
The shape and dimensions of the legs and wheels have great impact on the forces and the torque during movement. They also determine obstacle negotiation ability and driving ability. A number of simulations are done with multibody simulation software to determine the right configuration for the ZebRo.

(IV) How should the chosen concept be developed into a prototype module for evaluation?
To evaluate the final concept, it must be completely designed and developed into a prototype. Before the complete robot is built, we will first build one module and only proceed to a full robot once it has been evaluated.

(V) How should the module be tested in order to evaluate it with the previously determined criteria?
Here we look at the testing set-up in order to examine the parameters that the prototype will be evaluated on.

(VI) Would the prototype be able to achieve an overall higher speed?
This is an evaluation of the prototype on its potential speed gain.

(VII) Can the new robot maintain the rough terrain mobility in comparison to a conventional ZebRo?
Here we evaluate the torque and walking capability of the module.

(VIII) Can the new prototype achieve a greater energy efficiency than a conventional ZebRo?
Here we want to know if the prototype module is performing as expected in relation to power consumption.

(IX) Would the new robot maintain high robustness?
An evaluation of the complexity and reliability of the module.

(X) What recommendations can be made for future research?
When the previous questions are answered, we can make predictions of the performance of ZebRo when equipped with six of the prototype modules. We will then be able to determine if the new design is worthy of further development.

(XI) What are the potential societal effects of Hybrid Walker-Wheeler robots?
Here we want to do an evaluation of the potential consequences of this research.

Each sub-question will be discussed in the following chapters of this thesis. In table 1-1 we give an overview of the sub-questions and chapters.

Table 1-1: Research Questions versus Chapters

Sub-question	Chapter
I	2. Design Requirements
II	3. Concept Design
	4. Concept Selection
III	5. Simulation
IV	7. Concept Development
	8. Systems & Control
V	9. Testing
VI	10. Evaluation
VII	10. Evaluation
VIII	10. Evaluation
IX	11. Conclusions & Discussion
X	11. Conclusions & Discussion
XI	11. Conclusions & Discussion

Chapter 2

Design Requirements

In this chapter we will discuss the requirements for a new hybrid walker-wheeler robot. The new design will be incorporated with the Zesbenige Robot (ZebRo). ZebRo is to be an autonomous robot, intended for missions on the moon or possibly Mars. So we will explore the requirements from such a mission and the compatibility with ZebRo. From these requirements, we will determine the criteria for the prospective design.

2-1   Chapter Overview

An overview of this chapter is shown in table 2-1. We will first explore the requirements deriving from the mission. Then we will discuss the requirements for compatibility with ZebRo. We will then set-up the criteria on which prospective concepts will be evaluated. Finally, we will list the target goals that will be used to determine weights for the criteria.

Table 2-1: Section Overview

Section	Subject
2-1	Chapter Overview
2-2	Mission Requirements
2-3	Compatibility Requirements
2-4	Criteria
2-5	Target Goals

2-2   Mission Requirements

Two of the most important considerations in the new design are the environment and the mission in which it will function. In this research, we have chosen to consider a possible outer-space mission such as the moon or Mars, which will have a big influence on its parameters. It will demand a high degree of autonomy and reliability of the robot. In this thesis, we will mainly focus on the surface of Mars. The balancing point between walking and wheeling ability is a very important parameter in the design of a hybrid robot and greatly influences its effectiveness on a certain mission, which is why the expected surface should be studied. For the real mission, factors such as gravity, temperature and radiation would also have to be considered, but these will be omitted for the scope of this research.

Figure 2-1 is a picture of the Martian surface, taken by the NASA Curiosity rover[5]. This figure shows an overview of the types of surfaces that can be expected.

Type 1: This is the terrain seen in the middle and background of figure 2-1. This is the easiest type of terrain and consists of a relatively flat surface with a few rocks, bumps and ditches. This is where the wheels should mostly be used, with occasional help of the legs.

Type 2: This type can be seen on the foreground of figure 2-1. It is soft with sandy slopes and mull sand. The robot should be able to surmount this using a combination of its wheels and legs.

Type 3: Depicted on the right and left sides of picture 2-1. This is terrain that consists of a rough surface with many rocks, ditches and ridges. The robot might have to climb or descend because it is often located on a hill or on the edge of a crater. It is the most difficult type of terrain and the robot will mostly have to rely on its legs in these scenarios.
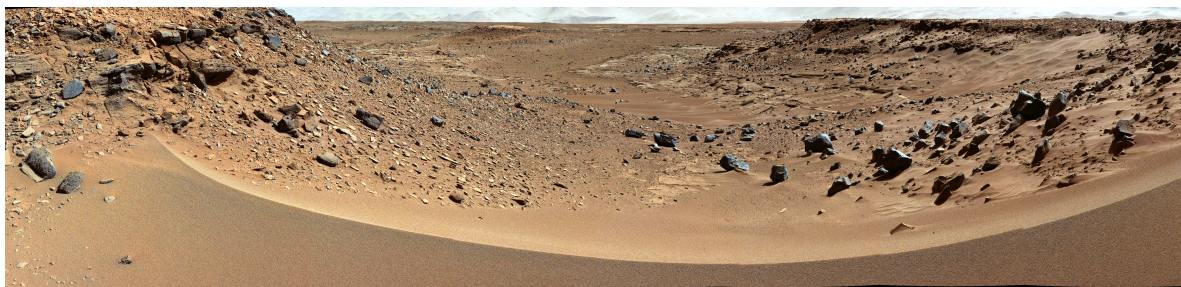
Figure 2-1: Martian Valley, captured by Curiosity

From the types of terrain, we can conclude that driving will be most dominant. Because the driving ability is expected to be used for both types 1 and 2 surfaces, wheeling ability should be developed most. The legs should only have to be used on the very rough surfaces. The basic idea will be a wheeled robot, which is in wheel-mode by default, paired with simple legs to be used for difficult terrain. Table 2-2 is a summary of the mission requirements.

Table 2-2: Mission Requirements

Parameter	Requirement
Walking Ability	Can negotiate sand, ditches and rocks
Driving ability	Can negotiate moderate bumps and ditches
Efficiency	High
Robustness	dust-proof, shock-proof
Speed	medium speed

2-3   Compatibility requirements

The next thing to consider is the compatibility with the ZebRo Platform (figure 2-2). ZebRo is a six legged robot platform which aims for a modular design. It has a central body structure with interchangeable leg-modules. It uses one-Degree-of-Freedom (DoF) legs, powered by stepper motors. The robot is approximately 30cm in length and the latest model weighs 7kg. Few actuators helps to reduce weight and complexity and it is a characteristic of the ZebRo. So the future design should match this and have no more then six motors as well. It should also consist of leg-wheel modules that can be interchangeable with the main body.

With ZebRo, the standard choice of motor is the Nanotec-ST4118-X1404B in combination with the GPLL40-24 Gear-reduction. Specifications are documented in Appendix A. This motor offers a high torque, small dimensions and the availability of elaborate documentation by the manufacturer, which is essential in the development of the design.

Parameter	Requirement
Modular	Interchangeable modules
Motors	maximum of 6
Type of Motor	Nanotec-ST4118-X1404B
Weight	10kg
Cost	Low production costs

Table 2-3: Platform Requirements
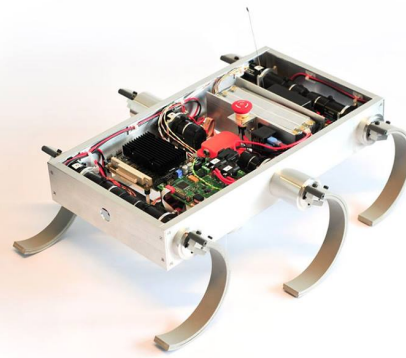
Figure 2-2: Zebro Platform

2-4   Criteria

Prospective concepts for the new design will be evaluated on a set of criteria which are derived from the previously conducted Literature Survey, the stated mission and the compatibility with ZebRo.

Walking Capability: This is a criterion to measure the performance of a hybrid walker-wheeler robot. It is a measurement for the robot's ability to negotiate rough-terrain and is divided into speed on rough terrain, obstacle negotiation and manoeuvrability.

Driving Capability: The counterpart of walking capability which is a measure for the concepts' ability on flat terrain. It is measured by the speed on flat terrain, Obstacle Negotiation and manoeuvrability.

Robustness: This criterion has already shown to be very important from the Literature Survey, but even more so for an outer-space mission. When no assistance is available, the robot has to be fully autonomous and survivability is of the essence. Robustness is a vague term that will be described as a combination of complexity, gait reliability and toughness. Complexity is important, because many, or vulnerable, parts makes a robot vulnerable to shocks. Gait reliability relates to the likelihood of a robot getting stuck. Toughness is about the robot being able to withstand dust, water or temperature influences.

Efficiency: Efficiency is the biggest challenge for a hybrid walker-wheeler robot and will be important in determining its viability for real-life missions. It is divided in efficiency on rough terrain and efficiency on flat terrain. In a final design, efficiencies are commonly evaluated in Cost of Transport (CoT), but this is too elaborate for concepts. Therefore in the design process, efficiency will be estimated based on the weight and amount of actuators that will be used.

ZebRo Compatibility: We look at how easy a concept can be integrated with the ZebRo platform. Concepts should have a modular and low-weight design, which allows a prototype module to be easily connected with an available body. The prototype should also be built within a reasonable budget.

2-5   Target Goals

Of course we aim for the new design to excel by all criteria, but concepts often involve trade-offs and have different strengths and weaknesses. We will set some expectations derived from the mission, which will help to prioritise each criterion and to set the weights in evaluating the concepts.

Table 2-4: Target Goals

Criterion	Sub-criterion	Target
Walking Ability	Speed	Low
	Obstacle Negotiation	very good
	Manoeuvrability	very good
Driving Ability	Speed	medium
	Obstacle Negotiation	medium
	Manoeuvrability	good
Robustness	Complexity	maximum 6 motors, few components
	Gait Reliability	can't get stuck
	Toughness	shock-proof, dust-proof
Efficiency	on Flat terrain	very good
	on Rough terrain	moderate
ZebRo Compatibility	Integratable	Modular design
	Cost	500 Euro

Chapter 3

Concept Decision Tree

In this chapter we will discuss the development of the concepts. The purpose of the methodology is to keep an open mind about the design and not miss any potentially good options. We will create an overview of the most important parameters and list all possible options for each parameter. Using a decision tree, these options are then combined to create different concepts. We find this results theoretically in 8880 possibilities. Subsequently, we remove options and combinations, and narrow down the decision tree, until only 5 combinations are left. These combinations have the most potential and will be examined more closely in chapter 4.

3-1 Chapter Overview

This chapter consists of 4 sections, listed in table 3-1. We will start with an overview of all the possible parameters and options. From this we can set-up the decision tree and reduce the options to determine the best combinations. The final concepts are formulated from these results.

Table 3-1: Section Overview

Section	Subject
3-1	Chapter Overview
3-2	Parameters and Options
3-3	Decision tree and Reductions
3-4	Resulting Concepts
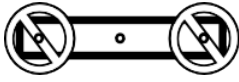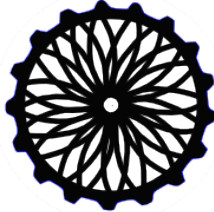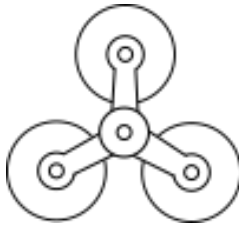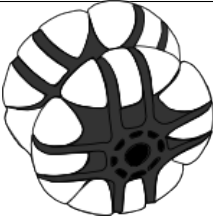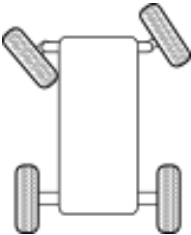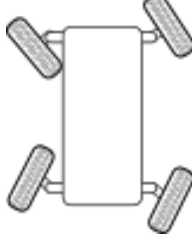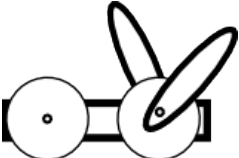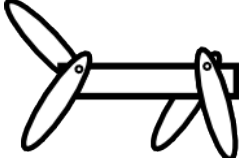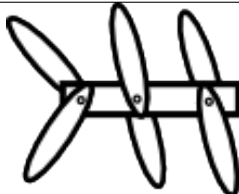
3-2 Parameters and Options

In the next three tables we will list 9 parameters for the new design. These are key decisions in its architecture, such as what type of leg or wheel to choose. We then consider every possible option for each parameter, for example 5 different wheel types. Options are found logically or originate from the Literature Survey[3], which identified a lot of good hybrid walker-wheeler robots and many different attributes.
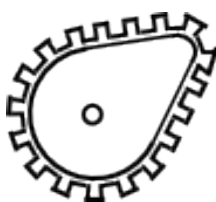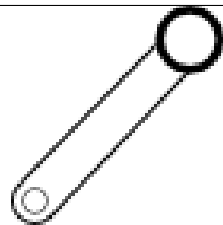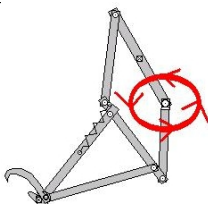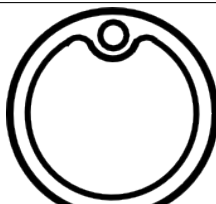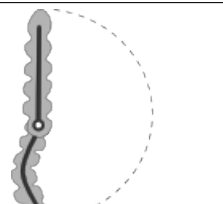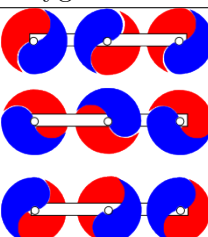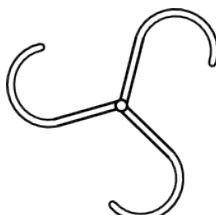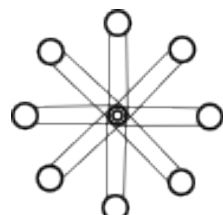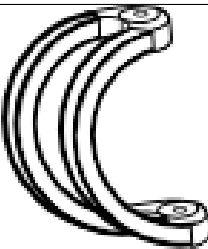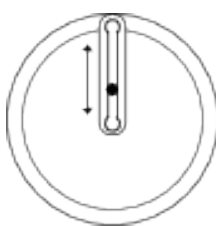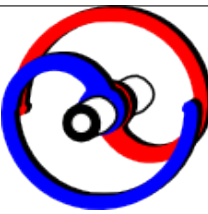
1. *Number of Wheels* - This is a parameter to consider, because it affects the robot in terms of balance, traction and weight. We have 3 options: 2, 4 or 6 wheels. These options are drawn schematically in table 3-2 and it can be seen how each option affects the architecture. Uneven numbers are disregarded, because a wheel in the middle would be incompatible with the Zesbenige Robot (ZebRo) architecture and an uneven number of wheels on each side would cause an imbalance.

2. *Wheel Type* - Naturally this is an important parameter, because the choice effects driving ability and complexity. The rigid wheel is the most basic option, with a firm rim and one axle. A flexible wheel has one center axle, but combined with a flexible outer rim. A stair-climber is a wheel with three smaller wheels, with the axis parallel to the center axis at the rim. The stair-climber was designed to climb steps. The omni-wheel is a wheel with smaller wheels, with the axis lengthwise to the center pivot, around its rim, enabling the wheel to slip sideways. The last option are tracks. Tracks consist of two or more wheels with a belt running around them.

3. *Steering* - The reason why Steering is mentioned as a parameter, is because its implementation has great consequences for the architecture of the design. Type of steering can be regarded as a consequence of the chosen architecture, however there are differences in performance such as traction, wear, required torques and manoeuvrability. The listed options are Ackermann-steering, Four-Wheel-Drive and Skid-steering (also called Differential steering).

4. *Number of Legs* - Similar as the number of wheels, we also want to consider the number of legs. 6 is the natural choice, but we still want to weigh over all the options. With regards to the architecture of the ZebRo, only even numbers are compatible. Therefore we can either choose 2, 4 or 6 legs.

5. *Leg shapes* - The chosen type of leg influences walking ability, weight and complexity. There are many possibilities, but because low complexity is a requirement with regard to the ZebRo platform, we have limited the options to one Degree-of-Freedom (DoF) shapes. These options are a C-shaped leg, wedge shape, a simple rigid bar, a polygramm truss, the eccentric wheel and a flexible bar.

6. *Combined Wheel-Leg shapes* - Instead of a separate wheel and leg, the two can also be combined into one shape. These wheel-leg shapes have the advantage of fewer parts and lower complexity, but driving and walking ability might be compromised. Options include a wheel-leg, multiple hook-shapes and a spokes-wheel. The schematic drawings in table 3-3 depict how this would work.

7. *Reconfigurable shapes* - These use an actuator, such as a servo or pneumatic piston, that transforms the shape between a leg and a wheel. They are more complex than a combined wheel-leg shape, but could have greater driving and walking ability. We have limited the possibilities to options with only one movement for reconfiguration. In the folding-1 option the shape pivots lengthwise. With the moving-center option the shape slides relative to the central axis. The folding-2 option uses a parallelogram mechanism to transform the shape. And the folding-3 option lets the shape rotate around the central pivot.

8. *Suspension* - We include suspension as a parameter because it can greatly increase traction ability or replace other features. In the case of Curiosity[5], its entire obstacle negotiation ability is based on a simple passive bogey-rocker suspension. Options are none, adaptive spring-damper, vertical spring-damper, Octopus-style suspension, bogey-rocker suspension and diagonal arms with spring-damper.

9. *Connection wheel-leg* - The final parameter is how a wheel and leg can be combined into a single module. This is only a parameter if the design would consist of a separate wheel and leg, as reconfigurable or combined shapes are already connected. There are 4 options. One option is to use a passive free-wheel coupling, the leg connected to the wheel connected to the body, wheel connected to the leg connected to the body or two axles with an active coupling.
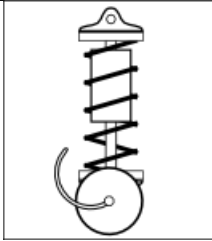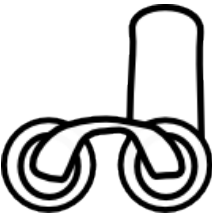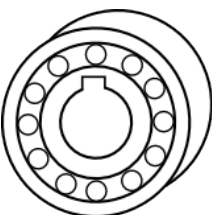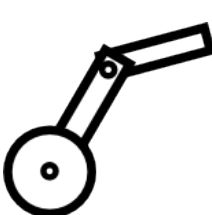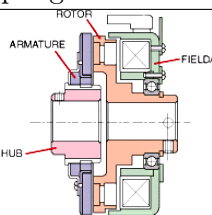
Table 3-2: Parameters and Options

Parameter	Options		
1. Number of wheels	2 wheels	4 wheels	6 wheels
2. Wheel type	Rigid wheel	Flexible wheel	Stair-climber
	Omni-wheel	Tracks	
3. Steering	Ackermann	Skid Steering	Four-wheel Drive
4. Number of Legs	2 legs	4 legs	6 legs

Table 3-3: Parameters and Options *continued*

Parameter	Options		
5. Leg shapes	C-Shape	Wedge	Simple rigid bar
	Polygramm truss	Eccentric round	Flexible Bar
6. Combined Wheel-Leg shapes	Wheel-Leg	Multiple hook-wheel	Spokes-wheel
7. Reconfigurable Shapes	Folding-1	Moving-center	Folding-2
	Folding-3		

Table 3-4: Parameters and Options *continued*

Parameter	Options		
8. Suspension	None	Adaptive spring-damper	Vertical spring-damper
	Octopus-style	Bogey-rocker	Diagonal arms with spring-damper
9. Connection Wheel-leg	Free-wheel coupling	Leg to wheel to body	wheel to leg to body
	Active coupling		

3-3   Decision tree and reductions

By choosing different parameters and options we can create possible combinations that can become concepts. But not every parameter combination is possible. For example, we could either choose a separate leg and wheel or a combined shape or a reconfigurable shape. And the wheel-leg connection parameter is only applicable when we choose a separate wheel and leg. These choices, with the options, are depicted in a decision tree, figure 3-1. By travelling along the nodes and pathways we then arrive at concepts. This entire diagram would entail a number of 8880 possible combinations. With this number, it is not possible to evaluate each combination individually, therefore we have to make decisions to narrow down the field.

Easy reductions - These are various options and combinations that can be easily omitted because they are, for instance, impractical or too complicated.
Omitted Options:

- Octopus-Suspension: Too complex with many parts and actuators. This would make the robot vulnerable to shocks.

- Spokes-wheel: The spokes do not allow much stepping height, which would hamper Obstacle Negotiation Ability.

- Multiple C-Shapes module: Too little driving ability.

- Tracks: Very susceptible to dust and wear, not reliable enough for long-term missions.

- Omniwheel: The small wheels on the rim are not functional with rough-terrain.

- Bogey-rocker suspension: Not easily compatible with the modular ZebRo platform.

- 2-wheels: Not stable enough and impractical for rough-terrain missions.

- Polygramm truss: Complicated, too limited stepping surface.

- Vertical spring-damper suspension: It is similar to a diagonal spring-damper, when the angle is a variable.

- Adaptive spring-damper suspension: costs additional actuators but is not beneficial enough for its cost in complexity and weight.

- Folding-1: Too complex and fragile.

- Simple Bar: little obstacle negotiation and no better than wedge.

- Moving-center:Too complex and reconfiguration would be slow.

- Four-wheel drive: Although it provides additional manoeuvrability in comparison to Ackermann-steering, the increase in complexity is too costly.

- 2-legs: Not enough climbing ability.

- 4-legs: Not stable enough and not enough climbing ability.
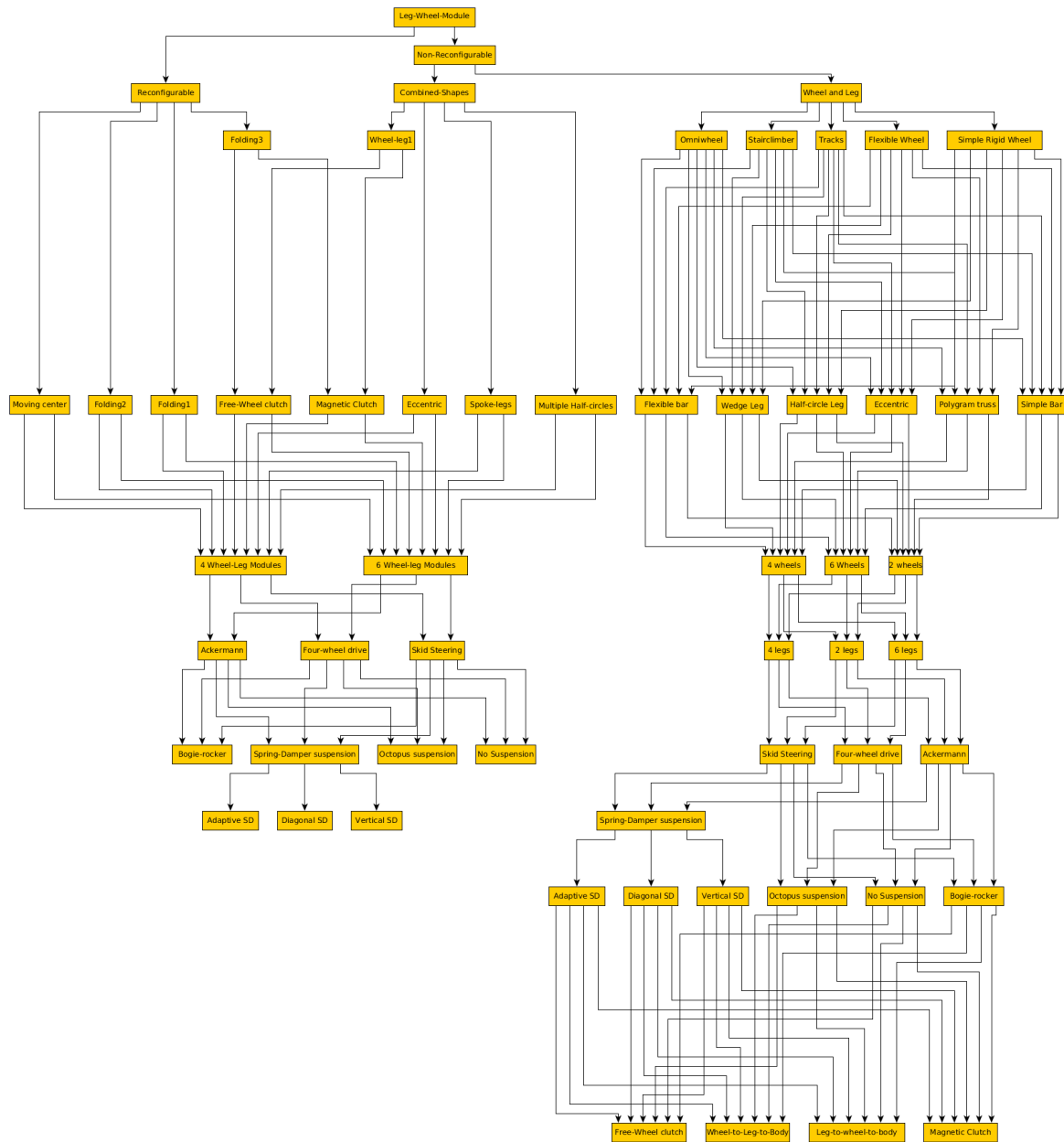
Figure 3-1: Complete Decision Tree

Omitted combinations:

- For the concept with separate wheel and leg configurations, to have only 4 modules is not possible, because it would make the robot unstable. It needs to have 6 modules alternating on the ground for it to work.

- 6 wheel-leg modules is necessary for concepts with reconfigurable shapes, because they transform into C-shaped legs and then need 3 alternating contact points for stability.

Further reductions - With the before mentioned reductions, there are still over 190 possible combinations. This is still far too many to handle, but now there are no easy or intuitive choices left. We will have to take a closer look at the options and weigh the benefits and drawbacks.

Steering Options - The remaining steering options are Ackermann-steering and Skid-steering. Four-Wheel-drive was previously omitted because the additional manoeuvrability is unlikely to be beneficial enough to justify the additional cost in complexity. In Maclaurin [6] and Wu [7], Ackermann- and Skid-steering are compared using simulation models. Skid-steering has the advantage of greater internal volume, better manoeuvrability, the ability to turn without lateral movement and it does not require a steering axle to turn the wheels. On the other hand, Ackermann-steering requires considerable less torque on the wheels and thus less power-consumption. Grip is higher because the wheels are faced towards the heading-direction and there is little longitudinal slip on the wheels, which will reduce wear considerably. This is especially true for low speeds, small turning radii and rough terrain. Ackermann-steering would be more desirable for its reduced wear and lower required torques, however it also requires an additional steering mechanism which is very costly in terms of complexity and difficult to integrate with the ZebRo platform. Each Leg-Wheel module will be individually actuated, due to its legs, and therefore the ZebRo is Skid-steered by default. The benefits of Ackermann-steering might be explored in future research, however in this thesis the scope will be limited to skid-steering.

Number of Wheels - Since the option of 2 wheels was previously omitted, we now have two options: 4 or 6 wheels. The choice between 4 and 6 wheels depends on the trade-off between the cost of added weight (2 more wheels and switching mechanisms) and the benefit of increased traction and stability in wheel mode. From an intuitive perspective, 6 wheels would be better because rough terrain mobility is most important and we intend to use light wheels.

Separate Leg and Wheel choice - The different options for leg and wheel types makes the decision tree very large. However, they have no particular influence on the architecture. The legs are all one DoF with an eccentric pivot and the options for wheel type all consist of bodies with one central pivot. Therefore we will condense the Leg and Wheel options into one block and evaluate them separately at a later stage.

Suspension Options - Because Bogey-rocker, Octopus-suspension and active suspension were previously omitted, the choices for suspension are now a passive spring-damper system or no suspension at all. This basically comes down to whether the suspension system is beneficial enough to justify the investment in complexity. A suspension system would greatly benefit obstacle negotiation, particularly in wheel-mode. It will increase wheel contact with the ground and distribute the body mass to increase traction of the wheels. Additionally, although of a lesser concern here, it will provide a more stable body movement. The drawback is the addition of springs and/or dampers and a double cardan axis, or similar mechanism, to the drive train. This will increase costs, weight and complexity. There is also the question of what the implications are in leg-mode, because no research has been done on this topic yet. Although a suspension system offers great benefits in traction and rough-terrain mobility, we decide it is too complex for the scope of this thesis. This option might be explored in future research.

Free wheel coupling - This is an option to drive a separate wheel and leg with one motor. The free-wheel coupling drives the wheels when the motor spins in one direction and drives the legs when the motor spins in the other direction. The advantage of this system is that no additional actuator is required for switching, but it needs an additional transmission between the coupling and the leg to have it turn in the correct direction. Furthermore, there would have to be a system to keep the leg upright when not in use. Finally, because the wheels and legs can not spin backwards, the robot can not walk or drive backwards, or make turns around its axis, thereby greatly hindering its manoeuvrability.

3-4   Resulting Concepts

After the reductions, the original decision tree, with 8880 possible combinations, has been greatly reduced. We will condense the options for wheel and leg shapes into one block, as those can be refined in the later research without impacting the concept choices. The new tree is as shown in figure 3-2. If we now follow the different pathways we get a total of 5 possible combinations. This is an acceptable number to work with and we can translate these into concepts.
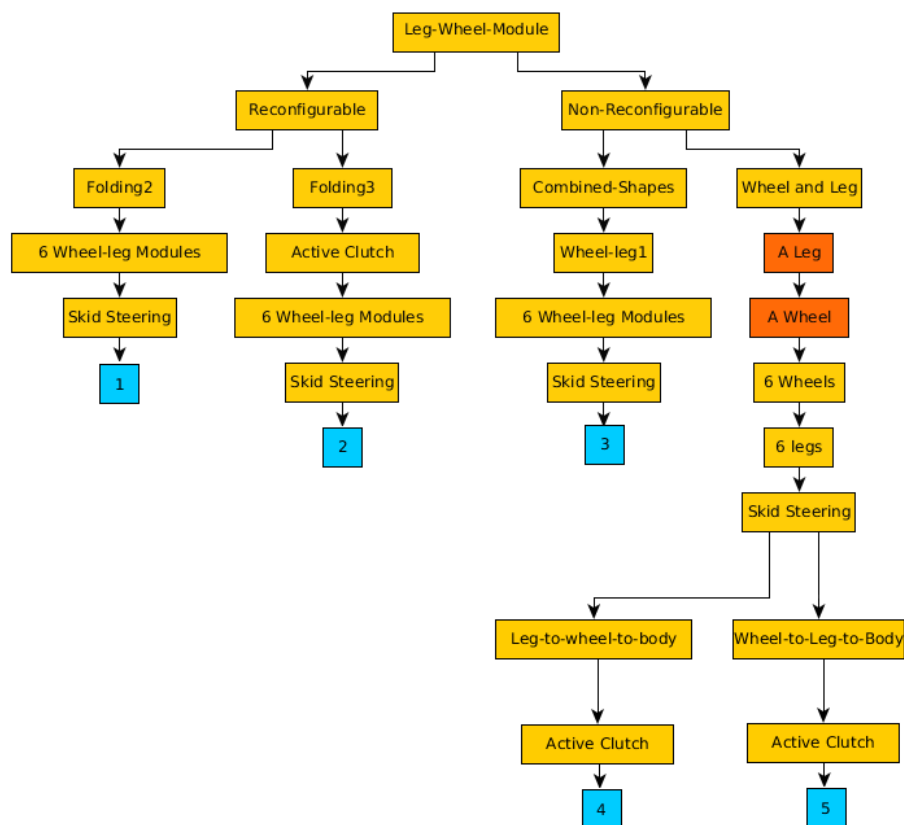
Figure 3-2: Reduced Decision Tree

Concept 1 - The first concept is the combination of 6 modules with a reconfigurable wheel-leg and a Folding-2 mechanism. The reconfiguration is based on a parallelogram, that moves part of the wheel relative to the central pivot. This transforms the wheel into a C-shaped leg that can be used for walking. The parallelogram will likely be controlled by a small servo-motor or a pneumatic cilinder, located inside the wheel. Switching would require a single movement, so it is quick and easy to use.

Concept 2 -This is the combination of 6 reconfigurable modules with a reconfigurable wheel-leg design. Reconfiguration is based on part of the wheel rotating around the center pivot, thus forming either a wheel or a leg shape. The rotation mechanism would be powered with an active coupling or a small actuator inside the mechanism, like a pneumatic cilinder or a servo-motor.

Concept 3 - Here we have 6 modules, each with a combined wheel-leg shape. The 6 modules together form a continuous ground contact, thereby creating driving ability. But there is also walking ability due to the leg-shape. There is no additional actuator, nor does the concept need any reconfiguration or connection mechanisms.

Concepts 4 - This is the combination of 6 modules with a separate wheel and leg, each with its own axle, connected through a central pivot. An active coupling is used to switch the engagement from motor between leg and wheel axle.

Concept 5 - This is the combination of 6 modules with a separate wheel and leg, where the wheel is connected to the end of the leg. With only one motor, power to the wheel would have to be transmitted with a transmission drive along the leg. To control the leg and wheel, an active coupling would have to be used to switch between leg and wheel.

These 5 final concepts represent the combinations, of parameters and options, with the greatest potential. We will take a closer look at their possible architectures in chapter 4. To determine the best option, the concepts will be judged on the criteria that were mentioned in chapter 2. The best concept will be developed into a prototype design.

Chapter 4

Concept Selection

In this chapter we will evaluate the 5 concepts that resulted from the decision tree in chapter 3. We will explore possible configurations and use the criteria as stated in chapter 2 to judge them on their feasibility. The final concept will subsequently be developed into a prototype module for the Zesbenige Robot (ZebRo).

4-1 Chapter overview

This is a quick overview of the sections in this chapter. We first give an overview of the concepts and in subsequent sections discuss them based on the criteria that were determined in chapter 2. We will compare the concepts to each other and score them on a scale from 1 to 5. They will then receive a weighted score for each criteria. In the final section, all scores are combined and we will obtain the final result.

Table 4-1: Section Overview

Section	Subject
4-1	Chapter overview
4-2	Overview Concepts
4-3	Criterion: Walking Ability
4-4	Criterion: Driving Ability
4-5	Criterion: Robustness
4-6	Criterion: Efficiency
4-7	Criterion: ZebRo Compatibility
4-8	Final Scores

4-2 Overview Concepts

In this section we will give an overview of the 5 concepts and how the architecture could look like.

Concept 1 - This concept is based on 6 reconfigurable modules. Figure 4-1 shows a depiction of what the concept could look like in driving and walking mode. The robot drives with 6 wheels, but these can reconfigure to C-shaped legs for walking. Reconfiguration is done with a parallelogram mechanism, shown in figure 4-2, that moves part of the wheel relative to the central pivot. The mechanism will be controlled by a small servo-motor, located inside the wheel. This concept allows for big wheels that are not hampered by other parts and the C-legs are similar to the ones used in the conventional ZebRo.
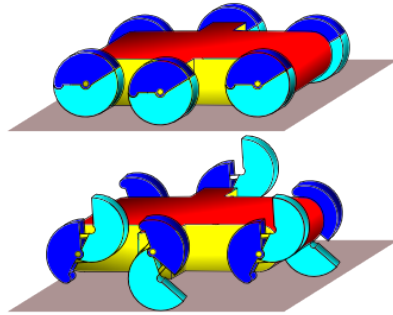
Figure 4-1: Concept 1
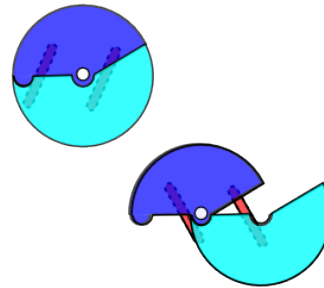
Figure 4-2: Detail Concept 1

Concept 2 - Similarly to Concept 1, this concept has 6 modules that can reconfigure between a wheel and a leg-shape. But the reconfiguration is based on a rotating mechanism with a small servo-motor. The mechanism rotates part of the wheel around the center pivot, thus creating a leg-shape. The concept allows for big wheels and C-shaped legs similar to the conventional ZebRo. In figure 4-3, Concept 2 is depicted in driving and walking mode. The rotating mechanism is shown in figure 4-4.
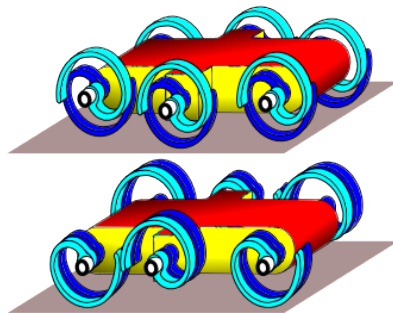
Figure 4-3: Concept 2
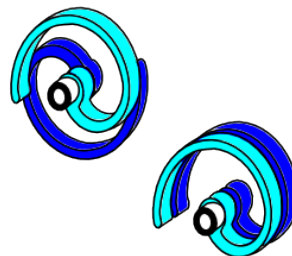
Figure 4-4: Detail Concept 2

Concept 3 - This concept, figure 4-6, uses 6 modules that combine a wheel and leg into one shape. Together, when seen from the side as in figure 4-6, the modules form continuous ground contact, thereby creating driving ability. But the modules also enable steps with the front part, thus enabling walking ability. The modules consist of one single part with one axle and do not require any reconfiguration or connection mechanisms.
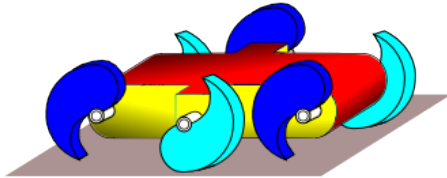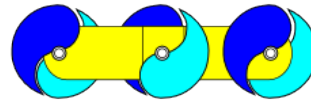
Figure 4-5: Concept 3   **Figure 4-6:** Side-view Concept 3

Concepts 4 - With this concept, depicted in figure 4-7, a separate wheel and leg with two axles are connected to a center pivot. An active coupling is used to switch the driving shaft between the Leg-axle and the Wheel-axle. This concept would have a large wheel and the leg can be adjusted to the design. With the coupling, the leg can be held fixed in its position to keep it from falling over.
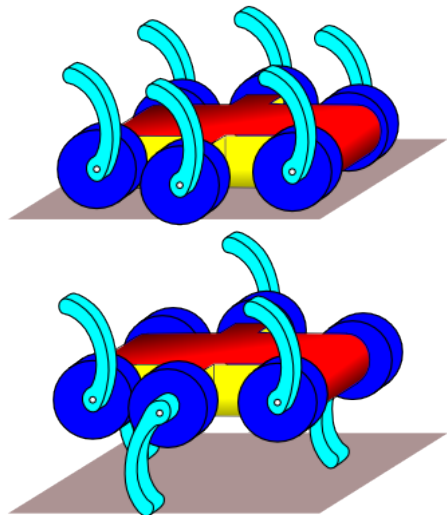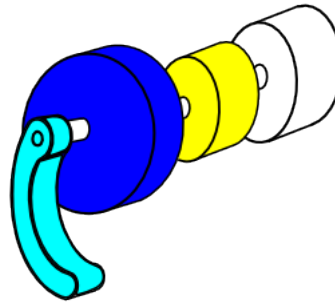
Figure 4-7: Concept 4   **Figure 4-8:** Detail Concept 4

Concept 5 - The last concept, shown in figure 4-9, consists of modules with a separate wheel and leg, where the wheel is connected to the end of the leg. Power to the wheel would have to be transmitted by a belt inside the leg. The mechanism is shown in figure 4-10.
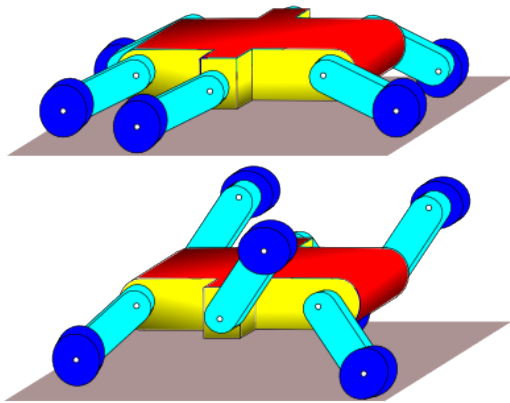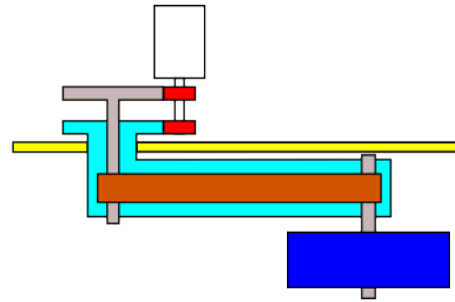
Figure 4-9: Concept 5   **Figure 4-10:** Detail Concept 5

There are now 5 concepts that can be considered for further development. To determine the best option, we will judge them in the remainder of this chapter with the criteria that were mentioned in chapter 2: Walking ability, Driving ability, Robustness, Efficiency and ZebRo Compatibility.

4-3 Criterion: Walking ability

In this section we discus the walking ability of the concepts. This criteria is divided into Obstacle Negotiation, Manoeuvrability and Speed.

Speed of walking and manoeuvring obstacles is influenced by the moment of inertia experienced by the motor axis. With a low moment of inertia we can achieve greater accelerations and thereby speeds with the same amount of torque. We can therefore expect differences among the concepts by comparing the anticipated weight at the axis. In Concept 4, the motor drives only the C-shaped leg, without any additional weight. Similarly Concept 3, drives a single semi-circular leg. Being lightest, we can expect these concepts to be the fastest. Concepts 1, 2 and 5 have a lower score, because they have to swing the leg with an additional servo or even an entire wheel.

Obstacle Negotiation. All concepts are, by default, equipped with a C-shaped leg, but they have slightly different geometry. Concepts 1 and 2 might be modified into a different leg-geometry, without consequences for the architecture, giving them more

opportunities for increased Obstacle Negotiation Limit (ONL). And with concept 4 and 5, the wheel could hinder the effectiveness of the leg. Concept 3 has semi-circular wheel-legs that are expected to function similar to regular C-legs, but it has not been tested yet.

Manoeuvrability depends on the Degree-of-Freedom (DoF) of a concept in walking mode. For this, there is not much difference between concepts: All have six modules, with one DoF-legs and are equipped with Differential (skid) steering. The exception is concept 3: it is unknown how the half-wheels will influence steering and there is a possibility they would hinder movement.

The comparisons are summarised in table 4-2 with a weighted final score. Speed and Obstacle Negotiation are given a weight of 2 and Manoeuvrability of 1. Manoeuvrability is deemed slightly less important in the overall walking ability, as a few potential detours are unlikely to be critical to the robot's mission.

Table 4-2: Walking Abilities of Concepts

	Speed	Obstacle Negotiation	Manoeuvrability	**Weighted Score**
	Weight:2	Weight:2	Weight:1	
Concept 1	3	5	5	4.2
Concept 2	3	4	5	3.8
Concept 3	4	4	3	3.8
Concept 4	4	5	5	4.6
Concept 5	2	5	5	3.8

4-4   Criterion: Driving Ability

Driving ability is divided in Speed, Obstacle negotiation and Manoeuvrability analogous to Walking Ability.

Speed is influenced by the weight of the wheel. A low weight wheel can achieve greater acceleration and speeds. If we look at the rotating weight, or inertia, all concepts drive only the wheel and score approximately the same. But concepts 1 and 2 have an additional servo, built into the wheel, making them heavier. Concept 3 has a somewhat reduced weight, because it uses semi-circular wheels, but this also reduces traction, as only half of each rotation gets is in contact with the surface. We can expect therefore that concept would be slowest. Concepts 4 and 5 score highest, although concept 5 loses some torque in the transmission from the motor to the leg.

Obstacle Negotiation is largely determined by the wheel diameter. A larger wheel can negotiate larger obstacles. Wheel thickness is another factor, because this increases the

surface contact. But since this parameter can be freely chosen amongst the concepts, we can omit it here. For concepts 1 and 2, the diameter of the wheel is not restricted by other features and can be freely chosen. For concept 4 and 5, the size of the wheel is restricted by the leg. If the wheel is too large, the leg can not function and the size of the leg is dependent on torque and the effects on stability. Finally, for concept 3, the diameter of the wheel can be freely chosen, but it has only half wheels, which could influence Obstacle Negotiation.

Manoeuvrability. All concepts have 6 individually powered modules, with one-DoF-legs and Differential steering. So we can expect manoeuvrability to be comparible. The exception is concept 3, as it does not have continuous grip which could hamper manoeuvring.

The weighted scores of this criterion are shown in table 4-3. Similarly to Walking Ability, Speed and Obstacle Negotiation are weighted 2 and Manoeuvrability 1.

Table 4-3: Driving Abilities of Concepts

	Speed Weight:2	Obstacle Negotiation Weight:2	Manoeuvrability Weight:1	**Weighted Score**
Concept 1	3	5	5	4.2
Concept 2	3	5	5	4.2
Concept 3	3	3	3	3
Concept 4	4	4	5	4.2
Concept 5	4	3	5	3.8

4-5 Criterion: Robustness

Robustness is divided into Complexity, Reliability and Toughness.

Complexity is important as it relates to vulnerability. If there are many parts there are more possibilities for parts to break, bend or cause misalignment. Alternatively, if concepts have fragile parts or small tolerances they are also more vulnerable to shocks. Concept 3 has the least amount of parts and no coupling, reconfiguration mechanism or fragile components, so it gets the best score. Concept 4 does not have fragile parts, but it does have an additional coupling mechanism. Couplings can be considered shock-proof, but it makes the concept more complex. Concept 5 has the additional coupling mechanism combined with a transmission system to the wheel, which means even more parts and possibly small tolerances. Concept 1 has a servo mechanism and many more parts due to the reconfiguration mechanism. Concept 2 also has a servo mechanism and many parts, but the mechanism would have to be confined to the central pivot, so the parts might have to be small as well. Therefore concept 2 is estimated to be most

complex.

Reliability is the likelihood for a robot to free itself from difficult situations, such as landing in a ditch. A robot with greater manoeuvrability and obstacle negotiation would have more options, so in this way we can approximate Reliability. All concepts have 6 individually powered modules with 1 DoF legs, but Concepts 1 and 2 would first have to reconfigure, which might not be possible if the robot is stuck in a difficult position. Concept 5 might be hindered by the wheel at the end of the leg. Concepts 3 and 4 should do well in this category.

Toughness relates to the vulnerability to temperatures fluctuations, dust or water. Though the concepts mostly operate with mechanical parts without risk, concepts 4 and 5 utilize a (electro-magnetic) clutch, which generates heat that has to be dissipated and which is possibly vulnerable to extreme temperatures. Dust can cause parts to jam or cause abrasion and water can cause erosion. All concepts have parts that can be easily coated or sealed though for protection. And they do not have small seams where dust can enter. With the exception of concepts 1 and 2; dust might be scooped up inside the split with the servo-mechanism and cause it to jam, thus preventing it from closing.

The weighted scores of the concepts are shown in table 4-4. All sub-criteria are very important for creating a robust and reliable robot. Therefore it was decided to give give them all the same weight.

Table 4-4: Robustness of Concepts

	Complexity	Reliability	Toughness	**Weighted Score**
	Weight:1	Weight:1	Weight:1	
Concept 1	3	4	3	3.3
Concept 2	3	4	3	3.3
Concept 3	5	4	4	4.3
Concept 4	4	5	4	4.3
Concept 5	3	4	4	3.7

4-6 Criterion: Efficiency

Efficiency is divided into walking efficiency and driving efficiency.

Walking Efficiency relates to the amount of surface contact during a step-cycle as most energy is lost during the swing-phase. Therefore a short swing phase is important. All concepts utilize the same C-shaped leg, except concept 3, which has an elongated swing

phase due to the half-circle attached. Secondly, it depends on the power to weight ratio. So we want a small weight in walking mode.

Driving Efficiency The driving efficiency can be judged on the inertia. A wheel with a high inertia, or large diameter will have a better efficiency. And again, the weight in driving mode will be a factor.

The scores for Efficiency are shown in table 4-5. Walking Efficiency is weighted 1 and Driving Efficiency at 2. We put a higher weight to Driving Efficiency, because the robot will be in driving mode most of the time and this is where the benefit of a hybrid robot comes from. Walking ability mostly serves for traversing rough-terrain.

Table 4-5: Efficiencies of Concepts

	Walking Efficiency Weight:1	Driving Efficiency Weight:2	**Weighted Score**
Concept 1	4	3	3.3
Concept 2	4	3	3.3
Concept 3	5	4	4.3
Concept 4	4	5	4.7
Concept 5	4	3	3.3

4-7   Criterion: ZebRo Compatibility

We divide the compatibility into Integration and Costs.

Integration. The concept should be modular and be able to fit with different ZebRo bodies. Upon examination it appears there is little difference between the concepts however. All concepts have 6 modules that can be easily switched or changed.

Cost. The costs of a robot will depend on its complexity, the materials and the processes that are involved. There are custom-made parts and bought components. All concepts use custom-made wheel and leg parts, made from a polymer or 3D-printed. Concept 3 has only the custom made wheel-leg and no other special parts, therefore this will likely be the cheapest concept to make. Concepts 1 and 2 utilize an additional servo, but these are not very expensive. Concepts 4 and 5 use an additional coupling, which could be relatively expensive. Concept 5 could be even more expensive, due to the additional drivetrain that is needed for power transmission.

The weighted scores for ZebRo Compatibility are shown in table 4-6. Both sub-criteria are deemed equally important and therefore both are weighted at 1.

Table 4-6: ZebRo compatibility of Concepts

	Integration	Cost	**Weighted Score**
	Weight:1	Weight:1	
Concept 1	4	4	4
Concept 2	4	4	4
Concept 3	4	5	4.5
Concept 4	4	3	3.5
Concept 5	4	3	3.5

4-8   Final scores

We can now summarize all the previous scores into a final overview and arrive at the final concept. We will be using weights derived from chapter 2 and the target goals in table 2-3. Robustness is deemed most important, so it is weighted at 3. ZebRo compatibility, where the only relevant factor is Costs, is somewhat less important, so it is weighted at 1. All the remaining criteria will be weighted at 2. The result is shown in table 4-7. Although the scores of concepts 3 and 4 are close, it is the much better Walking and Driving ability of Concept 4 that wins it.

We therefore conclude that Concept 4 should be chosen for further development.

Table 4-7: Final Scores of Concepts

	Walking	Driving	Robustness	Efficiency	Compatibility	Weighted Grade
	Weight:2	Weight:2	Weight:3	Weight:2	Weight:1	
Concept 1	4.2	4.2	3.3	3.3	4	3.73
Concept 2	3.8	4.2	3.3	3.3	4	3.65
Concept 3	3.8	3	4.3	4.3	4.5	3.96
Concept 4	4.6	4.2	4.3	4.7	3.5	4.34
Concept 5	3.8	3.8	3.7	3.3	3.5	3.64

Chapter 5

Simulations

In this chapter we want to go back to the fundamental principles of a wheel and a C-shaped leg. There are many possibilities for the design of a hybrid walker-wheeler robot, but the challenge is to make the hybrid technology advantageous over other robots. Therefore we do a number of simulations with MSC ADAMS, a multi-body dynamics simulation software. The advantage of a simulation is that we can create an equal comparison, easily change parameters and eliminate disturbances. We can thus examine the respective strengths and limitations of a wheel and leg. If we know what the most important characteristics are, we can apply these in the design of the module and give the new concept a better chance of success.

5-1   Chapter overview

An overview of the chapter is shown in table 5-1. We will set out a number of objectives, in order to get a clear scope for the simulations. We will then describe the set-up and the results of the simulations. With these we are able to formulate answers to the objectives. Finally we will summarize the lessons that will be taken into account for the new module design.

Table 5-1: Section Overview

Section	Subject
5-1	Chapter overview
5-2	Objectives
5-3	Overview Simulations
5-4	Simulation Results
5-5	Answers to Objectives
5-6	Notions for Module Design

5-2   Objectives

A C-Leg is obviously better at climbing an obstacle and a wheel is obviously more effi-
cient on flat terrain. But the purpose of the simulations is to quantify their differences
and to identify the parameters that make them effective. A full description of all the
objectives is listed below.

1. *Obstacle Negotiation Limit (ONL)* - This is defined by the maximum obstacle height
   a body can overcome and will be expressed as a percentage of the wheel-radius
   or length of the leg. The leg will perform better then the wheel, but we want to
   extrapolate what size of wheel would be required to have the same ONL as a leg.

2. *ONL Torque* - We want to find the torque corresponding with each ONL. This is
   important for the comparison, but it is also important in the dimensioning of the
   new robot. We could determine what the limitation would be with the selected
   motor.

3. *ONL Energy consumption* - We will measure the energy consumption corresponding
   to the ONL. A wheel could do better at energy conservation, provided it can
   negotiate the obstacle. It might also be used to get an estimate of the energy
   savings that can be expected with the use of hybrid technology.

4. *ONL Speed* - We will also measure the time it takes to negotiate an obstacle. This
   factor is of lesser concern, as ONL and energy consumption are more important.
   However if there are big differences, it might be something for consideration.

5. *Speed on flat terrain* - The speed on a flat piece of terrain is an important parameter
   to compare a leg and a wheel. The wheel will perform much better then the C-leg,
   but we would like an estimate of the gains that could be achieved with hybrid
   walker-wheeler technology.

6. *Torque on flat terrain* - The wheel should be take much less torque, but we would
   like to have an figure to estimate the gains.

7. *Energy consumption on flat terrain* - One of the benefits of a hybrid walker-wheeler
   is less energy consumption. By making a comparison we can get an estimate of
   the expected gains.

5-3   Overview Simulations

To make a comparison between a C-leg and a Wheel, we did two different experiments. We first simulated a Wheel or C-Leg climbing over an obstacle with the focus on torque and maximum heigh. In the second experiment we simulated the bodies while travelling over a straight horizontal piece and focus on their speed and energy consumption. This section will give a quick overview the set-ups of the simulations. All the simulations are described in detail in Appendix B.

Set-up Obstacle Negotiation Experiments - The set-up is kept very simple, as shown in figure 5-1. It consists of a single wheel or leg suspended by two massless beams which allow frictionless movement in a 2-dimensional frame. A constant vertical load is applied at the axis, which simulates the weight of the robot, and an obstacle is placed at a distance from the axis. Between the body and the obstacle is a contact force, modelled with Coulomb friction. So when the simulation runs, the body hits the object and attempts to climb it. Torque T is increased until it just accomplishes the task or an upper limit of 2Nm is reached. The height of the obstacle is increased incrementally, until the body can no longer climb it. This height will be the ONL.

Speed and energy consumption are measured through the MSC ADAMS software. We will then have all the data to answer the objectives.
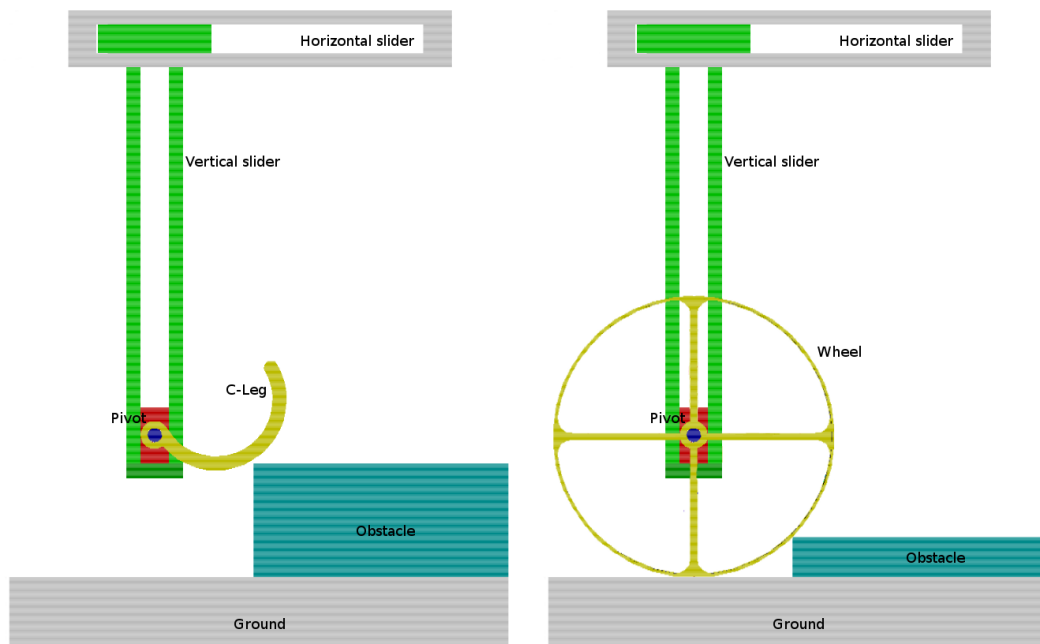
Figure 5-1: Obstacle Negotiation Set-up with C-Leg(a) and Wheel(b)

The C-Leg would normally be supported by the robot during its swing-phase. This is simulated by the the vertical slider in the general set-up that generates a horizontal and vertical reaction force to keep it from falling down. The pivot of the C-Leg is suspended above the ground by the same height as the wheel axis. In contrast, a wheel always touches the ground and so the weight is solely supported by a contact force, modelled through Coulomb friction, with the ground.

Many parameters, such as the radius, vertical load or thickness of the body, are likely to influence the ONL, but in order to limit the scope of the research all parameters will be kept equal and we will focus solely on the different geometries.

Set-up Straight-Piece Experiments - We use a similar framework as in the previous test set-up, shown in figure 5-2. A single C-Leg or Wheel is supported by two massless sliders that enable movement in a 2-dimensional frame. However the obstacle is removed and instead there is a straight piece of 1 meter. Between the body and the ground is a contact force, modelled by Coulomb friction. The body is initiated from rest, with zero initial velocity. We then impose a constant angular velocity on the center pivot so the body will travel over the surface. Using the MSC ADAMS software, we measure the horizontal speed of the axis, torque and energy consumption.
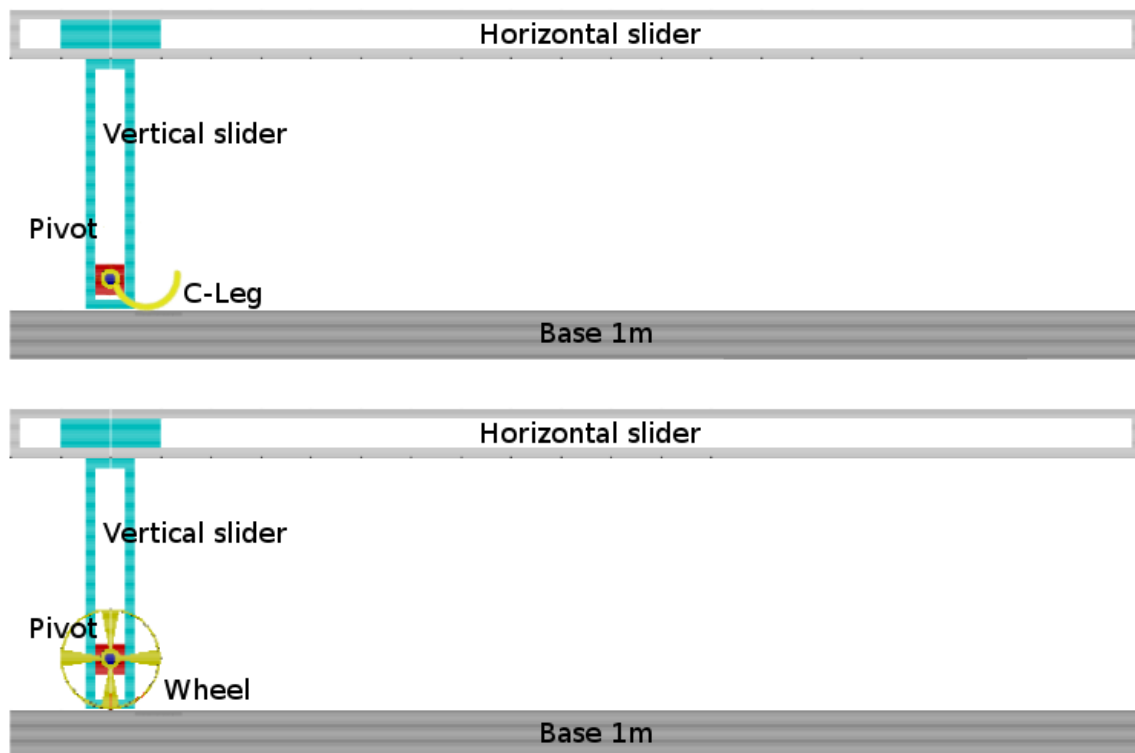
Figure 5-2: Straight Piece Set-up with C-Leg(a) and Wheel(b)

5-4   Simulation Results

All the tests are documented in appendix B. This includes the raw data and the resulting graphs. In this section we will summarise some of the results.

Obstacle Negotiation experiments -   Figure 5-3 shows the maximum surmountable height versus distance. The C-Leg shows an optimum of 12cm at distance 5cm. With length of the leg 10cm, this translates to an ONL of 120%. A polynomial best-fit through the data shows a parabolic trendline which relates to the curved shape of the leg. For the wheel, the polynomial has a root-like shape, with an asymptote at a height of 5cm. This corresponds to an ONL of 50%. This is due to the rim of the wheel having less grip with increasing obstacle height.

In the second graph, figure 5-4, the obstacle height is plotted versus the minimum torque required to mount it, along with two polynomial best-fit lines for the data. Although the two lines are close together for small obstacle heights, it can be readily observed that the C-Leg requires much less torque to overcome large obstacles. The trendline for the wheel shows a relation to the rim of the wheel. When the height increases, the contact angle with the surface of the obstacle decreases and thus converts a smaller portion of the torque in gripping the obstacle.
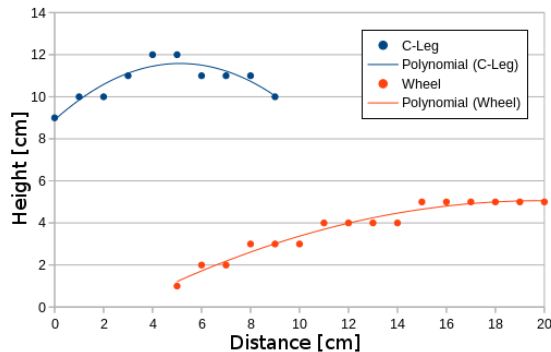
Figure 5-3: H vs d
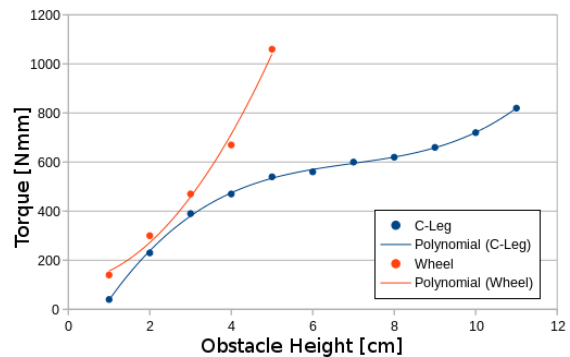
Figure 5-4: T vs H
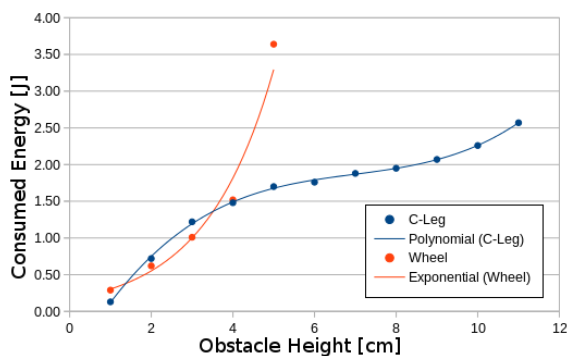
Figure 5-5: E vs H
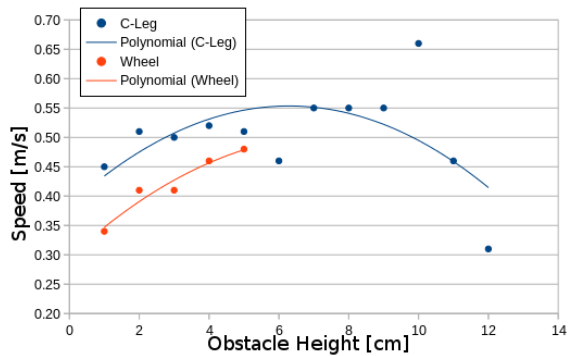
Figure 5-6: v vs H

Thirdly, figure 5-5 displays the obstacle height versus energy consumption with two polynomial best-fit lines. The two lines are rather close to each other and there are only a few measurement points for the wheel, because it could only climb a maximum height of 5cm, so we can not draw any definitive conclusions. But the trendlines suggest there is not much difference in energy consumption for smaller obstacles. With increasing obstacle height, energy consumption for the wheel increases dramatically, consistent with the increasing torque requirement for increasing obstacle heights.

The last graph, figure 5-6, displays obstacle height versus average horizontal speed. Again, there are too few measurement points of to wheel to draw definitive conclusions, but the trendlines suggest that the wheel could be faster when it is able to overcome the obstacle.

Straight Piece experiments - It is clear that the C-Leg and the Wheel have a different behaviour. For the wheel, imposing a constant angular velocity $\dot{\theta}$ on the center pivot translates to a constant horizontal velocity. In contrast the C-Leg takes steps that lead to fluctuating accelerations and speed. We can see from figure 5-7, that the wheel is a minimum of 50% faster and that the difference increases with increasing angular velocity of the pivot.

As can be seen from figure 5-8, the Wheel is sustained with a much smaller torque requirement compared to the C-Leg. It is at least 100 times smaller. This is due to the wheel being in constant contact with the ground and torque is used only to overcome friction, whereas the C-leg has to push the entire weight of the load with each step. We can also see the torque requirement of the C-leg increases with increasing speed $\dot{\theta}$. With increasing speed, the C-leg is accelerating faster with each step, which requires more torque. By contrast, because we are doing the simulations at constant velocity, the forces against the wheel vary little and we see only a moderate increase in torque. Finally, the large inertia of the wheel helps it to preserve momentum.

Furthermore, from figure 5-9, it can be seen that the wheel needs fewer rotations to travel the 1m distance. The rolling surface contact means angular rotation is transferred linearly to horizontal distance. Whereas the C-Leg has no contact in the swing phase and thus takes more rotations to travel the same distance. Because geometries and length of the straight piece are the same, the amount of required rotations is independent of angular speed.

The combination of less torque requirement and fewer rotations needed, means the wheel requires far less energy in the simulations when compared to the C-leg. This can be shown in figure 5-10. Energy consumption of the wheel is at least 100 times smaller then the C-Leg.
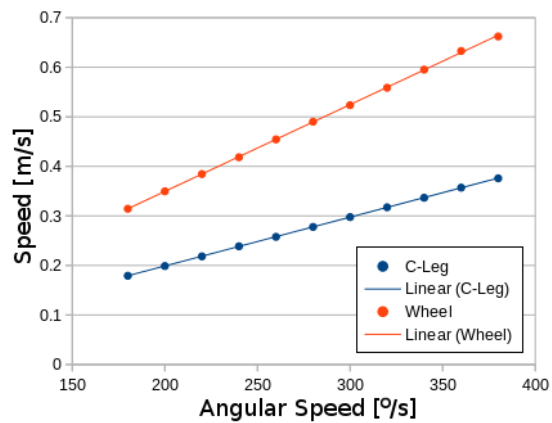
Figure 5-7: Horizontal Speed vs $\dot{\theta}$
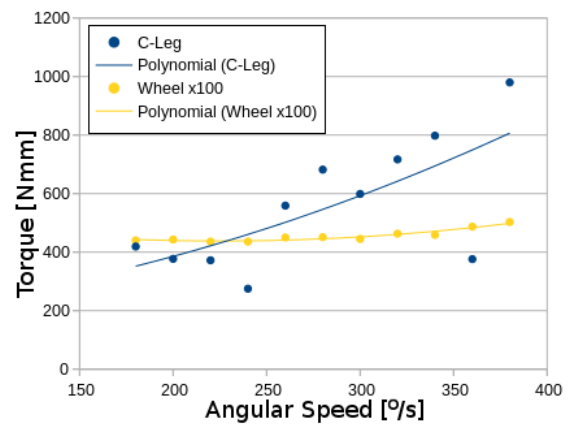
Figure 5-8: RMS Torque vs $\dot{\theta}$
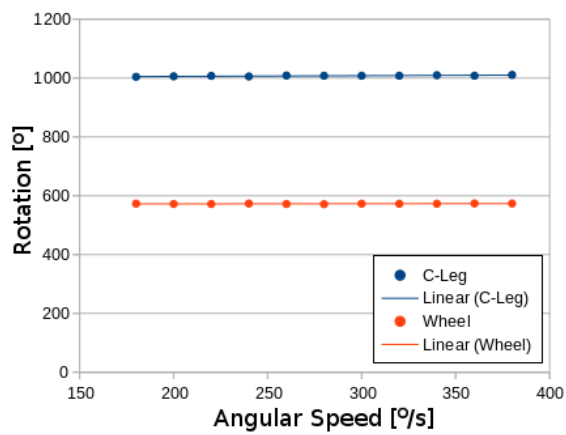
Figure 5-9: Rotation vs $\dot{\theta}$
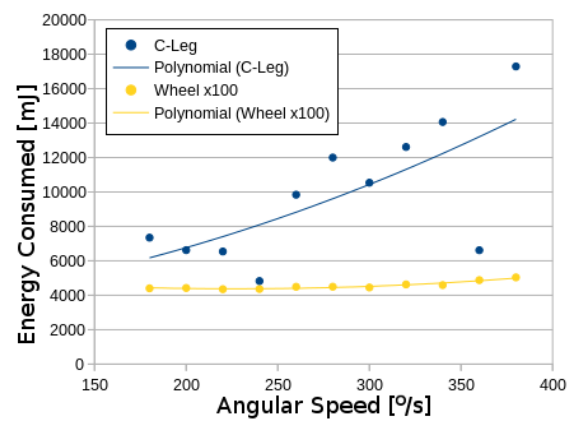
Figure 5-10: Energy consumption vs $\dot{\theta}$

5-5　Answers to Objectives

With the results from the simulations, we can now formulate answers to the objectives that were set out for the simulations in section 5-2.

Obstacle Negotiation Limit -　The C-Leg performed much better in obstacle negotiation. An ONL of 120% for the leg versus 50% for the wheel. This was expected, but we can also see structural differences. The C-Leg has an overall better grip, with an optimum point for climbing found halfway its radius. This is where the angle between the C-Leg and the obstacle is approximately perpendicular to the surface and the C-Leg has the best grip due to friction force. For the wheel, climbing becomes increasingly difficult with increasing obstacle height. This is due to an increasingly smaller portion of the acting moment being used for the vertical normal force and the wheel has increasingly less grip. Giving the wheel a head-start by increasing distance d, increased its ONL, but only up to a point. We could also see that the wheel would need to have a diameter that is four times the length of the C-Leg in order for it to have the same ONL as the C-Leg.

ONL Torque -　The C-Leg requires less torque to overcome large obstacles. This is caused by the contact angle between the leg and the obstacle, converting a greater portion of the torque into a useful vertical component. Whereas the rim of the wheel causes the effective angle between wheel and obstacle to decrease with increasing obstacle height. Thus a smaller portion of the torque is used effectively.

ONL Energy Consumption -　The wheel and leg performance was found rather close together for small obstacles. Too few measurement points meant we were unable to draw definitive conclusions. However, the torque requirement for the wheel increases exponentially with increasing obstacle height and therefore energy requirement as well.

ONL Speed -　The experiments gave too few results to draw definitive conclusions, but trendlines suggest that a wheel is faster, provided that it can overcome the obstacle.

Speed on flat terrain -　The simulations have shown that the wheel is much better in converting angular rotation to horizontal movement. If we plot angular velocity against horizontal speed, the wheel scores a minimum of 50% higher then the C-Leg. Because the wheel is always in contact with the ground, it has a continuous horizontal movement of the central pivot. Whereas the C-Leg has no horizontal movement with each step in its swing-phase.

Torque on flat terrain -　The simulations have shown a very large difference in torque requirement. This is because the weight on the axle causes a large counter moment on the C-Leg. Whereas with the wheel, this force is always counteracted by the normal force with the ground. So the wheel only uses torque to overcome friction, while the C-Leg has to push against the weight with each step. In addition, the wheel has a

moment of inertia that is five times larger then the C-Leg and less torque is required to maintain a constant velocity. This is also why its torque requirement only slightly increases with increasing angular velocity. In contrast, the C-Leg is accelerating between each step and torque increases greatly with greater speed. The torque increases, because a larger acceleration requires more torque.

Energy Consumption on flat terrain - The combination of a much smaller torque requirement and a greater horizontal movement from each rotation, means that the Wheel has a much lower energy consumption on flat terrain. And the simulations thus unsurprisingly show a big difference in the energy consumption on flat terrain between a C-Leg and a Wheel.

5-6   Notions for Module Design

We have seen from the simulations that the C-Leg and Wheel not only differ on quantitative performances, but also on operating principle. We now know what features and parameters are important in their functionality and we can draw conclusions that will be helpful in the design of the new Leg-Wheel Module.

From the Obstacle Negotiation simulations, we found that the climbing ability of a C-Leg is due to its ability to convert a greater proportion of torque into a positive moment around the contact point with the obstacle. This is caused by the angle between the leg and the obstacle surface, resulting in a large normal force and therefore in a large friction force. In verbal terms, the C-Leg has the ability to *grip* the obstacle. By contrast, the rim of the wheel reduces its grip with increasing obstacle height and its climbing ability, with the limited torque, was limited to approximately half of its radius.

For the design of the module this means that we should focus on the grip of the C-Leg in order to maintain, or possibly increase, its Obstacle Negotiation ability in comparison with the conventional Zesbenige Robot (ZebRo). A possibility to increase grip is to have a perpendicular angle between Leg and obstacle surface. Another possibility is to add texture to the surface of the leg so as to increase the friction coefficient with the surface. Adding texture to the wheel, like a rubber tire, would also increase its grip and therefore Obstacle Negotiation ability.

From the simulations on a Straight Piece we saw that, when a constant angular velocity is imposed on the center pivot, the horizontal speed of the wheel is at least 50% greater compared with the C-Leg. Its torque and energy consumption is much smaller as well. The wheel has three features that relate to this. Firstly, continuous contact with the ground means that angular rotation is converted linearly to horizontal movement and the wheel can maintain a steady constant velocity of its center of gravity. Secondly, the continuous ground contact means that the normal force with the ground, in reaction to

the body weight, is always directed towards the center pivot and does not work against the torque of the axle. So the wheel only needs torque to counteract friction force with the ground and therefore has a far smaller torque requirement in comparison to the C-Leg. Thirdly, because it has a much higher moment of inertia, it is easier to maintain a constant speed. The combination of fewer rotations and smaller torque requirement means a much smaller energy consumption.

We now know from the simulations that horizontal speed increases with increasing radius of the wheel and with very little cost in extra torque or energy consumption. A larger radius increases its Obstacle Negotiation as well. So for the design of the new module, we should choose a large radius for the wheel in order to maximize the benefits of the driving ability.

<div align="right">

Chapter 6

</div>

Module Development: Leg and Wheel

In this chapter we will design the wheel and the leg that will be used in the new prototype. We want to optimize the shape of the leg for it to have good grip. For the wheel, the most important parameter is the diameter and should be as large as possible. The design must also be compatible with capabilities of the motor that will be used, the Nanotec-ST4118-X1404B with the GPLL40-24 gear reduction. To get an estimate of the loads on the Leg and Wheel during walking and driving, we do another number of simulations in MSC ADAMS. Finally, the leg and wheel are integrated into one module.

6-1   Chapter overview

We can see an overview of this chapter in table 6-1. We will first describe the motor specifications, which will determine the torque loads on the wheel and leg. We will then give an overview of the design of the wheel and leg, respectively. And finally we will come to the integrated design of the leg and wheel.

Table 6-1: Section Overview

Section	Subject
6-1	Chapter overview
6-2	Motor Specifications
6-3	Wheel Design
6-4	Leg Design
6-5	Integrated Leg and Wheel

6-2   Motor Specifications

With the Zesbenige Robot (ZebRo), the standard choice of motor is the Nanotec-ST4118-X1404B in combination with the GPLL40-24 Gear-reduction, shown in figure 6-1. In designing the module, we need to look at its capabilities and determine what its torque and speed limitations are.
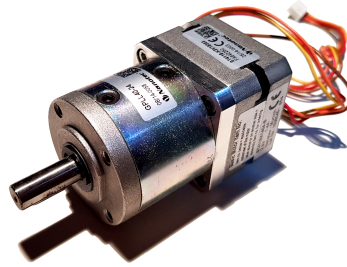
Figure 6-1: Nanotec ST4118-X1404B with GPLL40-24

The specifications of the motor, without gear reduction, are documented in Appendix A. The gear reduction of 24 means, when we neglect losses, that torque is multiplied by 24 whilst speed is divided by 24. When we apply this to the original speed-torque curve, we get the plot shown in figure 6-2. From the plot, we can read a maximum torque of almost 4000Nmm on the motor-axle. As a precaution, we will assume an upper limit of 3500Nmm for future calculations. This will be the maximum torque that is available to the Leg-axle or the Wheel-axle.
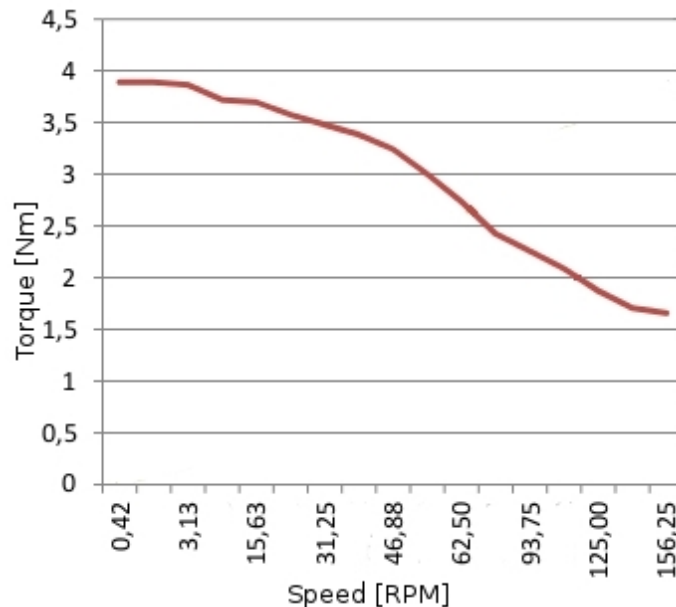
Figure 6-2: Speed-Torque curve

6-3   Wheel Design

In this section, we will design the wheel. The most important parameter is its diameter. As we know from chapter 5, large diameter wheels are preferable. They can negotiate higher obstacles, produce greater horizontal movement with each rotation and have a larger moment of inertia which enables better efficiency. We will also look at the thickness of the wheel and a tire to increase grip on rough terrain.

Wheel Diameter - Torque requirement by the wheel is expected to be superseded by the leg for climbing, so the limiting factor for the wheel diameter is the size of the robot. The ZebRo has a length of 30cm, so with three modules on each side that allows for a space of 15cm between the axles. By choosing a diameter of 12cm, we can fit the wheels and allow for some margin between the wheels.

Wheel Thickness - The thickness of the wheel is the second most important parameter of the wheel. In order to limit the scope of the research, the precise effect of wheel thickness was not examined in the simulations, so we will have to make an estimation. In general, a thicker wheel has more traction and thus better Obstacle Negotiation Ability, but at the cost of more torque and energy consumption. Because the wheel is to be used on rough terrain and the additional torque is less important, we will choose for a thicker wheel. As a basis we will start with a wheel with a thickness of 4cm.

To see if this wheel is compatible with the motor, we do another simulation with MSC ADAMS. The model, diameter 12cm and thickness 4cm, is shown in figure 6-3. The wheel is run on a straight piece with 40RPM and then climbs over an obstacle of 3cm. If we neglect torque spikes that come from noise in the simulation, we see a maximum torque around 1000Nmm in figure 6-4. So we know that torque requirement does not exceed the motor limitation of 3500Nmm.
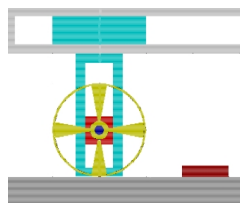
Figure 6-3: Wheel Simulation Model
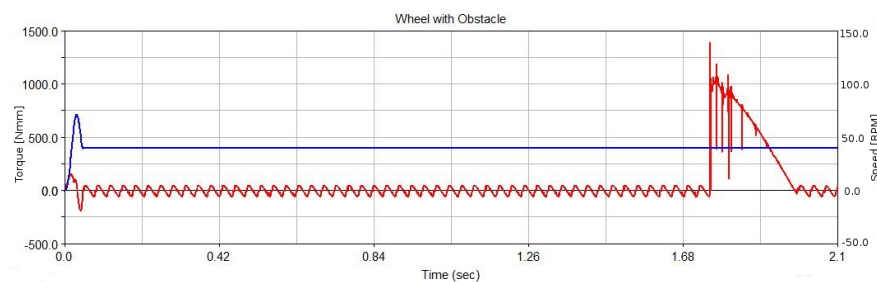
Figure 6-4: Wheel-Torque vs time

Wheel Tire - We also want to take a look at increasing traction by adding a tire around the wheel. The robot is to be used on rough-terrain and this would increase the functionality of the wheel. A tire increases friction between the wheel and other surfaces, thus increasing grip and Obstacle Negotiation Ability. The tire will be made out of silicone rubber, which is easy to buy and process. The tire will be cast using a 3D-printed mould.

Final Wheel Design - The final Wheel design is shown in figures 6-5 and 6-6. It has a diameter of 12cm, thickness 4cm and a silicone tire with nipples for good grip. To spare weight, the inside will be mostly hollow, apart from the spokes and bolt-holes for mounting on an axle. The wheel will be 3D-printed and the tire will be cast from silicones.
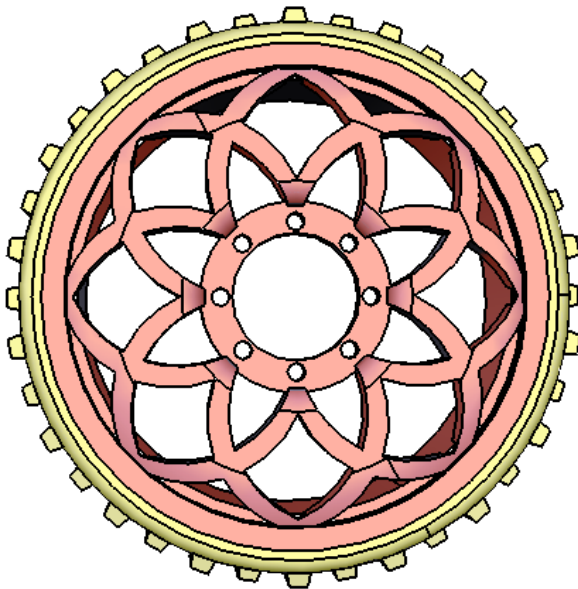
Figure 6-5: Wheel design front
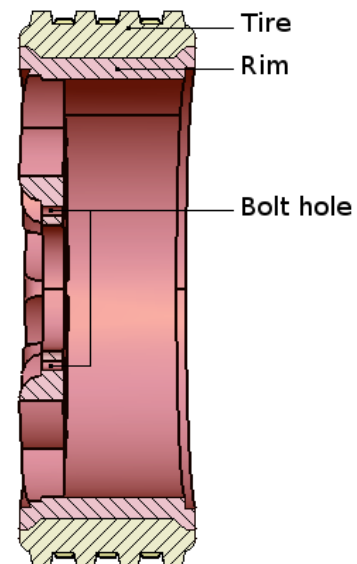
Figure 6-6: Wheel design cross section

6-4 Leg Design

In designing the Leg, we want to focus on the grip of the leg, since this is what relates to its Walking ability. We will also have to consider that the leg will be used in conjunction with the wheel, which impacts its functionality. And finally we will look at its thickness and add a sleeve for better traction.

Leg geometry. The wheel, when configured in parallel with the Leg, renders the first half a C-Leg non-functional. We know from chapter 5 that the half-way point of the leg is the most effective part of the leg. Therefore it was decided to deviate from the conventional C-Leg. We move the convex part of the leg outside the wheel rim, which results in a hook-like design. From figures 6-7 till 6-10, we can see the benefit of the hook-shaped design while climbing over an obstacle with height 12cm. A constant angular velocity of 40RPM is applied to the center pivot. When we look at the torque plots, the conventional C-leg shows a large spike when the leg hits the obstacle, which goes beyond the 3500Nmm threshold. Whereas the hook-shaped leg has a more even motion.
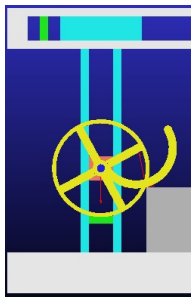
Figure 6-7: C-Leg + Wheel model
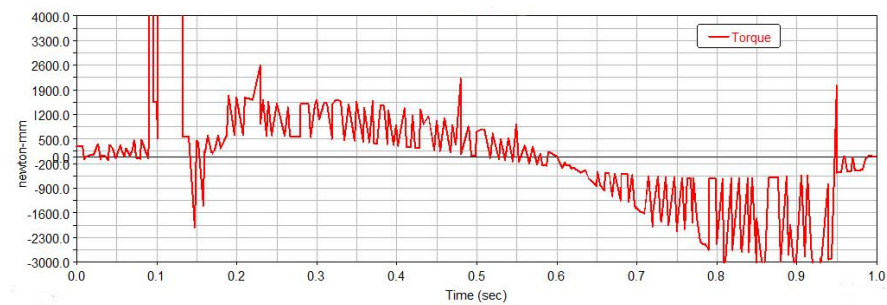
Figure 6-8: C-Leg+Wheel: Torque vs time
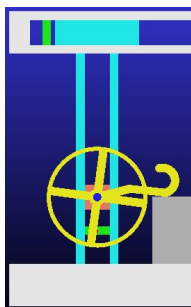
Figure 6-9: Wheel + Hook model
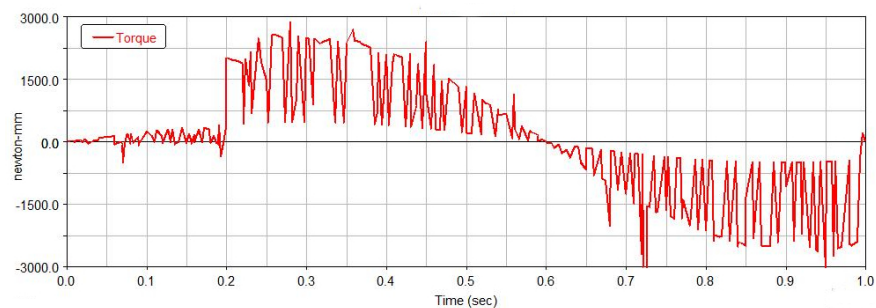
Figure 6-10: Wheel+Hook: Torque vs time

Leg thickness - Similar to the wheel design, we do not know what the precise impact of the thickness is on the functionality of the leg. This is something that might be left for future research. So we will choose a thickness of 3cm. This is based on the need for good grip and stability, but also balances weight and size.

Leg sleeve - Because grip is so important to the functionality of the leg, an added sleeve would also be beneficial. The sleeve will increase friction and add to the gripping ability of the leg. Similarly to the wheel-tire, the sleeve will be cast from silicone, using a 3D-printed mould.

Final Leg Design - The final leg design is shown in figure 6-11.
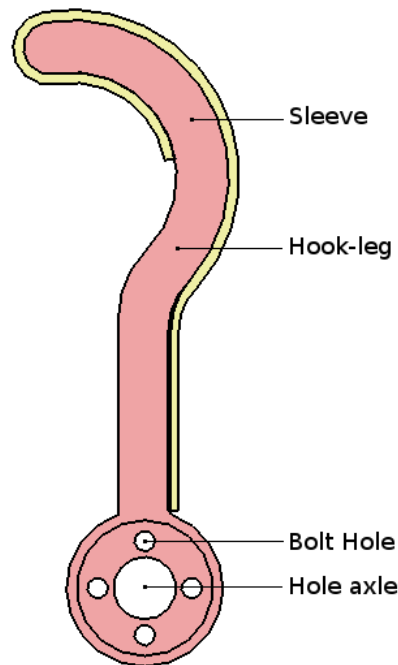
Figure 6-11: Leg Design - side view

6-5 Integrated Leg and Wheel

We now look at the design for the combined Leg and wheel into one module.

The final design of the wheel and leg is shown in figures 6-12 and 6-13. It combines the hook-shaped leg, for good grip and Obstacle Negotiation, with a large 12cm diameter wheel, for good driving ability. Both leg and wheel are driven by an axle, that have to turn around the same axis. Since the leg is on the outside, the leg-axle is to run inside the wheel-axle, supported by bearings.

Steel end-caps are bolted on each side of the leg or wheel using the bolt-holes. These caps have slots with which they can slide over a spie attached to the axle. The reason for using steel caps is that it should be a tight fit and the slots in the caps can be made using machining with high accuracy. Furthermore, steel is stronger then 3D-printed material and will be able to withstand the force during movement.

The reason to use a spie and slot for assembly is that it is a strong connection, yet easy to assemble and disassemble. So the axles can be moved through bearings, then the spie is inserted and the leg or wheel slides over the axle.
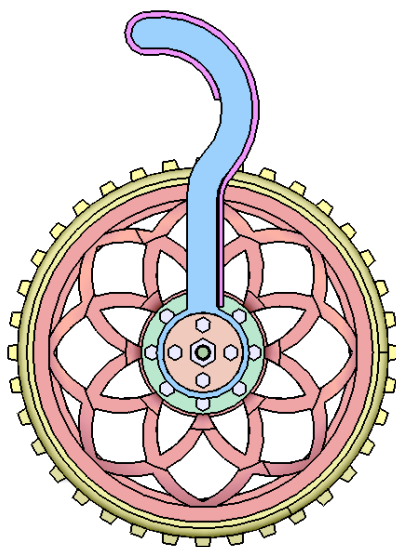
Figure 6-12: Integrated Leg and Wheel
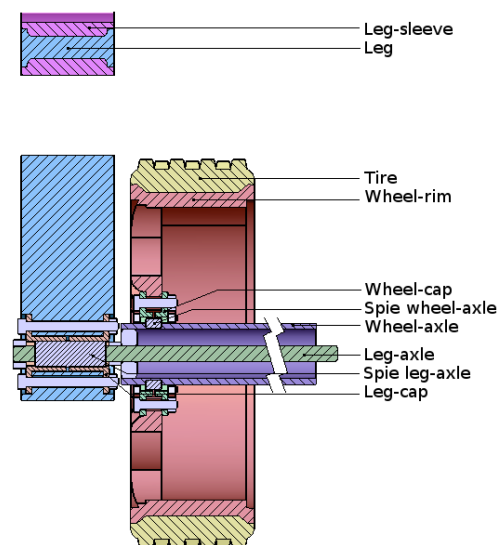
Figure 6-13: Leg and Wheel Cross view

Chapter 7

Module Development: Coupling

In this chapter we focus on the coupling that is used in the new design. The concept uses an active coupling to switch power from the motor between the Leg-axle and the Wheel-axle. Because we were unable to find an appropriate existing coupling, this coupling was specifically developed for this application.

7-1 Section Overview

There are many different aspects in the design of the coupling. We will discuss each of the features in different sections as outlined in Table 7-1. We will start by determining the specifications for the coupling. Next, we will discuss and develop each of its design features in the subsequent sections. In the final section, we will merge all parts into the final design for the module.

Table 7-1: Section Overview

Section	Subject
7-2	Principle of Operation
7-3	Coupling Specifications
7-4	Friction Plates
7-5	Actuator
7-6	Springs
7-7	Planetary Gear Drive
7-8	Integrated Rotation Sensor
7-9	Bearings
7-10	Final Assembly

7-2   Principle of Operation

In this section we will explain the principle of operation of the coupling. During the development of the new module, we encountered a complication. The module requires an active coupling to switch between two axles and hold the Leg-axle fixed when it is not engaged. Existing couplings are not designed to switch between two axles. They can brake and release or they can couple and decouple, but only one axle. In addition there are specific requirements for this application, such as size and torque loads, that make this a very specific coupling. It was therefore decided to build a custom electro-magnetic coupling.

We use the principle of operation of an electro-magnetic coupling and adapt it for this specific application. The coupling has one motor shaft going in and two axles, one for the wheel and one for the leg, going out. After an evaluation in section 7-5, an electro-magnet was chosen as the actuator for switching. A combination of friction-plates, on the armature and on the brake-pad, springs and a moving armature are used to engage and disengage between the axles.

When the magnet is switched off, figure 7-1, springs are pushing the armature to the left. The Wheel-axle is engaged by the friction-plate on the armature, which is connected to the motor-shaft, and which thus drives the Wheel-axle. Meanwhile the Leg-axle is fixated with a brake-pad pushed against the friction-plate on the Leg-axle. When the magnet is switched on, figure 7-2, the brake-pad (made of steel) is pulled to the right against the springs. This in turn pulls the armature to the right and engages the Leg-axle through the friction-plates while the Wheel-axle is disengaged. Now the Leg-axle is connected and is driven by the motor.
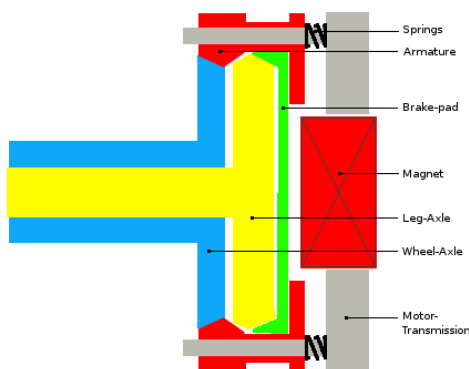
Figure 7-1: Coupling actuating Wheel-Axle
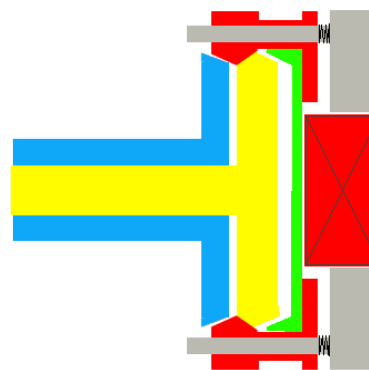
Figure 7-2: Coupling actuating Leg-Axle

7-3   Coupling Specifications

The first step in designing the coupling is to determine its requirements. This involves the torque load, dimensions and switching time.

Torque Requirements - For torque requirements we look at the data from chapter 6. In the first situation, when the magnet is turned off, the coupling must push both the armature against the friction-plate on the Wheel-axle and the brake-pad against the Leg-axle. Holding the Leg-axle takes 2000Nmm and the actuating the Wheel-axle takes 1000Nmm, so the combined torque is 3000Nmm. In the second situation, when the magnet is turned on, the coupling has to pull the armature back against the friction-plate on the Leg-axle. It must thus transfer a total of 2000Nmm.

Dimensions - The wheel has a diameter of 12cm. The coupling, which is positioned in-line with the wheel- and leg-axles, has to fit within this circle. A large diameter of the coupling is beneficial for the operation of the friction plates, but there should also be enough ground clearance. At this point, we proceed with an outer diameter of 60mm. This leaves enough space for the housing and components and enough clearance between the coupling and the ground. Lengthwise, there are no direct limitations, but the coupling should preferably be short.

Switching Time - The switching time is the time it takes to change between wheel- and leg-mode. During switching, neither the leg or the wheel are fixated and can fall down or the body can lose position. Fast switching also enables good controllability and therefore increases performance. So we want the coupling to have a short switching time. Another remark is that in both coupling and decoupling, engagement can occur between a stationary disk and a slow rotating friction-plate, at a maximum of 50RPM.

7-4   Friction Plates

Toothed coupling vs Friction plates - For the choice of engagement plates, we evaluated the choice between a toothed plate and friction plates. Toothed plates have the advantage of transmitting torque without slippage and therefore automatically have an μ of 1.0. But the disadvantage is that engagement must be done at low speed, to prevent damage to the teeth. Manufacturing the toothed plates would also be difficult and buying them would be costly in comparison to the manufacturing of friction plates. So we will therefore proceed with friction plates.

The equations shown in the figure:

$$dF = P sin\beta dA,$$
$$dA = 2\pi r dr$$
$$F = P sin\beta \pi \left[r_2^2 - r_1^2 \right]$$
$$\Rightarrow P = \frac{F}{sin\beta\pi\left[r_2^2 - r_1^2\right]}$$

$$dM = \mu r dF, \ dF = P2\pi r dr$$
$$\Rightarrow M = \frac{2}{3}\mu\pi \left[r_2^3 - r_1^3 \right] P$$

$$\Rightarrow M = \frac{2 \left[r_2^3 - r_1^3 \right]}{3 sin\beta \left[r_2^2 - r_1^2 \right]} \mu F$$
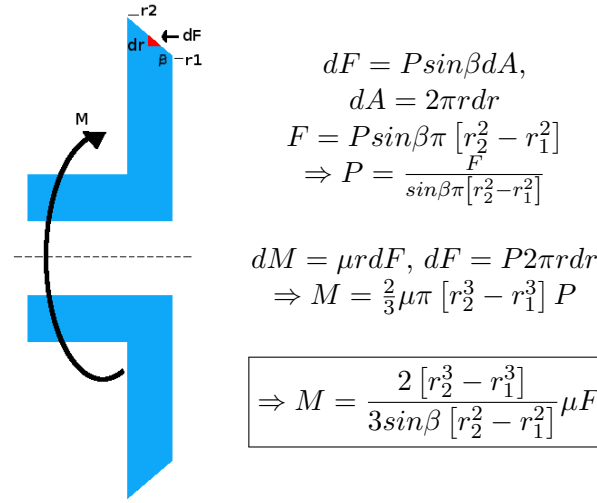
Figure 7-3: Derivation of Friction Moment

Geometry - In figure 7-3 is the relation derived between the moment transferred to the axle and the exerted force F on the disk. This is a linear relationship with a constant factor that is dependent on the inner radius r_1, outer radius r_2, the angle β of the plane and the friction coefficient μ between the surfaces. P is the pressure, in N/mm, as a result of the exerted force F. With values of $\beta = 90°$, $r_1 = 5mm$, $r_2 = 25mm$, we get $M = \frac{155}{9}\mu F \approx 17.2\mu F$.

When we examine the equation, it is apparent that an increasing r_1 and r_2 increases the factor, because pressure is concentrated on the outer rim and where it has a larger moment around the axis. If we take for example $r_1 = 20mm$, $r_2 = 25mm$, we find a factor of $M = \frac{610}{27}\mu F \approx 22.6\mu F$.

Another way to greatly increase the factor is by setting the plane at an angle, forming a conical shape. This increases the contact surface and therefore increases friction. If we take for example β as 30°, with $r_1 = 5mm$ and $r_2 = 25mm$, the equation becomes $M = \frac{310}{9}\mu F \approx 34.4\mu F$.

To maximise the factor, we combine a plate thickness of 5mm with $r_1 = 28mm$ and $r_2 = 30mm$, which leads to an angle of $\beta = 21.8°$. We then arrive to the final transfer function of:

$$M = \frac{1953}{25}\mu F \tag{7-1}$$

This is a factor of $\approx$78. 4.5 times greater then the original number of 17.2.

Friction material - Now we look at possible friction materials. Commercial brake-pads and couplings often use friction coefficients around 0.4, because wear and heat characteristics during dynamic friction, slippage, are crucial. They are made from ceramic and metallic composites and are quite expensive. In this case however, the armature transitions between a stationary disc, friction plate mounted on the Leg- or Wheel-axle, and a slowly rotating disc, the Armature, with a maximum of 50RPM. So the static friction requirement is profoundly dominant. It is also important to have a low actuating force and so we will choose a material with a higher friction coefficient. Lower costs and ease of manufacturing is also beneficial. We will assume that we can omit dynamic friction at this stage.

Rubber is a cheap material that can be easily applied as a lining on the friction discs. From internet sources, such as www.engineersedge.com, we find the minimum friction coefficient between rubber and steel is usually around 0.6. It should be noted however that friction coefficients are very susceptible. They are influenced by factors such as surface roughness, material chemistry, heat treatments and wear. The exact μ can only be determined when the exact materials are tested in the configuration.

Final configuration - With the afore mentioned geometry and a minimum friction coefficient of 0.6 we can now calculate the actuating forces on the friction plates. When the actuator is switched off, the Leg-axle requires 2000Nmm and the friction plate thus requires an axial force of 42.6N. The friction-plate mounted on the Wheel-axle needs 21.33N. However, when an axial force is applied to the armature, the force is divided equally and both plates receive the same force. So to provide both plates with the required force, the total axial load must be 85.35N. When the actuator is switched on, only the friction plate on the Leg-axle is engaged with a moment of 2000Nmm. This corresponds to an axial force of 42.6N. In figure 7-4 the final design of the friction plates are shown, with the conical shapes and rubber pads.
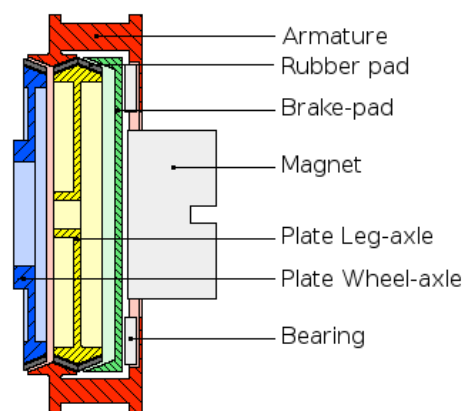
Figure 7-4: Design Friction Plates

7-5   Actuator

In this section we will look at the choice of actuator that is used to move the Armature in a linear fashion. We will make a comparison between two apparent choices: a solenoid magnet and a linear actuator.

Solenoid magnet - When using an electro-magnet, or solenoid magnet, it must provide enough force to overcome the 86N in the OFF-state and provide the 43N in the ON-state. This is a total of 129N. Solenoid magnets are easily obtained in online stores with various specifications. One possibility is the solenoid magnet as shown in figure 7-5. It is documented with a force of 180N, outer diameter 34mm, length 18mm, mass 90g and costs around 8 Euro. Its dimensions make it very suitable to fit inside the coupling and operation is smooth and easy with DC current. Speed of engagement has to be further examined and depends on the supplied current, the gap to the armature and the specific conditions, but electro-magnetic waves travel at $2.9978e^8 m/s$ and engagement times of 20ms are typical for commercial electro-magnetic couplings.

Linear Actuator - The advantage of a linear servo, or actuator, is that it has the ability to both pull and push. It would thus eliminate the need for springs and does not have to counteract any force when actuating the Leg-axle. So it will only need to provide 86N in the OFF-state and 43N in the ON-state. One possible actuator is the NEMA-11, a linear stepper motor, made by Koco Motion. It has a recommended operating limit of 125N, for both push and pull, has size 30x30mm, length 34mm, weight 130g and a speed of around 3mm/s. If the armature needs to move 1mm, this would mean an engagement time of 0.33s.

Based on this analysis, the magnet was found to be the better choice of actuator. It is faster and easier to integrate with the coupling. In addition, it is smaller and lighter.

Figure 7-5: Solenoid Magnet
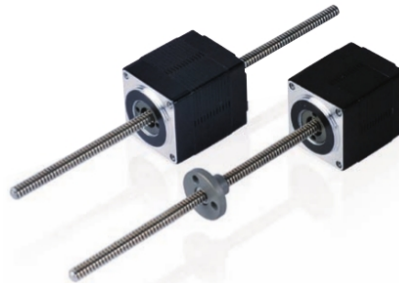
Figure 7-6: Linear Stepper NEMA-11

7-6   Springs

Having decided on the choice of actuator, the next crucial elements are the springs. Four linear springs will be placed in parallel between the armature and the outer gear and together provide the 86N, in preloaded condition, to engage the friction plates in the OFF-state. They will be distributed evenly over the diameter of the outer gear and each spring will have a preloaded length of 5mm. A suitable type of spring was found on Amatec.nl, the C0180-026-0310M, as shown in figure 7-7 and table 7-2.

The unloaded length of these springs is 7.87mm, so at a loaded length of 5mm and a stiffness of 8.23N/mm, the exerted force would be 23.6N. With 4 springs in parallel, the resulting stiffness would be 32.9N/mm and the total force would then be 94.5N. So this will be sufficient to keep the armature engaged.

Figure 7-7: Amatec C0180-026-0310M

Table 7-2: Specifications C0180-026-0310M

Wiresize **d**	mm	0,66
Outside Diameter **Do**	mm	4,57
Unloaded Length **Lo**	mm	7,87
Material **M**	-	Steel
Spring Constant **k**	N/mm	8,23

7-7   Planetary Gear Drive

In this section we take a closer look at the power transmission from the motor shaft to the armature. This mechanism is shown in figure 7-8 with a cross-section and a back-view. The magnet is placed in between the friction plates and the motor shaft, so the torque from the motor has to be transferred to the armature while the magnet is kept fixated. This is done by a planetary gear drive, which creates space for the plate in the middle where the magnet is mounted on. However, a gear reduction is undesirable because it would cause additional stresses on the coupling and the friction plates. Therefore the sun-gear was designed to have the same amount of teeth and diameter as the outer gear, which results in a horizontal orientation.
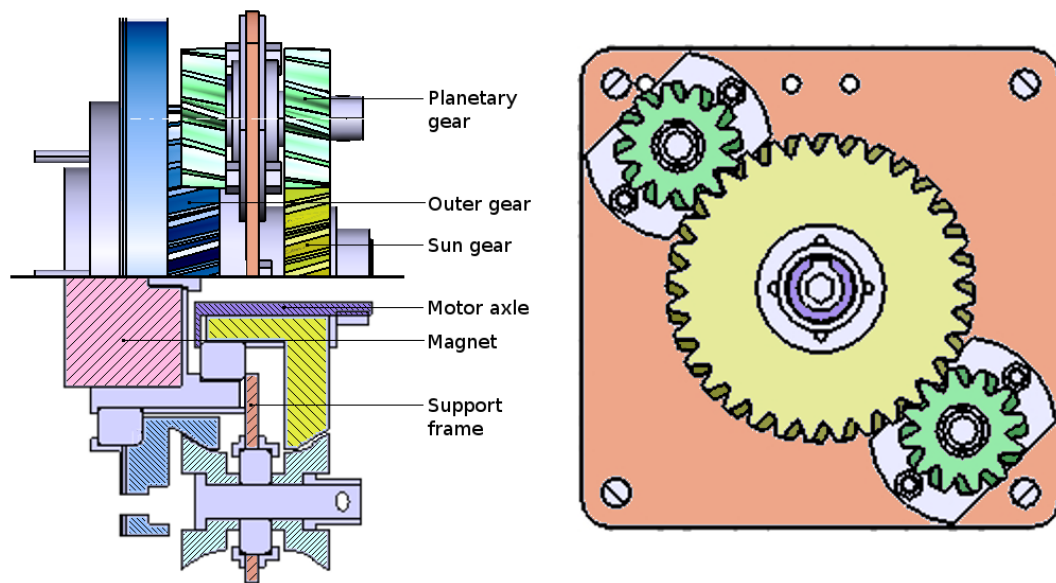
Figure 7-8: Planetary Gear

Because this is a specific gear configuration, it will have to be custom made. We will draw a model in CAD software, print it in 3D and then cast it in Polyurethane (PU). With this method we can easily and cheaply make a complex model. But the drawback is that PU is less strong in comparison to steel. So therefore the gears had to be made relatively large.

In appendix G the contact ratio and the stresses on the gears were calculated to determine if it is suitable for this application. We chose a module of 1.5mm, tooth width 8mm, pressure angle 20° and helix angle of 15°. The large gears have 32 teeth and the small gears have 12 teeth. With this configuration the contact ratio was found to be 1.86. As this is larger then 1.25 the gears can be expected to run smoothly. For a maximum torque of 3000Nmm, the stresses on the teeth were found to be $72 N/mm^2$ for the large gears and $89 N/mm^2$ for the smaller gears. As the maximum stress for PU was calculated to be $93 N/mm^2$, this means the gears should hold.

7-8   Integrated Rotation Sensor

Good control of the legs and wheels is crucial to achieve a stable walking gait and the correct angle position of the wheel- and leg-axles are the most important parameters to achieve this. Therefore the module should incorporate a rotation sensor. As this sensor is to be incorporated into the module we will refer to it as the Integrated Rotation Sensor (IRS). The IRS will be based on a standard incremental encoder. An incremental encoder consists of three Light Emitting Diodes (LEDs) emitting light beams and three light sensitive resistors placed across. A disc with gaps at regular intervals is attached to the axle and passes between the components, causing a signal with HIGH and LOW pulses. In figure 7-9 we see an example of such a disc and signals in a schematic representation. Each change in the signals A and B corresponds with a step on the encoder disc, which matches a fixed increment in rotation. So by counting the pulses, we know how much the axle has rotated. The phase between signals A and B is used to tell the direction of rotation. Signal Z has one gap on the encoder disc and only one pulse with each rotation. This is used to get the absolute position of an axle, which is required to know the position of the leg.
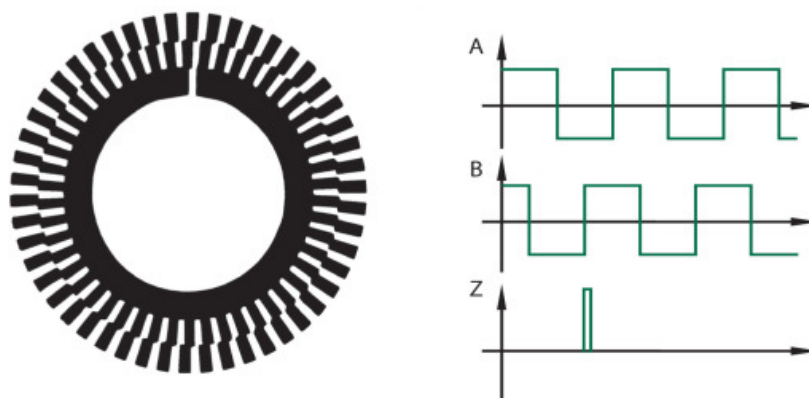
Figure 7-9: Encoder with signals

With the new module, we need to measure the rotation of two axles. Therefore the IRS consists of two parts. An overview of the IRS is shown in figure 7-10. The IRS-L measures the rotation of the leg-axle. The position of the leg-axle is first measured using 3 Surface Mounted Devices (SMDs) and 3 Photo-Resistors (PRs). These electronic components are held within a 3D-printed inlay, attached to the wheel-axle. A 3D-printed encoder is mounted to the leg-axle and passes between the SMDs and the PRs as the axle rotates. Because of the limited space between the leg-axle and the wheel-axle, the gaps on the encoder and the components are placed lengthwise, in parallel to the axles. Now we still have to power and read the electronic components. Because the wheel-axle is rotating we use 5 slip-rings: one for each PR, a positive voltage lead and one neutral lead. Slip-rings are metal rings with a ball-point pressed against its surface by a spring. So when the ring rotates, the ball-point keeps electrical contact.

The position of the wheel-axle is measured with the IRS-W. Similarly to the IRS-L, the IRS-W uses 3 SMDs and 3 PRs. They are held within a 3D-printed inlay mounted to the housing around the wheel-axle. A 3D-printed encoder is mounted to the wheel-axle and passes between the components. As there is now more space along the radius between the wheel-axle and less space lengthwise, the components are placed along the radius of the axle.
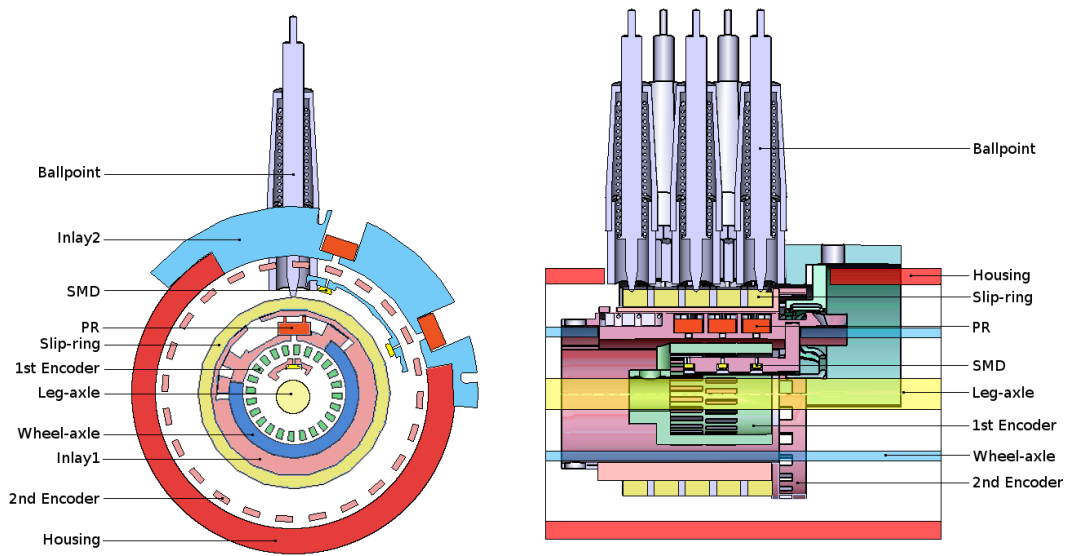
Figure 7-10: Integrated Rotation Sensor

7-9 Bearings

The next crucial element in the design are the bearings. Bearings ensure a smooth rotation of the axles and the armature and they have to be carefully selected and integrated in the design.

The armature pushes the Brake-pad against the friction-plate mounted on the leg-axle while at the same time rotating to drive the wheel-axle. This requires a thrust bearing, or needle bearing, that can take a normal force of 43N at a rotating speed of approximately 50RPM. A suitable bearing is the Axk-4060 (figure 7-11). The axial load requirement appears to be no problem at all, as ball bearings can endure much higher loads.

Figure 7-11: AXK-4060 Thrust Bearing

Then there are bearings to support the axles, armature and the planetary gear drive. Groove ball bearings are the best choice, because these bearings are able to take both radial load and thrust loads. They are also easily available in different sizes. Figure 7-12 shows the three different type of groove ball bearings that are used. They support the leg-axle inside the wheel-axle, the wheel-axle inside the housing and the armature around the magnet and the friction-plates. With the chosen diameters, as specified in table 7-3, they can fit inside each other.

Table 7-3: Specifications Groove Ball Bearings

Bearing	D_o mm	D_i mm	t mm	W g	F_{st} kN	F_{dy} kN	n_{max} RPM
SKF625	16	5	5	5	0.38	1.14	48000
SKF61804	32	20	7	18	2.32	4.03	28000
SKF61808	52	40	7	34	3.45	4.94	16000

Figure 7-12: Bearings 3x

7-10   Final Assembly and Prototype

In this final section all previous elements are merged into one design together with the
Leg and Wheel. The result is shown in Figure 7-13 with a side view. The coupling
is held inside a frame that is mounted to a plate which represents the outside of the
robot. At the other side of the plate is the motor that drives the module.
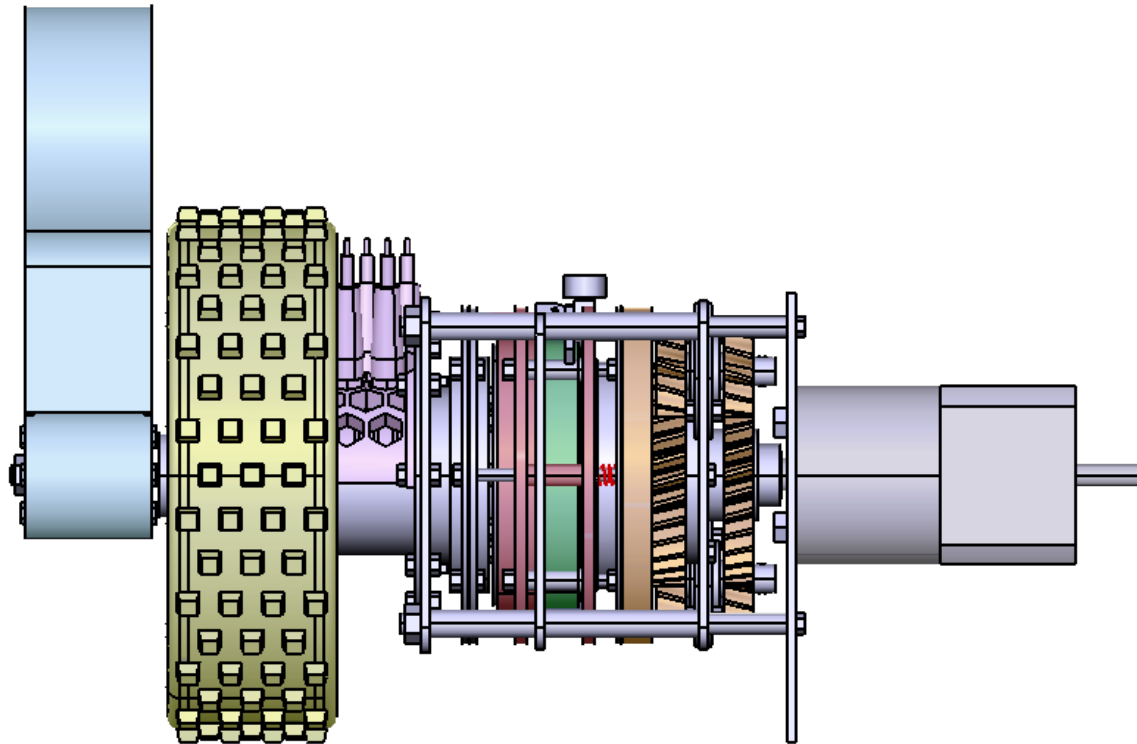
Figure 7-13: Final Assembly - side view

In the figure on the next page, figure 7-14, we see a cross section of the module. We
can see the placement of several bearings that support the axles and the armature and
ensure a smooth rotation. Each bearing needs to be clamped on the inner and outer
diameter by spacers or bolts. In addition there are multiple features and nuts and bolts
for assembly. An example is the armature which is divided into three parts in order
for the friction-plate on the leg-axle and the brake-pad to be put in front of the magnet.

In figures 7-15 and 7-16 we can see the final prototype of the module as it was built.
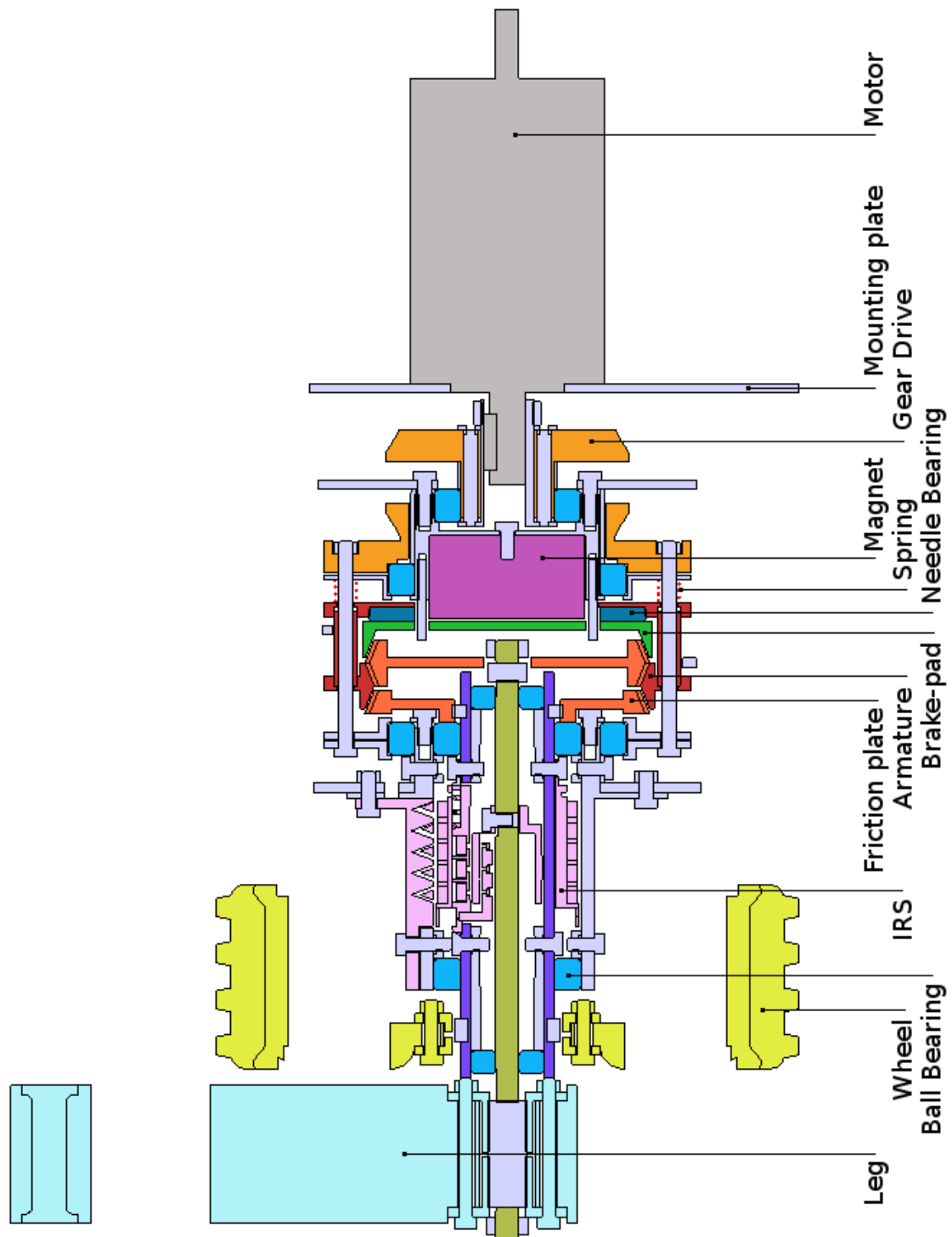
Figure 7-14: Final Assembly - cross section
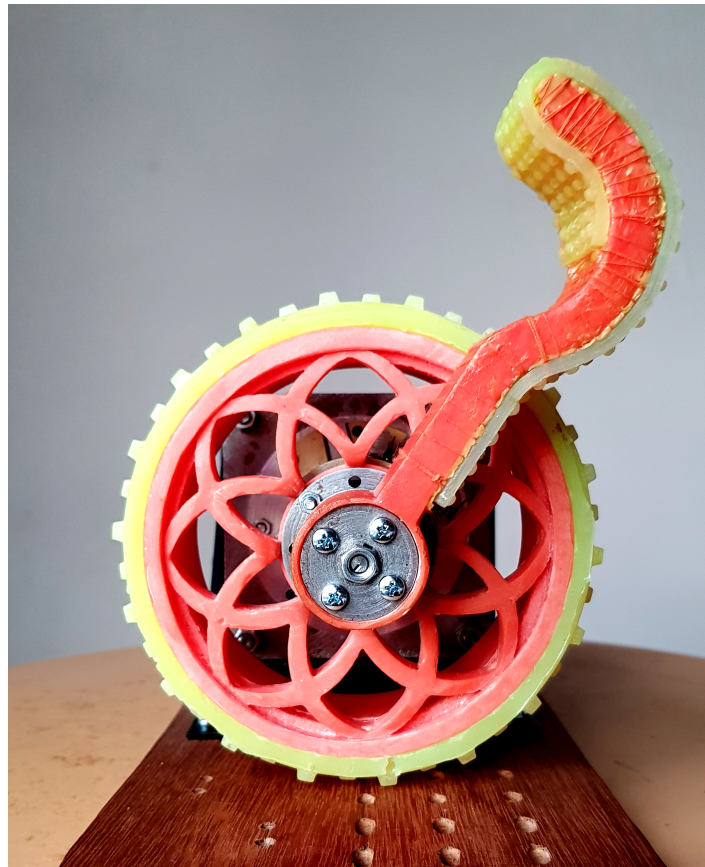
Figure 7-15: Module Prototype - front view
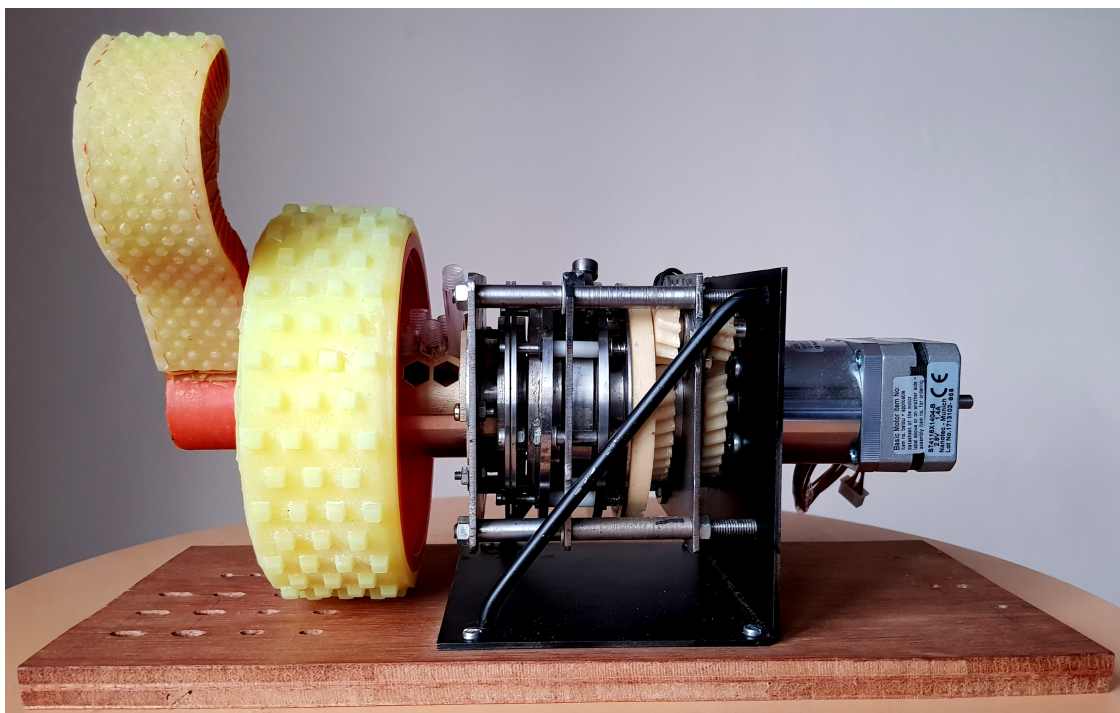
Figure 7-16: Module Prototype - side view

Chapter 8

Systems and Control

In this chapter we will cover the electronic equipment and circuit diagrams of the module. The module uses a motor, an electro-magnet and a rotation sensor. But in addition we will need equipment to power and control these and to read and measure signals.

8-1 Chapter Overview

We will discuss the different elements and circuit diagrams in sections. In table 8-1 the different subjects are outlined. We will start with the motor, which needs to be operated with the use of a driver. Then the Electro-magnet, the Integrated Rotation Sensor (IRS), the microprocessor and the Power supply. The final electronic circuit will be shown in the last section.

Table 8-1: Section Overview

Section	Subject
8-2	Motor Driver Circuit
8-3	Electro-Magnet Circuit
8-4	Integrated Rotation Sensor Circuit
8-5	Microprocessor
8-6	Power Supply
8-7	Total Electronic Circuit

8-2 Motor-Driver Circuit

Stepper Motor - With the ZebRo, the standard choice of motor is the stepper motor Nanotec-ST4118-X1404B in combination with the GPLL40-24 Gear-reduction. Because of its standardization and common usage it is the logical choice in this project. The motor is documented at 24V, 2Ω, 1.4A per winding and 200 steps per rotation. The full specifications are documented in Appendix A. This motor needs to be controlled with a driver between the microprocessor and motor.

Driver - The function of a driver is to generate pulses to the motor and to separate the high current power circuit from the fragile microprocessor circuit. The complementary driver will be the *StepStick DRV8825*, purchased on 123-3d.nl. With an added heatsink, it is suitable for bipolar steppermotors up to 2.2A per phase. The driver can operate in full-step mode, half-step mode or microstepping mode. In full-step mode, 200 pulses equals one rotation of the motor shaft. In half-step mode, 400 pulses equals one rotation, resulting in a smoother movement of the motor. Microstepping offers the smoothest control and best resolution, but only if the microprocessor is able to feed the pulses fast enough to get the required speed. Microstepping is usually done only for low speeds.
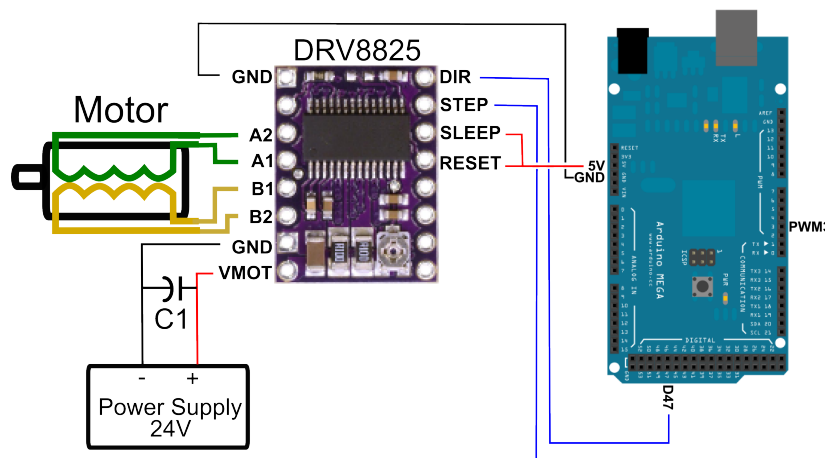
Figure 8-1: Motor driver Circuit

Circuit - The circuit for the motor and driver is shown in figure 8-1. The driver uses two active ports on the processor. One digital output port sets the direction and one Pulse Width Modulation (PWM) output port feeds pulses for stepping. Four wires go from the driver to the motor: a positive and a negative lead to each phase. The final two wires go to a power supply. The power supply must have a minimum of 24V and able to provide 4A for the two phases combined. It is generally recommended to put a capacitor over the leads to protect the driver from current spikes. The capacitor, C1 in the schematic, has a capacity of $100\mu F$.

Programming - To control the steppermotor, we need a program to feed pulses to the driver at the right intervals. Setting the step-pin from low to high generates one pulse, one pulse equals one step and, in full-step mode, 200 steps equal one rotation. So the time duration t_{step} for one step, in μs, can be calculated by equation 8-1. Where speed is in RPM and steps is the number of steps per revolution.

$$t_{step} = \frac{60E6}{speed \cdot steps} \tag{8-1}$$

By continuously switching the step-pin between high and low and delaying the loop with t_{step}, we get the desired speed for the stepper motor. The program is shown in figure 8-2. t_{step} is divided by half and put after each switch, so that the high and low stages are about the same size.

```
//Define pins
const byte stepPin = 6;    //PWM pin to feed pulses to the motor
const byte dirPin = 7;     //pin to set motor direction

//Variables
const int stepRev = 200;   //full mode=200 steps/rev
int speedRPM = 100;        //Set speed in RPM
int steptime = 500;        //is calculated from speedRPM

//Function to calculate step time, in us, from speed in RPM
void step_us(int RPMspeed){
  long b = 60000000;       //60E6 microseconds in one minute
  long c = long(RPMspeed) * long(stepRev);

  steptime = round((b/c)/2);
}

//Function to run once
void setup() {
  pinMode(stepPin,OUTPUT);
  pinMode(dirPin, OUTPUT);
  step_us(speedRPM);
}

//Main loop to run continuously
void loop() {
  //run motor for 1 step:
  digitalWrite(dirPin, HIGH);
  digitalWrite(stepPin, HIGH);
  delayMicroseconds(steptime);
  digitalWrite(stepPin, LOW);
  digitalWrite(dirPin, LOW);

  delayMicroseconds(steptime);
}
```

Figure 8-2: Program to control motor

8-3   Electro-Magnet Circuit

The next part is the electro-magnet circuit, seen in figure 8-3. Similarly to the motor, the electromagnet draws high current, 0.25A, and the power circuit must be separated from the microprocessor. A FET NPN bipolar transistor is used for switching the magnet on and of with voltage control, regulated by a digital port on the processor. For the transistor, T1 in the schematic, the TIP120 NPN is a natural choice. It is cheap, readily available and can transfer up to 5A/60V on its collector-emitter circuit. Its base-emittor circuit operates on a maximum of 5V/0.1A, compatible with the 5V generated by the digital port of the processor when paired with a 1kΩ resistor.
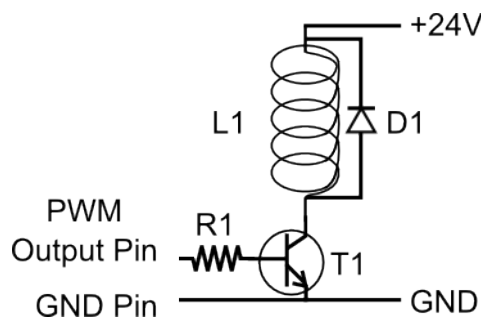
Figure 8-3: Electro-magnet circuit

Because electromagnets are inductors, they create an opposite voltage on the leads when the current is switched off. The kickback can induce a strong backward current that could damage the microprocessor or other components. So to compensate, a diode is placed over the leads of the electro-magnet. The diode needs to be able to withstand the current and voltage that the electromagnet will endure. For the diode, D1 in the schematic, the 1N4004 is used. Again, it is cheap and easily available and can block 400V/1A currents.

Programming - To merely turn the magnet on and off with a microprocessor, the program only has to set a positive voltage on the pin connected to the transistor. HIGH will turn it on, LOW will turn it off. But the magnetic force is much stronger when the attracted plate is close by. So the magnet only needs to exert full power for attracting the armature, whereas holding the armature in place takes considerably less force. This means we can save much energy by using PWM. With PWM, the microprocessor rapidly turns the magnet on for a short period and then off again for another short period. The ratio between on and off is set by the duty cycle. Duty cycle is set by a variable between 0 and 255. With a duty cycle of 255, the magnet is turned on 100% of time. With a duty cycle of 25, the magnet is turned on 10% of the time. An example of the code is shown in figure 8-4. The minimum duty cycle value that still holds the armature must be found empirically and is done in the next chapter.

```
//Define pins and variables
const byte pin_magnet = 11;                      //PWM pin to control transistor
const byte pin_button_magnet = 2;                //pin as input for button
bool magnet_state = false;                       //variable to track magnet on/off
int duty_cycle = 255;                            //duty cycle in PWM mode

//Code to run once on start-up
void setup() {
  pinMode(pin_button_Magnet), INPUT);
  pinMode(pin_magnet, OUTPUT);
}

//Main loop, runs continously
void loop() {
    if (digitalRead(pin_button_Magnet) == HIGH) {   //if magnet button pressed, run program
        if (magnet_state == false){                 //if magnet is off, turn magnet on
          digitalWrite(pin_magnet, HIGH);           //run magnet on full power for 1sec,
          delay(1000);                              //to allow coupling to switch
          analogWrite(pin_magnet, duty_cycle);      //proceed with PWM and set duty cycle
          magnet_state = true;                      //adjust variable to indicate magnet is on
        }
    } else {                                        //if magnet button not pressed,
        digitalWrite(pin_magnet, LOW);              //stop magnet
        magnet_state = false;                       //and reset variable
    }
}
```

Figure 8-4: Program magnet

8-4 Integrated Rotation Sensor Circuit

The IRS measures the rotation angle of the leg and wheel axles and then deduces speed and acceleration by using multiple steps and the time difference. The sensor uses two incremental rotary encoders, one for each axle. Each encoder consists of three Photo-Resistors (PRs), three Surface Mounted Devices (SMDs) and six resistors. The sensor uses 6 analogous inputs on the microprocessor. Together with the 5V power line, they create voltage dividers over the PRs and detect when their resistance changes.

The electrical circuit is depicted in figure 8-5. The Perkin-Elmer VT93N1 is chosen for the PRs. It has small dimensions so it can fit inside the axles and electrical properties, max 100V, well within range. Its resistance varies from 12kΩ in light to 300kΩ in dark. For the SMDs is the HuiYuan SMD-0805 chosen, again for its small dimensions and electrical properties (3.2V,30mA) compatible with a small processor.The two resistors are chosen to supply the PRs and SMDs with the appropriate voltage and current. R1 is 68Ω and R2 is 10kΩ.

To read the sensors and convert the signals using the microprocessor we need to test and tune the programming. This will be described in chapter 9 and appendix I.
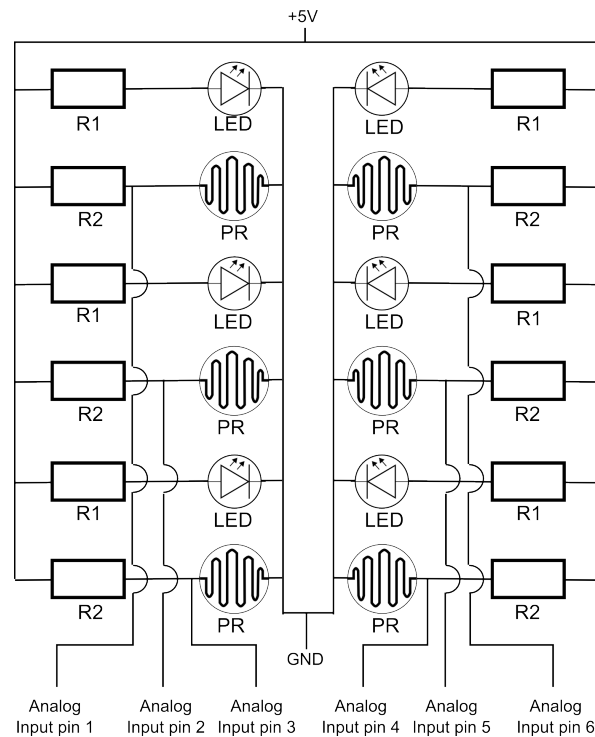
Figure 8-5: Electrical Circuit Rotation Sensor

8-5 Microprocessor

The choice of the microprocessor was based on the number of ports required. The microprocessor should have enough input and output connectivity to connect all the sensors and outputs. It should have at least 6 analog inputs for the IRS and 1 digital and 2 PWM outputs to control the magnet and the driver. We also want a fast clock-speed in order to control the motor and read the sensors with a small sample rate.

A suitable microprocessor is the Arduino Mega2560 Rev3, figure 8-6. It has 54 input/output ports, of which 16 are analog. It has an ATmega2560 microchip with a clock-speed of 16MHZ, which is expected to be fast enough. It can be easily connected to a computer with an USB-port and programmed using C++. It is also readily available, around 25Euros, with electronics stores.

Figure 8-6: Arduino Mega2560 Rev3

8-6   Power Supply

Motor and Magnet - For the choice of power supply the requirements of the motor and electromagnet are the most dominant. Both operate at 24V and require high currents: 0,25A for the electromagnet and 1,4A/winding for the motor. For a complete robot, we would have to look at batteries, but at this stage we will only be looking at one module for testing. Therefore a fixed power supply is the most easy solution. A fixed power supply does not require charging and there is no issue with power running low. The desired voltage and current is continuously provided. A suitable power supply is shown in figure 8-7. It is a generic power supply purchased at 123-3D.nl and can provide 24V at a maximum of 15A and 360W. Input is a standard power socket of 220V.

Figure 8-7: Power Supply 24V 15A

Microprocessor - The Arduino microprocessor requires a much lower operating voltage of 5V. It is also sensitive to high-current spikes so the power is supplied separately from the high-current circuit used for the motor and magnet. The low power can be supplied by a 9V battery, but commonly an USB-cable is used which is simultaneously required for the connection with the computer.

8-7   Total Electronic Circuit

We can now combine all the different circuits into the total configuration, depicted in figure 8-8. It shows the motor, electro-magnet, IRS, microprocessor, the power supply and the various components and wires.
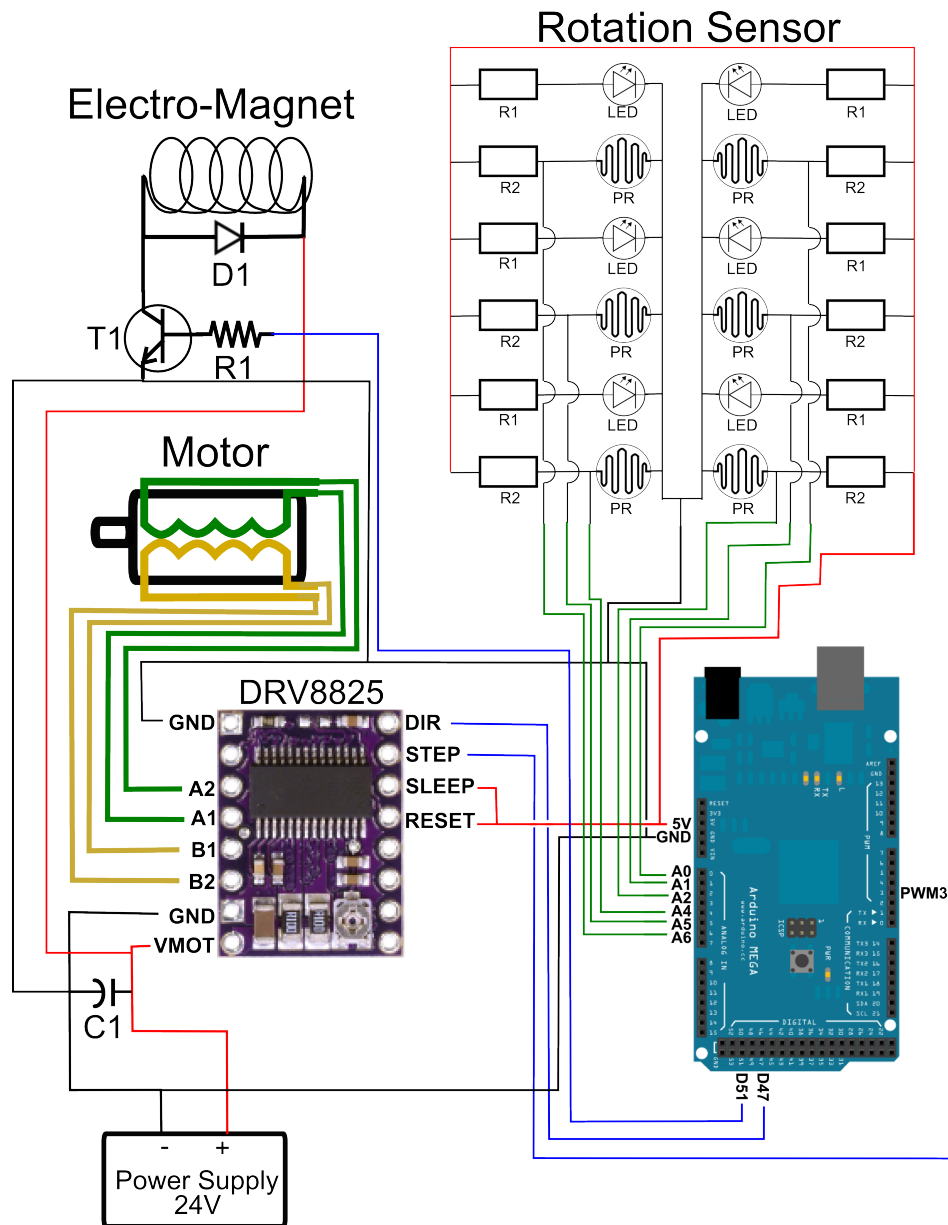
Figure 8-8: Total Electronic Circuit

<div align="right">

Chapter 9

</div>

<div align="right">

Testing & Results

</div>

In this chapter we will test the module. First, the features of the coupling are evaluated in different sections. After all the individual parts have been verified, we can move to the second part, which is to test the module as a whole. We will measure rotational speed, torque and energy consumption of the leg and wheel axles. With these we can then evaluate the overall performance of the module.

9-1 Chapter overview

An overview of the chapter is shown in table 9-1. We will measure the friction coefficient of the rubber used in the armature, the spring force exerted by the springs and the magnetic force by the magnet. We then measure the accuracy of the Integrated Rotation Sensor (IRS). When these are known, we can evaluate the overall performance of the module in the final section.

Table 9-1: Section Overview

Section	Subject
9-1	Chapter overview
9-2	Friction coefficient
9-3	Spring force
9-4	Magnetic force
9-5	Integrated Rotation Sensor
9-6	Static Torque
9-7	Module Performance Tests

9-2 Friction coefficient Rubber

The armature is made from steel and the friction-plates are made from aluminium with a layer of rubber. This combination of steel and rubber was chosen because it is easy to work with and it offers a large friction coefficient. However the exact coefficient must be found empirically, because it depends heavily on the type and condition of the rubber and the steel. We use the set-up shown schematically in figure 9-1. The rubber is glued to an aluminium weight and placed on a steel surface. The surface is hoisted in an angle until the force of the gravity surpasses the friction force and the weight starts to slip. The friction coefficient is determined from $F_w = F_g \cdot sin\alpha$. The experiments and results are described in detail in Appendix C. From the experiments, the resulting friction coefficient μ was found to be 0.45 ± 0.02.
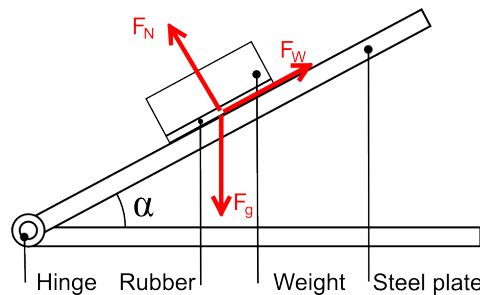
Figure 9-1: Experiment set-up Friction Coefficient

9-3 Spring Force

In this section we want to verify the spring force from the purchased springs. From chapter 7, the expected spring stiffness is 32.9N/mm, so that it can provide 94.5N at a preloaded length of 5mm, enough to provide the 86N required to keep the coupling engaged. To verify this, we will do a basic load test: apply a load, measure the displacement and then obtain the stiffness k using the relationship $F = k \cdot \delta x$. Where k is the stiffness and δx the displacement. This set-up is shown in figure 9-2.

Because the displacement is only a few millimetres, we need a very accurate way to measure it. Displacement is measured with an array of 6 VCNL4010 Infra-Red proximity sensors that can detect a reflective surface within a range of 5 to 200mm. By taking the average of 6 sensors, their combined error decreases to reach an accuracy of 0.1mm. Averaging also effects to cancel out any uneven balancing of the reflective plate. The verification of the sensor array is documented in Appendix D. Subsequently, the spring stiffness is measured in Appendix E. A load test is done by applying weights and measuring the displacement. The stiffness was found to be $27N/mm$. This means that the springs, from a unloaded length of 7.87mm to a preloaded length of 5mm and with a standard deviation of 1.1, can provide $77.5N \pm 2.2$.
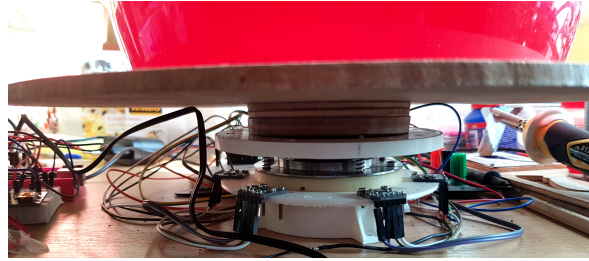
Figure 9-2: Test set-up Spring force

9-4   Magnetic Force and Duty-cycle

To verify the magnetic force exerted in the coupling matches, we use a similar configuration as was used to verify the springs, shown in figure 9-3. The magnet attracts a steel plate and pushes against the springs and a detection screen. The displacement is then measured with the displacement sensor array previously used for the verification of the spring force. With the displacement and the spring stiffness known, we can obtain the magnetic force.
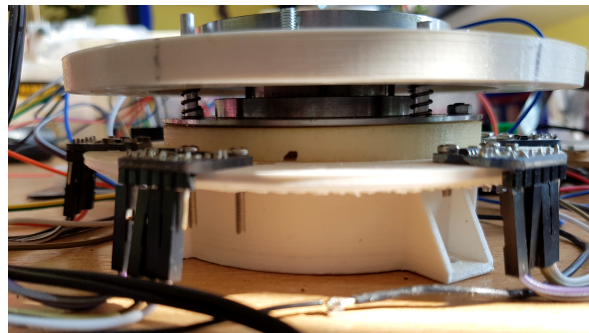
Figure 9-3: Test set-up Magnetic force

The tests are described in detail in Appendix F. The magnet was found to be able to hold the steel plate against a spring force of $108N \pm 2.2$. After that, the plate hit the magnet and could not lower any further. The magnet was only able to hold the plate though and failed to attract on its own. A push was needed to help to attract the plate. Therefore another set of springs, with lower stiffness, was used in the overall module performance tests.

Duty-cycle - After pulling the armature with the magnet at full power, we continue holding it with Pulse Width Modulation (PWM) to save energy. From Appendix F, it was found that a duty-cycle of 25% is enough to hold the armature in place. Figure 9-4 shows the resulting power curve for one test cycle. The magnet runs on full power for 1 second, continues with PWM for 2 seconds and turns off for another 2 seconds. Full power takes approximately 5400mW, but this drops to about 800mW for a duty-cycle of 25%. Thus we save a power consumption of about 85%.
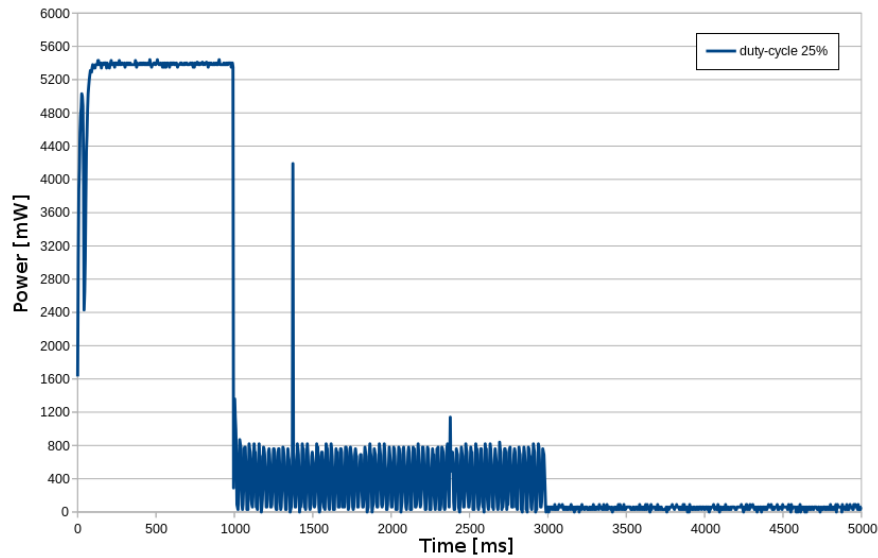
Figure 9-4: Power curve magnet

9-5 Integrated Rotation Sensor

The IRS will be used to control the module and we want to verify its accuracy. The set-up is shown in figure 9-5. The leg and wheel are replaced with 3D printed encoder discs and we will use two External Rotation Sensor (ERS) to measure the rotation and speed of the axles. The ERS was verified in Appendix H so we can compare its values with the values measured from the IRS.
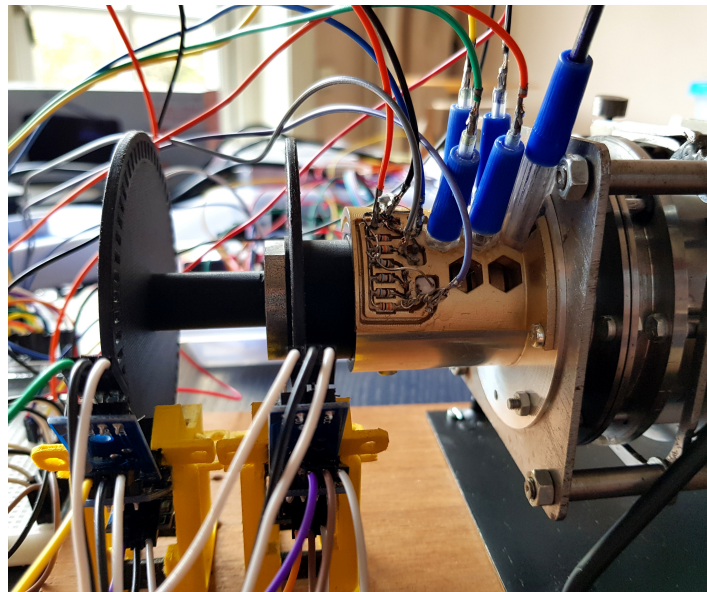
Figure 9-5: Test set-up IRS Sensor

The encoder fixed to the Leg-axle has a step of 15° and the encoder attached to the Wheel-axle has a step of 7.5°. So measurements are expected to be within this accuracy. The tests are described in detail in Appendix I. The resulting measurements are shown in figures 9-6 and 9-7. We can distinguish the Z-signals, in blue, and 12 and 24 pulses in between them. This corresponds to the 15° and 7.5° step of the IRS-L and IRS-W respectively. We can also see a phase difference between the A and B signals, in red and blue, so the IRS is able to identify the rotational direction.
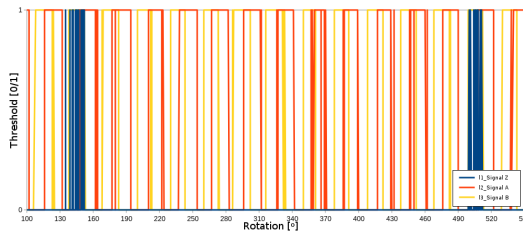
Figure 9-6: IRS-L: Signal measurements
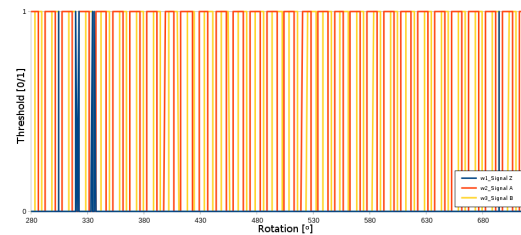
Figure 9-7: IRS-W: Signal measurements

9-6 Static Torque

In this section we will measure the maximum static torque that can be put on the axles. Static torque is the maximum load that can be held by an axle, when it is not rotating. Static torque is usually higher then the dynamic torque, which is the torque supplied by the axle while rotating. The set-up is kept very simple, a lever is attached to an axle and weights are added at the end until the axle starts to slip. The test is done for the wheel-axle and for the leg-axle, with the coupling in both the ON and OFF state, and with two types of springs used in the coupling.
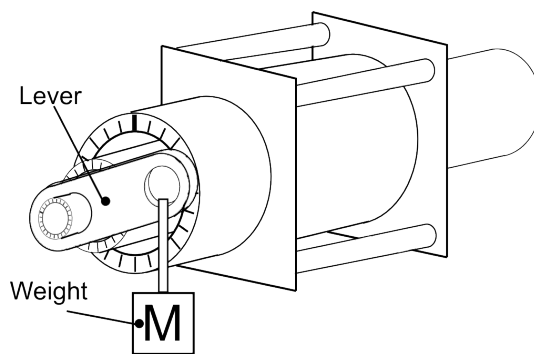
Figure 9-8: Set-up Static Torque Test

Figure 9-9: Static Torque Measurement

The tests are described in detail in Appendix K. From the tests we found the results in table 9-2.

Table 9-2: Static Torque Test Results

Springs	Axle	Total
[-]	[-]	[Nmm]
Type 1	Wheel-axle	279
Type 1	Leg-axle OFF	92
Type 1	Leg-axle ON	70
Type 2	Wheel-axle	463
Type 2	Leg-axle OFF	146
Type 2	Leg-axle ON	146

9-7   Module Performance Tests

We can now evaluate the performance of the module. An overview of the general test set-up is shown in figure 9-10 and a picture of the set-up is shown in figure 9-11.

The tests cover two parts. In the first part, the magnet is turned off and the Wheel-axle is engaged through the coupling. Rotational speed is measured with an ERS, as described in appendix H. An ERS-G is used for the motor shaft and an ERS-L is used for the Wheel-axle. A Prony sensor measures torque output at the Wheel-axle. An adafruit INA260 sensor is used to measure the electrical power consumed by the circuit. Output torque and mechanical power from the motor are read from the specifications in appendix A.

In the second part, the magnet is turned on and the Leg-axle is engaged through the coupling. Again, an ERS-G is used for the motor shaft, an ERS-L is used for the Leg-axle and a Prony sensor measures torque output. An adafruit INA260 sensor is used to measure the overall electrical power consumed by the circuit, but we use another INA260 sensor to measure the electrical power consumed by the magnet. Output torque and mechanical power from the motor are read from the specifications.

Because the magnet proved unable to pull the armature with the selected springs, the tests were done with a different set of springs. These have a lower stiffness, so the coupling is able to switch during the tests. All the tests, settings and results are described in detail in Appendix L.
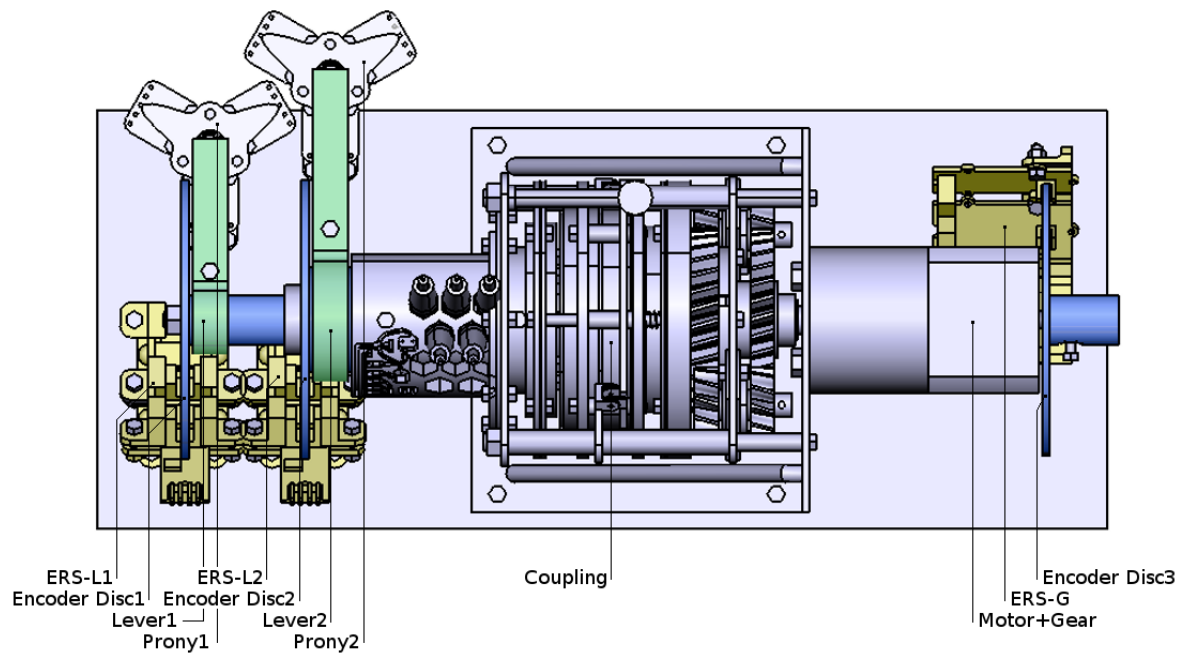
Figure 9-10: Overview Test set-up
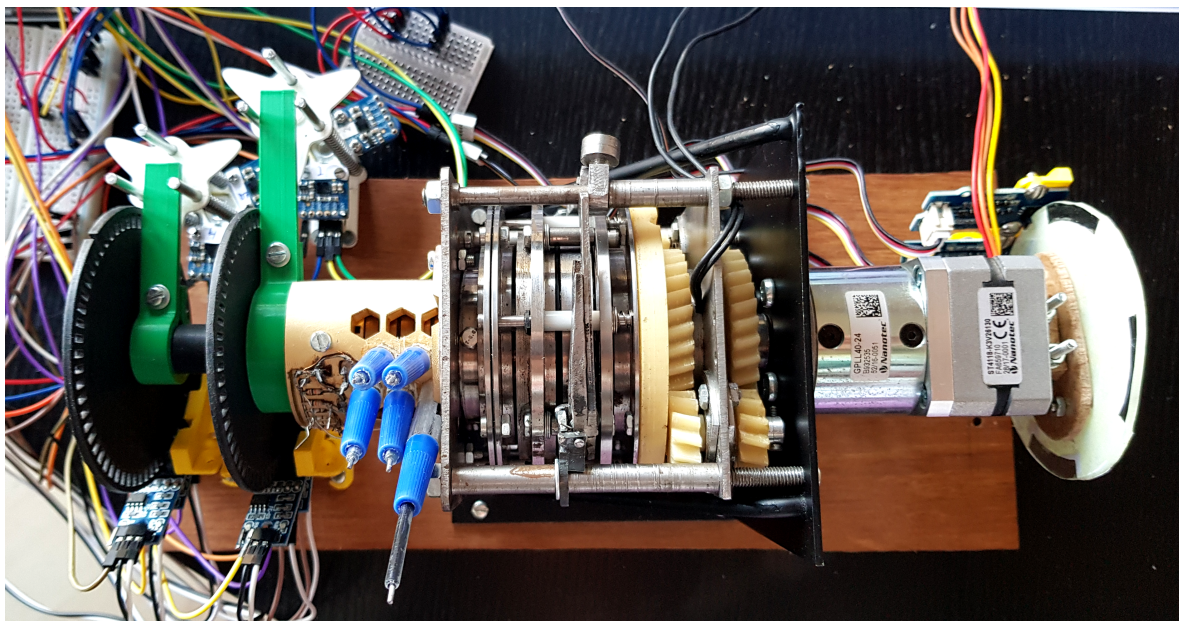
Figure 9-11: Top view Test set-up

Each experiment was done with 7 different speeds for a total of 14 tests. The results are summarised in tables 9-3 and 9-4.

In table 9-3, Speed set is the speed that was set for the motor. Speed M is the speed of the motor shaft as measured by the ERS-G. Speed G is the speed of the motor after the gear reduction. Speed was measured by the ERS with an accuracy of ± 5RPM. We assume the power loss by the gear box is negligible, so speed G was calculated by dividing Speed M by 24. PE_tw is the overall electrical power consumed by the circuit as measured by an INA260 sensor with an accuracy of ± 24mW. PM and Tm are the mechanical power and the torque produced by the motor as read from the motor specifications. Speed W is the speed of the Wheel-axle as measured by the ERS-L. And finally, the Tw is the torque produced by the Wheel-axle as measured by the Prony sensor. The Prony sensor is only accurate enough to measure indicative values.

Table 9-3: Test results - Wheel-axle engaged

Speed set [RPM]	Speed M [RPM]	Speed G [RPM]	PE_tw [W]	PM [W]	Tm [Nmm]	Speed W [RPM]	Tw [Nmm]
50	49.7	2.1	13.5	0.7	162	2.0	200
75	73.9	3.1	14	1.2	161	2.9	200
100	98.3	4.1	14	1.3	160	4.1	150
125	122.9	5.1	14	1.9	160	5.1	160
150	146.8	6.1	14	2	158	6.1	160
175	170.9	7.1	14.5	2.5	156	7.1	150
200	195.1	8.1	15	3.1	156	8.1	175

In table 9-4, most of the numbers are the same as in the previous table. PE_tl, Speed L and Tl are measured in the same way, but for the Leg-axle. The additional term PE_m stands for the electrical power consumed by the magnet, measured with a second INA260 sensor with an accuracy of ± 24mW.

Table 9-4: Test results - Leg-axle engaged

Speed set [RPM]	Speed M [RPM]	Speed G [RPM]	PE_tl [W]	PE_m [mW]	PM [W]	Tm [Nmm]	Speed L [RPM]	Tl [Nmm]
50	48.1	2.0	14	800	0.7	162	1.9	70
75	71.8	3.0	14	800	1.2	161	2.8	70
100	94.4	3.9	14	800	1.3	160	3.8	70
125	117.1	4.9	14	800	1.9	160	4.8	75
150	139.8	5.8	14	800	2	158	5.6	70
175	161.6	6.7	14.5	800	2.5	156	6.7	60
200	179.2	7.5	14.5	800	3.1	156	7.1	50

By comparing the input and output speed we can determine the slippage of the coupling. These are shown in tables 9-5 and 9-6. On average, we can see an error of 1.6% and 3.2% for the Wheel- and Leg-axle respectively.

Table 9-5: Slippage Wheel-axle

Speed set [RPM]	Speed G [RPM]	Speed W [RPM]	Error [RPM]	Error [%]
50	2.1	2.0	0.1	4.8
75	3.1	2.9	0.2	6.4
100	4.1	4.1	0	0
125	5.1	5.1	0	0
150	6.1	6.1	0	0
175	7.1	5.1	0	0
200	8.1	8.1	0	0
Average error [%]				1.6

Table 9-6: Slippage Leg-axle

Speed set [RPM]	Speed G [RPM]	Speed L [RPM]	Error [RPM]	Error [%]
50	2.0	1.9	0.1	5
75	3.0	2.8	0.2	6.7
100	3.9	3.8	0.1	2.6
125	4.9	4.8	0.1	2.0
150	5.8	5.6	0.2	3.4
175	6.7	6.7	0	0
200	7.5	7.1	0.2	2.7
Average error [%]				3.2

The torque that is produced by the motor is dependent on the speed, but the limiting factor on what can be transmitted to the axles is the friction force in the coupling. The springs push the armature against the friction-plates and we expect the armature to slip at a certain torque limit. The Prony sensors have a large error margin, but by averaging, shown in table 9-7, we can get an estimation of the maximum torque for each axle. Torque limit is 171Nmm for the Wheel-axle and 66Nmm for the Leg-axle.

Table 9-7: Test results - Output Torque

Speed set [RPM]	Tw [Nmm]	Tl [Nmm]
50	200	70
75	200	70
100	150	70
125	160	75
150	160	70
175	150	60
200	175	50
Average Torque[Nmm]	171	66

Finally we look at the average electric power consumption in table 9-8. Two INA260 power sensors measured the power consumption during the experiments. The power heavily fluctuates during the tests, so the upper boundary of the plot was taken as the measurement for the power consumption during a test. For the experiments where the magnet was engaged, we measure the electric power consumption after the first second, when the magnet was running with PWM. The results show that the overall power consumption rises moderately with increasing speed. Power consumption by the magnet appears to be constant with speed and to have a small effect on overall power consumption.

Table 9-8: Test results - Power consumption

Speed set [RPM]	PE_{tw} [W]	PE_{tl} [W]	PE_m [mW]	PE_m/PE_{tw} [%]
50	13.5	14	800	5.9
75	14	14	800	5.7
100	14	14	800	5.7
125	14	14	800	5.7
150	14	14	800	5.7
175	14.5	14.5	800	5.5
200	15	14.5	800	5.3
Average Values	14.1	14.1	800	5.6

Chapter 10

Evaluation

In this chapter we take a look at the results of the tests in chapter 9 and compare them to the expected values. We will also make projections for the performance of a future robot with the new module.

10-1 Overview Chapter

An outline of the chapter is shown in table 10-1. We will start with a discussion of the different features of the modules. Then we will the performance of the module as a whole. In the final section we will use the results to calculate some estimated projections for a hybrid robot with 6 of the prototype modules.

Table 10-1: Section Overview

Section	Subject
10-1	Overview Chapter
10-2	Features Evaluation
10-3	Module Evaluation
10-4	Performance Projections

10-2   Features Evaluation

An evaluation of the different features of the coupling is important in the analysis. A summary of the expectations and measurements is listed in table 10-2.

Friction coefficient - We used a standard rubber with a thickness of 1mm, bought at a hardware store. The friction coefficient between rubber and steel was expected to be a minimum of 0.6. However it was also noted that the coefficient is highly susceptible to the exact material and the conditions in which it is used. After measuring, the coefficient was found to be 0.45±0.02. Although much lower then anticipated, this will allow us to adjust the expectations of the coupling and leave open the possibility for improvement.

Spring force - The 4 C0180-026-0310M springs, placed in parallel, were expected to have a combined stiffness of 32.9N/mm. In reality, the stiffness was measured at 27N/mm. This means that at the preloaded length of 5mm, with standard deviation of ± 1.1N, the spring force will be 77.5 ± 2.2N instead of 94.5N. This is lower then anticipated, but this will allow us to recalculate the expectations of the coupling and leave open the possibility for improvement.

Magnetic force - The magnet is required to pull the armature against the springs, and push it against the friction pad of the Leg-axle, with a total of 129N. After testing, the magnet was able to hold the steel brake-pad against a spring force of $108N \pm 2.2$. But the magnet was not able to attract the armature by itself and the armature needed a push. This is another point of improvement for future research. In order to proceed with testing, we evaluated the module with another set of springs with lower stiffness. With the weaker springs, the magnet was able to couple and decouple the armature between the friction plates.

Table 10-2: Features: expectations and measurements

Feature	Expected Value	Measured Value
Friction coefficient	0.6	0.45
Springs stiffness	32.9N/mm	27N/mm
Magnet force	129N	108N

10-3   Module Evaluation

Coupling behaviour - From the experiments it was shown that the coupling was able to successfully couple and decouple between the Wheel-axle and the Leg-axle. When the magnet is off, the Wheel-axle is engaged with the motor shaft and the Leg-axle is held fixed by the brake-pad. When the magnet is turned on, the Leg-axle was successfully engaged with the motor shaft and able to turn in both directions. This means that the module is successful in switching from driving to walking mode.

Speed transfer - From the test results, we have found there is a small difference between the measured speed from the motor and, after compensating for the gear-reduction, the speed measured from the axles. The slippage from the motor to the Wheel-axle was found on average to be 1.2%. Slippage from motor to the Leg-axle was found to be 3.4%. This means that the speed loss is limited.

Torque - Torque produced from the motor is dependent on speed, but the torque transmitted to the axles is limited by a threshold value. This is because the limiting factor is the friction force between armature and the friction-plates in the coupling. Because we used springs with a low stiffness, the applied spring force to the armature was 7.4N. The rubber and steel combination was found to have a friction coefficient of 0.45. Therefore, from equation 7-1, we calculate a maximum expected torque of 260Nmm.

The torque sensors had a large error margin, but by averaging the measurements, we were able to obtain indicative values. The average measured dynamic torque from the Wheel-axle was 171Nmm with a maximum value of 200Nmm. A possible reason why it is much lower is because the armature and friction-plate were not correctly making contact and the force was not transferred properly. Average torque from the Leg-axle was measured at 66Nmm. This is possibly because the armature was pulled completely against the magnet and the force was not transferred to the friction-plate of the Leg-axle. In any future development of the module, tuning of the armature and the friction plates will need to be improved.

Power consumption - We measured electrical power consumption of the module with and without the coupling engaged. There is a large spike when the magnet is engaged in order to attract the armature. After switching to Pulse Width Modulation (PWM) with a duty-cycle of 25%, we observed only a moderate increase in power consumption in comparison to the OFF-state. The magnet consumed 800mW, which is 5.8% of the average overall power consumption when only the motor is actuated. The increase in overall power consumption, was even smaller. Just 3%. It is possible that the magnet is getting full power in this situation, but the motor gets throttled as they were using the same power supply. Measured speed of the motor shaft appears to be slightly lower with the same settings, which supports this theory, but it is not a significant decrease. We used two Adafruit INA260 power sensors that had an accuracy of ±24mW.

10-4 Performance Projections

In this section we want to look at some performance projections for a Zesbenige Robot (ZebRo) equipped with 6 of the hybrid walker-wheeler modules. We do not have a complete robot to test at this point, but we are able to make estimations so as to judge the feasibility of the newly proposed hybrid robot. We compare the hybrid robot with a conventional ZebRo by having them both travel over a fixed trajectory and will calculate a rough estimation, using crude assumptions, of the potential gain in energy savings and speed. In the calculations, we neglect the additional weight of the coupling and assume a constant speed over the trajectory.

We compare the hybrid robot with a conventional ZebRo by having them both travel over the same trajectory with length Z. The conventional ZebRo will walk the entire length using its legs, depicted in figure 10-1. It will travel with a constant horizontal speed of v_1, so that $Z = v_1 t_C$. Where t_C is the time duration. We also want an estimation of the consumed energy. The legs are directly powered from the motor, with power P_m. So the energy spend, E_C, to travel is $E_C = t_1 P_m$.
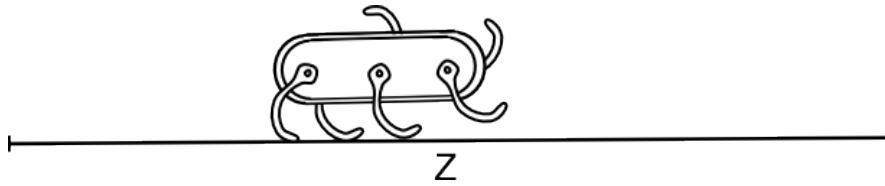
Figure 10-1: Conventional ZebRo

The hybrid robot travels over the same trajectory, as shown in figure 10-2. But the trajectory is divided into a two parts with a ratio a between 0 and 1. In the first part, Za, the robot will walk using its legs. We assume that problems with the coupling have been resolved, so that there is adequate torque transfer. We further assume that the legs on the conventional and hybrid ZebRo produce the same horizontal speed, so the hybrid ZebRo will travel with speed v_1 in this part. To power the legs, both motor and coupling are activated. From section 9-7, we will assume this takes approximately 5.6% more in comparison to just the motor. So power consumption is $1.056P_m$.
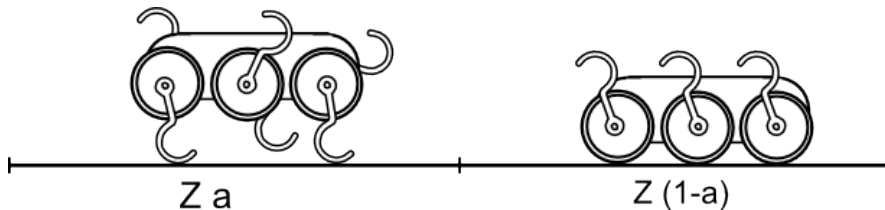
Figure 10-2: ZebRo with Hybrid Modules

In the second part of the trajectory, $Z(1-a)$, the hybrid ZebRo will drive with its wheels. From section 5-5, we know that the horizontal speed in driving mode can be estimated as to be at least 50% higher then in walking mode. The wheels are directly driven from the motor so that power consumption is P_m.

When we combine the first and second part of the trajectory then time duration for the hybrid robot, to travel the length Z, is $t_H = \frac{Za}{v_1} + \frac{Z(1-a)}{1.5v_1}$. Energy consumption is determined by $E_H = 1.056P_m\left(\frac{Za}{v_1}\right) + P_m\left(\frac{Z(1-a)}{1.5v_1}\right)$.

We now have two formulas for both the conventional and for the hybrid robot. One for the time taken to travel over the trajectory and one for energy consumption.

$$t_C = \frac{Z}{v_1} \tag{10-1}$$

$$t_H = \frac{Za}{v_1} + \frac{Z(1-a)}{1.5v_1} \tag{10-2}$$

$$E_C = P_m\frac{Z}{v_1} \tag{10-3}$$

$$E_H = 1.056P_m\left(\frac{Za}{v_1}\right) + P_m\left(\frac{Z(1-a)}{1.5v_1}\right) \tag{10-4}$$

We can see from the equation 10-2 that any ratio of a lower then 1 decreases the time duration, as driving is faster. However equation 10-4 shows the feasibility in terms of energy consumption is dependent on the number of a. The higher power consumption in walking mode initially leads to an increase in overall energy consumption. Only when the proportion of driving mode increases, overall energy consumption decreases due to the better efficiency in driving. We can solve equations 10-3 and 10-4 to find the tipping point for a where the hybrid robot becomes more energy efficient then the conventional robot.

$$P_m\frac{Z}{v_1} = 1.056P_m\left(\frac{Za}{v_1}\right) + P_m\left(\frac{Z(1-a)}{1.5v_1}\right)$$

$$1 = 1.056a + \frac{1-a}{1.5}$$

$$a = 0.85$$

This means that the hybrid robot becomes more energy efficient then the conventional ZebRo when it can drive on more then 15% of the trajectory.

We can now determine the factor $\frac{t_H}{t_C}$.

$$
\begin{aligned}
\frac{t_H}{t_C} &= \frac{\frac{Za}{v_1} + \frac{Z(1-a)}{1.5v_1}}{\frac{Z}{v_1}} \\
&= \frac{\frac{Z}{v_1}\left(a + \frac{1-a}{1.5}\right)}{\frac{Z}{v_1}} \\
&= a + \frac{1-a}{1.5}
\end{aligned}
$$

Implementing $a = 0.85$ results in a factor of 0.95. This result means that, when the hybrid robot is able to drive for a minimum of 15% of the trajectory, the time duration is reduced with 5% in comparison to the conventional ZebRo with the same amount of energy consumption. The hybrid robot becomes more beneficial with a larger proportion of driving in the trajectory. If we plot $\frac{E_H}{E_C}$ and $\frac{t_H}{t_C}$ against the driving proportion, we get the plot in figure 10-3.
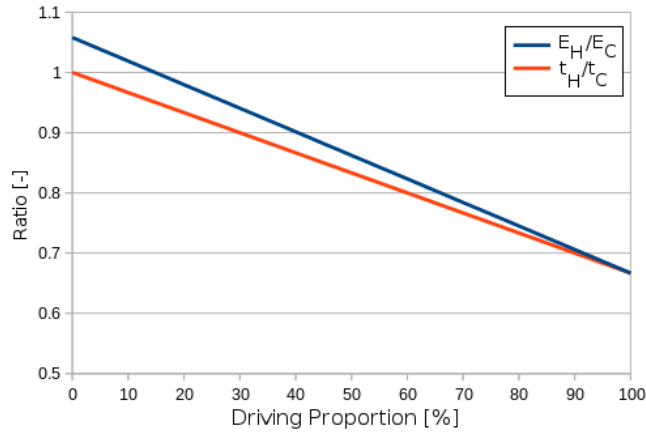
Figure 10-3: Reductions E and t versus Driving ratio

From the figure, we can see $\frac{E_H}{E_C}$ crossing 1 at a driving proportion of 15%. This is the crossover point where the hybrid robot becomes more efficient then the conventional ZebRo. We can also see that the maximum reduction in both energy consumption and time duration is approximately 33%.

Chapter 11

Conclusions & Discussion

This is the final chapter in which we will look back at the research, answer the research questions, draw conclusions, discuss the positives and drawbacks of the module and make recommendations for future research.

11-1   Chapter Overview

With table 11-1 we give an overview of the chapter. In the first section we will review the research questions. Then we will discuss the module in the conclusions. In the last section we will set out recommendations for future research.

Table 11-1: Section Overview

Section	Subject
11-1	Chapter overview
11-2	Review of Research questions
11-3	Conclusions and Discussion
11-4	Recommendations for Future Research

11-2 Review of Research questions

In chapter 1 we started with 10 research questions. With the work in this thesis we are now able to look back at those and formulate the answers.

I. What are the requirements for a Zesbenige Robot (ZebRo) robot equipped with hybrid Walker-Wheeler technology?
This topic was discussed in chapter 2. We looked at the requirements stemming from possible applications and the requirements for compatibility with the ZebRo platform. To function in outer-space missions, the robot needs a high degree of autonomy and robustness. Energy efficiency is important, because the robot will be dependent on a limited power supply. Furthermore, the robot needs to be able to cope with small bumps and ditches in driving mode and be able to negotiate mull sand and moderate slopes and ditches in walking mode. Speed is not an important requirement, because its tasks will not be time limited. To be compatible with the ZebRo platform, the robot should have a maximum of 6 motors and have a modular approach to the design.

II. What are the possible options and concepts for a hybrid walker-wheeler robot?
We looked at 9 different parameters and listed the possible options for each in chapter 3. This gave us a total of 8880 possible combinations. We narrowed these down based on practicality, complexity or feasibility. After the reductions we came to 5 prospective combinations that were developed into concepts. In chapter 4 these concepts were scored on Walking ability, Driving ability, Robustness, Efficiency and Compatibility. The most promising concept was found to be a combination of a separate wheel and leg, connected through a central pivot. An active coupling is to switch power from the motor between the leg-axle and the wheel-axle.

III. What are the characteristics of a C-Leg and a Wheel and how can we apply these in the design of a hybrid module?
In chapter 5 we did a number of simulations to examine the fundamental characteristics of a C-Leg and a Wheel and to apply these in the design of the module. We found that the climbing ability of the C-Leg is based on the way in which the reaction force, between C-Leg and surface contact, is decomposed into a large component directed normal to the surface of the obstacle. The C-Leg is able to *grasp* the surface. By contrast, the rim of a wheel decomposes the reaction force, with increasing obstacle height, into an ever larger component directed parallel to the obstacle's surface. The maximum obstacle height for a wheel was found to be 50% of the length of the radius whereas the maximum obstacle height for a the C-leg was 120% of its radius.
The benefits of the wheel were visible during the experiments on the straight piece. The wheel has continuous ground contact and rotation of the center pivot is translated linearly to horizontal movement. By contrast the C-leg has an intermittent ground contact and is accelerating and decelerating between steps. When a constant angular speed was applied to the central pivot, the horizontal speed of the wheel was found to be a minimum of 50% higher in comparison to the C-Leg. Corresponding torque and

power consumption were also found to be substantially lower for the wheel. The wheel only requires torque to overcome surface friction with the ground because the vertical reaction force is always directed to the center pivot and counteracts against the weight and load on the axis. The continuous horizontal movement and the large moment of inertia of the wheel preserve momentum and energy as well. By contrast, the C-leg has to push against its body weight with each step.

In designing the new module, the shape of the leg should be optimized for grip during climbing. In designing the wheel, its radius should be made as large as possible to optimize driving ability and maximize energy preservation.

IV. How should the chosen concept be developed into a prototype module for evaluation?

In chapter 6, the leg and wheel were designed. The leg was developed into a hook-shaped design so that the convex part reaches beyond the rim of the wheel and it will have better grip. Radius of the wheel was chosen to be 12cm. This was the maximum that is compatible with the bodylength of the robot and length of the leg. In chapter 7, a custom electro-magnetic coupling was designed specifically for this application. The coupling was developed to match the requirements in functionality, dimensions and torque capabilities. When the coupling is not engaged, it keeps the Leg-axle fixated and drive the Wheel-axle through an armature. When the coupling is engaged, it will drive the Leg-axle and the Wheel-axle is disengaged.

V. How should the module be tested in order to evaluate it with the previously determined criteria?

Testing of the module is described in chapter 9. The first part was to evaluate the features of the coupling individually. In the second part, the complete module was tested with the coupling disengaged and engaged. The set-up measured electrical power consumption of the motor and the coupling, angular speed of the motor and the dynamic torque and angular speed of the outgoing axles.

VI. Would the prototype be able to achieve an overall higher speed?

With the results, we were able to make a few estimated performance projections of the new robot in chapter 10. With the assumption that horizontal speed in driving mode increases by 50%, we can state that the overall median speed would also increase if driving is possible during the mission. Driving is possible when encountered obstacles have an height of maximum 3cm. In the calculations we did not take into account the increase in weight.

VII. Can the new robot maintain the rough-terrain mobility in comparison to a conventional ZebRo?

For this question we must consider the torque transmitted to either the Leg-axle or the Wheel-axle. The coupling failed to transfer the required amount of torque and would thus fail to have a comparable walking ability to the conventional ZebRo. This would need to be resolved before the module can be developed in a full robot. If the problems

with torque transmission were to be resolved the hook-shaped leg is expected to have an obstacle negotiation ability of 12cm in walking mode. This is based on simulations of the model in chapter 6 and is equal to the simulated model of the conventional C-Leg.

VIII. Can the new prototype achieve a greater energy efficiency then a conventional ZebRo?
From the projections in chapter 10, we learned that initially overall power consumption increases because the power consumption in walking mode increases by about 5.6%. But the robot would be a minimum of 50% faster in driving mode and power consumption is reduced by one third over this distance. From the calculations we found that a mimimum driving proportion of 15% would make the robot feasible in energy preservation. The maximum reduction in energy usage would be 33%.

IV. Would the new robot maintain high robustness?
Amongst the requirements, great emphasis was put on the robustness of the module. This is important in order to achieve the durability and autonomy that is required for an outer-space mission. Robustness was split into different aspects. As all the parts can be sealed or covered, we can judge that the module would be water- and dust-proof. The module also has only two Degree-of-Freedom (DoF) with two active components. This would make control of the module easy and enable a good reliability. But the complexity of the coupling is still too high. It has many parts and fine tuning of the armature and friction plates means that it is still vulnerable to shocks. High temperature fluctuations could also have an impact as parts would expend and contract. For long term missions, the rubber between the armature and the friction pads could be prone to wear. For this module to be feasible, the coupling would need to be further simplified and developed in order to be sufficiently robust.

X. What recommendations can be made for future research?
This research has shown that we can expect great gains in overall speed and energy preservation if the robot is able to drive for parts of the mission. But the coupling is still insufficient in torque transmission and robustness, both of which result from its high complexity. Future research would need to focus on further simplification and development of the coupling.

XI. What are the potential societal effects of Hybrid Walker-Wheeler robots?
The emergence of autonomous mobile robots, including this robot, can have a drastic impact on society. In fact it already has. We see traditional workers being displaced in warehouses or we see robots being weaponized for use in battlefields. However they can also help people in dangerous missions or explore environments beyond our reach. It is therefore the belief that the good that autonomous mobile robots can bring will ultimately outweigh the bad.

11-3   Conclusions and Discussion

This thesis started with the question of whether it is possible to develop a hybrid walker-wheeler robot, applied with the ZebRo platform, that increases its overall speed and energy efficiency on flat surfaces, while maintaining its robustness and walking capability on rough terrain.

To examine the question, we designed and developed a new module with a hook-shaped leg, a wheel and a coupling to switch between the axles. The concept module was then build, tested and evaluated on energy consumption and torque transmission. It was found that the module offers large potential gains in speed and energy efficiency. Simulations, section 5-6, suggest a potential 50% increase in speed in driving mode. Driving would be possible on surfaces with obstacles of up to 3cm.

Test results, from section 9-7, found only a 5.8% increase in electric power consumption during walking mode. The module would be feasible in terms of energy efficiency, if a mimimum driving proportion of 15% during the mission is achieved. The maximum reduction in energy usage, if only the wheel is used, would be 33%.

Furthermore, from simulation models, it is expected that the module is able to surmount obstacles of 12cm in walking mode. A hybrid robot with these parameters would have sufficient walking capability to match a conventional ZebRo robot.

The prototype module failed however to transfer sufficient amounts of torque through the coupling. The magnet used in the coupling proved insufficiently strong to attract the armature, although it was able to hold it in place. Therefore the originally selected springs were replaced with springs with a lower stiffness. In this scenario, dynamic torque was expected to be 260Nmm for each axle. From the tests, section 9-7, the module was shown only to transfer 171Nmm to the Wheel-axle and 66Nmm to the Leg-axle. Possible cause for the result might be that the friction plates were not correctly aligned. The armature allowed movement in a torsional capacity and could not be properly tuned.

Robustness is another concern. Robustness is an important property in order for the robot to be feasible in autonomous missions. At this point, complexity of the module is still high with many parts and fine tuning of the armature. This makes the prototype vulnerable to shocks and temperature influences. We therefore judge that robustness is still insufficient at this point.

11-4   Recommendations for Future Research

From this research we can conclude that there are large potential gains from hybrid driving-walking technology, but there are still big challenges with robustness. At this point, we can identify 4 possible avenues for continued research.

1. *Further development of the current prototype* - The first possibility is to continue development of the current prototype. Focus would have to be on simplification and weight reduction of the coupling. It also might need a stronger magnet or it could continue with smaller springs and lower its torque capacity.

2. *Off-the-shelf components* - By focusing on the use of tested-and-tried components, we might be able to increase robustness and reliability. We were unable to find a coupling that could both switch between two axles and brake the axle not being engaged at the same time. But an alternative option might be to look at a combination of two or more existing couplings. If we separate the functions and use one coupling to switch the leg-axle, while another is used for switching the wheel-axle, we might achieve the same result. Downside might be that this increases power consumption.

3. *Second motor* - The prototype utilizes only one motor in order to keep weight and complexity low. However the coupling adds weight and complexity as well. If instead we choose to add a second motor we can achieve full control over each axle and do not lose any torque in transmissions. It would even allow us to separate the axles as they do not need to be aligned any more.

4. *Combined Leg-Wheel shapes* - The final option is to take another look at the possible concepts in chapter 4. If we add more importance to robustness and slightly less on driving ability, then concept 3 becomes the more interesting concept. The speed and efficiency of a wheel are due to its continuous ground contact and a combined leg-wheel shape takes advantage of that. This might achieve only a moderate improvement in speed and energy efficiency, but there is almost no cost in additional complexity.

Appendix A

Specifications ST4118X1404-B

This appendix is a documentation of the specifications of the nanotec ST4118X1404-B steppermotor. All data and figures where obtained from the nanotec website.
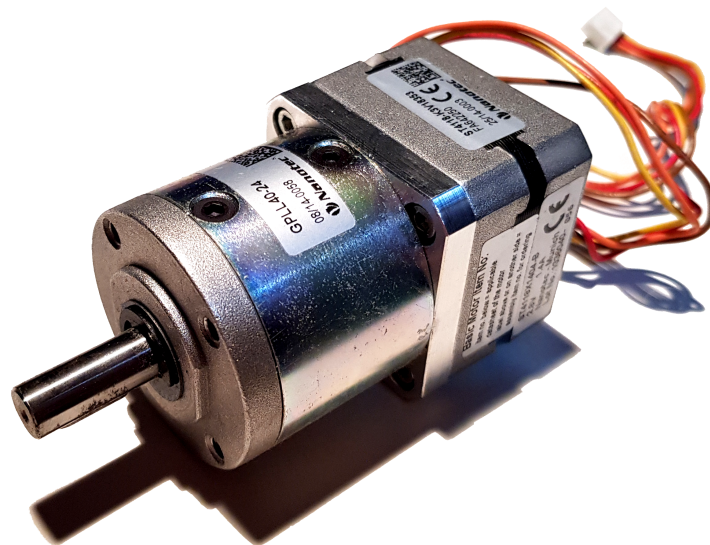
Figure A-1: Motor with Gear reduction
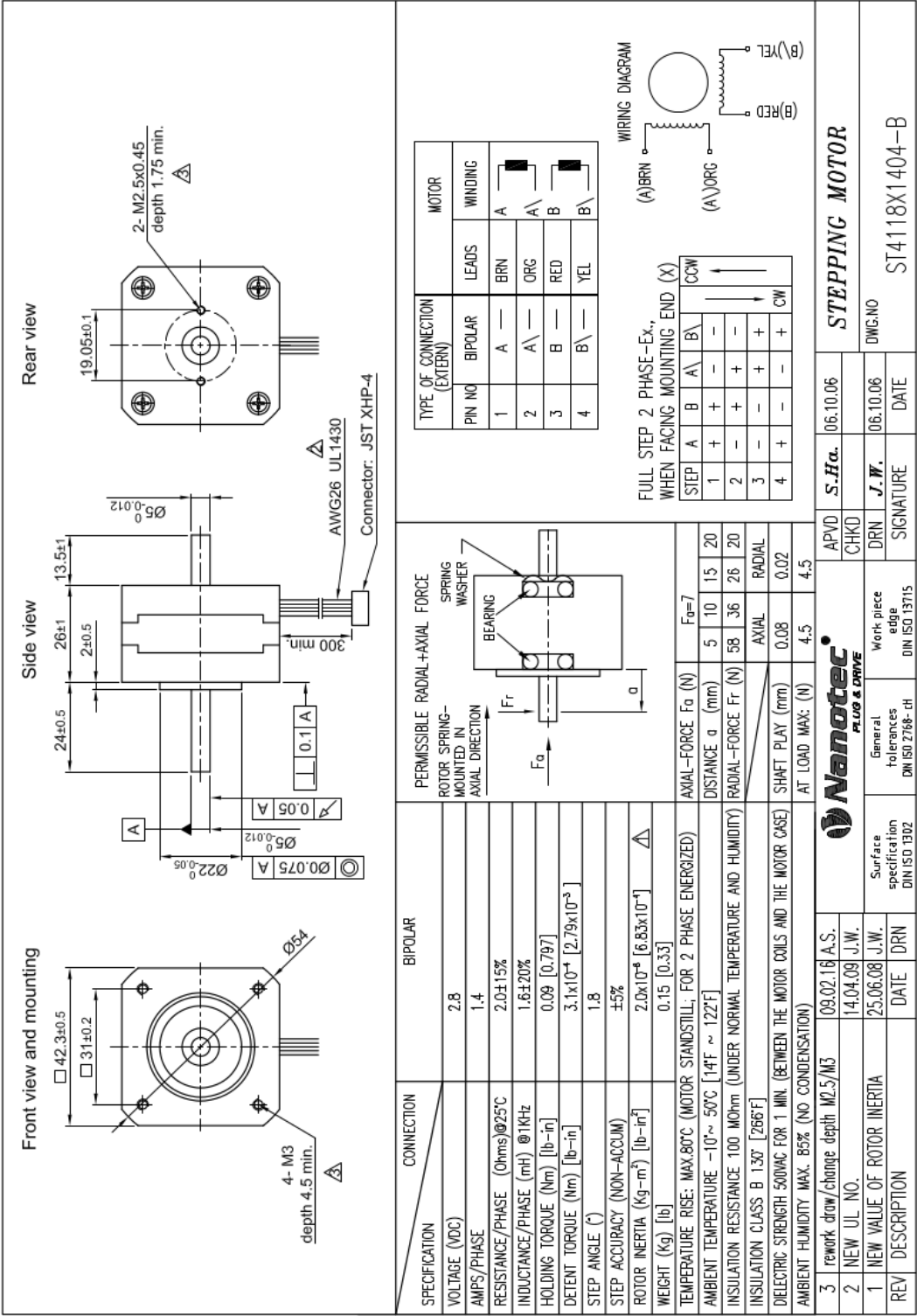
Figure A-2: Overview ST4118X1404-B
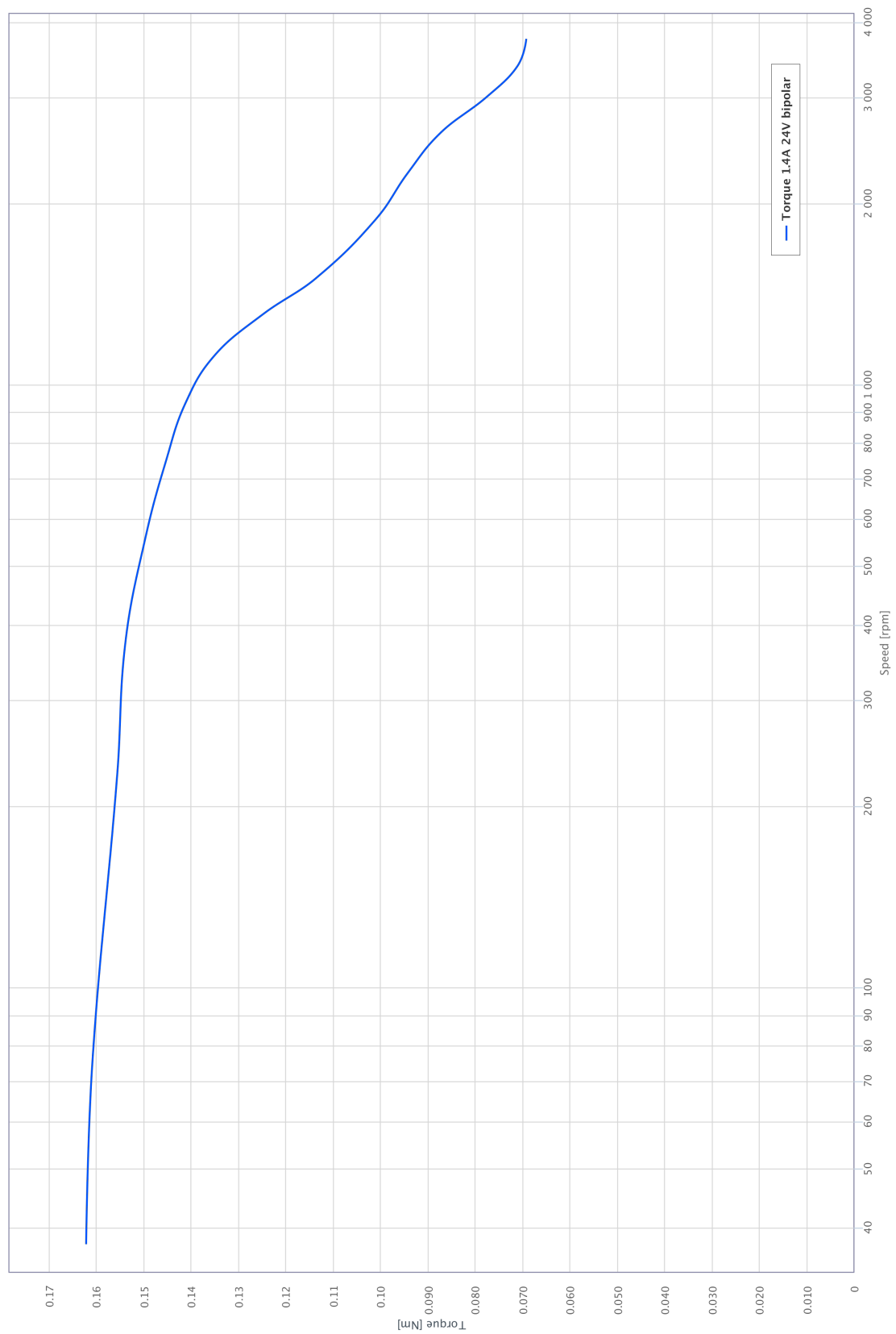
Figure A-3: Speed-Torque curve
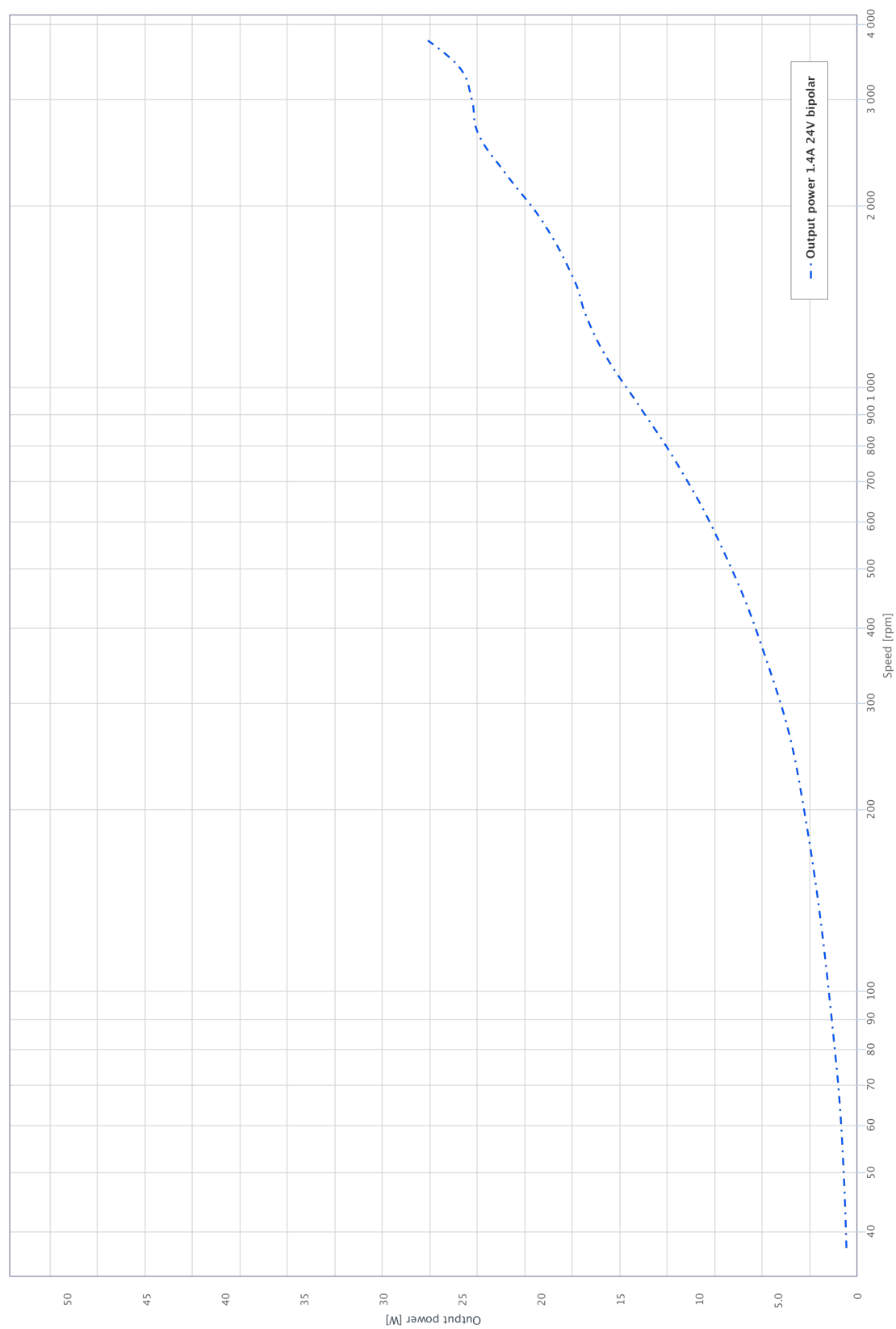
Figure A-4: Speed-Mechanical Power curve

Simulation Test Results

B-1   Set-up Simulations

Obstacle Negotiation experiment set-up - The test set-up is kept very simple, as shown in figure B-1. It consists of a single body, either a wheel or C-Leg, suspended by two mass-less beams. The beams allow movement without friction in a 2-dimensional frame. A constant vertical load is applied at the center axis, simulating the weight of the body. A step with height H is located at an initial horizontal distance d from the axis. So when the simulation runs, the body will hit the object and attempt to climb it. Torque T is increased until it either accomplishes the task or reaches an upper limit
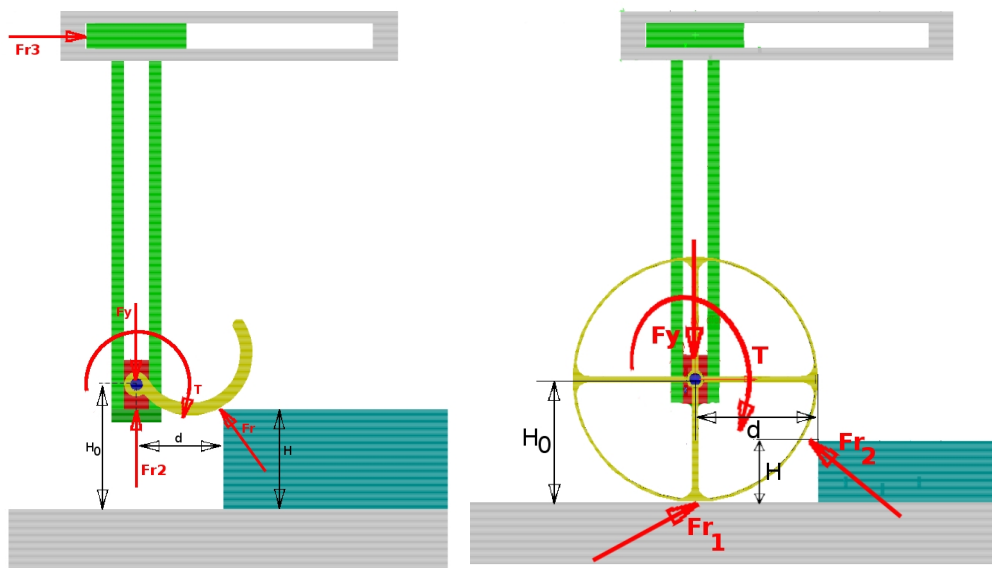
Figure B-1: Test set-up with C-Leg(a) and Wheel(b)

of 2000Nmm. Height H is increased incrementally, until the body can no longer climb it. This height will be the Obstacle Negotiation Limit (ONL) of the body.

The ONL can depend on where the leg or wheel hits the obstacle. So the simulations are repeated for a range of distance d. All other parameters are kept constant in the simulations. That is: vertical load on the axis, type of material, radius or length of the body, thickness, friction coefficients, geometry of the obstacle and initial velocity. It is possible these can also influence the results, but in order to limit the scope, we will solely focus on the difference between Wheel and C-Leg geometry.

With MSC ADAMS, most variables can be easily monitored, measured and plotted. This includes elapsed time, displacement of the center point in x and y direction and angular rotation. With the method as described, the torque related to the ONL is automatically determined. Energy consumption, in Joule, is calculated with $P = \theta \cdot T$. Speed can be found by measuring the horizontal displacement of the axis and divide it with the elapsed time.

C-Leg Configuration - An overview of the C-Leg model and the applied forces, as used in the simulations, is shown in figure B-2. The specifications are listed in table B-1. Torque T acts on the axis, which is normally supplied by the motor. A constant vertical load Fy of -20N is applied on the axis, that will simulate the weight of the robot acting on the leg. The axis would normally suspended by the robot, so a reaction force is modeled with the vertical beam to keep the C-Leg from falling down in the swing phase. A contact force with coulomb friction is modelled between the leg and the obstacle. The friction coefficient is 0.8 for static friction and 0.7 for dynamic friction.
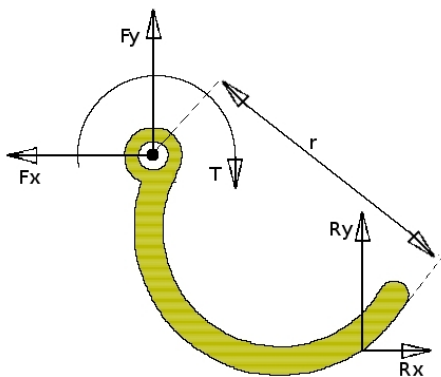
Figure B-2: C-Leg Model

Table B-1: Specifications C-Leg configuration

Length r	10cm
Width s	4cm
Mass M	0.5kg
Material	steel
Inertia Ixx	746,13
Inertia Iyy	679,29
Inertia Izz	201,09
Suspension Height H_0	10cm
Static friction μ	0.8
Dynamic friction ν	0.7
Vertical load Fy	-20N
Range distance d	0-10cm

Starting height H_0 of the axis is set at 10cm. Distance d is varied between 0 and 10cm, with incremental steps of 1cm. 10cm is the maximum reach of the leg, so this is the natural upper boundary. At each increment, height H is incrementally increased until the leg can no longer climb the obstacle. A climb is deemed successful if the axis passes the obstacle ($\Delta x \geq d$) and the leg does not fall back ($\Delta \theta \geq 180$). The corresponding torque T to subdue the obstacle is documented with each height. Speed is calculated by dividing the horizontal displacement with the elapsed time at the tipping point. Consumed Energy is determined by $T \cdot \theta$.

Wheel Configuration - The wheel is modelled similarly to the leg, shown in figure B-3. Specifications are listed in table B-2. It has a horizontal and a vertical force on the axis, a torque supplied by the motor and a contact force with the obstacle, modelled by coulomb friction. There is also a contact with the ground. For equal comparison, the wheel and leg have the same weight, radius or length and thickness. As a result, the wheel was hollowed out and has a very slim outer rim. Distance d was varied from 4 to 20cm. Due to the geometry of the wheel, it can not mount obstacles closer then 4cm, as it would clash with the rim of the wheel. Extending d beyond r, allows us to give the wheel a head-start and include the effects of that.

The wheel is deemed successful at a climb when the axis passes the obstacle, $\Delta x \geq d$. Torque T, Energy consumption and speed are again calculated similarly to the previous section.
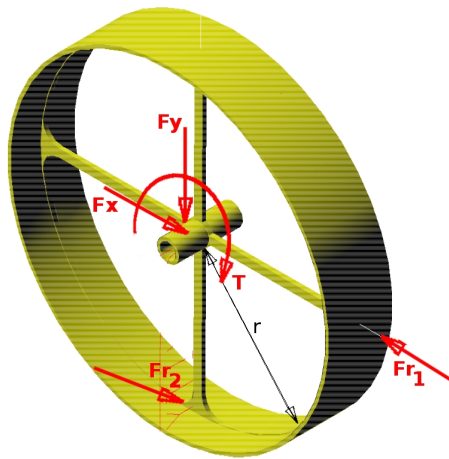
Figure B-3: Wheel Model

Table B-2: Specifications Wheel

Radius r	10cm
Width s	4cm
Mass M	0.5kg
Material	steel
Inertia Ixx	4022,06
Inertia Iyy	2065,95
Inertia Izz	2065,95
Suspension Height H_0	10cm
Static friction μ	0.8
Dynamic friction ν	0.7
Vertical load Fy	-20N
Range distance d	4-20cm

Straight Piece experiment set-up - To test the models on a Straight Piece, we use the same framework as used for the Obstacle Negotiation Tests and the same models for the wheel and C-Leg. But the obstacle is removed and a constant angular velocity is imposed on the pivot. The body then travels over a 1m piece of flat surface.

Speed, torque and energy consumption are observed through MSC ADAMS. Some plots are shown in figures B-4 and B-5.
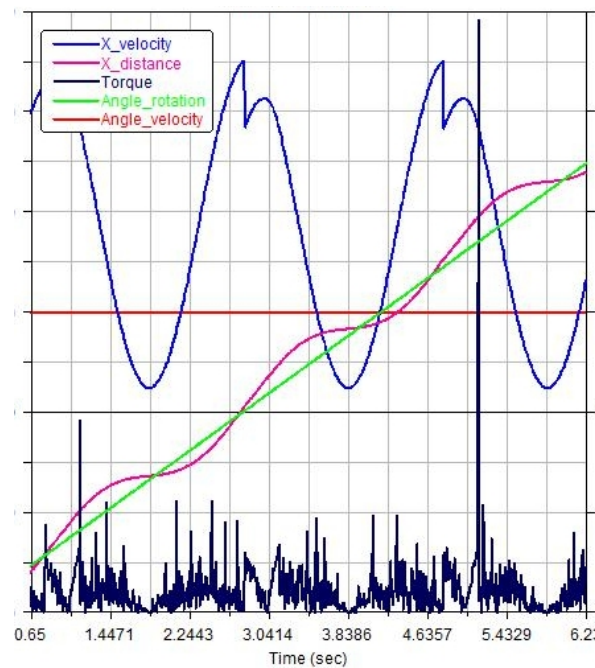
Figure B-4: C-Leg on Straight piece with constant velocity
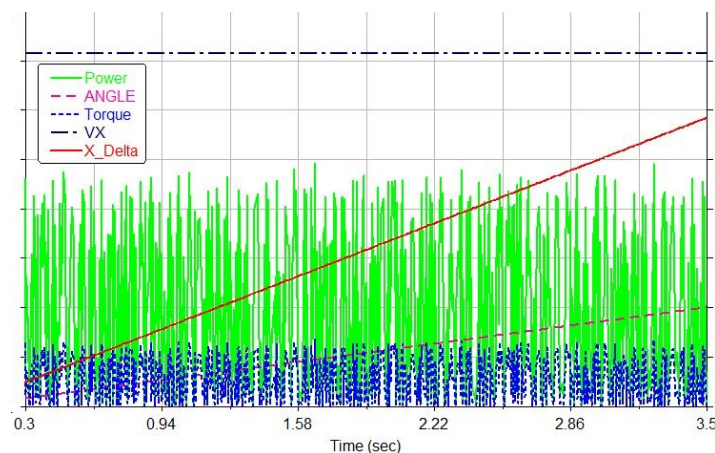
Figure B-5: Wheel on Straight piece with constant velocity

B-2   Obstacle Negotiation Simulations - Results C-Leg

A table with all the data from the experiments with the C-Leg. d=distance, H=height, T=Torque, t=time until tipping point, Δx= horizontal distance until tipping point, θ=angle rotation (both in degrees and radian), v=average speed, E=consumed energy.

Table B-3: C-Leg Experiment Data

d[cm]	H[cm]	T[mNm]	t[s]	Δx[cm]	θ[°]	θ[rad]	v[m/s]	E[J]
0	1	40	0,29	129,89	180	3,14	0,45	0,13
0	2	230	0,28	138,17	180	3,14	0,49	0,72
0	3	390	0,3	145,37	180	3,14	0,48	1,23
0	4	470	0,28	145,11	180	3,14	0,52	1,48
0	5	540	0,35	150,98	180	3,14	0,43	1,7
0	6	560	0,37	152,81	180	3,14	0,41	1,76
0	7	600	0,31	152,87	180	3,14	0,49	1,88
0	8	620	0,29	155,12	180	3,14	0,53	1,95
0	9	660	0,29	156,84	180	3,14	0,54	2,07
1	9	660	0,29	152,4	180	3,14	0,53	2,07
1	10	720	0,28	150,3	180	3,14	0,54	2,26
1	8	620	0,29	155,13	180	3,14	0,53	1,95
1	7	600	0,31	152,87	180	3,14	0,49	1,88
1	6	560	0,37	154,32	180	3,14	0,42	1,76
1	5	540	0,35	150,98	180	3,14	0,43	1,7
1	4	470	0,28	145,11	180	3,14	0,52	1,48
1	3	390	0,3	145,37	180	3,14	0,48	1,23
1	2	230	0,28	139,7	180	3,14	0,5	0,72
1	1	40	0,29	129,89	180	3,14	0,45	0,13
2	1	40	0,29	129,89	180	3,14	0,45	0,13
2	2	230	0,28	139,7	180	3,14	0,5	0,72
2	3	390	0,3	145,37	180	3,14	0,48	1,23
2	4	470	0,28	145,11	180	3,14	0,52	1,48
2	5	540	0,35	150,98	180	3,14	0,43	1,7
2	6	560	0,37	151,01	180	3,14	0,41	1,76
2	7	600	0,31	152,87	180	3,14	0,49	1,88
2	8	620	0,29	155,13	180	3,14	0,53	1,95
2	9	660	0,29	152,95	180	3,14	0,53	2,07
2	10	720	0,34	151,9	180	3,14	0,45	2,26
3	11	820	0,47	150,55	180	3,14	0,32	2,58
3	10	740	0,3	156,18	180	3,14	0,52	2,32
3	9	660	0,33	154,03	180	3,14	0,47	2,07
3	8	620	0,29	155,12	180	3,14	0,53	1,95
3	7	600	0,31	152,87	180	3,14	0,49	1,88
3	6	560	0,36	151,77	180	3,14	0,42	1,76

Continued on next page

Table B-3 – *Continued from previous page*

d[cm]	H[cm]	T[mNm]	t[s]	Δx[cm]	θ[°]	θ[rad]	v[m/s]	E[J]
3	5	540	0,35	151,27	180	3,14	0,43	1,7
3	4	470	0,28	145,11	180	3,14	0,52	1,48
3	3	390	0,3	143,01	180	3,14	0,48	1,23
3	2	230	0,29	139,84	180	3,14	0,48	0,72
3	1	40	0,3	129,89	180	3,14	0,43	0,13
4	1	40	0,29	129,42	180	3,14	0,45	0,13
4	2	230	0,28	137,52	180	3,14	0,49	0,72
4	3	390	0,3	143,01	180	3,14	0,48	1,23
4	4	470	0,28	145,74	180	3,14	0,52	1,48
4	5	540	0,37	149,39	180	3,14	0,4	1,7
4	6	560	0,36	150,7	180	3,14	0,42	1,76
4	7	600	0,31	152,09	180	3,14	0,49	1,88
4	8	620	0,29	154,62	180	3,14	0,53	1,95
4	9	700	0,3	152,57	180	3,14	0,51	2,2
4	10	770	0,48	151,72	180	3,14	0,32	2,42
4	11	870	0,37	148,78	180	3,14	0,4	2,73
4	12	1610	0,48	147,97	180	3,14	0,31	5,06
5	12	1690	0,51	152,63	180	3,14	0,3	5,31
5	11	960	0,37	151,11	180	3,14	0,41	3,02
5	10	840	0,37	153,75	180	3,14	0,42	2,64
5	9	760	0,36	150,16	180	3,14	0,42	2,39
5	8	680	0,28	154,54	180	3,14	0,55	2,14
5	7	600	0,31	152,69	180	3,14	0,49	1,88
5	6	560	0,37	152,7	180	3,14	0,41	1,76
5	5	540	0,35	152,06	180	3,14	0,43	1,7
5	4	470	0,28	145,11	180	3,14	0,52	1,48
5	3	390	0,3	143,01	180	3,14	0,48	1,23
5	2	230	0,28	139,24	180	3,14	0,5	0,72
5	1	40	0,29	129,42	180	3,14	0,45	0,13
6	1	40	0,3	129,89	180	3,14	0,43	0,13
6	2	230	0,28	137,54	180	3,14	0,49	0,72
6	3	390	0,3	143,01	180	3,14	0,48	1,23
6	4	470	0,28	145,11	180	3,14	0,52	1,48
6	5	540	0,35	151,56	180	3,14	0,43	1,7
6	6	570	0,33	149,38	180	3,14	0,45	1,79
6	7	670	0,31	154,25	180	3,14	0,5	2,1
6	8	770	0,35	151,45	180	3,14	0,43	2,42
6	9	870	0,31	153,15	180	3,14	0,49	2,73
6	10	960	0,33	143,52	180	3,14	0,43	3,02
6	11	1140	0,33	143,52	180	3,14	0,43	3,58
7	11	1450	0,29	134,82	180	3,14	0,46	4,56
7	10	1240	0,28	145,06	180	3,14	0,52	3,9

Continued on next page

Table B-3 – *Continued from previous page*

d[cm]	H[cm]	T[mNm]	t[s]	Δx[cm]	θ[°]	θ[rad]	v[m/s]	E[J]
7	9	1050	0,38	142,51	180	3,14	0,38	3,3
7	8	920	0,36	151,33	180	3,14	0,42	2,89
7	7	800	0,32	146,17	180	3,14	0,46	2,51
7	6	670	0,4	145,82	180	3,14	0,36	2,1
7	5	550	0,29	147,5	180	3,14	0,51	1,73
7	4	470	0,28	145,11	180	3,14	0,52	1,48
7	3	390	0,3	143,01	180	3,14	0,48	1,23
7	2	230	0,28	137,55	180	3,14	0,49	0,72
7	1	40	0,3	129,89	180	3,14	0,43	0,13
8	1	40	0,29	129,41	180	3,14	0,45	0,13
8	2	230	0,28	139,225	180	3,14	0,5	0,72
8	3	390	0,3	143,01	180	3,14	0,48	1,23
8	4	520	0,43	146,79	180	3,14	0,34	1,63
8	5	680	0,35	152,79	180	3,14	0,44	2,14
8	6	850	0,31	143,06	180	3,14	0,46	2,67
8	7	1010	0,36	151,19	180	3,14	0,42	3,17
8	8	1240	0,3	138,84	180	3,14	0,46	3,9
8	9	1460	0,24	131,67	180	3,14	0,55	4,59
8	10	1590	0,24	130,28	180	3,14	0,54	5
8	11	1690	0,28	119,22	180	3,14	0,43	5,31
9	10	2000	0,14	91,93	180	3,14	0,66	6,28
9	9	1710	0,28	122,62	180	3,14	0,44	5,37
9	8	1590	0,29	141,35	180	3,14	0,49	5
9	7	1450	0,27	147,38	180	3,14	0,55	4,56
9	6	1170	0,31	140,62	180	3,14	0,45	3,68
9	5	900	0,31	150,42	180	3,14	0,49	2,83
9	4	670	0,35	146,87	180	3,14	0,42	2,1
9	3	450	0,29	146,36	180	3,14	0,5	1,41
9	2	240	0,27	137,33	180	3,14	0,51	0,75

B-3 Obstacle Negotiation Simulations - Results Wheel

A table with all the data from the experiments with the Wheel. d=distance, H=height, T=Torque, t=time until tipping point, Δx= horizontal distance until tipping point, θ=angle rotation (both in degrees and radian), v=average speed, E=consumed energy.

Table B-4: Wheel Experiment Data

d[cm]	H[cm]	T[mNm]	t[s]	Δx[cm]	$\theta[°]$	θ[rad]	v[m/s]	E[J]
5	1	540	0,31	49,75	42,49	0,74	0,16	0,4
6	1	400	0,39	61,19	53,14	0,93	0,16	0,37
6	2	1380	0,43	60	54,6	0,95	0,14	1,31
7	1	340	0,36	70	58,73	1,03	0,19	0,35
7	2	730	0,36	70	79,9	1,39	0,19	1,01
8	2	570	0,41	80	89,82	1,57	0,2	0,89
8	1	300	0,49	80	63,32	1,11	0,16	0,33
9	1	280	0,37	90	68,22	1,19	0,24	0,33
9	2	490	0,42	90	97,62	1,7	0,21	0,83
10	3	910	0,39	100	290,72	5,07	0,26	4,61
10	2	440	0,37	100	107,61	1,88	0,27	0,83
10	1	260	0,39	100	71,21	1,24	0,26	0,32
11	1	240	0,41	110	75,42	1,32	0,27	0,32
11	2	400	0,41	110	111,13	1,94	0,27	0,78
11	3	690	0,4	110	210,34	3,67	0,28	2,53
12	3	580	0,49	120	193,15	3,37	0,24	1,95
12	2	370	0,46	120	114,38	2	0,26	0,74
12	1	220	0,45	120	80,98	1,41	0,27	0,31
13	1	200	0,53	130	86,2	1,5	0,25	0,3
13	2	350	0,42	130	122,35	2,14	0,31	0,75
13	3	350	0,56	130	193,08	3,37	0,23	1,18
14	3	470	0,57	140	187,76	3,28	0,25	1,54
14	2	330	0,47	140	126,05	2,2	0,3	0,73
14	1	190	0,49	140	91,97	1,61	0,29	0,31
15	1	180	0,5	150	98,17	1,71	0,3	0,31
15	2	320	0,43	150	132,49	2,31	0,35	0,74
15	3	440	0,47	150	184,85	3,23	0,32	1,42
16	4	1350	0,47	160	1337,63	23,35	0,34	31,52
16	3	410	0,55	160	184,42	3,22	0,29	1,32
16	2	310	0,43	160	135,7	2,37	0,37	0,73
16	1	170	0,51	160	104,25	1,82	0,31	0,31
17	1	160	0,54	170	109,21	1,91	0,31	0,31
17	2	300	0,44	170	139,92	2,44	0,39	0,73
17	3	390	0,49	170	190,96	3,33	0,35	1,3
17	4	830	0,46	170	620,66	10,83	0,37	8,99

Continued on next page

Table B-4 – *Continued from previous page*

d[cm]	H[cm]	T[mNm]	t[s]	Δx[cm]	θ[°]	θ[rad]	v[m/s]	E[J]
18	4	630	0,52	180	427,06	7,45	0,35	4,69
18	3	380	0,46	180	196,91	3,44	0,39	1,31
18	2	290	0,45	180	143,73	2,51	0,4	0,73
18	1	150	0,58	180	115,37	2,01	0,31	0,3
19	1	140	0,63	190	120,75	2,11	0,3	0,3
19	2	280	0,47	190	144,67	2,52	0,4	0,71
19	3	360	0,49	190	194,63	3,4	0,39	1,22
19	4	560	0,58	190	378,63	6,61	0,33	3,7
20	4	510	0,55	200	351,19	6,13	0,36	3,13
20	3	350	0,48	200	198,64	3,47	0,42	1,21
20	2	270	0,52	200	142,82	2,49	0,38	0,67
20	1	140	0,59	200	126,83	2,21	0,34	0,31
5	1	670	0,38	50	34,42	0,6	0,13	0,4
6	1	510	0,34	61,66	39,41	0,69	0,18	0,35
6	2	1470	0,37	62,19	52	0,91	0,17	1,34
7	1	420	0,35	70,96	44,25	0,77	0,2	0,32
7	2	940	0,36	72	50,72	0,89	0,2	0,84
8	1	360	0,37	80,03	49,21	0,86	0,22	0,31
8	2	770	0,43	78,53	54,24	0,95	0,18	0,73
8	3	1270	0,37	79,23	62,98	1,1	0,21	1,4
9	3	1060	0,37	89,95	65,37	1,14	0,24	1,21
9	2	670	0,39	90,94	59,74	1,04	0,23	0,7
9	1	320	0,36	90,07	54,66	0,95	0,25	0,3
10	1	280	0,44	100,65	60,91	1,06	0,23	0,3
10	2	590	0,49	99,36	65,17	1,14	0,2	0,67
10	3	930	0,4	98,54	69,37	1,21	0,25	1,13
11	4	1640	0,35	114,39	353,26	6,17	0,33	10,12
11	3	840	0,39	108,9	74,13	1,29	0,28	1,08
11	2	540	0,37	109,28	69,08	1,21	0,3	0,65
11	1	260	0,39	109,66	65,62	1,15	0,28	0,3
12	1	230	0,5	119,57	71,64	1,25	0,24	0,29
12	2	490	0,42	120,87	75,76	1,32	0,29	0,65
12	3	770	0,38	121,47	80,51	1,41	0,32	1,09
12	4	1130	0,41	119,58	101,55	1,77	0,29	2
13	4	1010	0,45	131,91	100,48	1,75	0,29	1,77
13	3	710	0,4	130,6	85,58	1,49	0,33	1,06
13	2	450	0,44	128,76	80,23	1,4	0,29	0,63
13	1	220	0,43	129,94	77,05	1,34	0,3	0,29
14	1	200	0,48	139,89	86,2	1,5	0,29	0,3
14	2	420	0,43	139,89	86,2	1,5	0,33	0,63
14	3	660	0,41	139,92	90,55	1,58	0,34	1,04
14	4	930	0,5	143,07	104,86	1,83	0,29	1,7

Continued on next page

Table B-4 – *Continued from previous page*

d[cm]	H[cm]	T[mNm]	t[s]	Δx[cm]	θ[°]	θ[rad]	v[m/s]	E[J]
15	5	1860	0,4	157,8	698,22	12,19	0,39	22,67
15	4	870	0,44	147,8	104,48	1,82	0,34	1,58
15	3	620	0,4	149,74	104,48	1,82	0,37	1,13
15	2	390	0,48	150,07	92,11	1,61	0,31	0,63
15	1	190	0,48	151,02	89,01	1,55	0,31	0,29
16	1	180	0,49	160,7	94,45	1,65	0,33	0,3
16	2	370	0,45	160,57	97,69	1,71	0,36	0,63
16	3	580	0,44	161,01	102,36	1,79	0,37	1,04
16	4	820	0,42	157,87	108,81	1,9	0,38	1,56
16	5	1610	0,39	157,55	475,86	8,31	0,4	13,38
17	5	1430	0,44	173,01	411,67	7,18	0,39	10,27
17	4	770	0,48	169,42	115,38	2,01	0,35	1,55
17	3	550	0,43	170,46	107,27	1,87	0,4	1,03
17	2	350	0,45	169,82	102,82	1,79	0,38	0,63
17	1	170	0,51	170,73	100,2	1,75	0,33	0,3
18	1	160	0,53	180,18	105,61	1,84	0,34	0,29
18	2	330	0,47	179,23	108,2	1,89	0,38	0,62
18	3	520	0,45	180	112,65	1,97	0,4	1,02
18	4	730	0,49	178,69	121,02	2,11	0,36	1,54
18	5	1280	0,44	183,04	294,64	5,14	0,42	6,58
19	5	1170	0,4	192,44	225,17	3,93	0,48	4,6
19	4	700	0,44	190,78	125,59	2,19	0,43	1,53
19	3	490	0,54	188,94	118,48	2,07	0,35	1,01
19	2	310	0,54	191,12	115,26	2,01	0,35	0,62
19	1	150	0,57	190,06	111,3	1,94	0,33	0,29
20	1	140	0,62	200,08	117,11	2,04	0,32	0,29
20	2	300	0,49	200,98	120,52	2,1	0,41	0,63
20	3	470	0,49	200,93	124,53	2,17	0,41	1,02
20	4	670	0,43	199,88	130,19	2,27	0,46	1,52
20	5	1060	0,44	200,06	196,26	3,43	0,45	3,64

B-4 Obstacle Negotiation Simulations - Plots
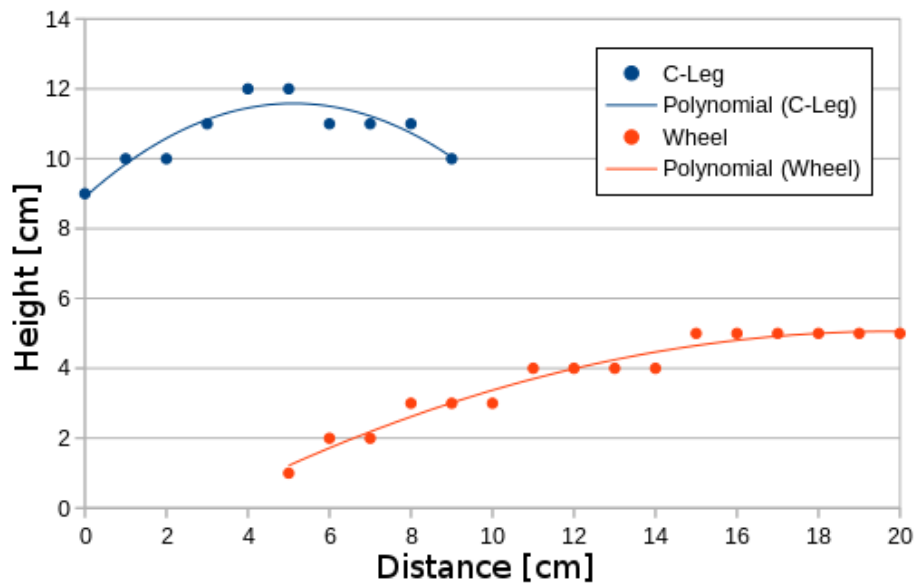
Figure B-6: Obstacle experiments - Height vs Distance d
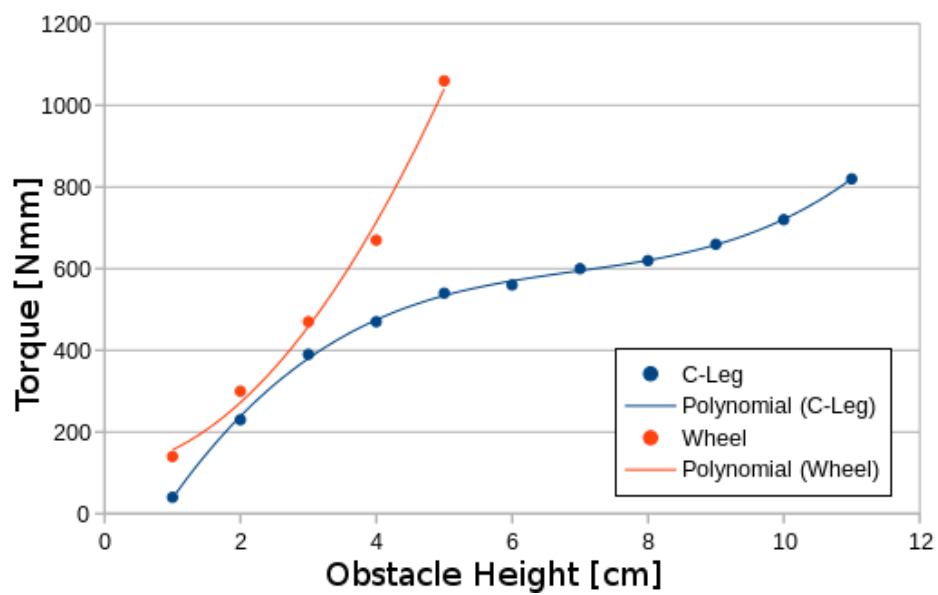
Figure B-7: Obstacle experiments - Torque vs Obstacle Height
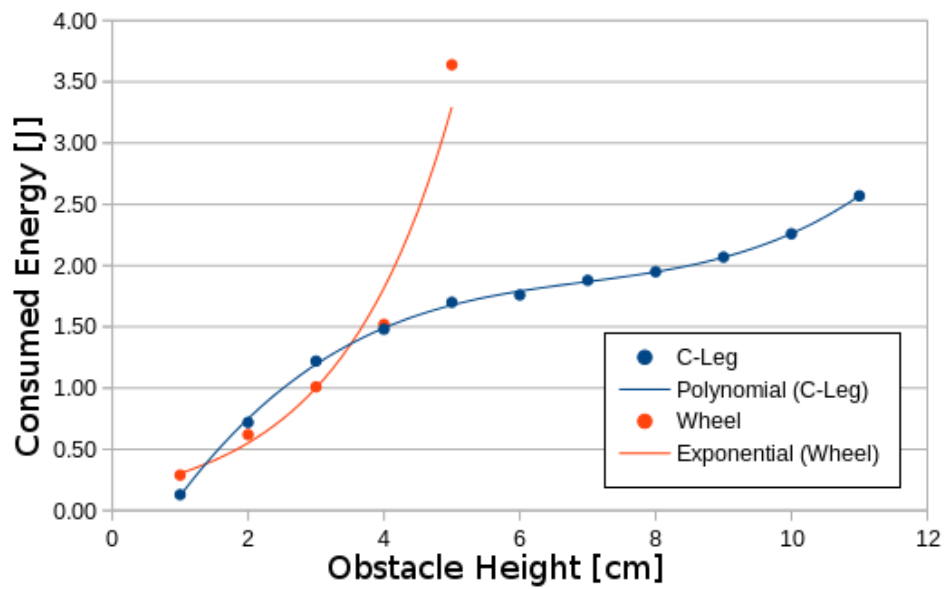
Figure B-8: Obstacle experiments - Energy consumption vs Obstacle Height
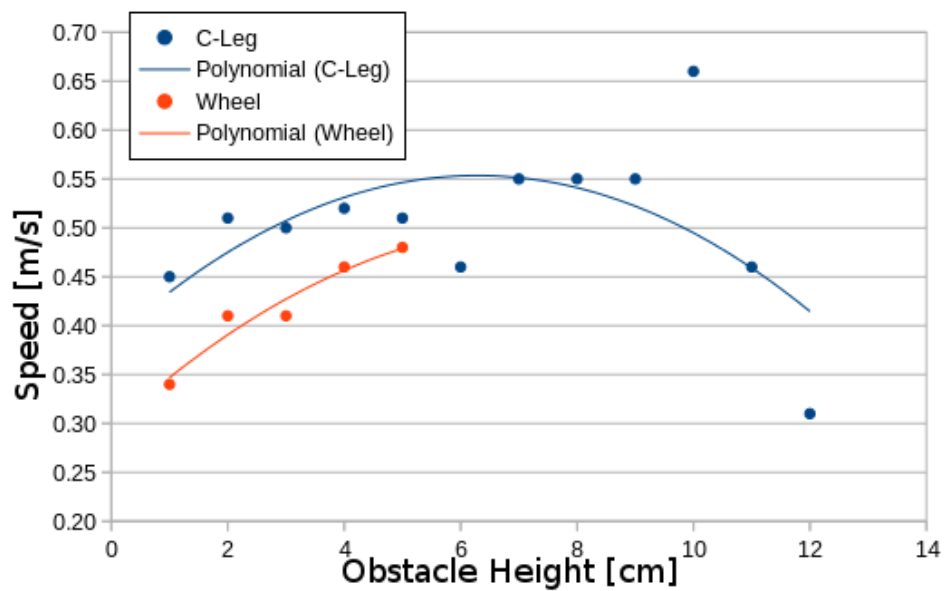
Figure B-9: Obstacle experiments - Speed vs Obstacle Height

B-5   Straight Piece Simulations - Results

Table B-5: Straight Piece Simulations - Test Data

Type	$\dot{\theta}$ $[°/s]$	**t** [s]	ΔX [m]	$\dot{X}_{avg}$ [m/s]	$\Delta\theta$ [°]	T_{RMS} [Nmm]	E_{RMS} [mJ]
Wheel	180	3.18	1	0.31	573.3	4.40	44.0
Wheel	200	2.86	1	0.35	572.0	4.43	44.2
Wheel	220	2.60	1	0.38	572.0	4.36	43.5
Wheel	240	2.39	1	0.42	573.6	4.36	43.6
Wheel	260	2.20	1	0.45	572.0	4.50	44.9
Wheel	280	2.04	1	0.49	571.2	4.51	45.0
Wheel	300	1.91	1	0.52	573.0	4.45	44.5
Wheel	320	1.79	1	0.56	572.8	4.63	46.3
Wheel	340	1.68	1	0.60	573.0	4.59	45.9
Wheel	360	1.58	1	0.63	573.9	4.87	48.8
Wheel	380	1.51	1	0.66	573.8	5.03	50.4
C-Leg	180	5.58	1	0.18	1004	4.19E2	7345
C-Leg	200	5.03	1	0.20	1006	3.77E2	6619
C-Leg	220	4.58	1	0.22	1008	3.72E2	6541
C-Leg	240	4.19	1	0.24	1006	2.75E2	4826
C-Leg	260	3.88	1	0.26	1009	5.59E2	9842
C-Leg	280	3.60	1	0.28	1008	6.82E2	11998
C-Leg	300	3.36	1	0.30	1008	5.99E2	10538
C-Leg	320	3.15	1	0.32	1008	7.17E2	12614
C-Leg	340	2.97	1	0.34	1010	7.98E2	14064
C-Leg	360	2.80	1	0.36	1008	3.76E2	6615
C-Leg	380	2.66	1	0.38	1011	9.80E2	17289

B-6 Straight Piece Simulations - Plots
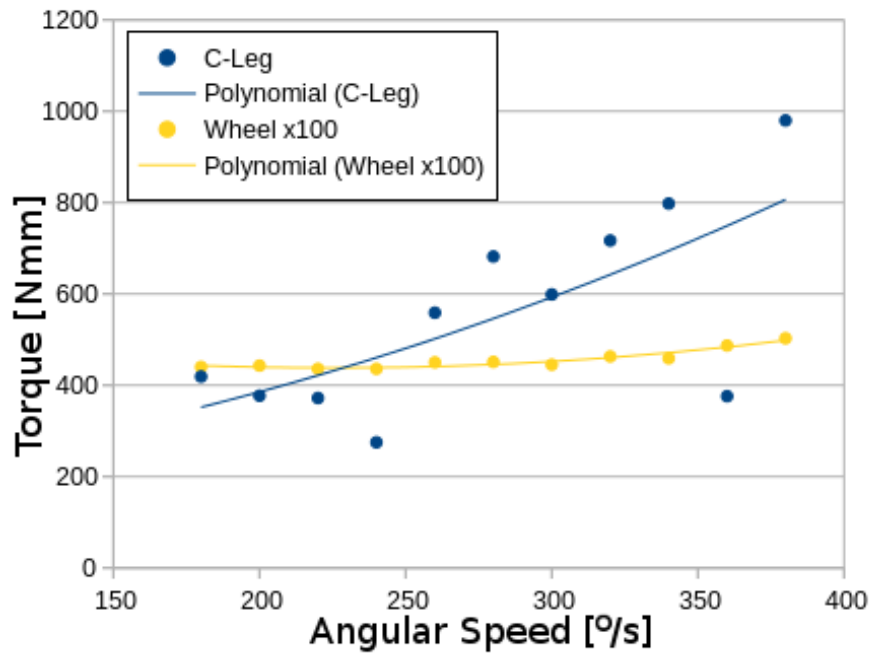
Figure B-10: Angular Velocity vs Torque RMS
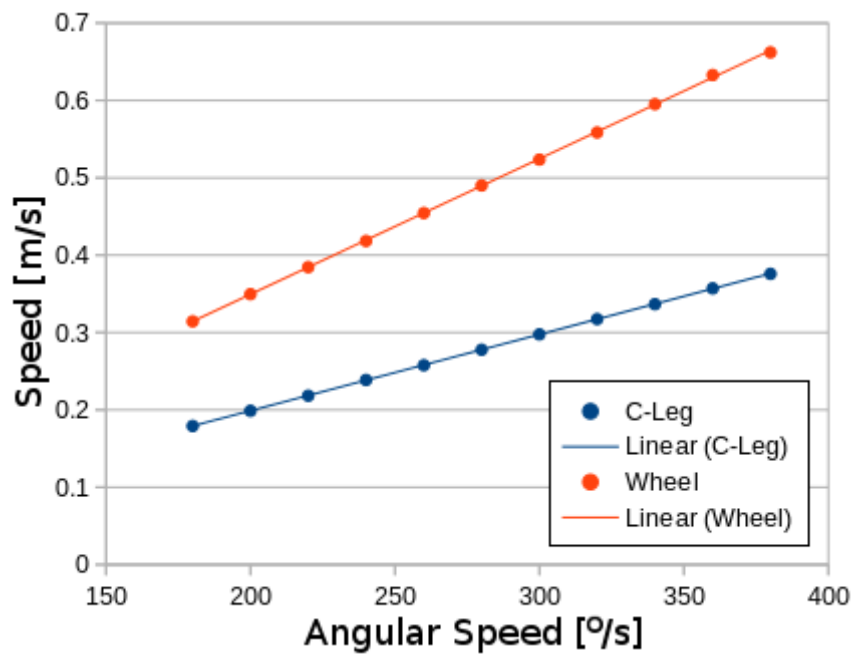
Figure B-11: Angular Velocity vs Horizontal Velocity
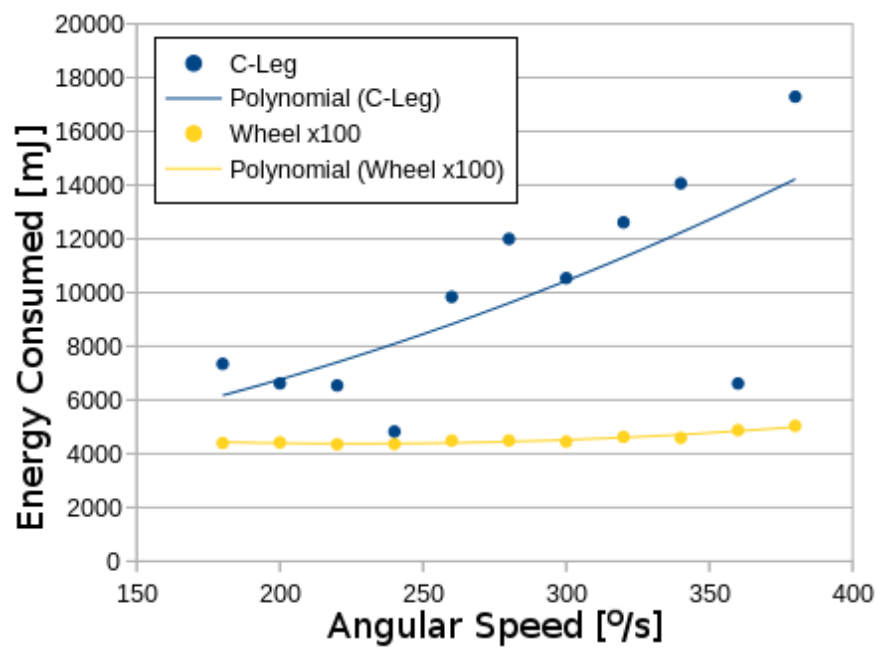
Figure B-12: Angular Velocity vs Energy consumption
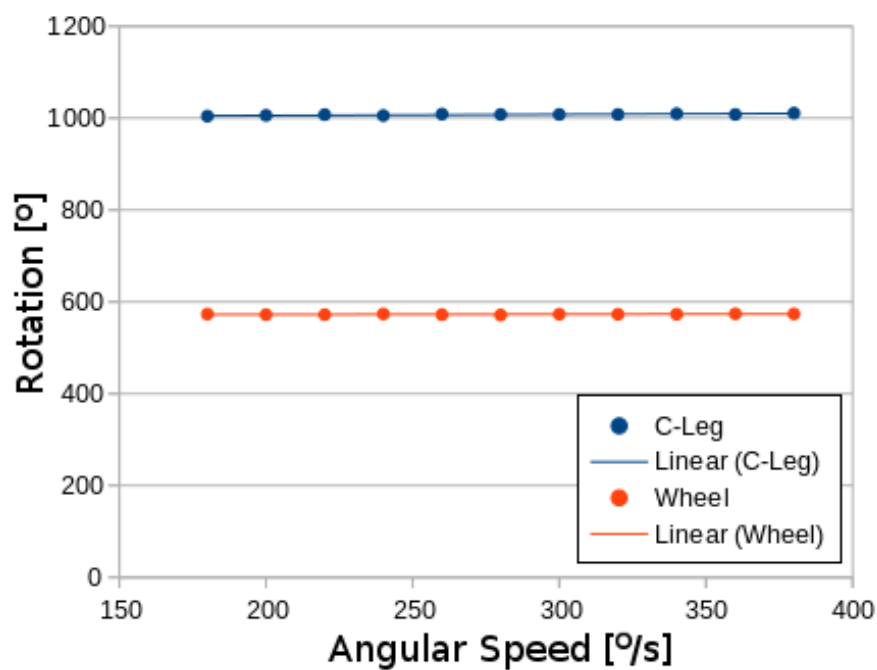
Figure B-13: Angular Velocity vs Rotation

<div align="right">

Appendix C

</div>

Friction Coefficient Evaluation

This appendix is a documentation of the tests done to obtain the friction coefficients of the rubber used between the friction pads and the armature of the coupling.

C-1   Test set-up

We find the friction coefficient by using the equilibrium between gravity and friction force, shown schematically in figure C-1. The rubber is glued onto an aluminium mass and placed on a metal surface at angle α. Gravity exerts a vertical force F_g, which causes a reactionary normal force F_N and a friction force F_w. The plate is slowly hoisted, increasing the angle. The angle α where the weight just starts to slip, is where the gravitational force overtakes the friction force. With this angle we can then calculate the friction coefficient.

$$F_{normal} = F_g \cdot cos(\alpha)$$
$$F_{friction} = \mu \cdot F_{normal}$$
$$F_{friction} = F_g \cdot sin(\alpha)$$
$$\Rightarrow \mu = \frac{sin(\alpha)}{cos(\alpha)}$$
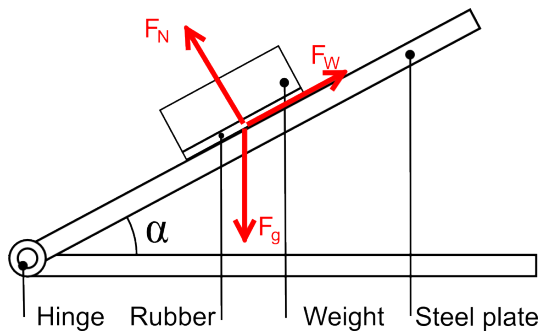
Figure C-1: Experiment set-up Friction Coefficient

Pictures of the set-up are shown in figures C-2 and C-3. The rubber was glued to three aluminium cilinders of different weights. These are then put on a steel surface that is hoisted at an angle with a hinge.

Figure C-2: Weights used

Figure C-3: Experiment Set-up

C-2 Results

The experiment was done multiple times with different weights to get a decent sample size. As was expected from the formula, the result varied little with different weights. An average of $\mu = 0.45$, with a margin of error of ± 0.02, was found.

Table C-1: Test Results

Test number	Weight used	α [degree]	μ [-]
1	Small	23	.43
2	Small	24	.45
3	Small	24	.45
4	Middle	24	.45
5	Middle	25	.47
6	Middle	25	.47
7	Large	23	.43
8	Large	24	.45
9	Large	24	.45
Average		24	.45

Appendix D

Displacement sensor: Tests & Results

This appendix describes the evaluation of the sensor array that was used in the tests to verify the spring force and the magnetic force in the coupling.

D-1   VCNL4010 sensor array

The Vishay VCNL4010 sensor, as shown in picture D-1, is a Proximity and Ambient Light Sensor. The sensor has an infrared emitter and a photo-pin-diode for proximity functionality, which can detect a reflective surface between 5 and 200mm. The signal is processed by means of an effective 16 bit resolution and connects to the micro-controller with standard I2C interface. The micro-controller receives a Proximity Value (cts) between 0 and 70000 based on the proximity of a reflective surface. After calibration, this value can then be converted to the distance in mm. To measure the small displacements in the experiments, we use an array of 6 sensors, as shown in figure D-2. By averaging their measurements, the error decreases and uneven balancing of the reflective platform is cancelled out.

To calibrate the sensor array, we use a testing set-up as shown in figure D-3. A reflective platform is attached to a micrometer and is suspended above the sensor array. The platform is hoisted, from 5 to 12 mm above the sensors, with increments of .1mm and the sensor values are measured with each increment. With these measurements we can construct a relationship which determines the distance to the reflective plate as a function of average cts.
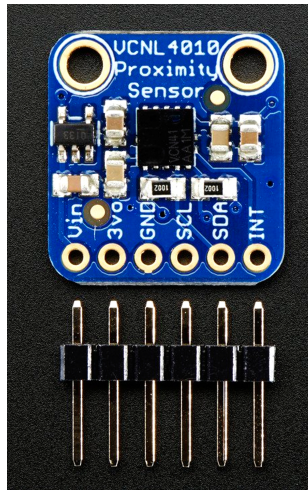
Figure D-1: Vishay VCNL4010
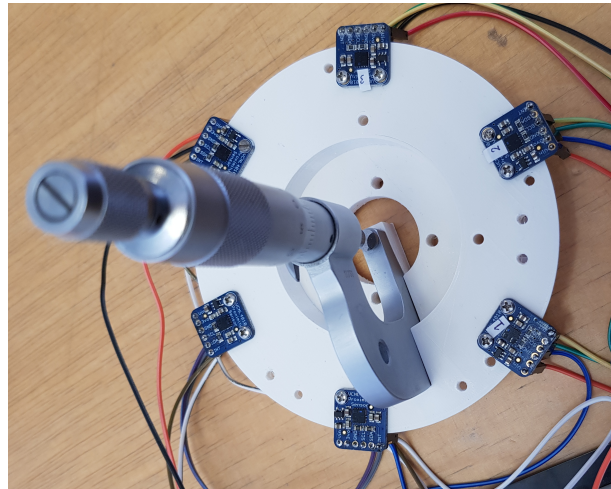
Figure D-2: Array of VCNL4010
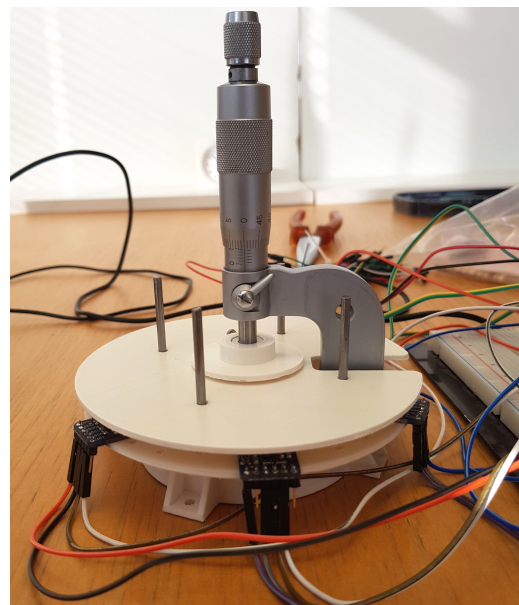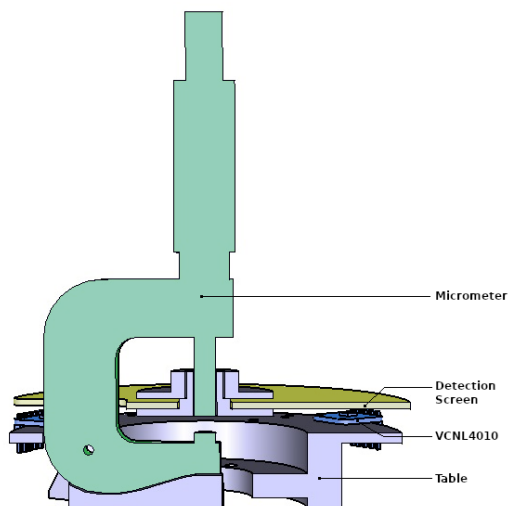
Figure D-3: Test set-up with sensor array and micrometer

D-2   VCNL4010 Calibration Results

Table D-2 is a list of the calibration results. d is the distance, in mm, of the reflective platform to the sensors. S1 to S6 are the proximity values, in cts, of the 6 VCNL4010 sensors. The final column is the average proximity value, in cts, of the 6 sensors.

Table D-1: Data VCNL4010 Experiment

d[mm]	S1[cts]	S2[cts]	S3[cts]	S4[cts]	S5[cts]	S6[cts]	Average[cts]
5,0	65535	57840	59788	57843	65535	65535	62012,67
5,1	65535	59669	59635	56296	65535	65535	62034,17
5,2	56150	58477	65535	65535	65535	53836	60844,67
5,3	62258	65535	65535	58670	54775	48479	59208,67
5,4	51726	63306	65535	61019	53152	42370	56184,67
5,5	55048	52867	56441	50611	58209	52498	54279,00
5,6	65535	63912	53499	39858	47790	54802	54232,67
5,7	64975	65535	62233	42354	43686	46062	54140,83
5,8	53174	57552	63655	51177	50840	44431	53471,50
5,9	44219	50761	63847	54121	49664	38905	50252,83
6,0	53764	48993	49638	43354	51126	48580	49242,50
6,1	57986	52924	48887	38977	45660	47682	48686,00
6,2	53786	50957	49287	39908	45128	44824	47315,00
6,3	46410	55264	60959	43864	39812	35402	46951,83
6,4	40425	48942	58365	44281	39005	32344	43893,67
6,5	49597	42324	39961	35039	43626	44587	42522,33
6,6	48884	41835	39999	35356	43875	44291	42373,33
6,7	46227	41871	40602	34688	40694	40221	40717,17
6,8	42938	46832	48226	36061	35472	33241	40461,67
6,9	35269	38737	46798	39911	38074	30911	38283,33
7,0	41515	37276	37037	32774	38731	37408	37456,83
7,1	39462	36108	37239	33409	38801	36231	36875,00
7,2	40557	38024	37487	31635	35692	34721	36352,67
7,3	37726	37691	39297	32707	34568	31902	35648,50
7,4	36949	35439	36091	30630	33641	31765	34085,83
7,5	37634	32793	32269	29110	35128	34377	33551,83
7,6	36708	32915	32513	28599	33503	32649	32814,50
7,7	35574	32768	32716	28475	32475	31187	32199,17
7,8	34912	34266	34077	27760	29799	28684	31583,00
7,9	34080	33306	32663	26304	28320	27714	30397,83
8,0	32425	28694	28977	26635	31656	29979	29727,67
8,1	33306	29815	28971	25235	29619	29259	29367,50
8,2	31661	29540	29247	25049	28181	27261	28489,83
8,3	30928	30990	31167	25157	26368	25250	28310,00
8,4	29927	28752	28927	24362	26559	25439	27327,67

Continued on next page

Table D-1 – *Continued from previous page*

d[mm]	S1[cts]	S2[cts]	S3[cts]	S4[cts]	S5[cts]	S6[cts]	Average[cts]
8,5	29899	27940	27232	22902	25704	25335	26502,00
8,6	29480	27649	27094	22788	25459	24989	26243,17
8,7	29699	27922	26696	21952	24500	24546	25885,83
8,8	28029	27052	26843	22340	24286	23444	25332,33
8,9	25973	25954	26790	22308	23426	21844	24382,50
9,0	27049	24410	23830	20788	24167	23775	24003,17
9,1	26091	23654	23616	20967	24246	23363	23656,17
9,2	25625	23593	23465	20520	23374	22509	23181,00
9,3	24162	22791	23660	21075	23408	21629	22787,50
9,4	23542	22344	23092	20348	22476	20888	22115,00
9,5	22881	20775	21372	19527	22558	21084	21366,17
9,6	24306	21833	21193	18495	21498	21311	21439,33
9,7	23311	22207	22206	18864	20673	19883	21190,67
9,8	20301	19971	22396	20487	21722	18545	20570,33
9,9	19724	19042	21237	19758	21214	18331	19884,33
10,0	21399	18803	19106	17911	21237	20089	19757,50
10,1	21257	18866	19056	17552	20552	19615	19483,00
10,2	21546	19938	19581	16917	18924	18555	19243,50
10,3	21692	20638	19798	16269	17687	17724	18968,00
10,4	19103	17393	18467	17504	19932	18034	18405,50
10,5	20402	17407	17075	15918	19231	18944	18162,83
10,6	19911	17304	17160	15895	18833	18350	17908,83
10,7	20108	19050	18421	15370	16713	16588	17708,33
10,8	18711	17956	18362	15910	17075	16074	17348,00
10,9	16434	15434	17295	16996	18725	15947	16805,17
11,0	18507	16187	15990	14817	17429	16954	16647,33
11,1	18328	16327	16051	14509	16735	16360	16385,00
11,2	18042	16364	16127	14417	16332	15885	16194,50
11,3	16211	15279	16497	15604	17061	15097	15958,17
11,4	15620	14034	15268	15393	17743	15473	15588,50
11,5	16684	14842	14833	13844	16020	15286	15251,50
11,6	16737	14999	14815	13548	15532	15027	15109,67
11,7	16210	15524	15758	13792	14820	13987	15015,17
11,8	15083	14217	15217	14355	15648	13945	14744,17
11,9	15080	13787	14334	13588	15275	13993	14342,83
12,0	16767	13622	12710	12140	15268	15706	14368,83

D-3   Plots VCNL4010 Experiments

The data is plotted in figure D-4. The 6 sensors show a diffuse picture, which can be attributed to variance in the sensors and an unbalanced reflective platform. However the average of the 6 values counteracts the unbalance and reduces the respective errors. The average thus shows a stable and concentrated line. The function $1^{E6} \cdot x^{-1.757}$ approximates the data with Coefficient of Determination R^2 of 0.9978.
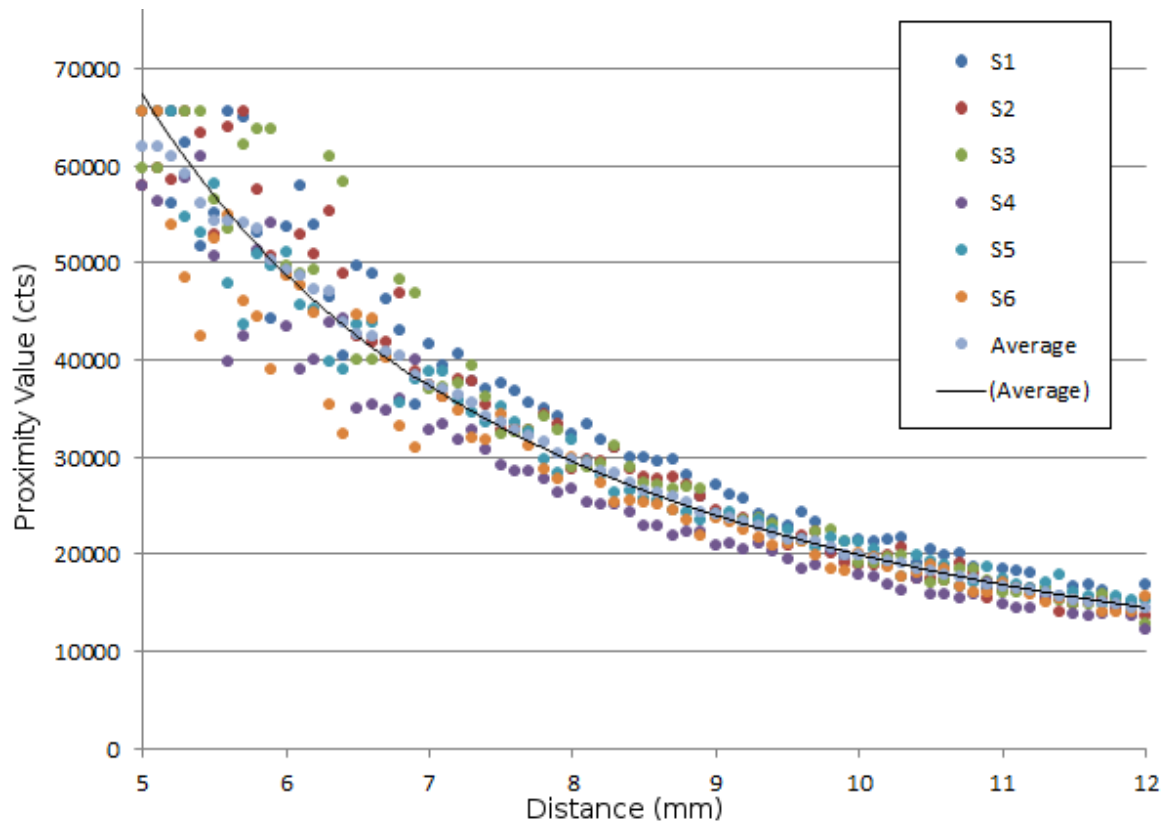
Figure D-4: VCNL4010 Calibration measurements

With the data, we can now model the measured Distance as a function of Average Proximity Value. From figure D-4, we can see the sensor is most stable and accurate in the middle part of the graph. So we model the function between 7 and 11mm, which is a sufficient range for the measurements. The function $D = 7^{E-9}x^2 - .0006x + 18.627$ approximates the data with a correlation R^2 of 0.9977. It is shown in figure D-5.
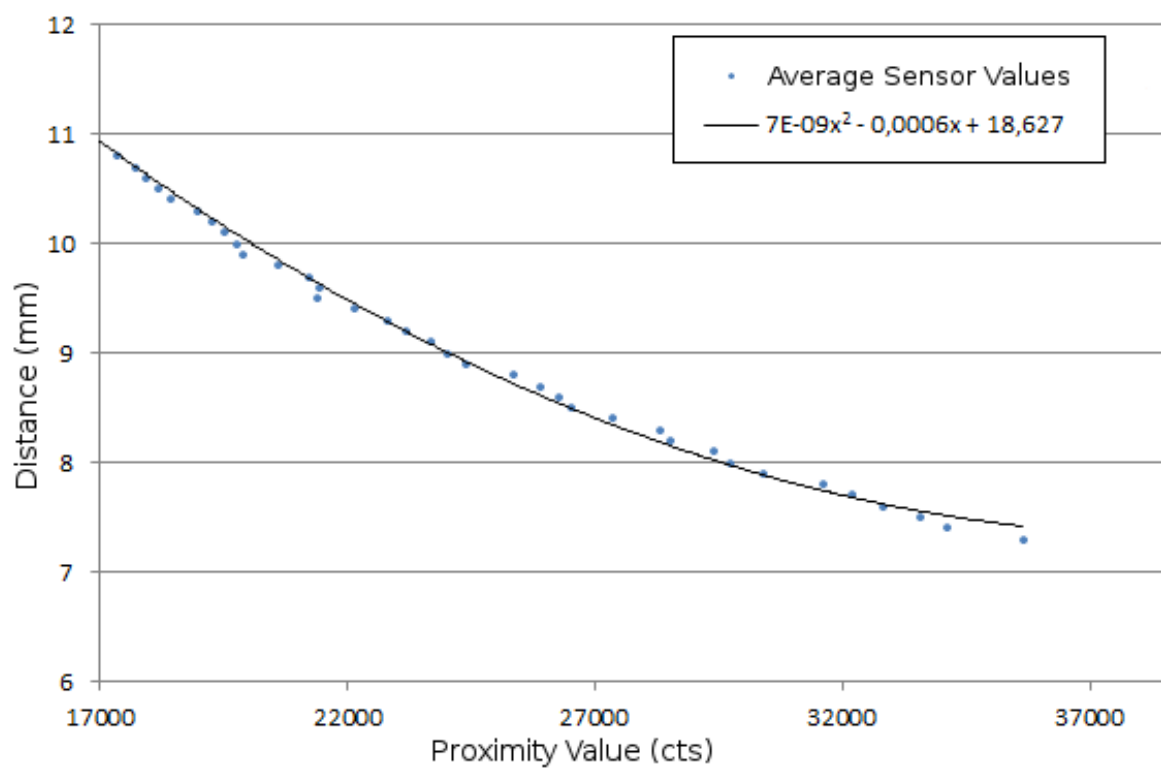
Figure D-5: distance as function of Proximity Values

Appendix E

Spring Force Verification

This appendix describes the evaluation of the spring force exerted by the springs in the coupling.

E-1   Springs and Test Set-up

We will determine the stiffness k with the relationship $F = k \cdot \delta x$, where F is the applied force and δx the displacement. In the experiment, the four springs are placed vertically, in accordance with the placement in the coupling. A detection screen is placed over the springs and a load is applied. The displacement is then measured with 6 VCNL4010 sensors, as described in Appendix D. The set-up is depicted schematically in figure E-1 and the real set-up shown in picture E-2.
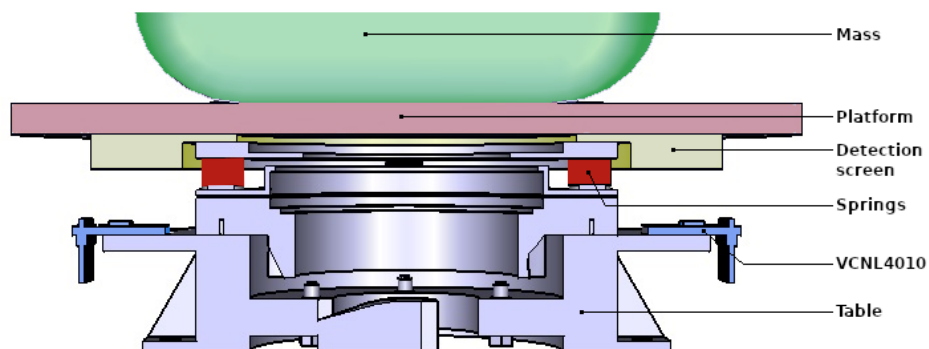
Figure E-1: Schematic Spring Test Set-up
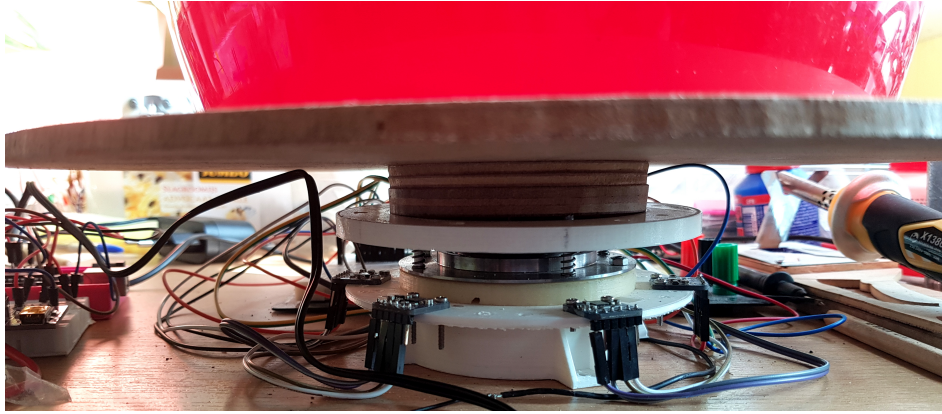
Figure E-2: Spring Test Set-up

From chapter 7, we know that the expected load for four contracted springs should be approximately 90N, or 8.5kg. Because this is a considerable amount, we use a system with water containers. A platform is placed on the detection plate with a large container on top of it. Water, measured in containers of 0.5 Liters, is added incrementally to the container and the sensor values are noted. The large container and smaller containers are shown in figure E-3.

Figure E-3: Water containers for Spring Tests

E-2   Spring data

Table E-1 is a list of the test results. W is the weight in water, in kg, added to the container. F, in N, is the total force applied to the springs. This includes 656gram for the platform and large container, therefore the count starts at 6.44N. S1 to S6 are the proximity values, in cts, of the 6 VCNL4010 sensors. Avg is the average proximity value, in cts, of the 6 sensors. H is the height, in mm, calculated using $H = 7^{E-9}x^2 - .0006 \cdot Avg + 18.627$ which was obtained in Appendix D. Finally D is the displacement in mm.

Table E-1: Spring Test Results

W[kg]	F[N]	S1[cts]	S2[cts]	S3[cts]	S4[cts]	S5[cts]	S6[cts]	Avg[cts]	H[mm]	D[mm]
0,0	6,44	14518	12754	13492	14359	16707	14806	14439,33	11,4	0
0,5	11,34	14921	12846	13545	14689	17511	15521	14838,83	11,27	0,16
1,0	16,25	15242	13152	13948	15171	18066	15915	15249	11,11	0,32
1,5	21,15	15578	13383	14199	15547	18673	16417	15632,83	10,96	0,46
2,0	26,06	16078	13781	14564	15904	19189	16936	16075,33	10,79	0,63
2,5	30,96	16374	14059	14962	16442	19879	17398	16519	10,63	0,80
3,0	35,87	16819	14281	15193	16901	20747	18095	17006	10,45	0,98
3,5	40,77	17317	14567	15470	17324	21543	18791	17502	10,27	1,15
4,0	45,68	17729	14773	15735	17839	22501	19499	18012,67	10,09	1,33
4,5	50,58	18230	14944	15888	18262	23501	20346	18528,5	9,91	1,51
5,0	55,49	18702	15125	16105	18784	24595	21224	19089,17	9,72	1,70
5,5	60,39	18957	15227	16319	19318	25548	21861	19538,33	9,58	1,85
6,0	65,30	19265	15367	16668	20204	26974	22716	20199	9,36	2,06
6,5	70,20	19561	15386	16785	20812	28401	23675	20770	9,18	2,24
7,0	75,11	20158	15574	17024	21600	30219	25064	21606,5	8,93	2,49
7,5	80,01	20263	15482	17203	22629	32234	26114	22320,83	8,72	2,70
8,0	84,92	20428	15238	17151	23571	34859	27602	23141,5	8,49	2,93
8,5	89,82	20694	14913	17025	24861	39078	29941	24418,67	8,15	3,27
9,0	94,73	20799	14809	16961	25275	40608	30801	24875,5	8,03	3,39
9,5	99,63	21037	14901	16960	25173	40595	31094	24960	8,01	3,41
10,0	104,54	21427	15056	16942	24900	40455	31509	25048,17	7,99	3,43

E-3 Plots and Results

The measured sensor values S1 to S6 are plotted against the applied force in figure E-4. They show a diffuse picture due to the unbalance in the platform, one side is slightly higher then the other side. However the average value is a smooth and stable line, which coincides with the center of the platform. At the end of the test, the platform rests on the support structure and can not lower any further. Therefore we see a horizontal line at the end, where the average values will not rise any further.
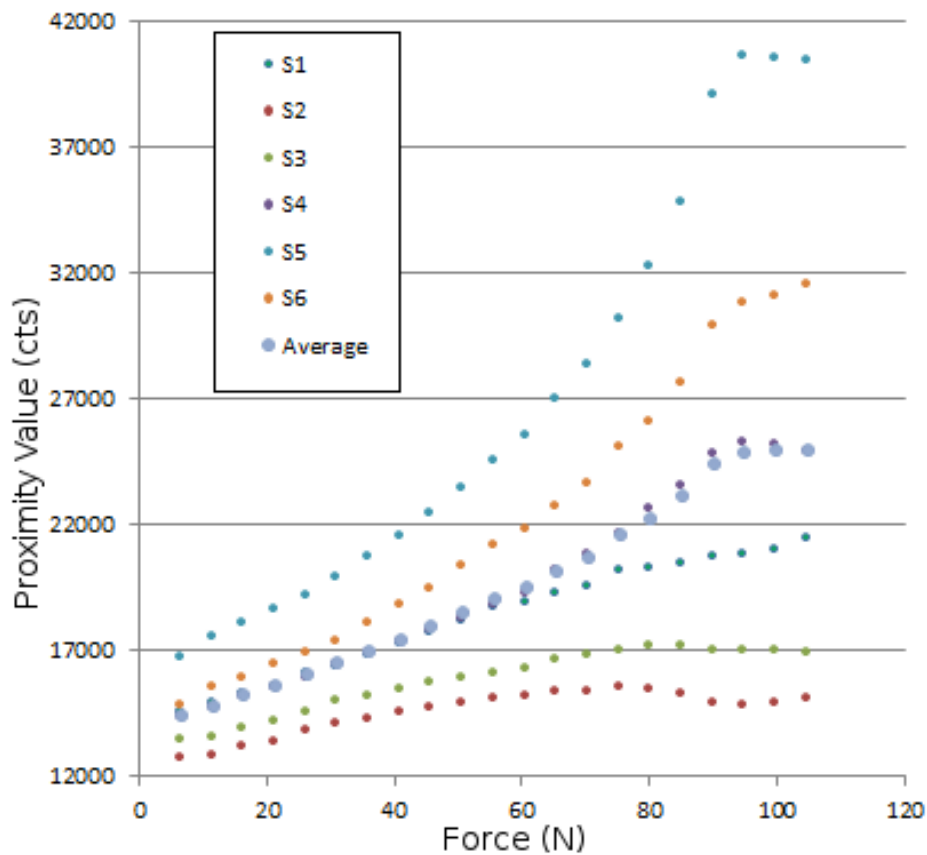
Figure E-4: Spring test measurements

In figure E-5, the measured height is plotted against applied weight. This figure clearly shows the linear relationship between height and applied force, as well as the three final points where the container could not lower any further.

In the last figure, E-6, applied force is plotted against displacement. By removing the last values and adding a linear best-fit to the data, we can identify the stiffness of the four springs. The trendline has a Coefficient of Determination R^2 of 0.9940 and was calculated to have a standard deviation of 1.1N. This shows that the springs have a stiffness of $27N/mm$.
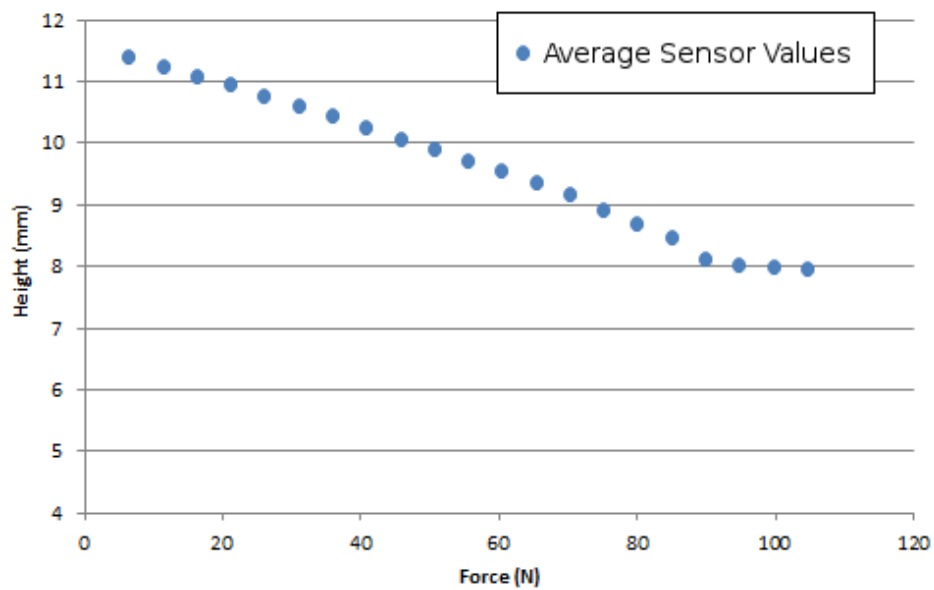
Figure E-5: Weight vs Height
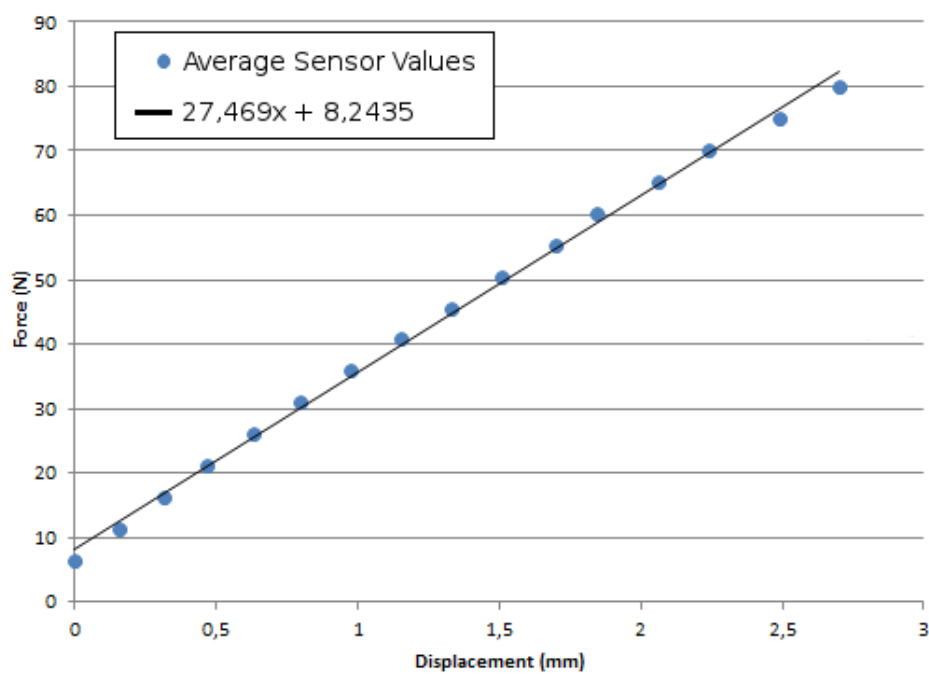
Figure E-6: Stiffness

Magnetic Force and Duty-Cycle

In this appendix we describe the verification of the magnetic force used in the coupling. We want to know if the magnet, in combination with the steel armature, is capable of pulling the armature in accordance with the expectations. We will describe the experiment set-up, the test results and the plots. After that, we will calibrate the duty-cycle of the Pulse Width Modulation (PWM) that is used for holding the armature in order to save energy.

F-1   Set-up verification

To measure the force exerted by the magnet, we use the displacement sensors as described in Appendix D and the springs as described in Appendix E. When the magnet is switched on, the steel armature is pulled against the 4 springs until it hits the magnet and the displacement is measured. With the stiffness of the springs and the displacement known we can then calculate the force exerted by the magnet. This set-up is schematically depicted in figure F-1.

A picture of the set-up is shown in figure F-2.
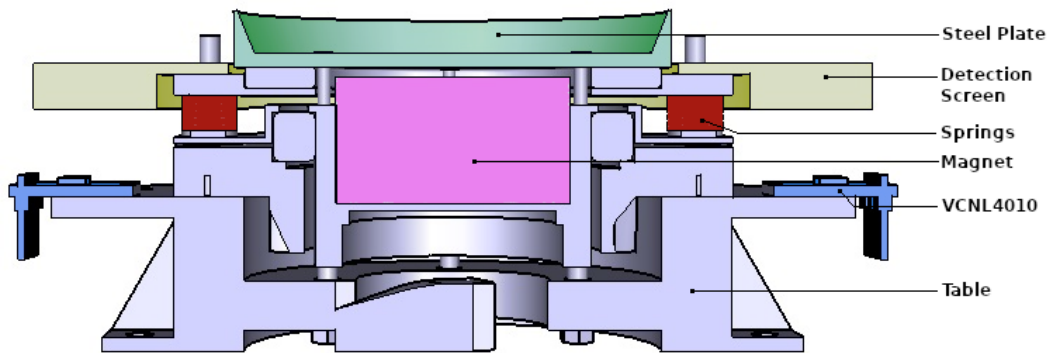
Figure F-1: Schematic set-up Magnet Test
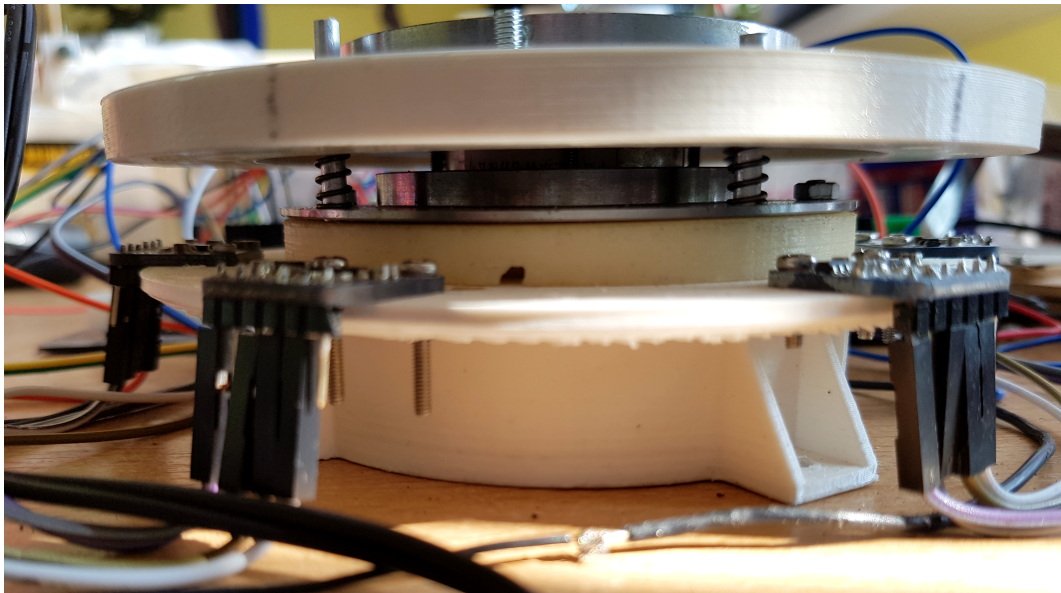
Figure F-2: Magnet Test set-up

F-2 Measurements

The test was repeated three times and the measurements are shown in table F-1. Status describes whether the magnet is On or Off, S1 to S6 are the Proximity Values of the six VCNL4010 sensors and Avg is the average value of the sensor. Height is the distance of the detection screen calculated with $H = 7^{E-9}x^2 - .0006 \cdot Avg + 18.627$.

Table F-1: Magnet Test Results

Test[nr]	Status[-]	S1[cts]	S2[cts]	S3[cts]	S4[cts]	S5[cts]	S6[cts]	Avg[cts]	H[mm]
1	Off	14610	13004	13291	14093	16491	14895	14397,33	11,44
1	On	28209	25399	25840	26596	31379	28245	27611,33	7,40
2	Off	14832	13339	13600	14029	16143	14759	14450,33	11,42
2	On	28099	25294	25637	26551	31192	28220	27498,83	7,42
3	Off	14856	13362	13631	14067	16172	14782	14478,33	11,41
3	On	28079	25301	25669	26539	31149	28206	27490,5	7,42

In figure F-3, the measured sensor values are plotted for the three tests, as well as their averages. When the magnet is switched on, the steel armature is pulled until it hits the magnet. When it is turned off, the springs push the armature back to its original position. We can thus see a clear difference between the on and off stages for the magnet.

In figure F-4, the calculated height of the detection screen is plotted for the three tests. The average height in the OFF stage is 11.42mm and the average height in the ON stage is 7.41mm, which means a displacement of 4mm. With spring stiffness k of 27N/mm and the a standard deviation of 1.1N for the calculated spring force, obtained from Appendix E, we now come to a magnetic force of $108N \pm 2.2$.

It was found that the magnet is capable of holding the plate, but was not able to pull it. A small push was needed to attract the plate.
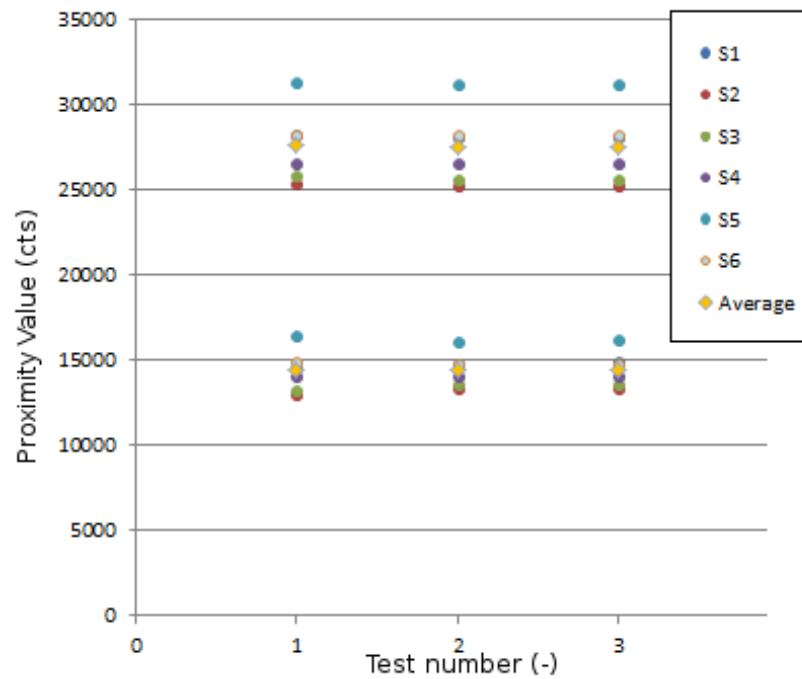
Figure F-3: Sensor measurements Magnet Test
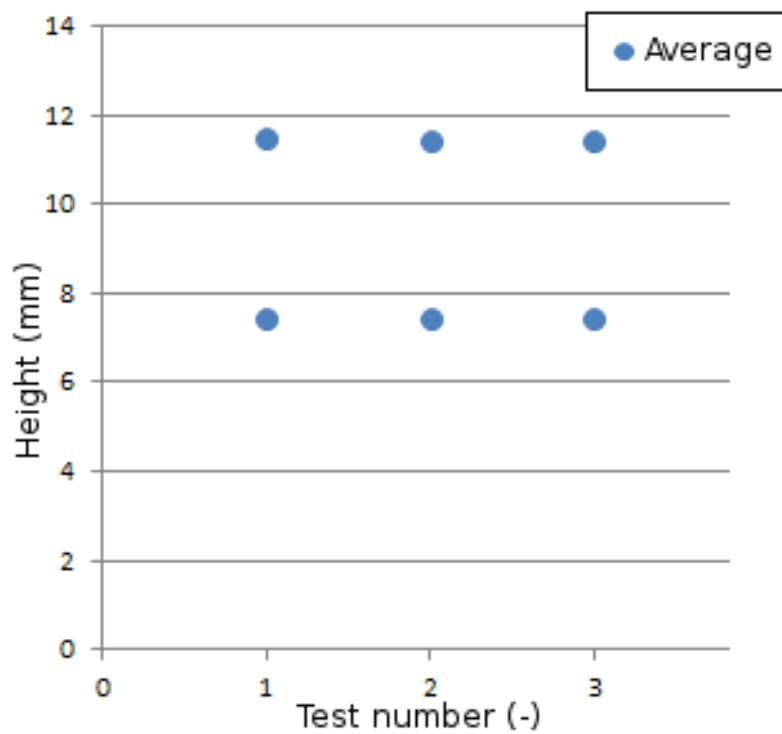
Figure F-4: Calculated Height Magnet Test

F-3   Duty-Cycle calibrations

In this section we will calibrate the duty-cycle that is used during PWM mode. Holding the armature in place takes much less force then attracting it, so much energy can be saved by running the magnet with less power after switching. But to find the duty-cycle that is still capable of holding the magnet, we need to do some tests. We set up the complete Leg-Wheel module, as shown in figure F-5, with the springs and armature as normal.
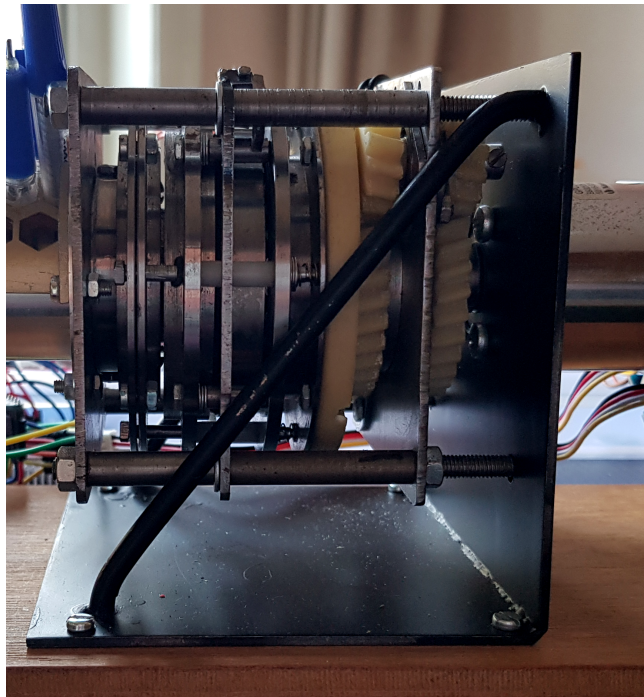
Figure F-5: Test magnet duty cycle

During the tests we turn the magnet on and, after 1 second, continue with PWM for 2 seconds. We try with decreasing duty-cycles until the magnet fails to hold the armature. An arduino UNO is used as a microprocessor, the code is shown in figure F-6. The measurements are done with a different microprocessor, an arduino MEGA. The code is depicted in figure F-7. An adafruit INA260 power sensor is used to measure current, voltage and power to the magnet, which is then printed on the serial monitor. The INA260 is documented as a high-accuracy sensor with maximum error of 0.15%. For the power measurements, with a maximum of 6000mW, that translates to a maximum error of ±9mW. After the test, the measurements are copied and processed with Excel.

```
const byte magnetPin = 11;              //PWM pin to toggle transistor
int dutyCycle = 255;                    //Set dutyCycle

void setup() {                          //Code to run once at start-up
  pinMode(magnetPin, OUTPUT);           //set pinmode
}

void loop() {                           //Main loop, runs continuously
    digitalWrite(magnetPin, HIGH);      //turn magnet on
    delay(1000);                        //Allow 1sec for coupling to switch
    analogWrite(magnetPin, dutyCycle);  //Run magnet on dutyCycle for 2sec
    delay(2000);
    digitalWrite(magnetPin, LOW);       //Turn magnet off again and wait 2sec
    delay(2000);
}
```

Figure F-6: Arduino UNO program for Duty Cycle Tests

```
#include <Adafruit_INA260.h>                       //library for INA260 sensor
Adafruit_INA260 ina260 = Adafruit_INA260();        //initialise IN260 sensor
const byte pin_magnet_button = 24;                 //pin connected to button
int button_state = LOW;                            //variable to track button state

void setup() {                                     //code to run once at start-up
    Serial.begin(500000);                          //start Serial Monitor at set bandwidth
    while (!Serial);                               //pause until connection ready
    delay(1000);
    Serial.println("Serial port Ready");           //confirm Serial Monitor is working
    Serial.println("\n");
    pinMode(pin_magnet_button, INPUT);             //initialize button pin as input
    pinMode(LED_BUILTIN, OUTPUT);                  //initalize built-in led as output
}

void loop() {                                      //main loop, runs continuously
  button_state = digitalRead(pin_magnet_button);   //read button, store in variable
  if (buttonState == HIGH) {                       //run program if button is pressed
    digitalWrite(LED_BUILTIN, HIGH);               //turn on led to indicate program runs
    Serial.print(ina260.readCurrent());           //read and print magnet current
    Serial.print(",");
    Serial.print(ina260.readBusVoltage());         //read and print magnet voltage
    Serial.print(",");
    Serial.print(ina260.readPower());              //read and print magnet power
    Serial.print(",");
    Serial.println(micros());                      //print time stamp in microseconds
  } else {
    digitalWrite(LED_BUILTIN, LOW);                //turn off led if button not pressed
  }
}
```

Figure F-7: Arduino MEGA Program for Duty Cycle Tests

The results for various duty-cycles are plotted in figures F-8, F-9 and F-10. The program was repeated 4 times and we can clearly see 4 peaks. The magnet was found to still work correctly with a duty-cycle of 64, or 25%. At 15%, the armature started to slip slightly. If we look at the power curve, for a duty-cycle of 25%, we see power goes from approximately 5400mW at full power to 800mW in PWM mode. By using the magnet in PWM mode, power consumption thus decreases by **85%**.
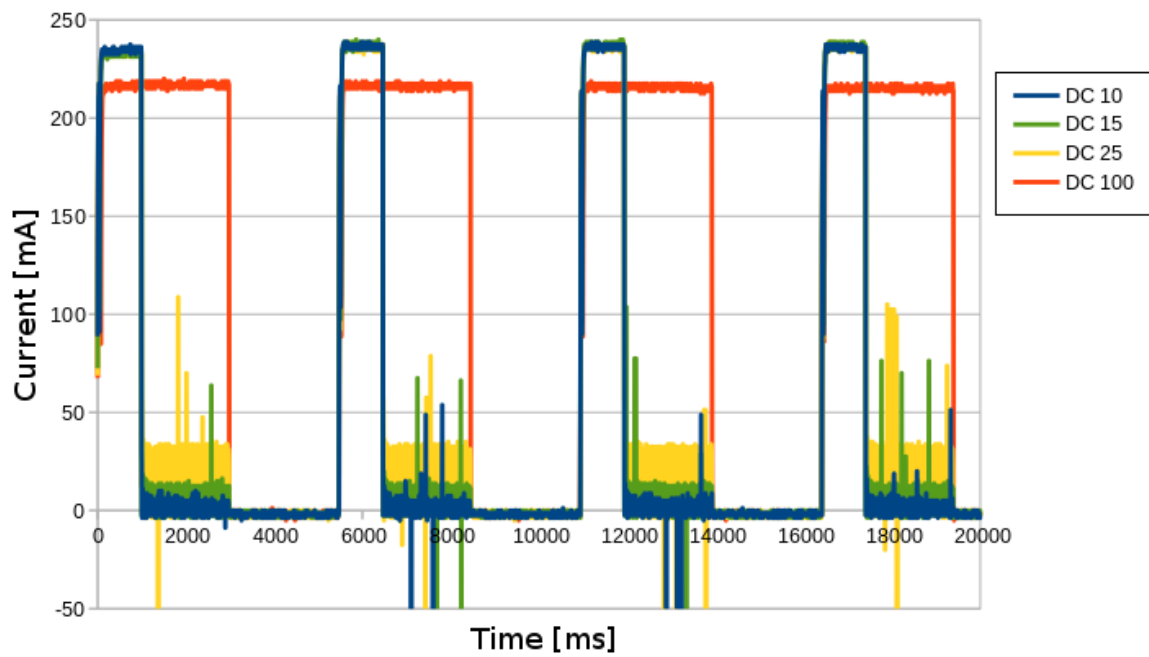
Figure F-8: Duty-cycle vs current
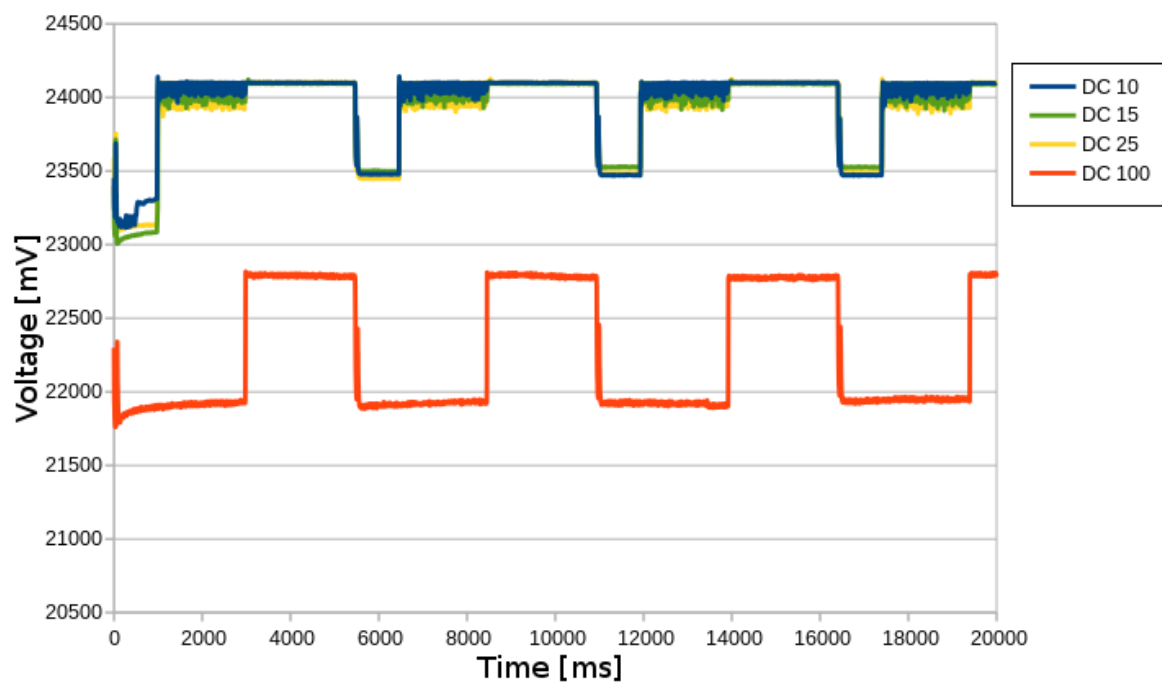
Figure F-9: Duty-cycle vs voltage
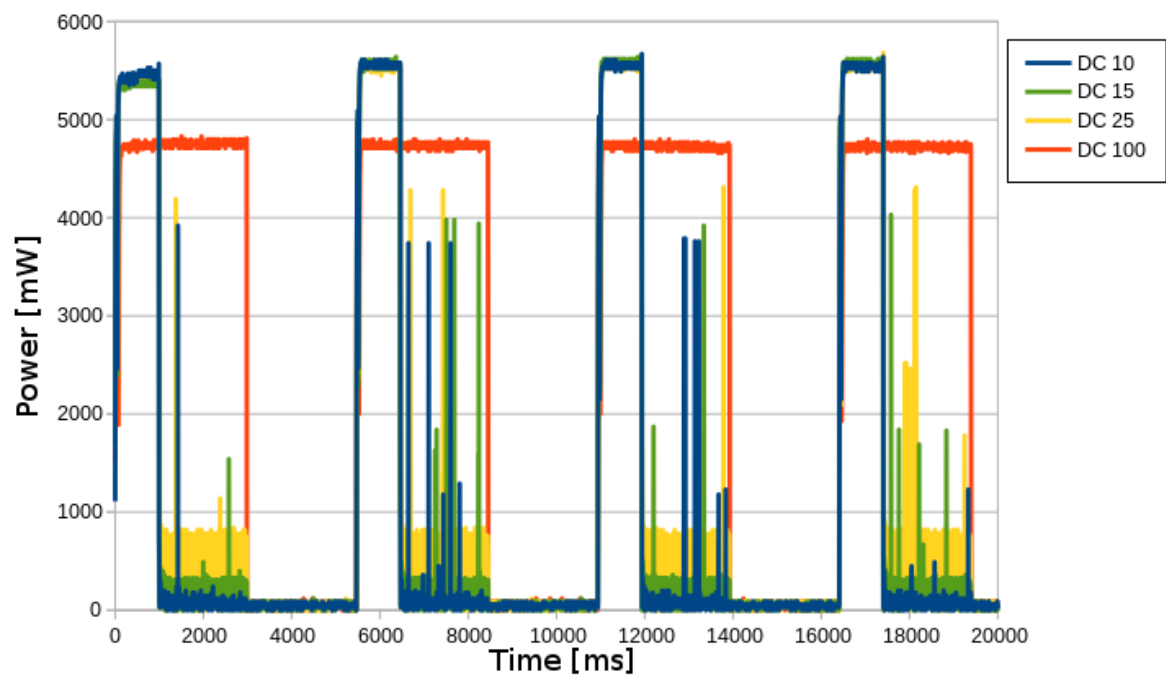
Figure F-10: Duty-cycle vs power

Appendix G

Planetary Gear Drive

In this appendix we elaborate on the planetary gear drive that is used to transfer torque from the motor to the armature. An overview of the drive is shown in figure G-1. The yellow gear is mounted onto the motor shaft, the green gears are the planetary gears and the blue gear is attached to the armature. The orange plate in the middle is where the magnet is mounted on. Because the yellow and blue gears have the same diameter and number of teeth, it can be assumed there is no change in torque between the input and output of the gear drive.

The drive is made by 3D-printing a model and casting it in polyurethane. With this method we can create a complex and custom design, but the material is weaker then steel. So we need to ensure that the gears run smoothly and can withstand the forces.
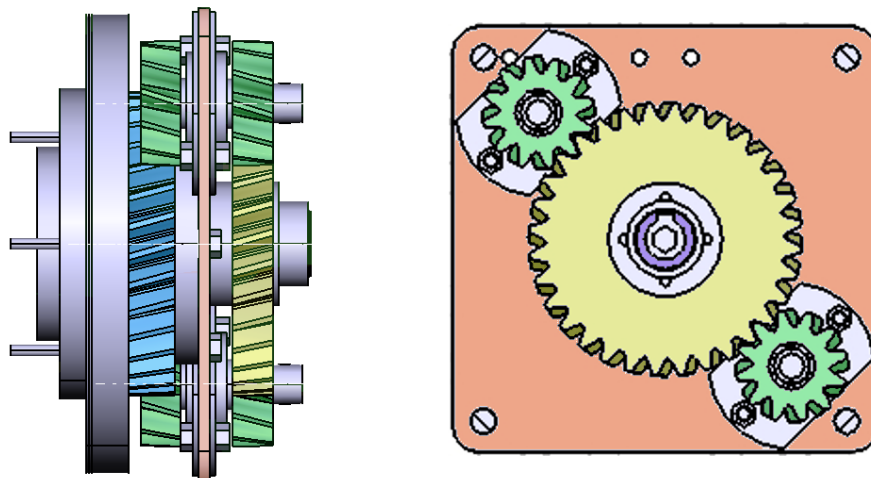
Figure G-1: Overview Planetary Gear
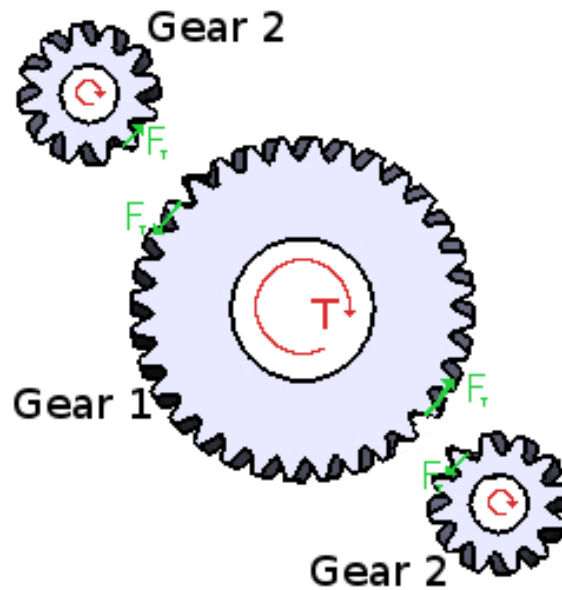
Figure G-2: Forces on Gears

We will follow the procedure as detailed in Roloff/Matek Machineonderdelen[8] in combination with the accompanying Tabellenboek[9]. The contact ratio is determined so we know the gears run smoothly. Then the maximum stress and stress loads on the gear teeth are determined to warrant against tooth failure.

The gear drive is mirrored around the middle plate and consists of symmetrically loaded planetary gears. So, for the calculations, we only need to consider the first gear mounted on the motor shaft, gear 1, and one of the planetary gears, gear 2, to cover the gear drive. An overview of the gears and the forces is shown in figure G-2. The motor exerts a torque T on gear 1, which is distributed in two equal tangent forces F_t on the planetary gears. The gears are chosen to have a normal module of 1.5mm, tooth width 8mm, pressure angle 20° and helix angle of 15 °. Gear 1 has 32 teeth and gear 2 has 12 teeth.

Table G-1 sequences the equations to determine the variables which then determine the contact ratio ε_γ. ε_γ was found to be 1.86. Because this is more then 1.25, it means there is enough interaction between the teeth and the gears will run smoothly.

The material used for the gears is Polyurethane Casting Resin 80 Shore D, which is a hard resin cast with two components. Tensile stress for polyurethane is $45N/mm^2$[10]. In table G-2 the maximum stress σ_{FP} is determined for the applied material. The table numbers are references to the Tabellenboek. We come to a maximum stress of $93N/mm^2$ on the gears.

Finally we determine the stress loads on gear 1 and gear 2 in table G-3. σ_{F1} is $72N/mm^2$ and σ_{F2} is $89N/mm^2$ for the maximum torque of $3000Nmm$. This means that the teeth should be able to withstand the stresses.

Table G-1: Determination contact ratio

Description	Symbol	Unit	Source or equation	Gear 1	Gear 2
normal module	m_n	mm	chosen variable	1.5	
number of teeth	z_1,z_2	-	chosen variable	32	12
width	b	mm	chosen variable	7	
pressure angle	α_n	deg\rad	chosen variable	20\0.35	
helix angle	β	deg\rad	chosen variable	15\0.26	
tangent angle	α_t	deg\rad	$tan^{-1}\left(\dfrac{tan\alpha_n}{cos\beta}\right)$	20.6\0.36	
tangent module	m_t	mm	$\frac{m_n}{cos\beta}$	1.55	
pitch diameter	d_1,d_2	mm	$z \cdot m$	49.7	18.6
base diameter	d_{b1},d_{b2}	mm	$d \cdot cos\alpha_t$	46.5	17.4
top diameter	d_{a1},d_{a2}	mm	$d + 2 \cdot m_n$	52.7	21.6
center distance	a	mm	$\frac{d_1+d_2}{2}$	34.2	
transverse contact ratio	ε_α	-	$\dfrac{0.5\left(\sqrt{d_{a1}^2-d_{b1}^2}+\sqrt{d_{a2}^2-d_{b2}^2}\right)-a \cdot sin\alpha_t}{\pi \cdot m_t \cdot cos\alpha_t}$	1.48	
face contact ratio	ε_β	-	$\frac{b \cdot sin\beta}{\pi \cdot m_n}$	0.38	
total contact ratio	ε_γ	-	$\varepsilon_\alpha + \varepsilon_\beta$	1.86	

Table G-2: Determination maximum tooth stress

Description	Symbol	Unit	Source or equation	Value
PU tensile strength	σ_{PU}	N/mm^2	material property	45
shape-kerb factor	Y_{ST}	-	NEN-ISO 6336-1 standard value	2
life-cycle factor	Y_{NT}	-	Table 21-21a	1
support factor	$Y_{\delta relT}$	-	Table 21-21b	1
roughness factor	Y_{RrelT}	-	Table 21-21c	1.03
size factor	Y_X	-	Table 21-21d	1
safety factor	S_{Fmin}	-	chosen variable	1
maximum stress	σ_{FP}	N/mm^2	$\sigma_{PU} \cdot \frac{Y_{ST} \cdot Y_{NT} \cdot Y_{\delta relT} \cdot Y_{RrelT} \cdot Y_X}{S_{Fmin}}$	93

Table G-3: Determination tooth stress

Description	Symbol	Unit	Source or equation	Gear 1	Gear 2
torque	T	Nmm	coupling specification	3000	
tangent force	F_t	N	$\frac{T/2}{d_1/2}$	60	
speed	n	RPM	coupling specification	50	
commission factor	K_A	-	Table 3-5	1	
factor	K_1	-	Table 21-15	8.5	
factor	K_2	-	Table 21-15	1	
factor	K_3	-	Table 21-15	0.0087	
gear ratio	u	-	$\frac{z_2}{z_1}$	0.375	
tangent speed	v_t	m/s	$d_1 \cdot \pi \cdot n/60$	0.13	
factor	K_4	m/s	$0.01 \cdot z_1 \cdot v_t \cdot \sqrt{\frac{u^2}{1+u^2}}$	0.01	
Dynamic factor	K_v	-	$1 + \left(\frac{K_1 \cdot K_2}{K_A \cdot (F_t/b)} + K_3 \right) \cdot K_4$	1.01	
factor	F_m/b	N/mm	$K_v \cdot K_A \cdot F_t/b$	8.75	
shape error	f_{sh}	μm	$0.023 \cdot (F_m/b) \cdot (b/d_1)^2$	0.0004	
teeth quality	q_t	-	Table 21-7	6	
factor	q_H	-	Table 21-15	1.32	
machining error	f_{ma}	μm	$4.16 \cdot b^{0.14} \cdot q_H$	7.21	
effective error	$F_{\beta x}$	μm	$f_{ma} + 1.33 \cdot f_{sh}$	7.21	
correction factor	y_β	μm	Table 21-17	6	
resultant error	$F_{\beta y}$	μm	$F_{\beta x} - y_\beta$	1.21	
height teeth	h	mm	$2.25 \cdot m_n$	3.375	
exponent	N_f	-	$\frac{(b/h)^2}{1 + b/h + (b/h)^2}$ because $b/h < 3$, $b/h = 3$	0.69	
flank factor	$K_{H\beta}$	-	$2 \cdot \sqrt{\frac{10 \cdot F_{\beta y}}{F_m/b}}$	2.35	
foot factor	$K_{F\beta}$	-	$K_{H\beta}^{N_F}$	1.81	
circle factor	$K_{F\alpha}$	-	Table 21-19	1.2	
tooth factor	K_{Ftot}	-	$K_A \cdot K_v \cdot K_{F\alpha} \cdot K_{F\beta}$	2.2	
virtual teeth nr	z_{n1}, z_{n2}	-	$\frac{z}{cos\beta^3}$	35.5	13.3
shape factor	Y_{Fa1}, Y_{Fa2}	-	Table 21-20a	2.5	3.5
kerb factor	Y_{Sa1}, Y_{Sa2}	-	Table 21-20b	1.725	1.525
normal ratio	$\varepsilon_{\alpha n}$	-	$\varepsilon_\alpha/cos\beta^2$	1.58	
contact factor	Y_ε	-	$0.25 + 0.75/\varepsilon_{\alpha n}$	1.44	
tooth angle factor	Y_β	-	Table 21-20c	0.95	
local tooth stress	$\sigma_{F01}, \sigma_{F02}$	N/mm^2	$\frac{F_t}{b \cdot m_n} \cdot Y_{Fa} \cdot Y_{Sa} \cdot Y_\varepsilon \cdot Y_\beta$	32.7	40.5
total tooth stress	σ_{F1}, σ_{F2}	N/mm^2	$\sigma_{F0} \cdot K_{Ftot}$	72	89

Appendix H

External Rotation Sensor

In this appendix we will elaborate on the External Rotation Sensor (ERS). The ERS is placed outside the Leg-Wheel module and is build from standard components. It is used during the tests to measure rotation and angular speed. There are two types of ERS: the ERS-G and the ERS-L. The ERS-G is build around the Grove Optical Rotary Encoder and will be placed on the motor shaft. The ERS-L is build around the LM393 speedsensor and is used for the Leg-axle and the Wheel-axle.

H-1   Set-up ERS-G

The ERS-G is build around the Grove Optical Rotary Encoder, figure H-1. It consists of one infrared emitter and two Photo-Resistors (PRs), placed 3mm opposite and .8mm apart. Two wires are connected to digital input ports on the microprocessor. When the PRs receive infrared light, the input ports detect a HIGH signal. When an object is placed between emitter and a PRs, the light is interrupted and the corresponding input port detects a LOW signal.
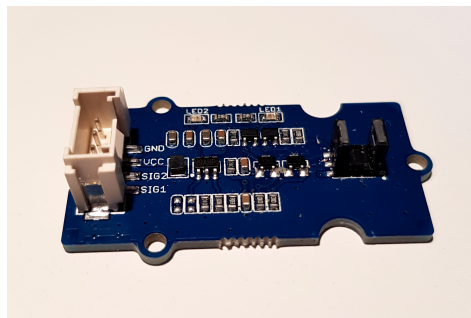
Grove - Optical Rotary Encoder:

VISHAY TCUT1600X01 sensor
1 IR-emitter and 2 phototransistors
2 digital outputs
3mm Gap

Figure H-1: Grove Optical Rotary Encoder
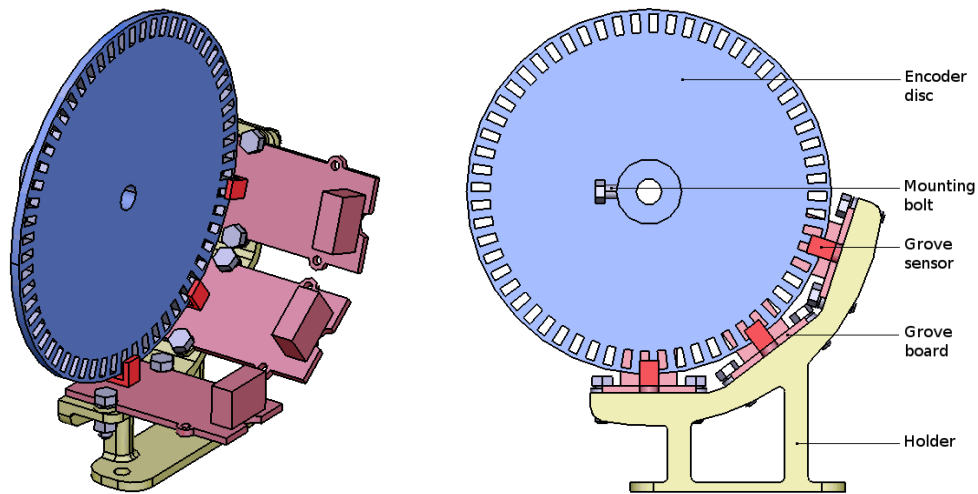
Figure H-2: Overview ERS-G

The ERS-G is constructed with three Grove Encoders that are bolted to a 3D-printed holder. A 3D-printed disc, with a diameter of 80mm and with gaps at evenly spaced intervals, is attached to an axis. An overview is shown in figure H-2. When the axis turns, the disc produces pulses at the outputs which can be converted to rotation. Speed is calculated with the change of rotation divided by time. The combination of the three sensors, and 6 output signals, is used to determine direction and to increase accuracy by averaging the signals. The ERS-G is tested and verified, as shown in figure H-3. The disc is placed on the motor shaft and the measured speed is compared with the set speed of the motor.
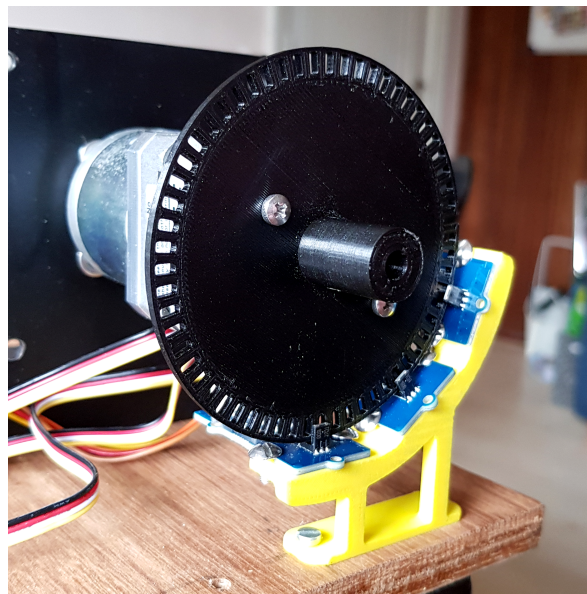
Figure H-3: Testing ERS-G

H-2   Set-up ERS-L

The ERS-L is constructed around the LM393 Speedsensor, depicted in figure H-4. It functions similarly to the Grove Encoder, but it has only one PRs and only one digital output. It is also different in that the gap of the sensor is placed lengthwise relatively to the board and the hole for mounting is placed at a distance from the sensor part.
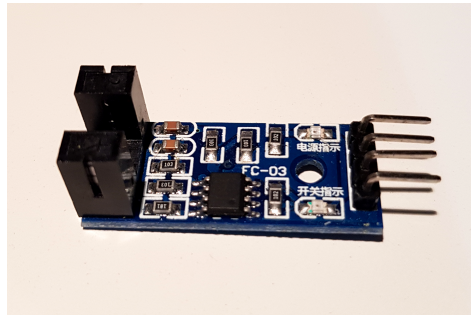
LM393 Speedsensor:

1 IR-emitter and 1 phototransistor
1 digital output
5mm gap

Figure H-4: LM393 Speedsensor

This means that the 3D-printed holder of the ERS-L looks very different to the ERS-G. Because the mounting hole is placed at a distance from the sensor, using bolts could result in the sensor part drifting from its intended position. Therefore the LM393 is clamped with the sensor part between two halves and held in place with plates from below. A schematic overview of the set-up is shown in figure H-5. Note that one half of the holder is shown transparent, so as to display the parts behind. Testing and verification is done in the same way as with the ERS-G. The encoder disc is put on the motor shaft and measurements are compared with set speed of the motor. A picture of the set-up is shown in figure H-6.
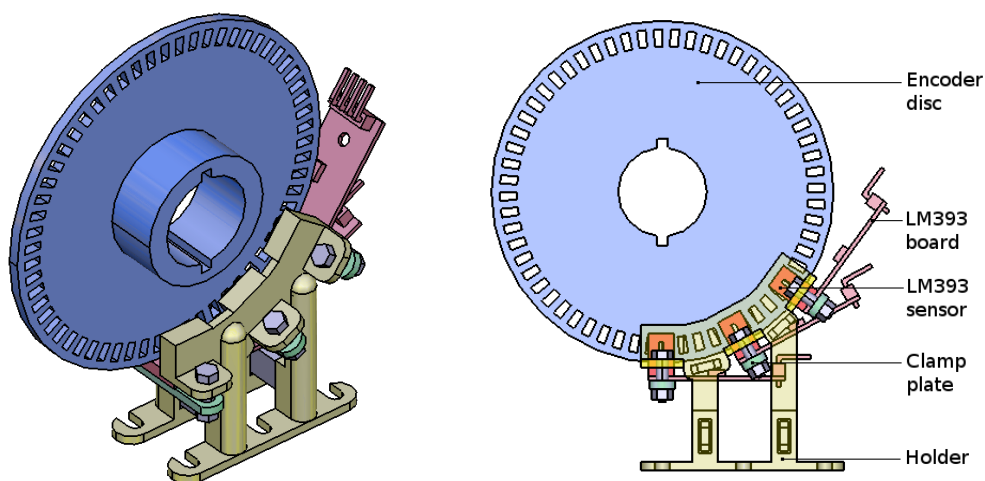
Figure H-5: Overview ERS-L
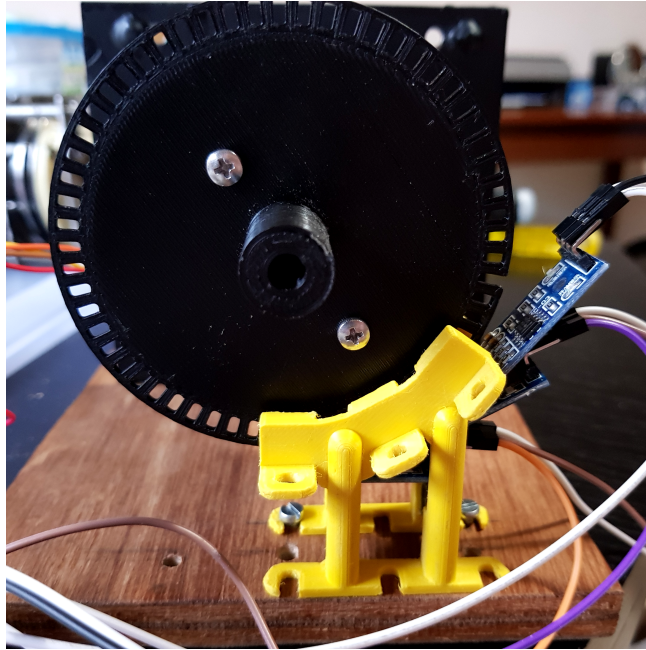
Figure H-6: Testing ERS-L

H-3 Signal processing: Rotation

Figure H-7 shows the raw signal as is produced by the ERS-G and the ERS-L plotted versus time. From these signals, rotation and speed of the axles are calculated. Direction is determined by the phase between the signals. At low speed, 50RPM, and a high sample rate, 500 samples per second, the pulses from the encoder disc are clearly distinguished. It also shows the 3 outputs of the ERS-L with an offset between them. The ERS-G has 2 PRs and 2 outputs per sensor, which results in a total of 6 outputs. But because the 2 PRs are close together, their signals are typically close together and often overlap, particularly with higher speeds or a lower sample rate. It is for this reason that the three sensors are placed apart along the rim of the encoder disc, this maximizes the offset between signals.
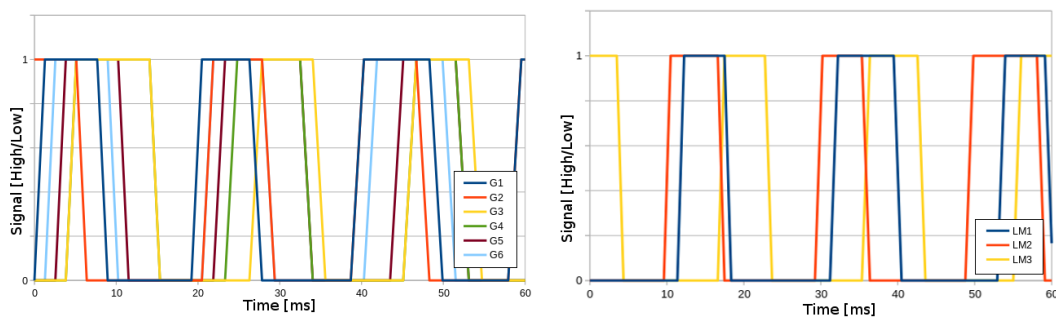
Figure H-7: ERS-G and ERS-L output signals

(a) Signal with fluctuations

(b) Corrected signal
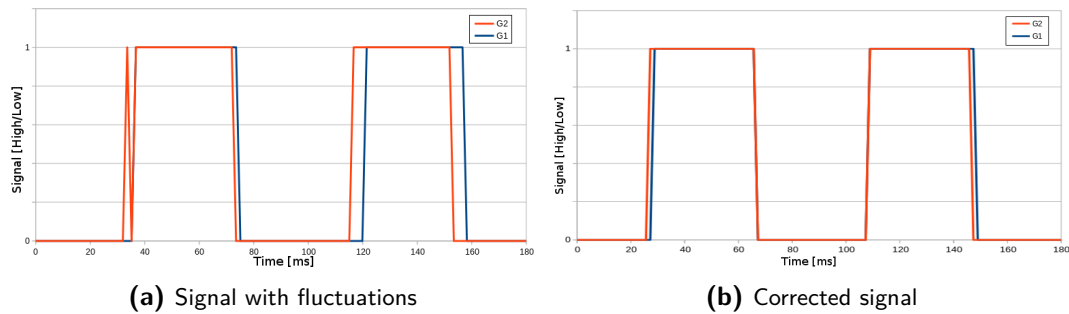
Figure H-8: Signal corrections

Change in rotation is obtained by adding or subtracting a step from the initial position every time a signal changes from high to low or from low to high. There are flaws in the signals however. When a signal changes between high and low, it sometimes briefly fluctuates. These fluctuations would greatly distort the counted rotation, so the signal is corrected by suppressing any change right after one just happened. This error and its correction is shown in figure H-8. The complete algorithm for reading the signal, correcting fluctuations and calculating the rotation is shown in figure H-9. The final rotation is obtained by averaging the output signals of the ERS. Figure H-10 shows the 6 rotations and their average as produced by the ERS-G with a motor speed of 50RPM. We can see a stepped line as a result of the steps by the encoder.

```
for(byte i=0;i<number_of_sensors;i++){
  value[i]= digitalRead(sensor_pin[i]);
  if(value[i] != previous_value[i]){
    if (value_changed[i]==false){
      angles[i]= angles[i]+step_angle;
      value_changed[i]= true;
    } else {
      value[i] = previous_value[i];
      value_changed[i]=false;
    }
  } else {
    value_changed[i]=false;
  }
}
```


Figure H-9: Algorithm for reading Rotation
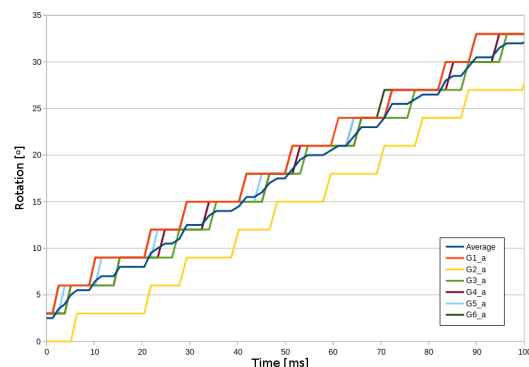
Figure H-10: ERS-G Rotation Measurement

H-4   Signal processing: Speed

With the rotation determined, we can now calculate the speed of the rotation. Time is documented with each sample by the Arduino function *micros(). micros()* returns the time since the program started running, in microseconds, with a maximum of 70 minutes. Speed then follows from the difference between two rotations divided by the difference in time and is converted from degrees per microsecond to speed in RPM. If this was done for just one sensor though, the resulting measurement would be highly irregular, as can be seen from figure H-11. Taking the average over multiple sensors, 6 for the ERS-G and 3 for the ERS-L, still does not improve much. The problem is that the steps from the encoder cause the rotation to increase incrementally and therefore the speed measurements fluctuate. Taking the average of 5 consecutive samples of the average rotation stabilises the signal, but it is still not good enough.
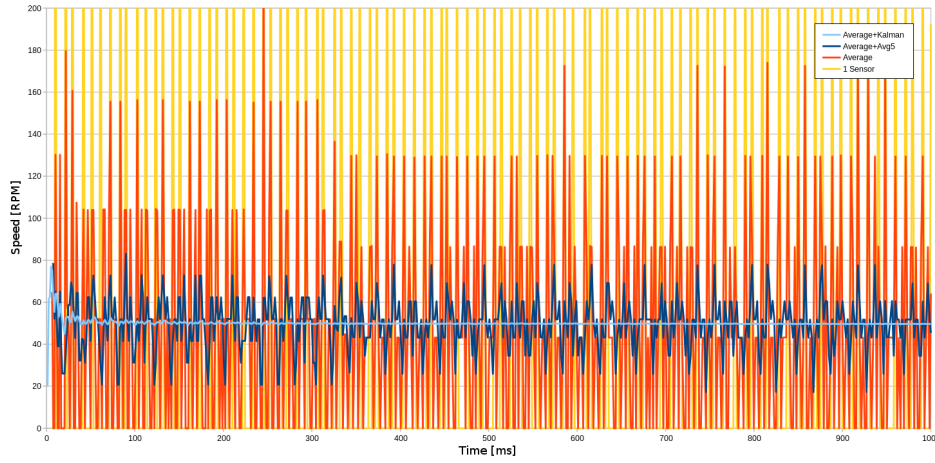
Figure H-11: Raw speed measurements

The solution was to apply a Kalman filter on the signal. The Kalman filter consists of three equations, as in figure H-12, for Kalman Gain (KG), Estimated Error (EE) and Speed Estimate (SE). The filter is initialised at n=0 with values chosen for EE_0, SE_0 and ME. ME stands for Measurement Error and relates to the accuracy of the sensor. ME is a fixed variable during the calculations. $Speed_n$ is the average speed measured at sample n. The three equations are iteratively applied after each sample which automatically adjusts the estimated values and Kalman Gain. With each step, the Speed Estimate comes closer to the actual value and the Estimated Error reduces.

$$KG_n = \frac{EE_{n-1}}{EE_{n-1} + ME} \qquad\qquad (\text{H-1})$$

$$EE_n = (1 - KG_n) \cdot EE_{n-1} \qquad\qquad (\text{H-2})$$

$$SE_n = SE_{n-1} + KG_n \cdot (Speed_n - SE_{n-1}) \qquad (\text{H-3})$$

Figure H-12: Equations Kalman Filter
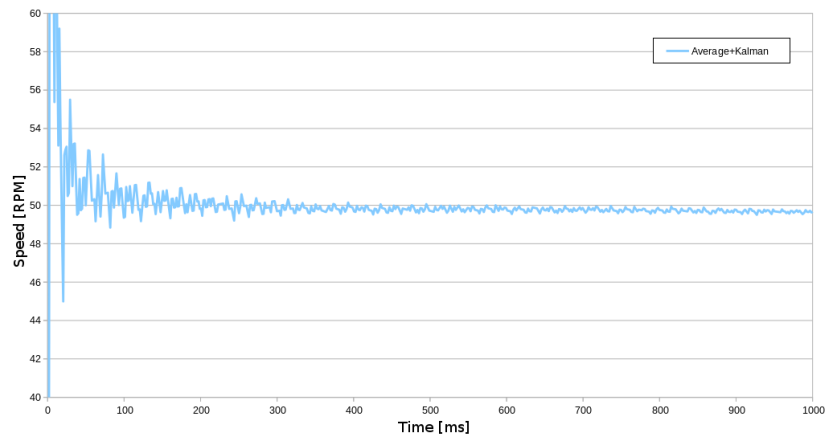
Figure H-13: Speed measurement after Kalman filter

The final result is shown in figure H-13. After a few iterations, the filter conjures around the value that best fits the measurements. The Kalman filter can be applied in Real-Time to discrete data. During these tests, Speed will be determined afterwards with all the samples and Excel. This is done to keep the load on the Arduino as low as possible and to minimize the sample time.

H-5 Signal processing: Encoder Step vs Sample time

Step was mentioned in previous sections and it refers to the angle, in degrees, between gaps in the encoder disc that is used to measure pulses. Figure H-14 shows two encoder discs, one has 60 gaps and a step of 3° and the other has 15 holes and a step of 12°.

(a) 3° per step   **(b)** 12° per step
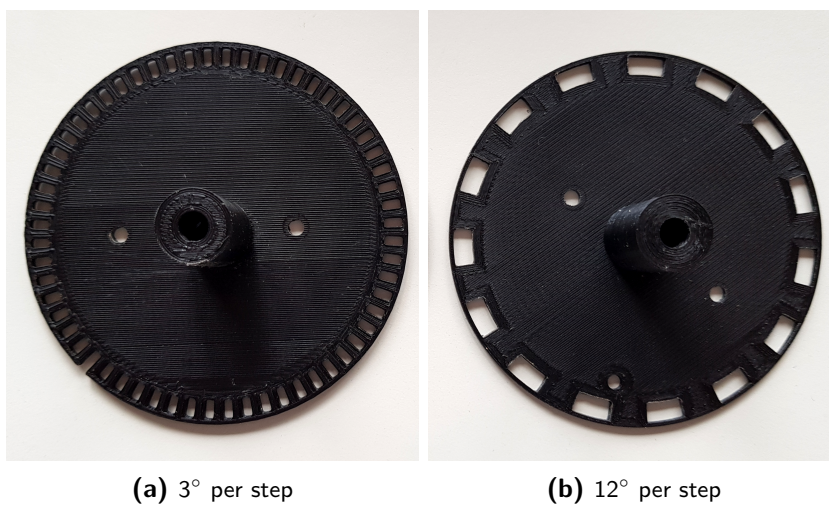
Figure H-14: Encoder discs with different step
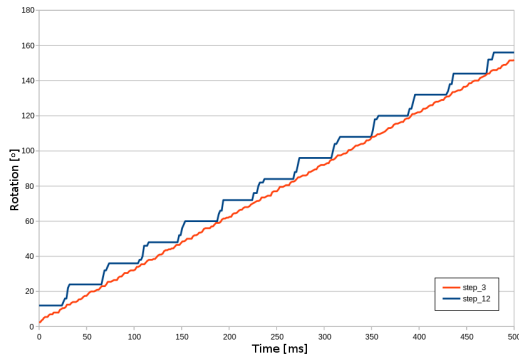
Figure H-15: Rotation measurement with different step
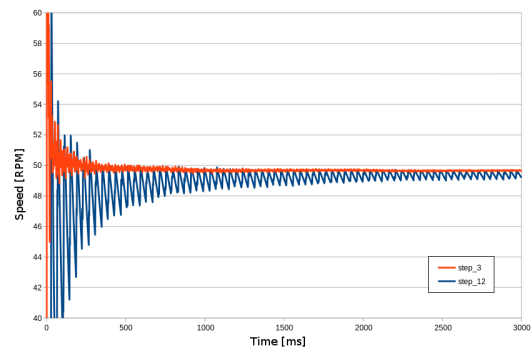
Figure H-16: Speed measurements with different step

Step determines the resolution with which rotation, and thus speed, can be measured. Figures H-15 and H-16 show the effect of different steps on the measurement of Rotation and Speed respectively. We can clearly see a smaller step gives a smoother result and better accuracy.

A small step is thus preferred, however it is limited by the minimum sample time. Sample time refers to the time between two measured samples. It is the time that is needed to read the sensors, process the values and print them on the Serial Monitor. Figure H-17 shows some Rotation measurements for an encoder disc with a step of 3° and a speed of 100RPM. Sample time was adjusted by adding a delay inside the loop. When the sample time is too large, the sensor misses steps and the measurement is off.
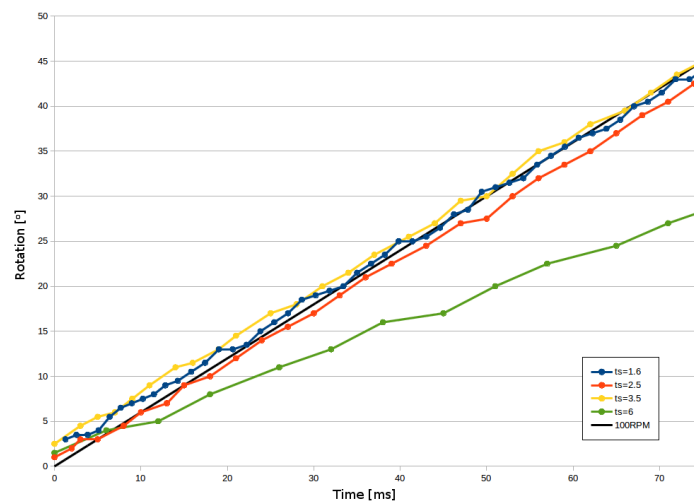
Figure H-17: Rotation with different sample times

If an axle turns with a constant speed of n RPM, then the time duration, in ms, for one step to pass along a sensor is $\dfrac{step \cdot 60000}{n \cdot 360}$. This is also the maximum sample time in order for the sensor to read it. But to accurately trace all steps and allow for the corrections as described in section H-3 we will set a minimum of 3 samples per step. This means that the sample time, in ms, is determined by:

$$t_s \leq \frac{step \cdot 60000}{3 \cdot n \cdot 360} \tag{H-4}$$

Unfortunately sample time can not be freely chosen, but is dependent on the capability of the microprocessor and other sensors in the loop. Particularly sensors that require an I2C interface, such as the VCNL4010, increase the sample time considerably. The only alternative is therefore to choose an encoder with a larger step.

H-6   Verification ERS

To evaluate the ERS, we attach an encoder disc to the shaft at the back of the motor and run the motor at a number of fixed speeds. Since there is no load attached to the motor, we can expect the output of the motor to be in accordance with the specifications. We then compare the measured speed with the input to determine the accuracy of the ERS. Because speed was derived from the measured rotation, we can assume that the accuracy for rotation is equal or better.

Table H-1: ERS-G Test Results

Set Speed [RPM]	step 3°		step 12°		Final Results	
	Measurement [RPM]	Error [RPM]	Measurement [RPM]	Error [RPM]	Smallest Error [RPM]	Smallest Error [%]
50	49.6	0.4	49.5	0.5	0.4	0.8
75	74.2	0.8	74	1	0.8	1.1
100	98.6	1.4	98.8	1.2	1.2	1.2
125	122.8	2.2	122.9	2.1	2.1	1.7
150	118.7	31.3	147	3	3	2
175	101.6	73.4	170.8	4.2	4.2	2.4
200	97.8	102.2	195.1	4.9	4.9	2.5

Table H-1 shows the results for the ERS-G. We run do the tests with an encoder disc of step 3° and of step 12°. The sample time, for reading 6 digital sensor inputs, was found to be 2ms. Equation H-4 tells us that, with a step of 3°, the maximum speed that can be measured reliably is 83RPM. This is why at speeds $\geq$ 100RPM we see a much better accuracy with the encoder disc of step 12°. At speeds $\leq$ 75RPM, we can see a better performance with the encoder disc of step 3° due to its higher resolution.

Table H-2 shows the test results for the ERS-L. Again, the tests are done with two encoder discs of different steps. Sample time was found to be 1.4ms. The ERS-L utilizes only 3 digital sensors, and requires less time, which is why the sample time turns out smaller then for the ERS-G. For a step of 3°, this translates to a maximum speed of 119RPM. And indeed we see that the encoder with step 12° performs better with speeds $\geq$ 125RPM.

Table H-2: ERS-L Test Results

	step 3°		step 12°		Final Results	
Set Speed [RPM]	**Measurement [RPM]**	**Error [RPM]**	**Measurement [RPM]**	**Error [RPM]**	**Smallest Error [RPM]**	**Smallest Error [%]**
50	49.7	0.3	51.7	1.7	0.3	0.6
75	74.1	0.9	74.1	0.9	0.9	1.2
100	98.6	1.4	98.5	1.5	1.4	1.4
125	122.7	2.3	123	2	2	1.6
150	145.5	4.5	147.2	2.8	2.8	1.9
175	165.9	9.1	171.1	3.9	3.9	2.2
200	180	20	195.1	4.9	4.9	2.45

With these results we can conclude that both the ERS-G and the ERS-L have a maximum error of **2.5%**, under the condition that sample time and encoder step satisfy equation H-4.

Appendix I

Integrated Rotation Sensor

This Appendix is to describe the set-up and testing results of the Integrated Rotation Sensor (IRS).

I-1 Test set-up

The IRS consists of two parts. The IRS-L measures the rotation of the Leg-axle and the IRS-W measures the rotation of the Wheel-axle. So we need to test and evaluate both parts. To do that we mount an External Rotation Sensor (ERS) on each axle. The ERS was evaluated in appendix H, so we know that it is accurate. We then actuate
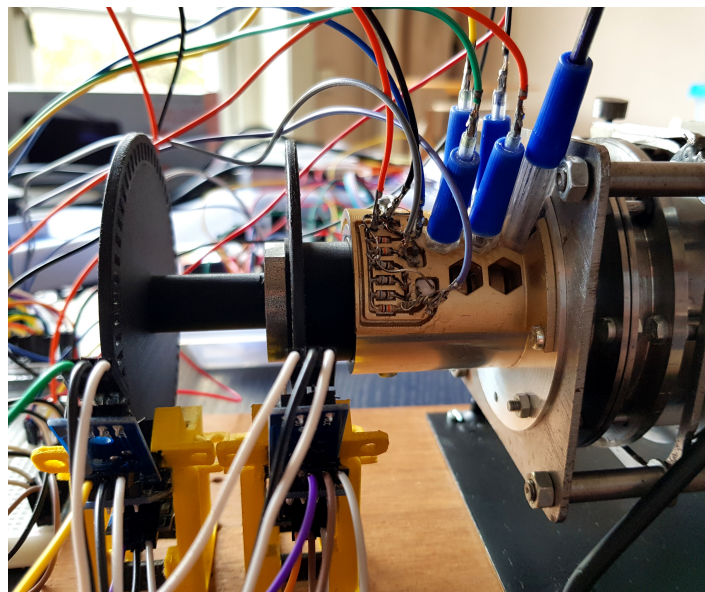
Figure I-1: Set-up IRS testing

the axles with the module and compare the measurements from the IRS with the ERS. Figure I-1 shows a picture of the set-up.

The IRS works on the same principles as the ERS. Surface Mounted Devices (SMDs) emit beams of light, that are received by photo-resisters (PRs) placed across. A disc, attached to the axle and with spaces at regular intervals, passes between the SMD and PR, thus causing a signal with pulses. This signal can then be converted to the rotation angle and to angular speed. But whereas the ERS generates digital high and low pulses, the IRS generates an analog signal which first has to be converted to pulses. PRs change resistance depending on the amount of light they receive, causing a fluctuating voltage potential at the input port of the microprocessor. This signal is then translated by the microprocessor to a voltage potential between 0 and 1000. If a PR receives a large amount of light, it will have a high resistance and the microprocessor will perceive a low voltage potential. If a PR is in the dark, it will have a low resistance and the microprocessor will perceive a high voltage potential.

For the experiments, we will use two microprocessors. An Arduino UNO will be used to control the stepper motor and the magnet. And an Arduino MEGA will be used for the measurements. The Arduino MEGA will monitor the 6 PRs from the IRS and the 6 LM393 sensors for the 2 ERS. The sample time for this was found to be around 3ms. The maximum speed for the motor will be 200RPM, which is approximately 8.3RPM after the gear reduction. This means that equation H-4 will be satisfied if we take an encoder disc with a step of 3° for the ERS:

$$
\begin{aligned}
t_s &\leq \frac{step \cdot 60000}{3 \cdot n \cdot 360} \\
3 &\leq \frac{3 \cdot 60000}{3 \cdot 8.3 \cdot 360} \\
3 &\leq 20
\end{aligned}
$$

The IRS-W has a step of 7.5° and the IRS-L has a step of 15°. Since this is larger then 3°, equation H-4 will satisfied for these as well.

I-2 Test results IRS-L

The raw signals for the IRS-L are shown in figures I-2, I-3 and I-4. Time, in ms, is plotted against the voltage potential in pt. We can see each PR fluctuating between an upper value and a lower value. These correspond to DARK and LIGHT measurements for the PRs.
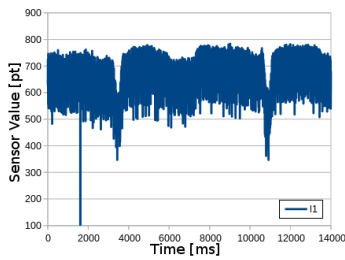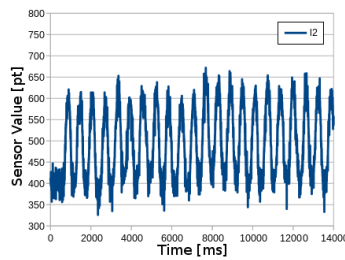
Figure I-2: PR1 **Figure I-3:** PR2 **Figure I-4:** PR3
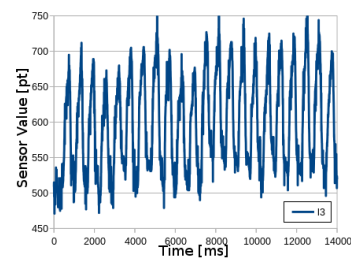
We now choose a threshold value for each signal halfway between the upper and lower boundary of the signal: PR1=450, PR2=475, PR3=590. By evaluating each measurement to 1, when smaller then the threshold, or 0, when not smaller then the threshold, we get high/low pulses. If we plot the values against the measured rotation from the ERS, we get the figure in I-5. In this figure we can clearly distinguish two pulses for PR1, approximately 360° apart, which is the Z-signal to get the absolute position of the axle. Between the two PR1 pulses, there are 12 pulses for PR2 and PR3. This matches the step of 15° for the encoder attached to the Leg-axle.
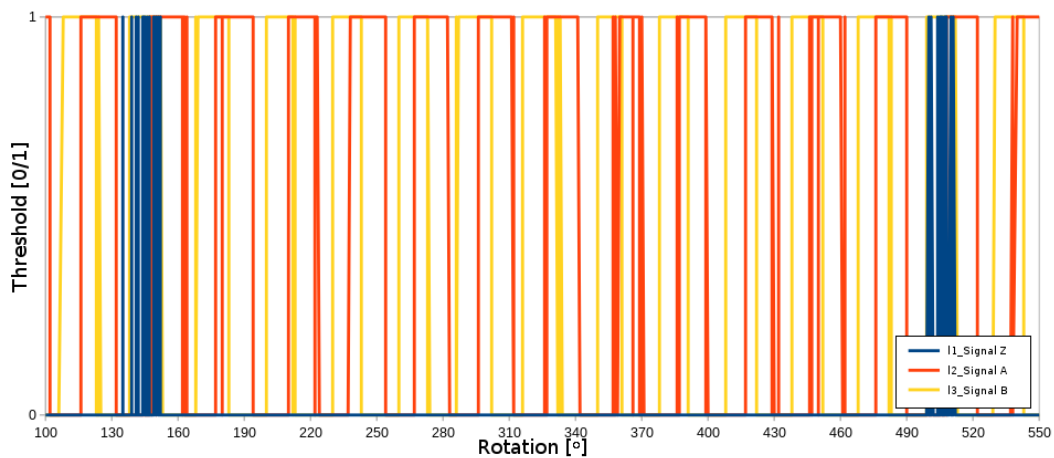
Figure I-5: Small encoder Threshold values

I-3   Test results IRS-W

We now repeat the previous procedure for the Wheel-axle with the IRS-W. We get the raw signals for PR4, PR5 and PR6 as shown in figures I-6, I-7 and I-8.
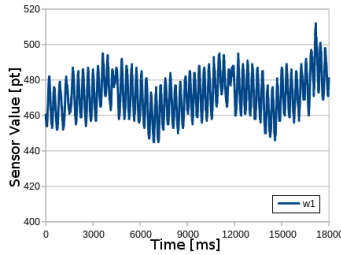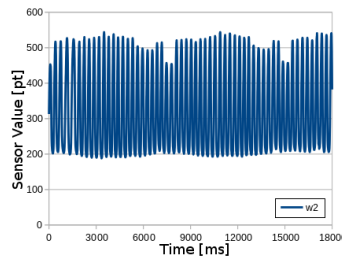
Figure I-6: PR4   **Figure I-7:** PR5   **Figure I-8:** PR6
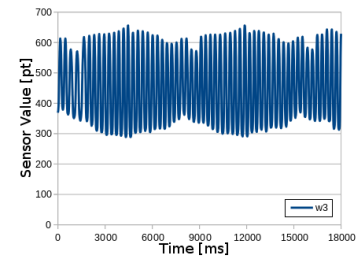
Similarly to the IRS-L, we can see each signal fluctuating between an upper and a lower boundary and we can set a threshold value approximately halfway. The signal for PR4 appears to be less distinct though, it might be that the sensor was still receiving too much ambient light. For this reason, threshold value was chosen close to the lower boundary, PR4=448. PR5 and PR6 were set to 350 and 425 respectively. Evaluating to 1 or 0 with these values, we get figure I-9. We see two pulses for PR4, which indicate the 0-position of the Wheel-axle. Between the 0-positions, there are 24 pulses for PR5 and PR6, corresponding to the 7.5° for the encoder attached to the axle.
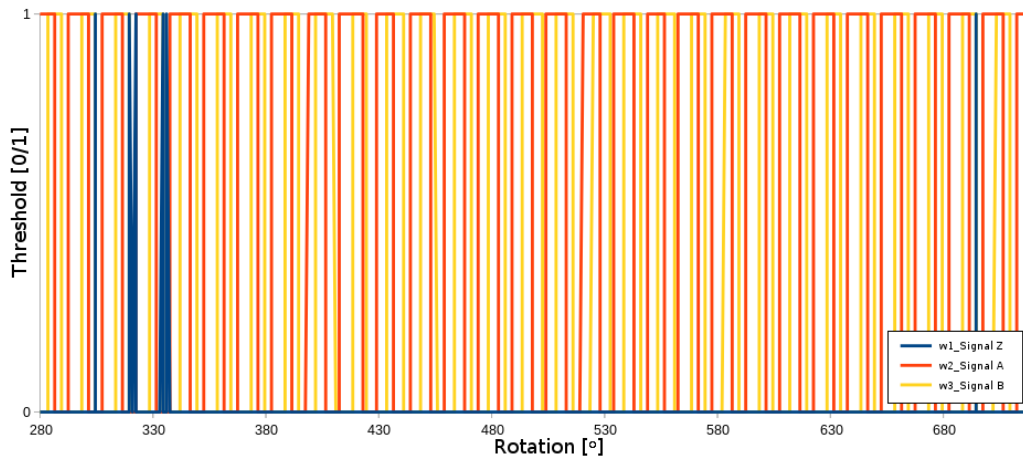
Figure I-9: Large encoder Threshold values

Torque measurement: Prony Brake

To measure the dynamic torque we use an adaptation of the Prony Brake Device, invented by Gaspard de Prony in 1821. Two of these, for the Leg-axle and for the Wheel-axle, are used in the overall evaluation of the Leg-Wheel module.

J-1   Set-up

An overview of the mechanism is shown in figure J-1. A lever is clamped around the shaft, but not completely tight, so that the shaft is just able to slip through it. Clamping force can be adjusted with a bolt through the lever. At the other end, the lever pushes against a set of springs and deflection is measured with VCNL4010 displacement sensors. With the stiffness of the springs we can calculate the spring force, and with this, the exerted torque.
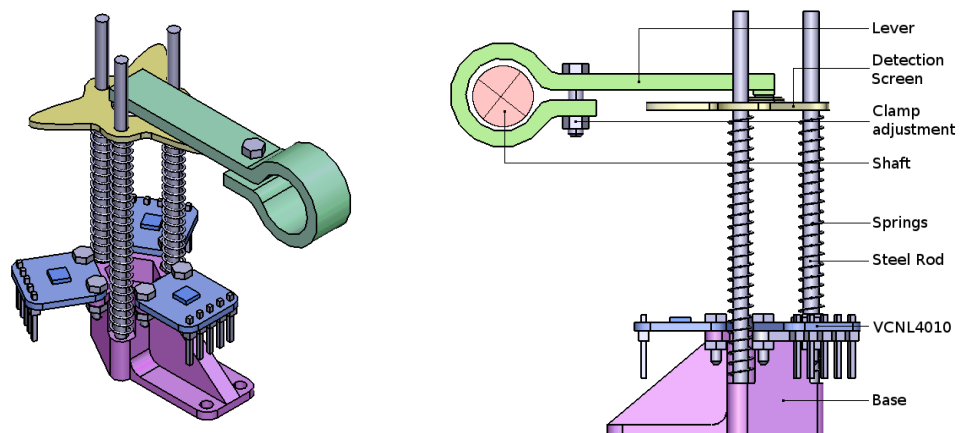
Figure J-1: Overview Torque measurement

With the Prony Brake Device, torque is transmitted to the springs by the friction force between the shaft and the lever. A decomposition of the forces is shown in figure J-2. Because friction force cancels out, we only need to know the length of the lever and the spring force, to calculate the torque.

Lever: Fw*r=Fs*L
Shaft: T=Fw*r

        -> T=Fs*L
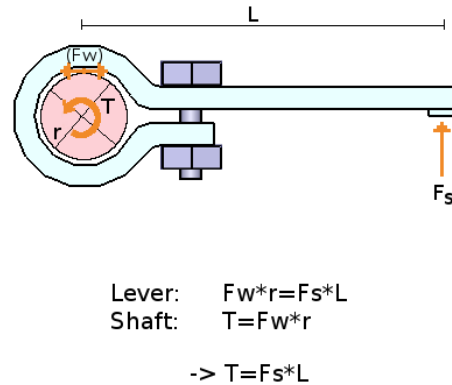
Figure J-2: Torque calculation

J-2   Calibrations: VCNL4010 Displacement function

To measure the spring force, we use an array of three VCNL4010 proximity sensors in combination with a set of springs. This method was previously used to measure the spring and magnetic force in Appendices D, E and F. So this approach has the benefit of using much of the same components and functions. As before, the set-up first has to be calibrated to find the precise relationship between displacement and VCNL4010 sensor readings.

The calibration set-up is shown schematically in J-3. A detection screen is suspended above the sensors by means of an M6 bolt and a nut. Another M6 nut is fixed inside the base, which keeps the bolt upright. M6 has a thread of 1 millimetre, so by rotating the bolt one rotation we lower the screen by 1 millimetre. A small bar, with a measurement scale glued onto it, is used to place the screen 50mm above the sensors. We then read the proximity values, in cts, whilst lowering the screen to 20mm.
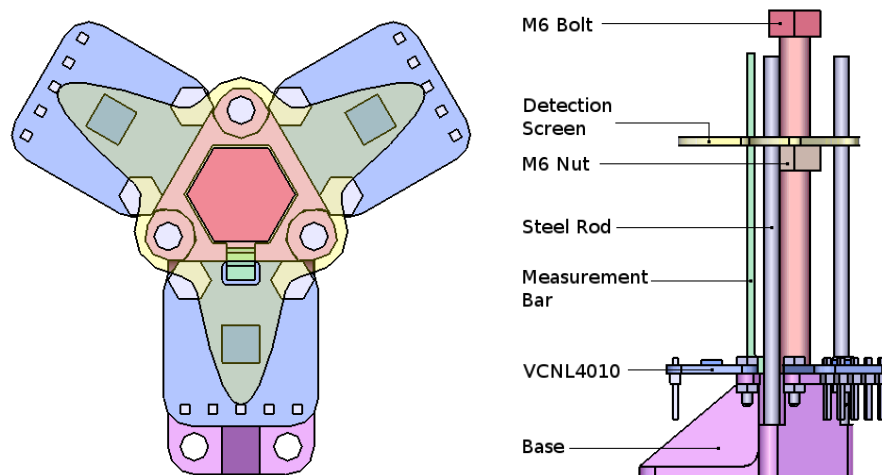
Figure J-3: Overview VCNL4010 Calibration

A picture of the set-up is shown in figure J-4. The measurement bar was also intended to serve as an extra check on the height of the screen. However it was found that the bar was too close to the sensors and distorts the readings. Therefore it was held next to the screen instead and removed between measurements. During tests the M6 bolt will protrude underneath the base, so the setup is held next to a table by means of a clamp and plate.
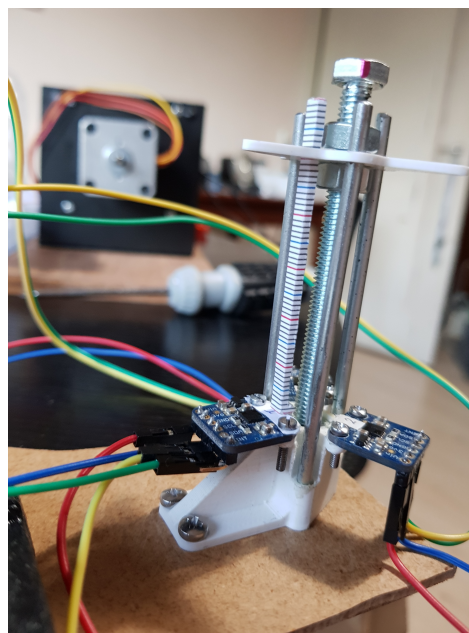
Figure J-4: VCNL4010 Calibration Set-up

The resulting measurements are displayed in table J-1. It shows the height in mm and the measurements, proximity values, in cts.

Table J-1: VCNL4010 Calibration Results

Height [mm]	S1 [cts]	S2 [cts]	S3 [cts]	Average value [cts]
50	2372	2353	2585	2436.7
49	2385	2365	2605	2451.7
48	2390	2361	2609	2453.3
47	2388	2364	2608	2453.3
46	2396	2374	2616	2462
45	2404	2374	2620	2466
44	2410	2385	2630	2475
43	2408	2384	2633	2475
42	2420	2392	2641	2484.3
41	2432	2408	2647	2495.7
40	2443	2420	2663	2508.7
39	2450	2427	2676	2517.7
38	2460	2434	2684	2526
37	2476	2447	2695	2539.3
36	2491	2463	2720	2558
35	2496	2478	2732	2568.7
34	2534	2508	2751	2597.7
33	2552	2520	2780	2617.3
32	2571	2554	2804	2643
31	2597	2583	2853	2677.7
30	2649	2613	2880	2714
29	2683	2657	2907	2749
28	2726	2702	2940	2789.3
27	2781	2767	2979	2842.3
26	2847	2817	3049	2904.3
25	2905	2894	3106	2968.3
24	2996	2984	3188	3056
23	3083	3072	3266	3140.3
22	3235	3182	3303	3240
21	3416	3309	3491	3405.3
20	3624	3464	3648	3578.7

The data is plotted in figure J-5. It clearly shows that the measurements follow a consistent line.
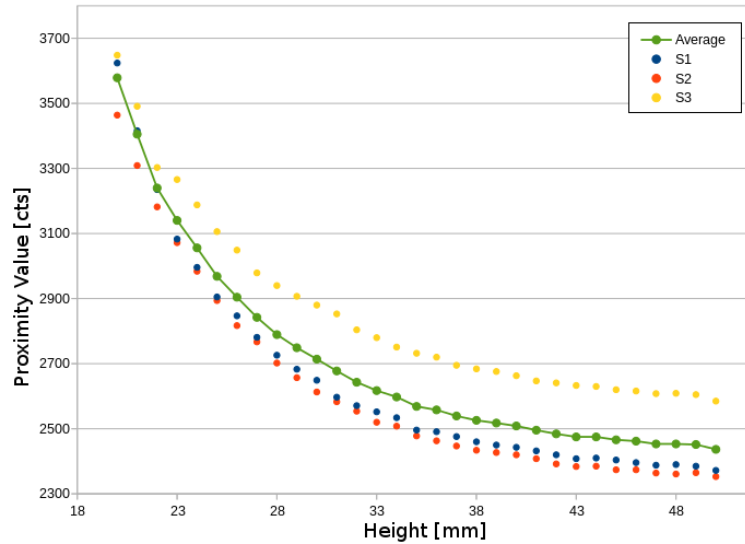
Figure J-5: VCNL4010 measurements

Because the measurements are consistent, we can obtain the height as a function of average proximity value. By using the trend-line application in Excel, we find an 8th order polynomial that approximates the data with a squared error of 0.998.

$$
\begin{aligned}
H(avg) =& 4.4114^{E-22} \cdot avg^8 - 1.1746^{E-17} \cdot avg^7 + 1.3555^{E-13} \cdot avg^6 \\
& - 8.8647^{E-10} \cdot avg^5 + 3.5966^{E-6} \cdot avg^4 - 9.2770^{E-3} \cdot avg^3 \\
& + 1.4865^{E1} \cdot avg^2 - 1.3537^{E4} \cdot avg + 5.3659^{E6}
\end{aligned}
\tag{J-1}
$$
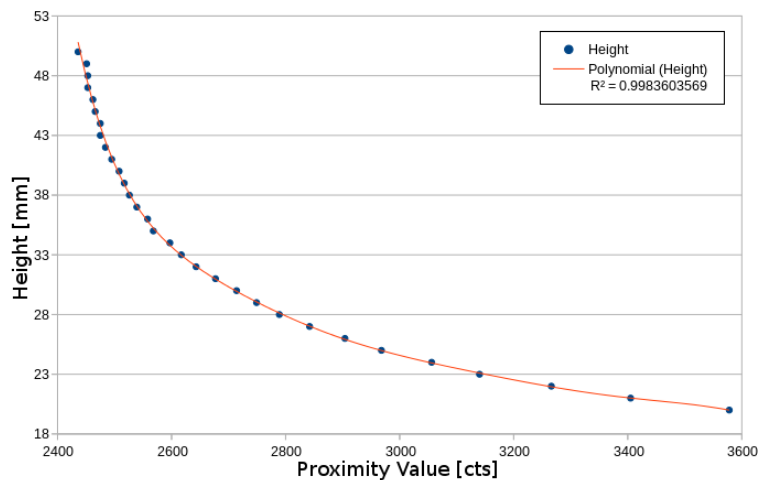
Figure J-6: Polynomial function fit

J-3   Calibrations: Spring stiffness

With the VCNL4010 sensors calibrated, we can now measure the stiffness of the springs. The springs are obtained from a random box, selected for their size, and we need to know the exact stiffness. An overview of the set-up is shown in figure J-7. Weights are placed on top of the springs by means of a platform that can slide over the steel rods. Displacement is then measured with the sensors and the stiffness k is obtained through the relation $F_s = m \cdot g = k \cdot \triangle H$.
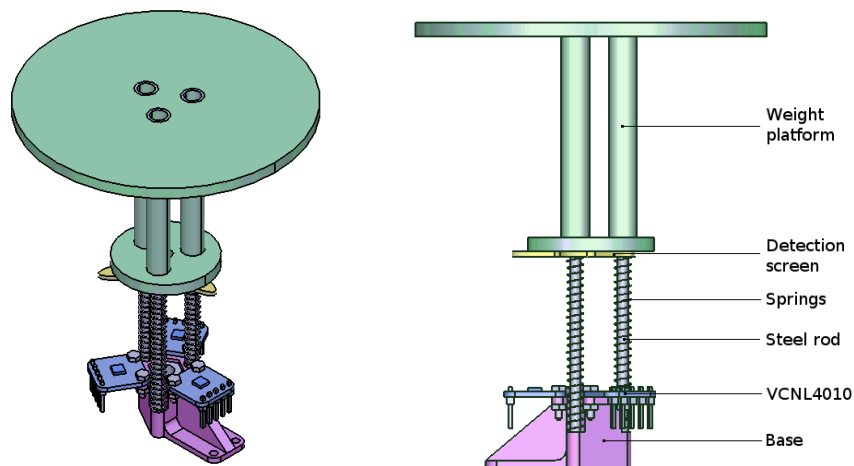
Figure J-7: Overview Spring stiffness test
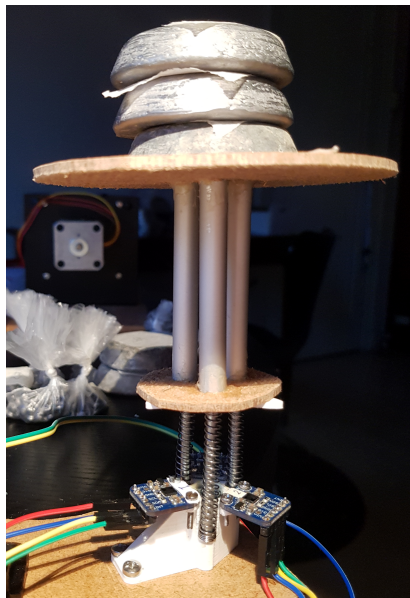
Figure J-8: Stiffness tests

In table J-2 the results are shown. The weight of the platform, 23g, is included in the applied weight. Height H is calculated with equation J-1 and displacement $\triangle$H is calculated from that.

Table J-2: Spring stiffness Results

Weight [g]	Force [N]	S1 [cts]	S2 [cts]	S3 [cts]	Avg [cts]	Height [mm]	$\triangle$H [mm]
0	0	2474	2352	2803	2543	37.3	
23	0.23	2485	2378	2840	2567.7	35.7	0
48	0.47	2487	2382	2842	2570.3	35.6	0.15
73	0.72	2502	2391	2845	2579.3	35.1	0.61
98	0.96	2515	2401	2858	2591.3	34.5	1.18
123	1.21	2533	2408	2872	2604.3	34.0	1.75
148	1.45	2549	2413	2884	2615.3	33.5	2.16
173	1.70	2549	2422	2883	2618	33.4	2.29
198	1.94	2559	2431	2893	2627.7	33.1	2.64
235	2.31	2573	2442	2901	2638.7	32.7	3.03
260	2.55	2578	2446	2900	2641.3	32.6	3.12
285	2.80	2609	2462	2915	2662	32.0	3.77
310	3.04	2615	2471	2923	2669.7	31.7	4.00
335	3.29	2617	2475	2937	2676.3	31.5	4.20
360	3.53	2624	2486	2948	2686	31.3	4.48
385	3.78	2629	2491	2953	2691	31.1	4.62
410	4.02	2653	2499	2976	2709.3	30.6	5.11
472	4.63	2697	2526	3004	2742.3	29.8	5.95
497	4.88	2703	2533	3014	2750	29.6	6.13
522	5.12	2712	2535	3021	2756	29.5	6.28
547	5.37	2741	2557	3044	2780.7	28.9	6.84
572	5.61	2750	2565	3059	2791.3	28.7	7.08
597	5.86	2769	2570	3067	2802	28.4	7.30
622	6.10	2790	2580	3086	2818.7	28.1	7.65
647	6.35	2821	2600	3105	2842	27.6	8.10
672	6.59	2842	2611	3120	2857.7	27.3	8.38
723	7.09	2881	2643	3157	2893.7	26.7	8.99

The measurements and the heights are plotted in figure J-9 and J-10. We can see the linear relationship between height and weight, meaning the springs are linear with a constant stiffness k.
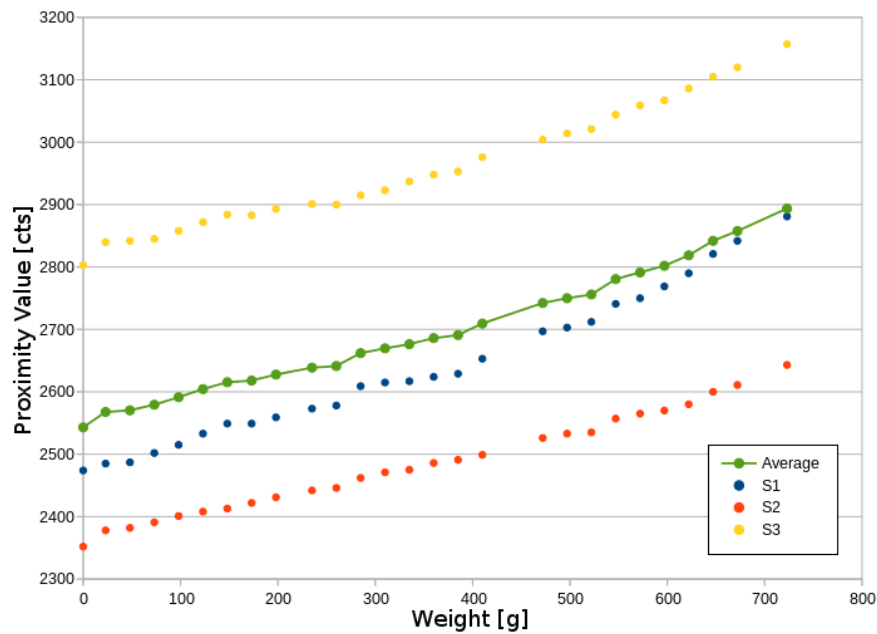
Figure J-9: Measurements Spring tests
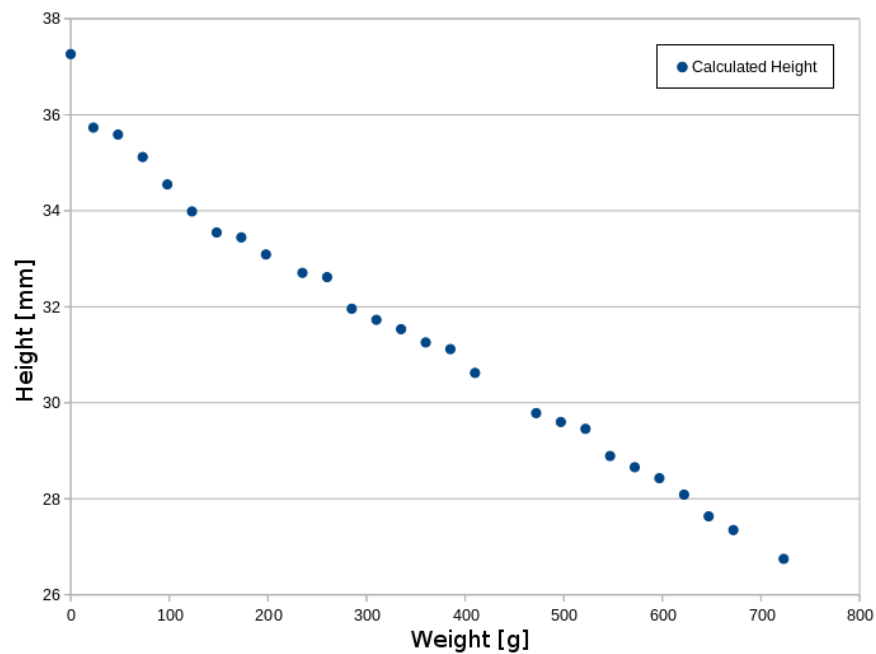
Figure J-10: Calculated heights Spring tests

With the measurements we can plot the displacement against force. A trendline gives us the stiffness k. k was found to be **0.781N/mm**.
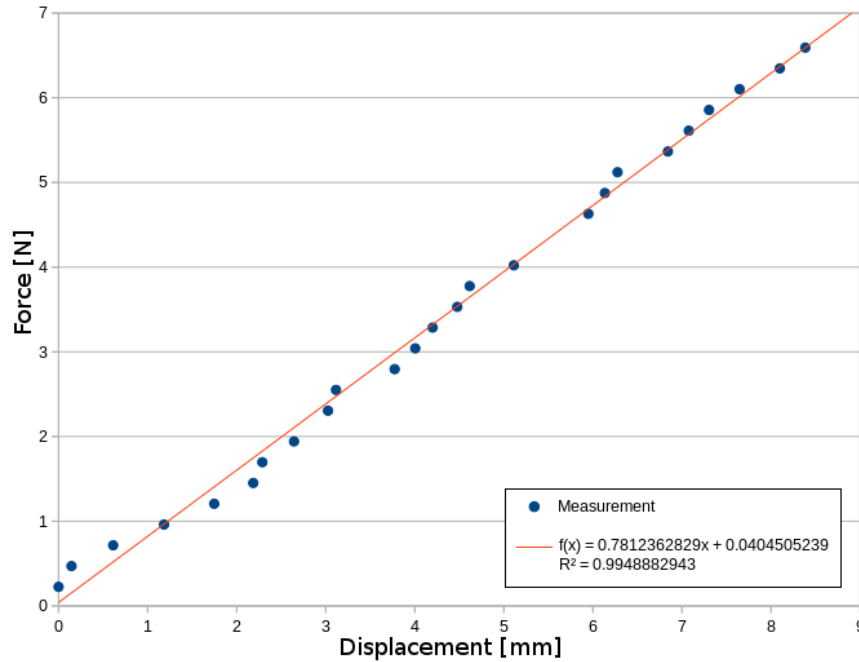
Figure J-11: Linear fit stiffness

J-4   Verification

We can now use the Prony sensor to measure torque. To validate the sensor we will first try the it in combination with the motor in unloaded condition. The speed-torque curve of the motor is documented in appendix A, so the torque is known.

The setup is shown in figure J-12. The lever is attached to the encoder disc with step 12°. The Prony sensor has three VCNL4010 sensors that use an I2C interface and which take a lot of time each loop. This is why, in combination with the External Rotation Sensor (ERS)-G, sample time was found to be 6ms. In accordance with equation H-4, this means the maximum speed that can be reliably measured is 111RPM.

The torque, in Nmm, is calculated by:

$$T = \triangle H \cdot k \cdot L \tag{J-2}$$

Here $\triangle$H is the measured displacement of the detection screen. k is the stiffness, 0.781N/mm and we use a lever with a length L of 50mm.
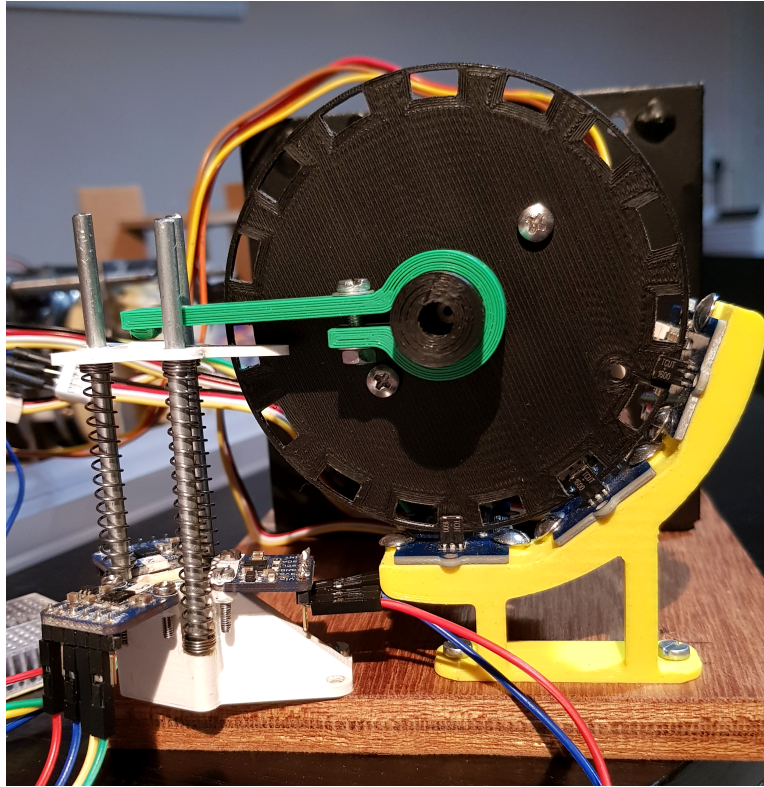
Figure J-12: Set-up Verification tests

The test is done for speed 50RPM, 75RPM and 100RPM. In figures J-13 to J-15, we show the measured heights and the calculated torques. The detection screen vibrates heavily during the test, so we use a Kalman filter to get a steady value. We see the screen starts at an height of 37.5mm and when the lever hits it drops to around 35.5mm. This corresponds to a torque of about 80Nmm. The motor specifications give an expected value of 160Nmm. This unfortunately means that the sensor is not accurate enough to get a precise value, but we can use it to get an indication.
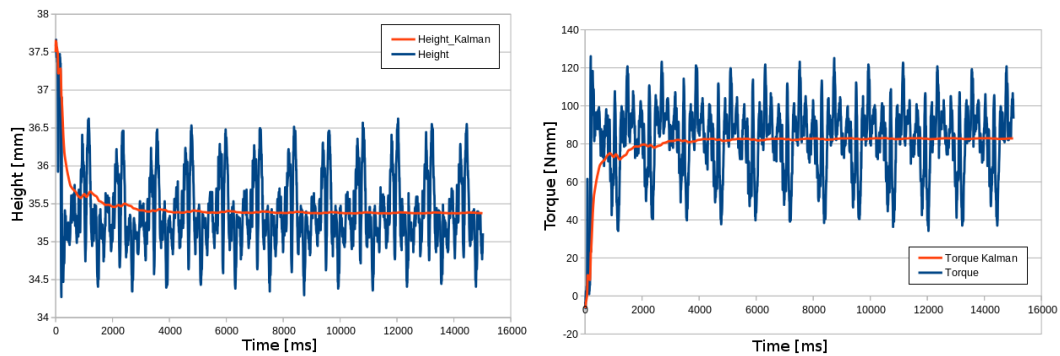
Figure J-13: Height and Torque measurments for speed 50RPM
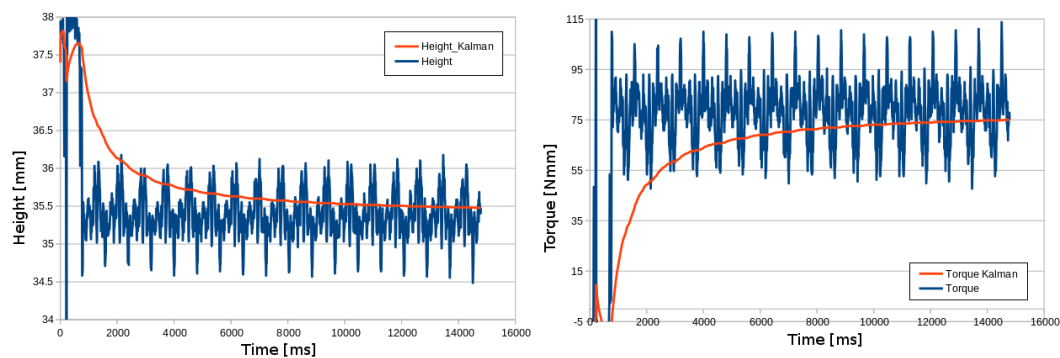
Figure J-14: Height and Torque measurments for speed 75RPM
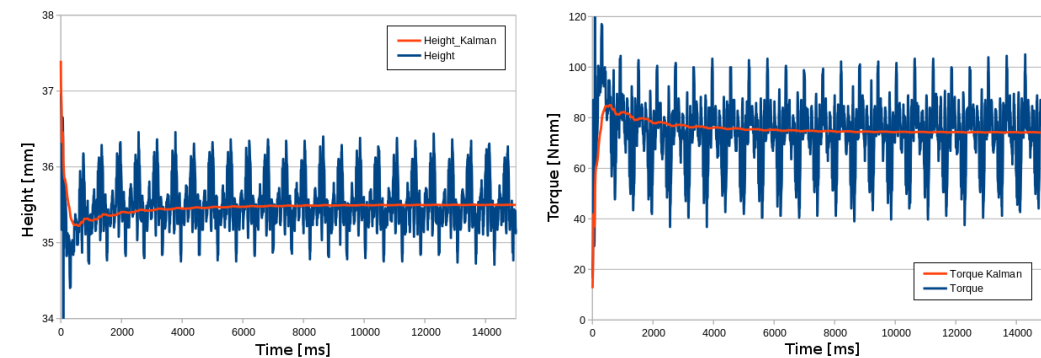
Figure J-15: Height and Torque measurments for speed 100RPM

Appendix K

Static Torque Evaluation

In this appendix we will describe the tests to evaluate the torque limit of the leg- and the wheel-axle when the motor is not running. This is called the Static Torque.

K-1 Test set-up

The test set-up is shown in figures K-1 and K-2. A lever with a length of 25cm is mounted on an axle and a small bucket is hung at the other end. Small weights are added until the lever just starts to slip. We can then calculate the maximum static torque the axle is able to hold.

Figure K-1: Static Torque test Leg-axle

Figure K-2: Static Torque test Wheel-axle

The test will be done for the wheel-axle with the coupling in the off-state and for the leg-axle both with the coupling in the off-state and in the on-state. The wheel-axle is not engaged in the on-state, and free to turn, therefore there is no need to measuring it.

The lever used for the Leg-axle has a weight of 42 grams and its center of mass was found to be 11cm from the center of the pivot. So the lever adds a moment of 45Nmm. The lever used for the Wheel-axle is slightly bigger and has a weight of 57 grams, with a center of mass 10cm from the center of the pivot. So the lever adds a moment of 56Nmm.

The spring force from the coupling has a large effect on the torque capacity of the axles. The coupling was intended to be used with springs with a combined stiffness of 27.5N/mm, but the magnet was found unable to attract the armature for switching. So in the evaluation of the module, springs with a combined stiffness of 5.2N/mm were used. We will determine the static torque for both types, as this will allow us to better evaluate the module.

K-2   Results

The results of the tests are listed in table K-1. Here, *springs* describes the type of springs that were used. Type 1 are the C0180-016-0250S with stiffness 5.2N/mm. Type 2 are the C0180-026-0310M with stiffness 27.5N/mm. *axle* describes which axle is measured. *Weight* is the total weight, including the bucket, at the end of the lever. *Moment* is the applied moment as a result of the weight. *Lever* is the moment added from the lever mounted at the axle. And *Total* is the combined static torque of the weight and lever.

Table K-1: Static Torque Test Results

Springs [-]	Axle [-]	Weight [g]	Moment [Nmm]	Lever [Nmm]	Total [Nmm]
Type 1	Wheel-axle	91	223	56	279
Type 1	Leg-axle OFF	19	47	45	92
Type 1	Leg-axle ON	10	25	45	70
Type 2	Wheel-axle	166	407	56	463
Type 2	Leg-axle OFF	41	101	45	146
Type 2	Leg-axle ON	41	101	45	146

Appendix L

Module Performance Tests

L-1 Set-up

An overview of the general set-up is shown in figure L-1. The tests cover two parts. In the first part, the magnet is turned off and the Wheel-axle is engaged through the coupling. Rotational speed is measured with an External Rotation Sensor (ERS), as described in appendix H and with an error of 2.5% or 5RPM. An ERS-G is used for the motor axis and an ERS-L is used for the Wheel-axle. A Prony sensor measures torque output at the Wheel-axle. Unfortunately this sensor is only accurate enough to get an indication. An adafruit INA260 sensor is used to measure the electrical power
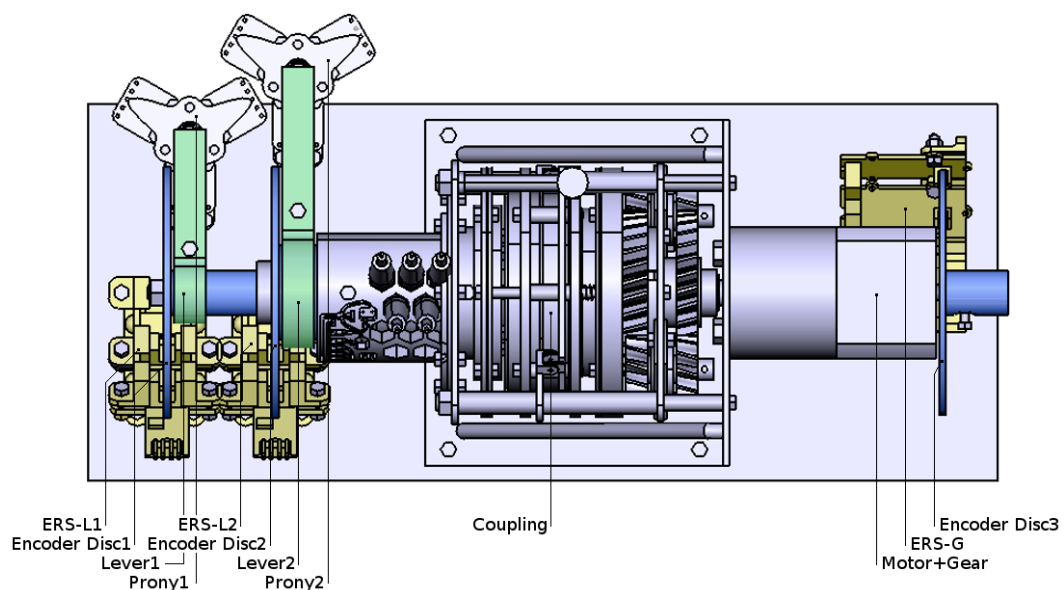
Figure L-1: Overview Test set-up

consumed by the circuit. The INA260 is documented with a maximum error of 0.15%, for the power measurements this translates to a maximum error of ±24mW. Output torque and mechanical power from the motor are read from the specifications in appendix A.

In the second part, the magnet is turned on and the leg-axis is engaged through the coupling. Again, an ERS-G is used for the motor axis, an ERS-L is used for the leg axis and a Prony sensor measures torque output. An adafruit INA260 sensor is once again used to measure the overall electrical power consumed by the circuit, but we use another INA260 sensor to measure the electrical power consumed by the magnet. Output torque and mechanical power from the motor are read from the specifications.

A picture of the set-up is shown in figure L-2. During the tests, the microprocessor is reading 14 input signals, 5 of which through an I2C interface. This is why the sample time was found to be 9ms. We therefore use an encoder disc with a step of 45° on the ERS-G. At the maximum speed of 200RPM, equation H-4 gives us 12.5, which is still larger then the sample time. The maximum speed after the gear reduction is 8.3RPM, so we can use an encoder disc with step 3° on the ERS-L. The result of equation H-4 is then 20.

Because the magnet was found unable to pull the springs selected for the coupling, the tests were done with a different set of springs. These are the C0180-016-0250S, bought from Amatec. They have a combined stiffness of 5.2N/mm and a unloaded length of 6.35mm. In the set-up they are configured with a preloaded length of 3.5mm and thus provide a combined spring force of 14.8N. When this is divided over the two friction pads, each receive a pressure force of 7.4N
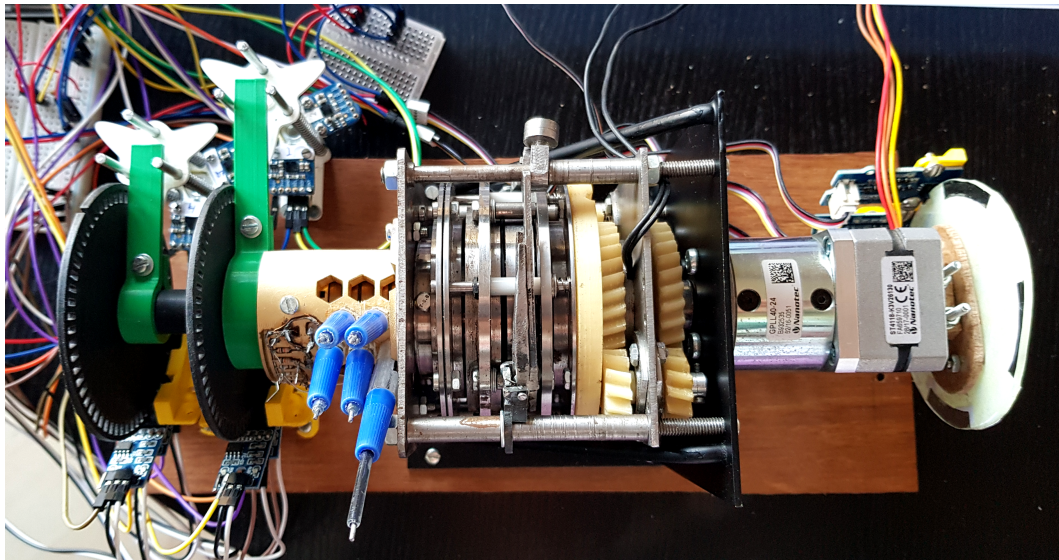
Figure L-2: Top view Test set-up

L-2 Test Results at 50RPM - Wheel-axle engaged
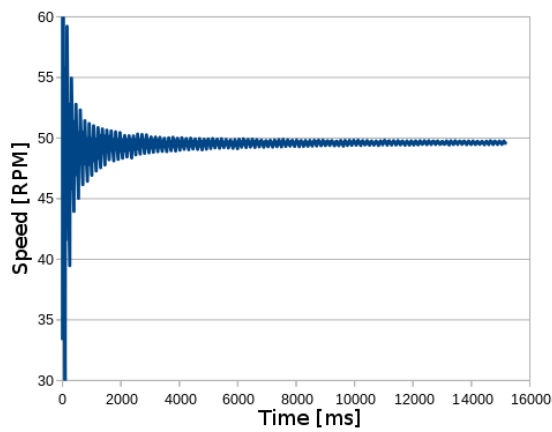
Figure L-3: Motor speed
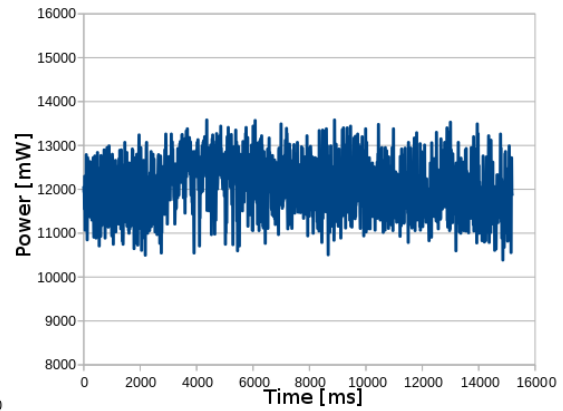
Figure L-4: Overall consumed Electrical Power
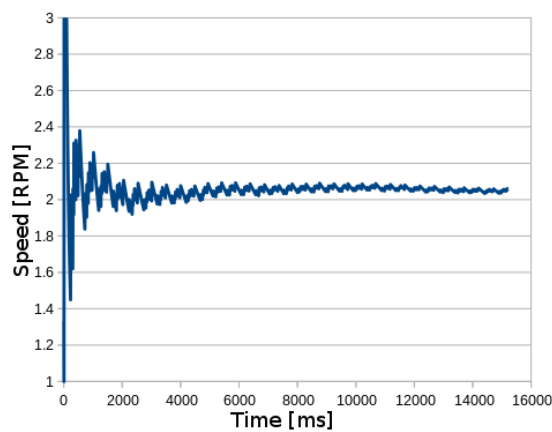


Figure L-5: Wheel-axle speed
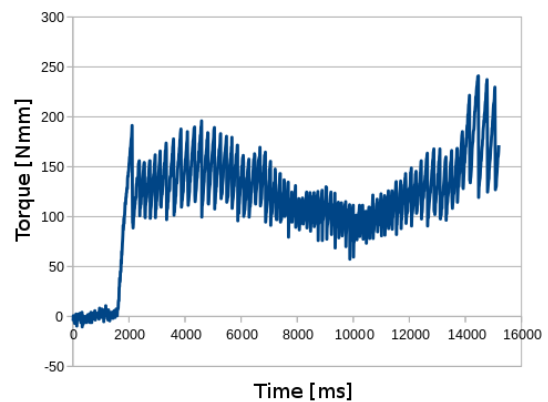
Figure L-6: Torque Wheel-axle

L-3   Test Results at 75RPM - Wheel-axle engaged
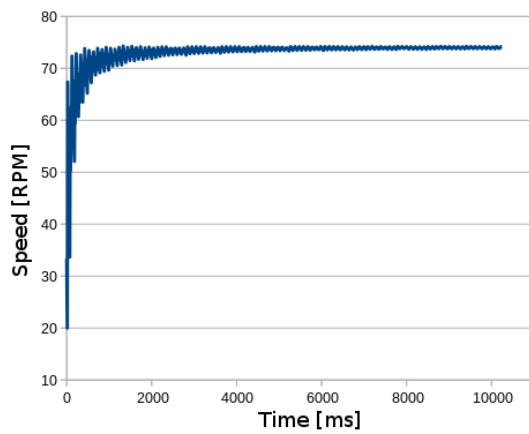
Figure L-7: Motor speed
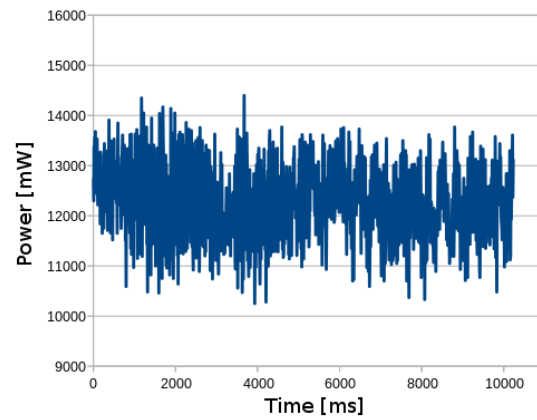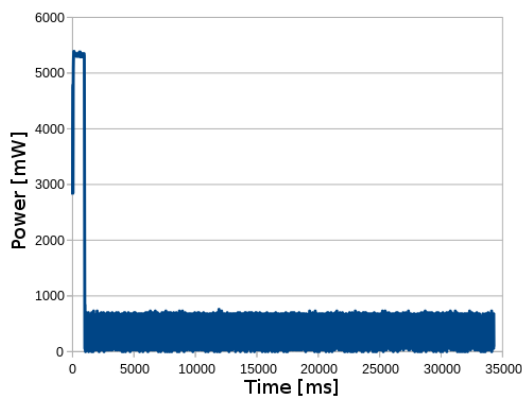

Figure L-8: Overall consumed Electrical Power
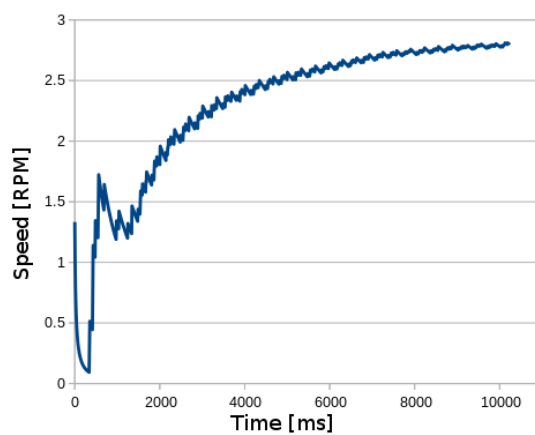
Figure L-9: Wheel-axle speed
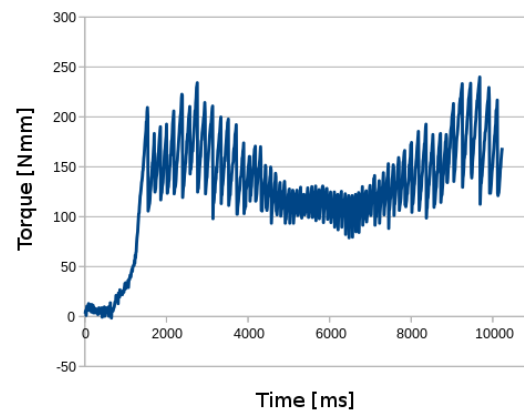
Figure L-10: Torque Wheel-axle

L-4   Test Results at 100RPM - Wheel-axle engaged
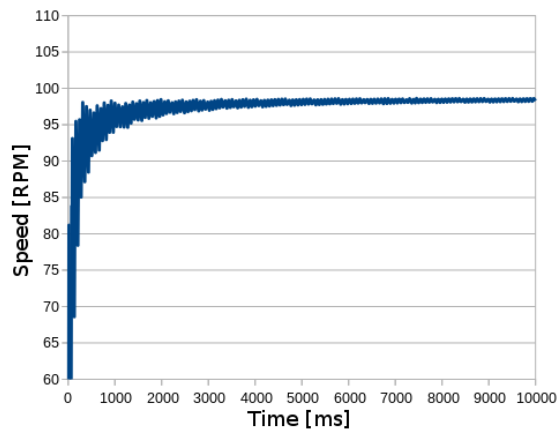
Figure L-11: Motor speed
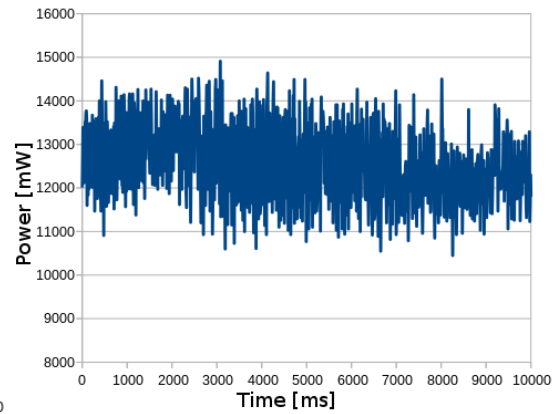
Figure L-12: Overall consumed Electrical Power
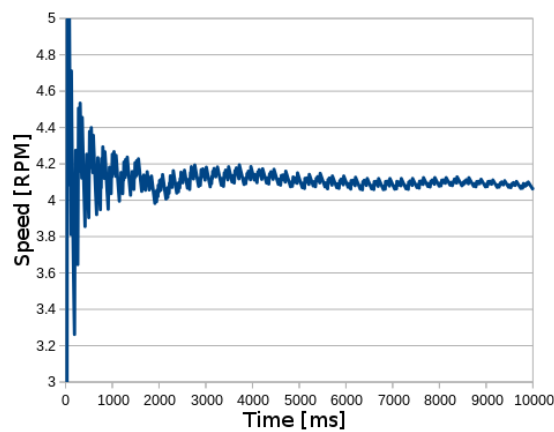


Figure L-13: Wheel-axle speed
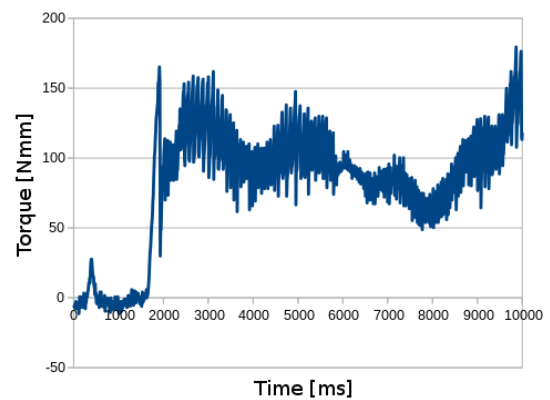

Figure L-14: Torque Wheel-axle

L-5   Test Results at 125RPM - Wheel-axle engaged
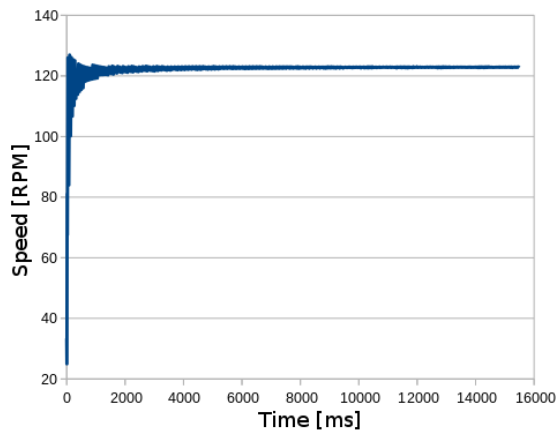
Figure L-15: Motor speed
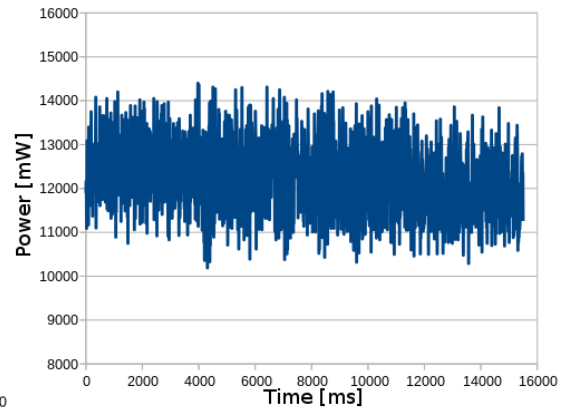
Figure L-16: Overall consumed Electrical Power
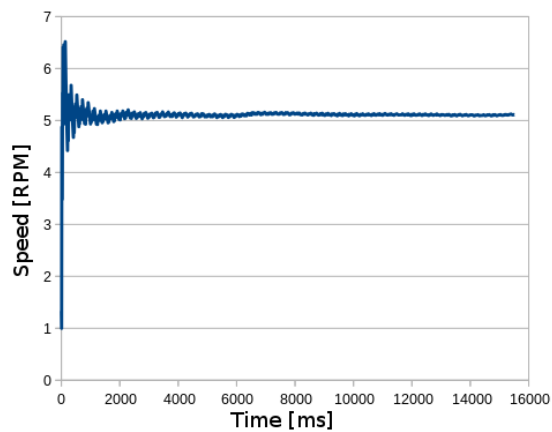
Figure L-17: Wheel-axle speed
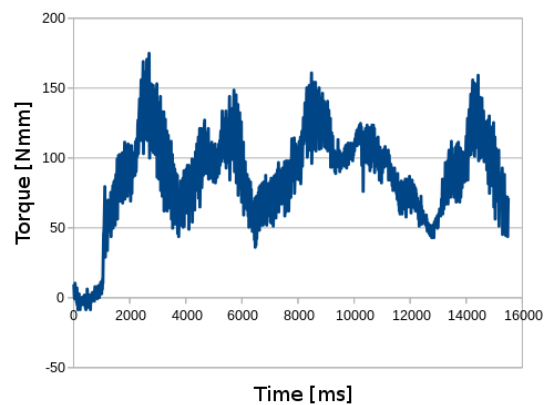
Figure L-18: Torque Wheel-axle

L-6 Test Results at 150RPM - Wheel-axle engaged
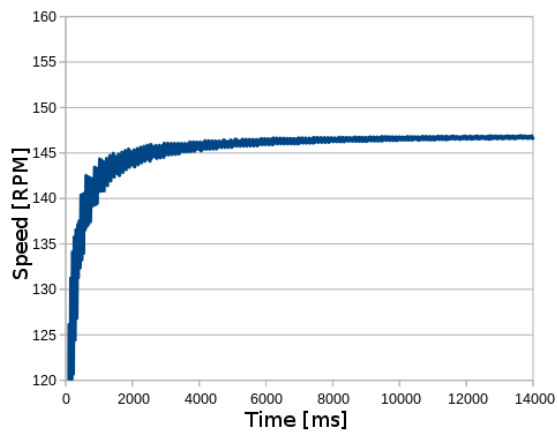
Figure L-19: Motor speed
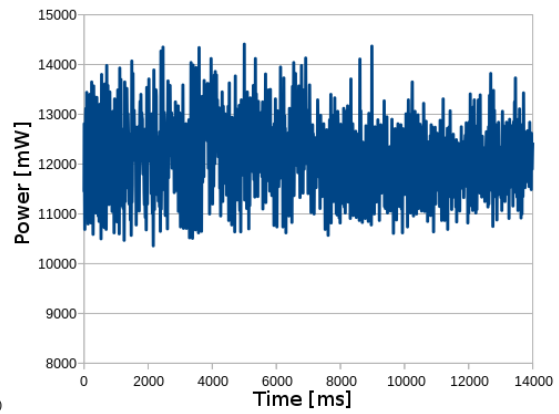
Figure L-20: Overall consumed Electrical Power
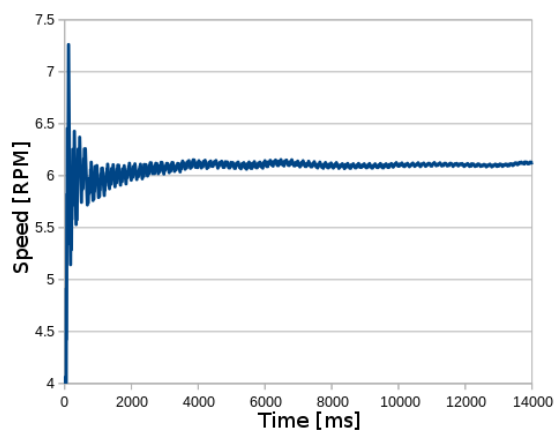
Figure L-21: Wheel-axle speed
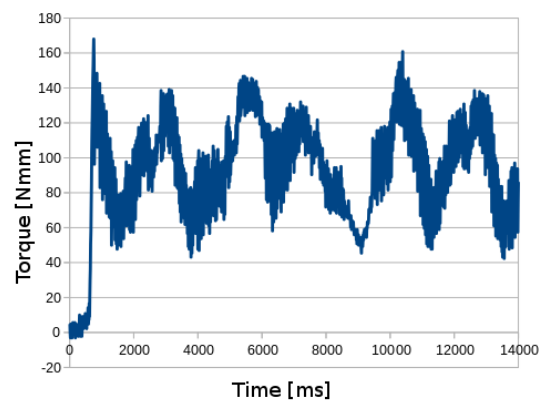
Figure L-22: Torque Wheel-axle

L-7 Test Results at 175RPM - Wheel-axle engaged
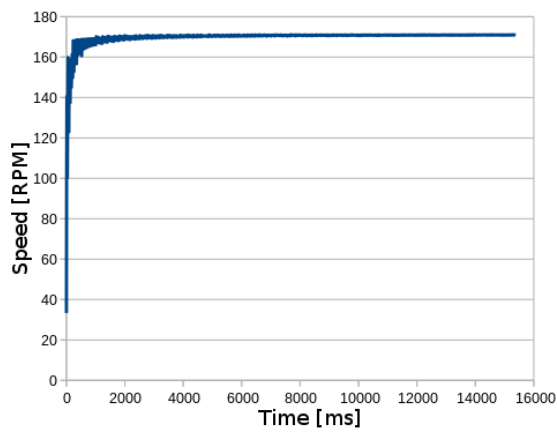
Figure L-23: Motor speed
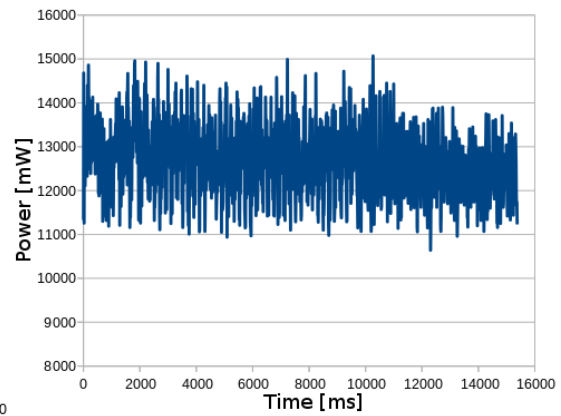
Figure L-24: Overall consumed Electrical Power
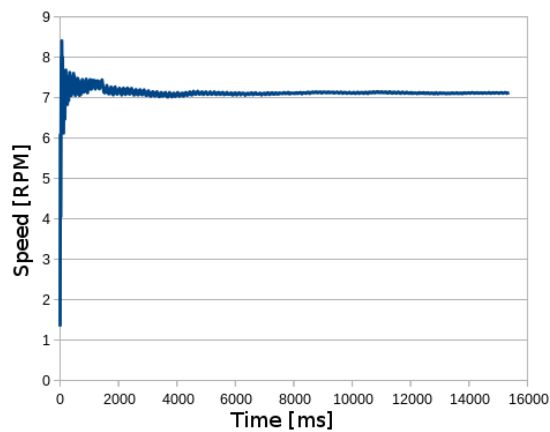
Figure L-25: Wheel-axle speed
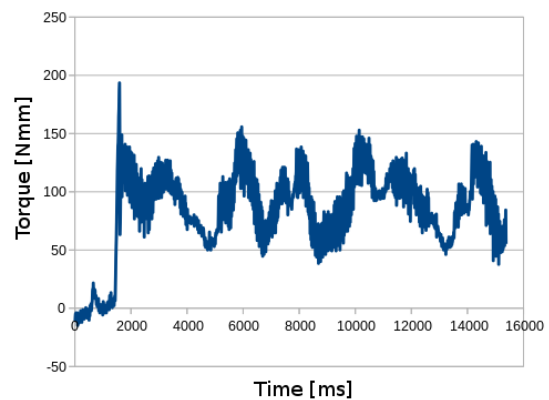
Figure L-26: Torque Wheel-axle

L-8   Test Results at 200RPM - Wheel-axle engaged
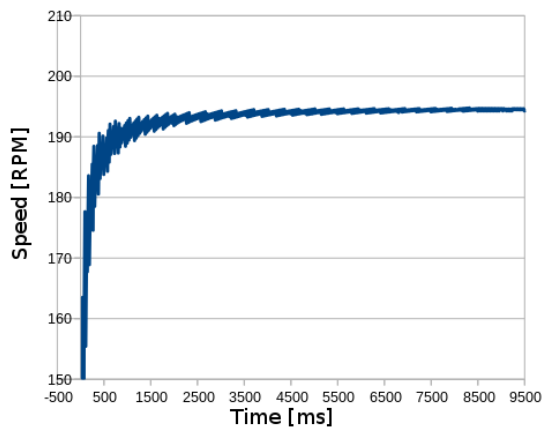
Figure L-27: Motor speed
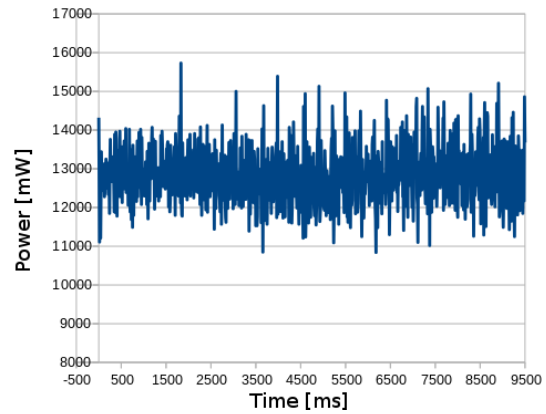
Figure L-28: Overall consumed Electrical Power
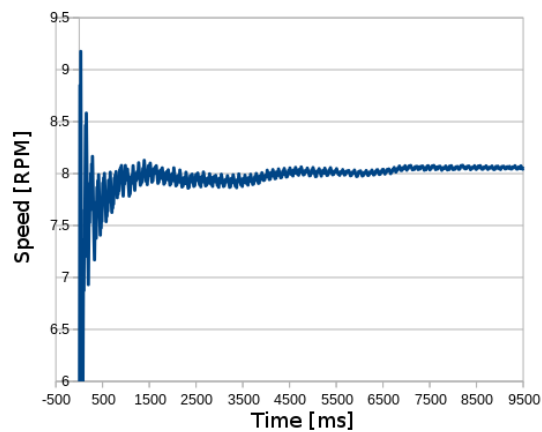
Figure L-29: Wheel-axle speed
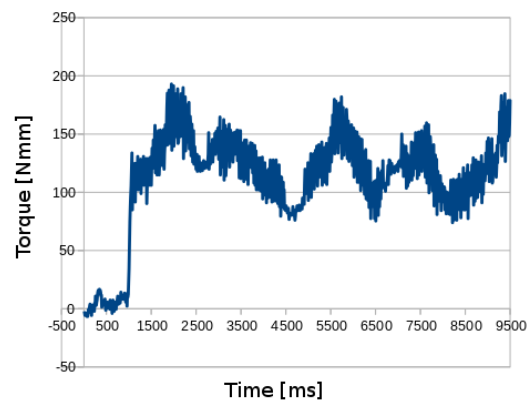
Figure L-30: Torque Wheel-axle

L-9   Test Results at 50RPM - Leg-axle engaged
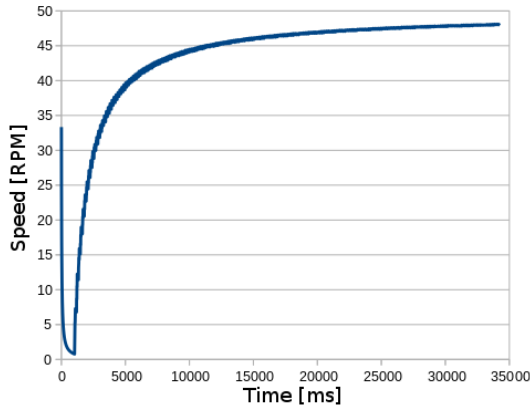
Figure L-31: Motor speed
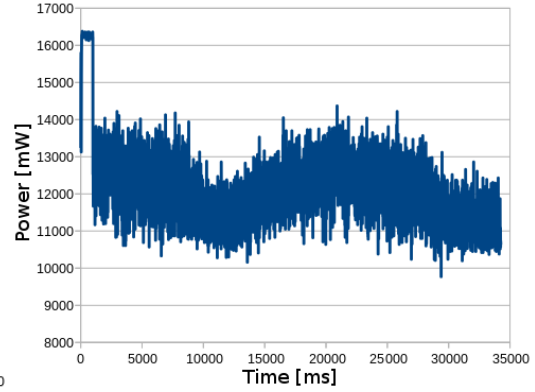
Figure L-32: Overall consumed Electrical Power
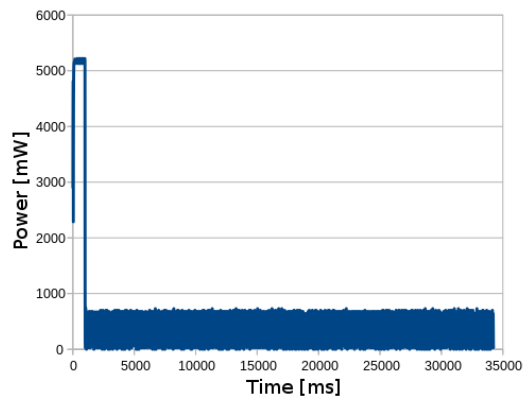
Figure L-33: Consumed Electrical Power by Magnet
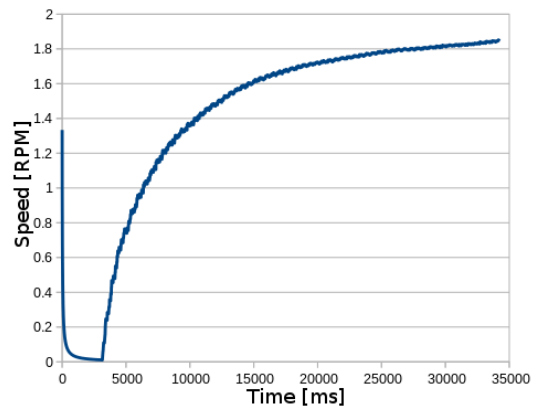
Figure L-34: speed Leg-axle
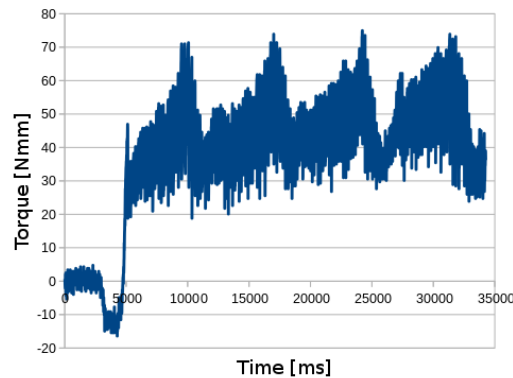
Figure L-35: Torque Leg-axle
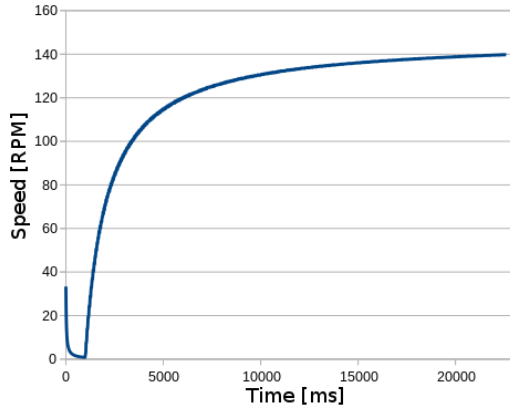
L-10 Test Results at 75RPM - Leg-axle engaged
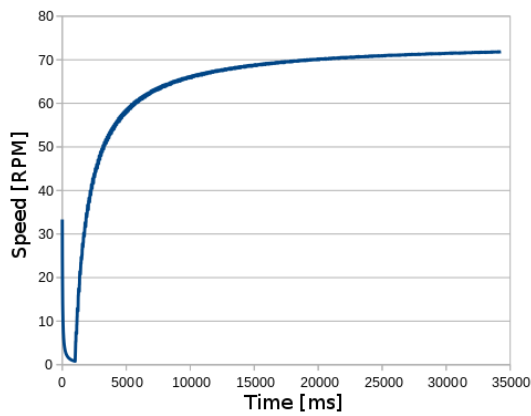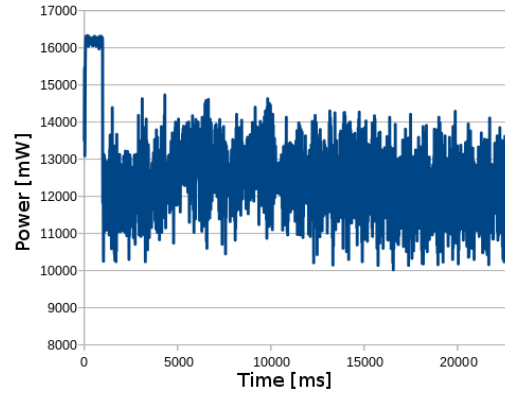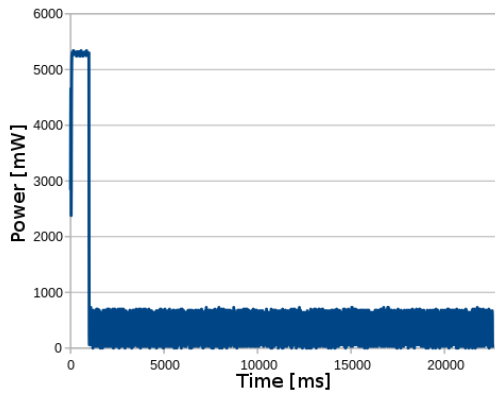

Figure L-36: Motor speed
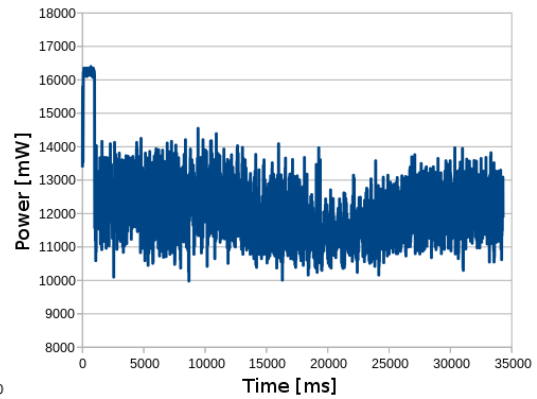
Figure L-37: Overall consumed Electrical Power

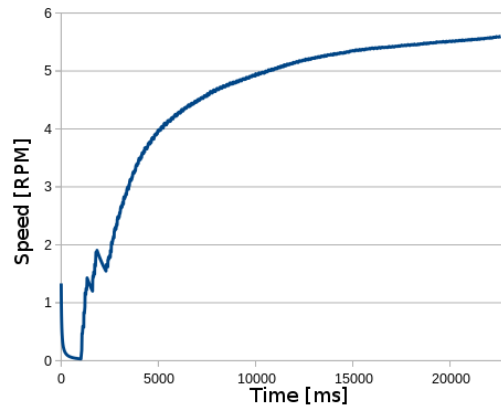**Figure L-38:** Consumed Electrical Power by Magnet
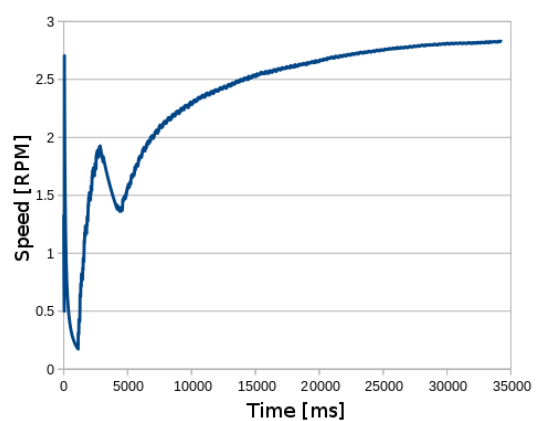
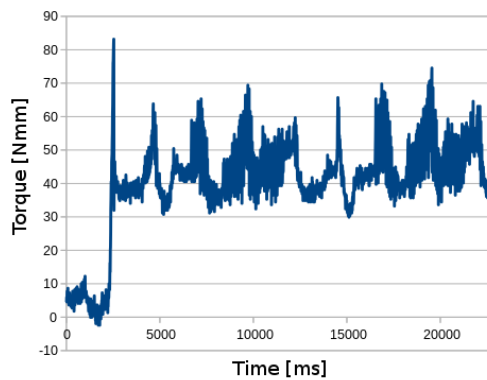**Figure L-39:** speed Leg-axle
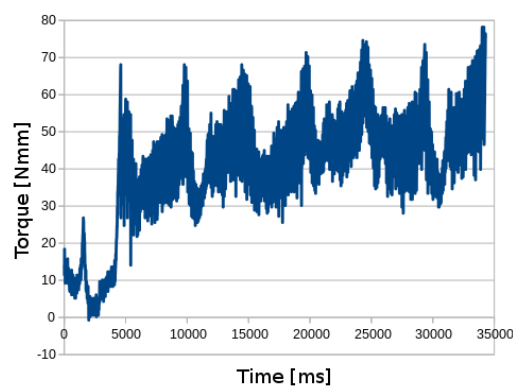
Figure L-40: Torque Leg-axle

L-11   Test Results at 100RPM - Leg-axle engaged
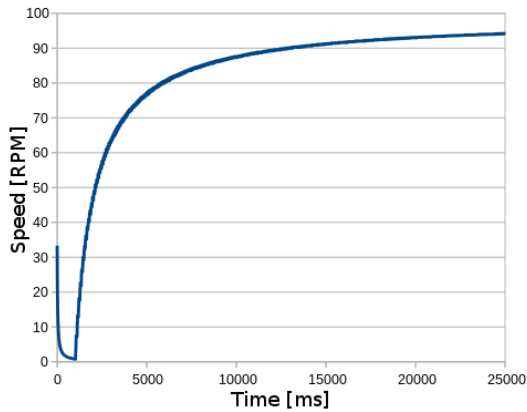
Figure L-41: Motor speed
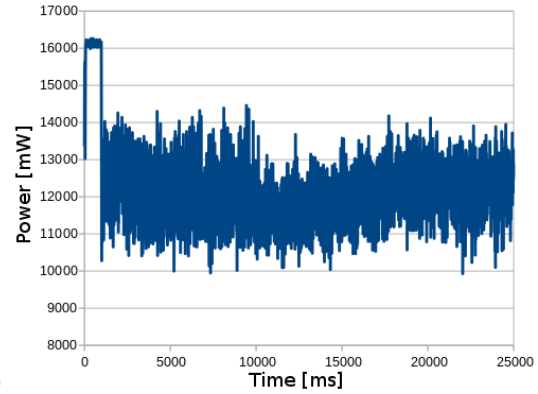
Figure L-42: Overall consumed Electrical Power
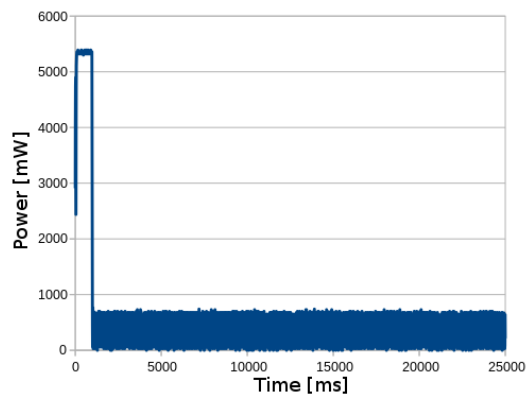
Figure L-43: Consumed Electrical Power by Magnet
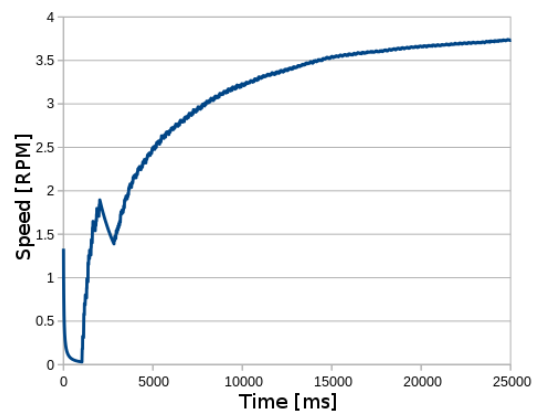
Figure L-44: speed Leg-axle
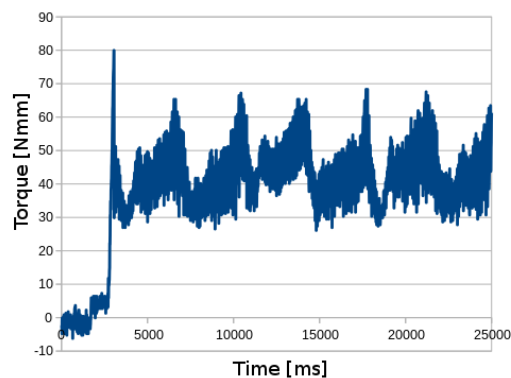
Figure L-45: Torque Leg-axle
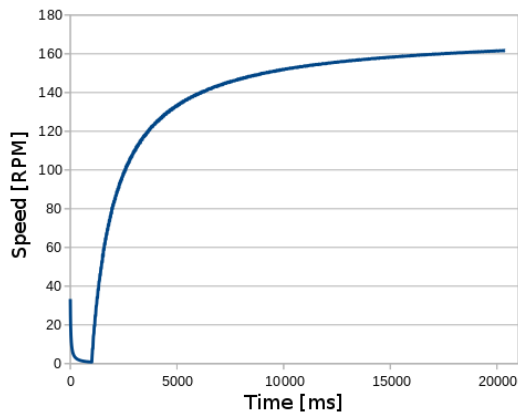
L-12   Test Results at 125RPM - Leg-axle engaged
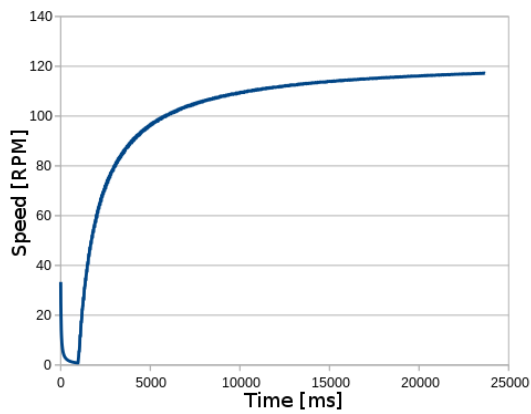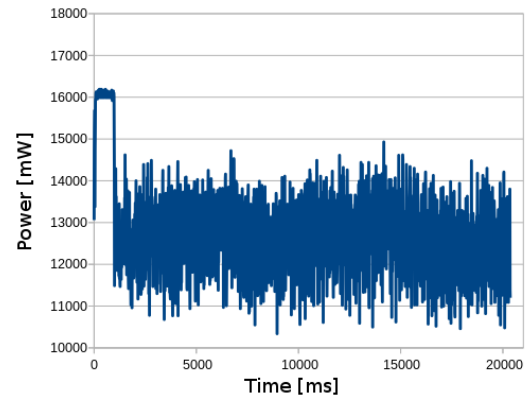

Figure L-46: Motor speed
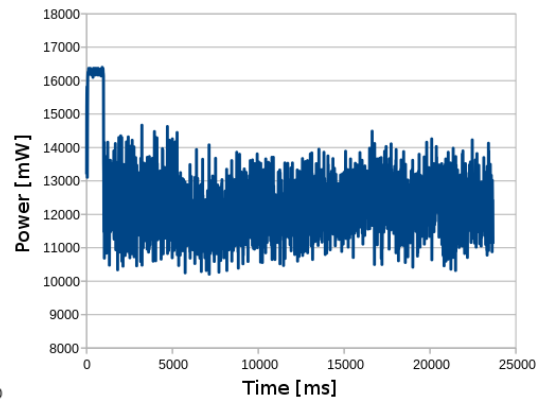
Figure L-47: Overall consumed Electrical Power
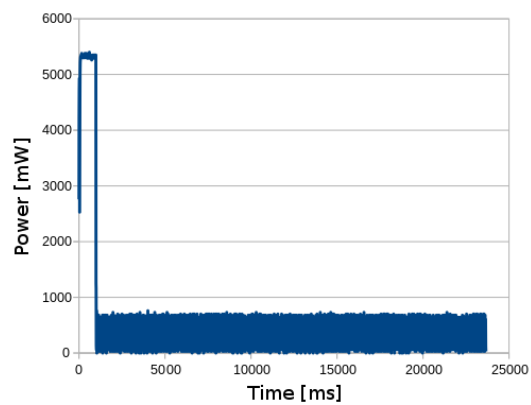
Figure L-48: Consumed Electrical Power by Magnet
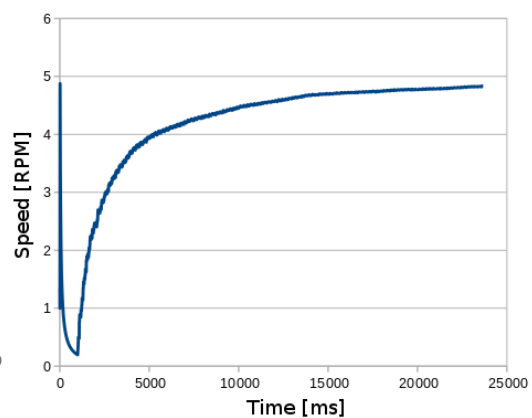
Figure L-49: speed Leg-axle
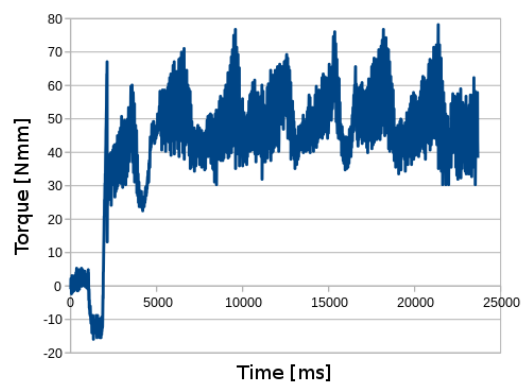
Figure L-50: Torque Leg-axle

L-13   Test Results at 150RPM - Leg-axle engaged

Figure L-51: Motor speed
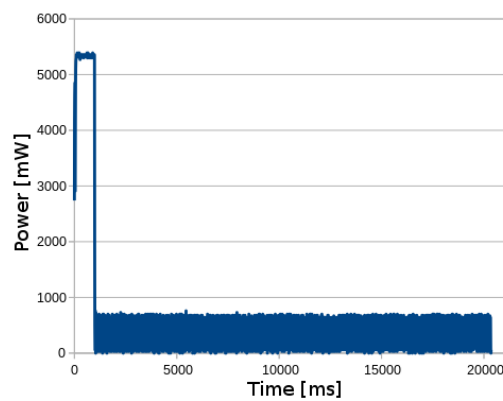

Figure L-52: Overall consumed Electrical Power

Figure L-53: Consumed Electrical Power by Magnet

Figure L-54: speed Leg-axle

Figure L-55: Torque Leg-axle

L-14 Test Results at 175RPM - Leg-axle engaged

Figure L-56: Motor speed

Figure L-57: Overall consumed Electrical Power

Figure L-58: Consumed Electrical Power by Magnet
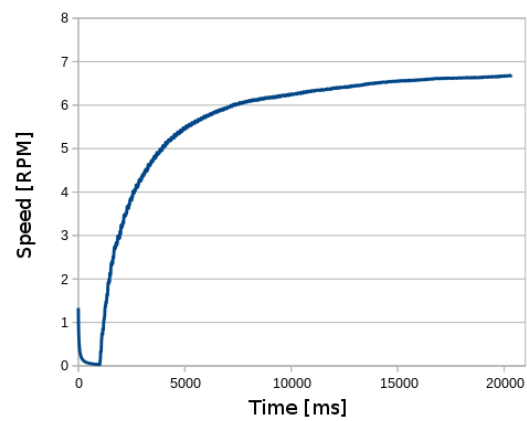

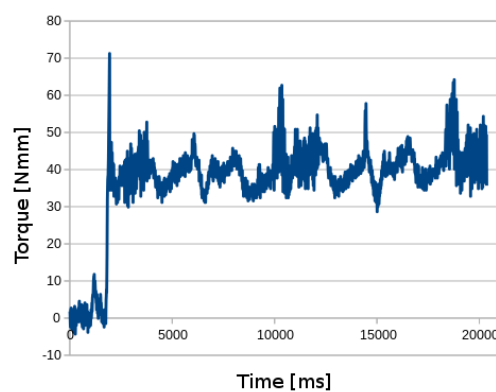**Figure L-59:** speed Leg-axle

Figure L-60: Torque Leg-axle
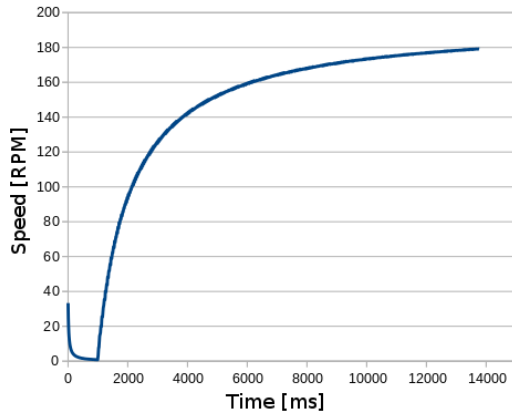
L-15   Test Results at 200RPM - Leg-axle engaged
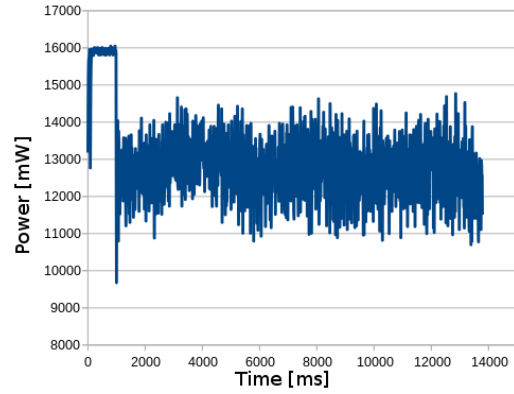

Figure L-61: Motor speed

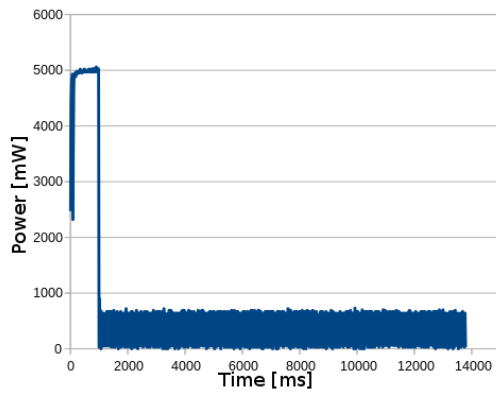**Figure L-62:** Overall consumed Electrical Power

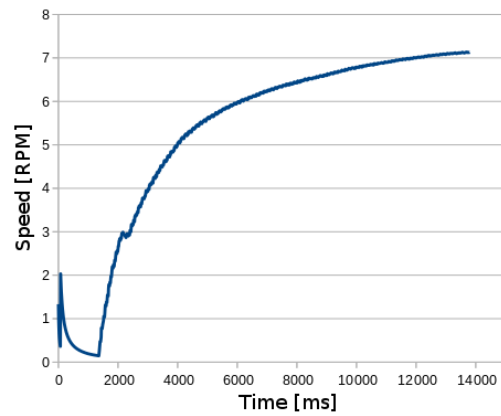**Figure L-63:** Consumed Electrical Power by Magnet

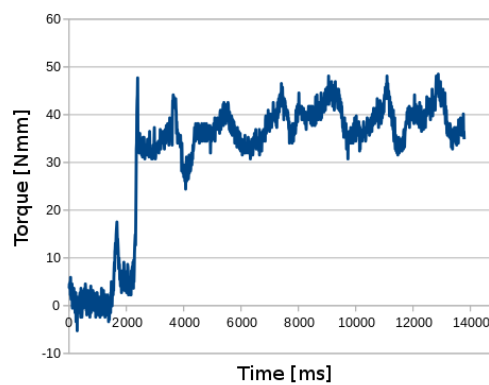**Figure L-64:** speed Leg-axle

Figure L-65: Torque Leg-axle

L-16   Final table

From the data, we can summarize the final results, listed in tables L-1 and L-2. Speed set, in RPM, is the speed set to the microprocessor. Speed M, in RPM, is the output speed from the motor as measured by the ERS-G. There's a discrepancy because of the load on the motor or because the Arduino microprocessor feeds pulses to slow to the steppermotor. Speed G, in RPM, is the calculated speed after the gear-box reduction of 24. PE_t, in W, is the consumed electrical power as measured and read from the graphs.

Table L-1: Test results - Wheel axis engaged

Speed set [RPM]	Speed M [RPM]	Speed G [RPM]	PE_t [W]	PM [W]	Tm [Nmm]	Speed W [RPM]	Tw [Nmm]
50	49.7	2.1	13	0.7	160	2.0	200
100	98.3	4.1	14	1.8	160	4.1	175
150	146.8	6.1	14	2	160	6.1	150
200	195.1	8.1	14.5	3	160	8.1	200

Table L-2: Test results - Leg axis engaged

Speed set [RPM]	Speed M [RPM]	Speed G [RPM]	PE_t [W]	PE_m [mW]	PM [W]	Tm [Nmm]	Speed L [RPM]	Tl [Nmm]
50	48.1	2.0	14	800	0.7	160	1.9	70
100	94.4	3.9	14	800	1.8	160	3.8	70
150	139.8	5.8	14.5	800	2	160	5.6	70
200	179.2	7.5	14.5	800	3	160	7.1	50

Bibliography

[1] ZebRo Group, "Zebro website." https://zebro.space, 2021.

[2] K. Huang, S. Chen, Y. Chou, S. Shen, C. Li, and P. Lin, "Experimental validation of a leg-wheel hybrid mobile robot quattroped," in *International Conference on Robotics and Automation*, pp. 2976–2977, 2011.

[3] L. I. Bongaardt, "Robots with driving and walking capability," Master's thesis, Delft University of Technology (TU-Delft), 2014.

[4] iRobot Corporation, "irobot-510-packbot-specs.ashx." http://www.irobot.com, 2012.

[5] National Aeronautics and Space Administration, "Msl_fact_sheet.pdf." http://www.nasa.gov/msl, 2012.

[6] B. Maclaurin, "Comparing the steering performances of skid- and ackermann-steered vehicles," in *Proceedings of the Institution of Mechanical Engineers*, vol. D, 2008.

[7] X. Wu, M. Xu, and L. Wang, "Differential speed steering control for four-wheel independent driving electric vehicle," in *International Journal of Materials, Mechanics and Manufacturing*, vol. 1, 2013.

[8] *Roloff/Matek Machineonderdelen.* Academic Service, 2002.

[9] *Roloff/Matek Machineonderdelen - Tabellenboek.* Academic Service, 2001.

[10] S. Group, "Poly optic 1490 clear polyurethane casting resin." https://syntecshop.com/en/poly-optic-1490-clear-polyurethane-casting-resin, 2019.

Glossary

List of Acronyms

TU-Delft	Delft University of Technology
DoF	Degree-of-Freedom
CoT	Cost of Transport
ONL	Obstacle Negotiation Limit
ZebRo	Zesbenige Robot
IRS	Integrated Rotation Sensor
ERS	External Rotation Sensor
PRs	Photo-Resistors
SMDs	Surface Mounted Devices
PWM	Pulse Width Modulation